

**Theoretical Investigation of Optical and Spectroscopic Properties of  
Organometallic Complexes and  
Design of Improved Electroluminescent Materials**

**A Thesis submitted to the University of North Bengal  
For the Award of**

**Doctor of Philosophy  
in  
Chemistry**

**By**

**Manoj Majumder**

**SUPERVISOR**

**Prof. Anirban Misra**

**Department of Chemistry  
University of North Bengal  
August, 2018**

## **DECLARATION**

I declare that the thesis entitled “**Theoretical Investigation of Optical and Spectroscopic Properties of Organometallic Complexes and Design of Improved Electroluminescent Materials**” has been prepared by me under the supervision of Prof. Anirban Misra, Department of Chemistry, University of North Bengal.

No part of this thesis has formed the basis for the award of any degree or fellowship previously.

*Manoj Majumder*

Manoj Majumder

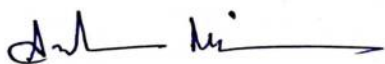
Department of Chemistry,  
University of North Bengal,  
Darjeeling-734013,  
West Bengal,

DATE: 23/08/2018

## **CERTIFICATE**

I certify that the thesis entitled “**Theoretical Investigation of Optical and Spectroscopic Properties of Organometallic Complexes and Design of Improved Electroluminescent Materials**” has been prepared by Manoj Majumder, for the award of Ph.D degree of the University of North Bengal, under my guidance. He has carried the work at the Department of Chemistry, University of North Bengal.

No part of this thesis has formed the basis for the award of any degree or fellowship previously.



Prof. Anirban Misra (Supervisor)

Department of Chemistry,  
University of North Bengal,  
Darjeeling- 734013,  
West Bengal

DATE: 23/08/2018

## Urkund Analysis Result

**Analysed Document:** Manoj\_chemistry .pdf (D40834885)  
**Submitted:** 8/16/2018 7:52:00 AM  
**Submitted By:** nbuplg@gmail.com  
**Significance:** 1 %

### Sources included in the report:

[https://www.researchgate.net/publication/283301167\\_Second-order\\_nonlinear\\_optical\\_properties\\_of\\_transition\\_metal\\_complexes](https://www.researchgate.net/publication/283301167_Second-order_nonlinear_optical_properties_of_transition_metal_complexes)  
<https://arxiv.org/pdf/1509.01532>  
<http://www.theses.fr/2012ENSL0736.pdf>

### Instances where selected sources appear:

16

*Manoj Majumder*

**Signature of Candidate**

*[Handwritten Signature]*

**Signature of Supervisor**

*[Handwritten Signature]*

**Signature of the Head of the Department with Seal**

## **ABSTRACT**

The first chapter addresses a concise history and momentous advances in the field of characterization of optical properties. This chapter introduces origin of several optical properties like nonlinear optical property, luminescence property, two-photon absorption property and also highlights current advancement in researches on designing of materials with improved optical properties. These optical properties are analyzed from the viewpoint of electronic structure theory for proper understanding of the structure property relationship. Special attention is given to the luminescent materials for their applicability as phosphorescent emitters for organic light emitting diodes (OLEDs) along with basic setup and working principles of OLED devices.

The second chapter represents a brief description of the basic theoretical background related to various optical properties along with theoretical techniques to quantify hyperpolarizability ( $\beta$ ) and two-photon absorption cross section ( $\sigma$ ). For theoretical determination of first hyperpolarizability ( $\beta$ ), early models, equivalent field model (EIF), additivity model and two-state model along with quantum chemical approaches *viz.*, sum over states (SOS) methods and coupled perturbed HF (CPHF) methods are discussed here. A short description of available methods *viz.*, few-states model for quantifying two-photon absorption cross section ( $\sigma$ ), is also presented. In case of luminescent materials, principles of computational phosphorescence are clearly stated.

The third chapter contains the results and analysis of the theoretical study on the NLO property of two synthesized aryl extended thiophene fused Nickel dithiolenes. Based on these two systems, a systematic modification of the molecules is done by substituting neutral and zwitterionic donor acceptor group at the aryl (phenyl and thenyl) ring to find their effect on NLO responses. Among the four designed systems, zwitterionic donor-acceptor group significantly reduces the HOMO-LUMO energy gap resulting an enormous increase in the first hyperpolarizability ( $\beta$ ) values. To judge their high NLO response, transition dipole moment (TDM) density is also plotted and it is found that electron dissipation occurs from one donor part to the acceptor part with a large  $\Delta r$  index value which is the quantitative measurement to understand the type of transitions. A charge transfer transition is also observed in case of zwitterionic systems. In order to highlight the NLO active segment in a molecule, a beta density analysis is also presented.

In fourth chapter six different diradical systems based on azulene coupler and nitronyl nitroxide radical moieties are studied theoretically. Among them, three ferromagnetic diradicals are chosen for further calculation to assess their usability in different biological applications such as two-photon absorption photodynamic therapy (TPA-PDT) and magnetic resonance imaging contrast agents (MRICA). The TPA cross-section values are calculated to judge their efficiency as TPA-PDT photosensitizing agents. Calculated values of TPA cross-section lie in the range of commonly used photosensitizers for PDT. It is seen that the ferromagnetic diradicals can act as very good MRI contrast agents due to their high magnetic anisotropy characteristics. The magnetic anisotropy is quantified in terms of zero-field splitting parameter using DFT. It is found that the proposed diradicals can show good relaxation behaviour and consequently act as efficient MRI contrast agents. Thus, one can anticipate the multifunctional biological activity of these diradicals.

The fifth chapter deals with designing of efficient luminescent materials based on octahedral hexaamminechromium(III) complex. It is found that distortion of the octahedral symmetry of  $[\text{Cr}^{\text{III}}(\text{NH}_3)_6]^{3+}$  by replacing the axial ligands with weaker halides influences the stability of the doublet state with respect to the quartet ground state. This replacement affects the doublet to quartet transition responsible for phosphorescence. The relative positions of the halides and ammonia in the spectrochemical series play an important role in tuning of emission wave length. The proximity of fluorine and ammonia in the spectrochemical series causes blue-shift in the emission wavelength and thus provides a rational way for designing blue emitting phosphorescent materials, essential in OLED application for full color display.

The sixth chapter provides a comprehensive study of molecular mechanism of excited state relaxation induced by intermolecular hydrogen-bond formation. The absorption and fluorescence property of 2-amino pyridine (2-AP) and its dimer  $(2\text{-AP})_2$  are analyzed theoretically in order to unveil the effect of intermolecular H-bonding interaction in the photochemical behavior of 2-AP. All the calculations (DFT and TDDFT) are performed using ADF suit of program with dispersion corrected methods (DFT-D). To reveal the cooperativity due to H-bonding, a decomposition analysis (EDA) in the framework of the Kohn-Sham molecular orbital (MO) model is performed. The ETS-NOCV calculations are performed for the equilibrium geometries of the ground and excited states of the dimer. The formation of H-bond has been confirmed by the calculation of synergy ( $\Delta E_{\text{syn}}$ ) from the difference of interaction

energy ( $\Delta E_{int}$ ) with and without H-bond interactions. H-bond interaction affects the energy of the electronic excited state of the dimer resulting red-shift in the emission spectrum.

General and comprehensive conclusions of all the chapters are given in the final chapter.

## **PREFACE**

Recent years have witnessed evolution of multifunctional materials to meet the urge of rapidly evolving technological world. To design such materials, optical properties are one of the important characteristics to delve into. Knowledge of the quantum chemical origin of different kind of optical properties in molecules are extremely important for tuning smart materials with desired functionality. We have put our effort to systematically increase the nonlinear optical (NLO) response in molecular systems, which can effectively guide the synthesis of molecules for use in three dimensional memory storage, optical limiting, optical switching etc. In our study, inclusion of zwitterionic substituents has been found to have significant effect on NLO response of molecules, where the push and pull of charges tremendously increase the first hyperpolarizability values. In continuation of our effort to design multifunctional material, coinciding useful magnetic and optical response in the same system seemed to be an interesting idea. There have been reports where organic molecules with both the magnetic and NLO response achieve multifunctionality and this feature is used in the field of biomedicine. From the urge of designing such molecules, we have proposed diradical systems with stable ferromagnetic ground state and reasonable two-photon absorption cross section. Simultaneous presence of these two features makes the systems a promising candidate for magnetic resonance imaging contrast agent and photo sensitizer. Our next work is based on the design of luminescent materials, which have become an indispensable part of our life. In order to construct luminescent devices, specific emitting materials are required amongst which blue emitting materials are rarest for high energy electron transition. This fact motivates us to find out the electronic structural criteria for blue emission, and thus we find appropriate choice of ligands around a 3d transition element can really lead to the electronic transition in blue wavelength region. Such luminescent materials based on 3d transition metals surmount the difficulty of luminescence quenching commonly found in heavy metal-based systems. We also explore the effect of weak interactions like H-bonding on fluorescence. Our study divulges that the H-bonding stabilizes the excited electronic state more compared to the ground state resulting red shift.

## TABLE OF CONTENTS

<u><i>Chapter 1: Optical properties of organic and metal based systems</i></u>	<b>1-23</b>
<b>1.1. Introduction</b>	<b>2</b>
<b>1.2. Nonlinear optical property</b>	<b>3</b>
1.2.1. Definition of nonlinear optics	3
1.2.2. Origin of NLO	3
1.2.3. Microscopic nonlinearities	6
1.2.4. Various types of second order NLO effects	8
1.2.4.1. Second harmonic generation (SHG)	8
1.2.4.2. Sum frequency generation or parametric generation	8
1.2.4.3. Linear electrooptic effect or pockels effect	9
1.2.4.4. Optical rectification	9
1.2.5. Applications of NLO effects	9
1.2.6. Present status of the field	10
1.2.6.1. Organic molecules for second-order nonlinear optics	11
1.2.6.2. Metal complexes for second-order nonlinear optics	12
<b>1.3. Luminescence</b>	<b>12</b>
1.3.1. Luminescence and stocks law	13
1.3.2. Types of luminescence	14
1.3.3. Basic principles of luminescence	14
1.3.4. Electroluminescence and OLEDs	15
1.3.4.1. The OLED structure	16
1.3.4.2. Mechanism of exciton formation	16
1.3.4.3. Triplet and singlet harvesting	18
1.3.4.4. Requirements of triplet emitters for OLEDs	19
1.3.5. Structural classes exhibiting room temperature phosphorescence	19
1.3.6. Recent status of the field.	20
<b>1.4. Aim of the present work</b>	<b>22</b>
<u><i>Chapter 2: Theoretical background of computational methods</i></u>	<b>24-36</b>
<b>2.1. Theoretical determination of first hyperpolarizability</b>	<b>25</b>
2.1.1. Early model for calculating $\beta$	25

<b>2.2. Quantum chemical approach for the calculation of <math>\beta</math></b>	<b>26</b>
2.2.1. Sum over states (SOS) methods	27
2.2.2. Coupled perturbed HF (CPHF) methods	28
<b>2.3. One and two-photon absorption</b>	<b>29</b>
2.3.1. Few state models	31
<b>2.4. Principles of computational phosphorescence</b>	<b>33</b>
2.4.1. Spin-orbit coupling and S-T mixing	34
2.4.2. Perturbation theory for S-T transitions	34
2.4.3. Phosphorescence intensity and lifetime	36
2.4.4. Quadratic response theory and Phosphorescence	36
<b><u><i>Chapter 3: Strategic design of thiophene-fused nickel dithiolenes for efficient NLO response</i></u></b>	<b><u>37-51</u></b>
<b>3.1. Introduction</b>	<b>38</b>
<b>3.2. Theoretical background</b>	<b>40</b>
<b>3.3. Computational details</b>	<b>42</b>
<b>3.4. Results and discussions</b>	<b>43</b>
3.4.1. The electronic structure of nickel dithiolenes (NiDT)	43
3.4.2. HOMO-LUMO gap, excitation energies and NTOs analysis	44
3.4.3. NLO properties	48
<b>3.5. Conclusions</b>	<b>51</b>
<b><u><i>Chapter 4: Multifunctional magnetic materials of organic origin for biomedical applications: A theoretical study</i></u></b>	<b><u>52-65</u></b>
<b>4.1. Introduction</b>	<b>53</b>
<b>4.2. Theoretical background</b>	<b>55</b>

<b>4.3. Computational details</b>	<b>58</b>
<b>4.4. Results and discussions</b>	<b>59</b>
<b>4.5. Conclusion</b>	<b>64</b>
<i><u>Chapter 5: Ligand induced symmetry breaking and concomitant blue shift of emission wavelength in octahedral chromium complex</u></i>	<b>66-75</b>
<b>5.1. Introduction</b>	<b>67</b>
<b>5.2. Computational methods</b>	<b>68</b>
<b>5.3. Results and discussions</b>	<b>69</b>
<b>5.4. Conclusions</b>	<b>75</b>
<i><u>Chapter 6: Photochemical study of 2-aminopyridine: A density functional investigation</u></i>	<b>76-82</b>
<i><u>Chapter 7: General conclusion</u></i>	<b>83-86</b>
<i><u>Bibliography</u></i>	<b>87-100</b>
<i><u>Index</u></i>	<b>101-102</b>

## LIST OF TABLES

Table	Caption	Page
<b>Table 1.2.1.</b>	Susceptibility functions ( $\chi^{(2)}$ and $\chi^{(3)}$ ) for various types for interacting field components, their effects and applications.	<b>9</b>
<b>Table 3.1.</b>	HOMO/LUMO energies and $\beta_{tot}$ values of NiTDT and its derivative computed in gas-phase at UB3LYP/6-311++g(d,p) level of theory.	<b>45</b>
<b>Table 3.2.</b>	TDDFT calculated transitions for thienyl (1a) and phenyl (2a) expanded analogues of NiTDT core and its derivative (1b, 1c & 2b, 2c) at CAM-B3LYP/6-311g(d,p) level of theory.	<b>46</b>
<b>Table 3.3.</b>	Transition energies (eV, nm), their oscillator strengths ( $f$ ) and transition dipole moment densities for three strong transitions for Ph-NiTDT. The purple color implies charge increase upon excitation and the turquoise color implies charge depletion. The isovalue is $4 \times 10^{-4}$ in a.u.	<b>49</b>
<b>Table 3.4.</b>	Major transition energies (eV, nm), their oscillator strengths ( $f$ ), $\Delta r$ index and eigenvalues for three strong transitions for two sets of complexes (1a, 1b, 1c & 2a, 2b, 2c) calculated at CAM-B3LYP/6-311g(d,p)	<b>49</b>
<b>Table 4.1.</b>	Calculated absolute energies in atomic units (au), $\langle S^2 \rangle$ values, intramolecular magnetic exchange coupling constants ( $J$ in $\text{cm}^{-1}$ ) between two radical centers for the designed diradicals at UB3LYP/6-311++g (2df, 2p) level.	<b>61</b>
<b>Table 4.2.</b>	The spin-spin ZFS parameter $D_{Total}$ ( $\text{cm}^{-1}$ ), static ZFS magnitude $a_2$ ( $\text{cm}^{-1}$ ), rhombic ZFS parameter ( $E$ ) for each ferromagnetic diradical at BPW91/EPR-II and two photon absorption cross section ( $\sigma_{TPA}$ in GM), for the same diradicals at UB3LYP/6-311++g(d,p) level.	<b>63</b>
<b>Table 4.3.</b>	The magnetic exchange coupling constants ( $J$ ) and ZFS parameter ( $D$ ) values for the proposed ferromagnetic diradical systems in gas phase, water and blood plasma media, computed using PCM model using UB3LYP/6-311++g(2df,2p) and BPW91/EPR-II method.	<b>64</b>
<b>Table 5.1.</b>	Bond distance between Cr and axial ligand (Cr- $L_{ax}$ ), Cr and equatorial ligand (Cr- $L_{eq}$ ) and energies of the $[\text{Cr}^{\text{III}}(\text{NH}_3)_6]^{3+}$ at quartet ground state ( $Q$ ), quartet excited state ( $Q'$ ), and doublet ground state ( $D$ ).	<b>70</b>
<b>Table 5.2.</b>	Comparison of absorption and emission wavelengths in nm (energies in $\text{cm}^{-1}$ ) with experimental value in $[\text{Cr}^{\text{III}}(\text{NH}_3)_6]^{3+}$ .	<b>71</b>

<b>Table 5.3.</b>	Bond distance between Cr and axial ligand (Cr-L <sub>ax</sub> ), Cr and equatorial ligand (Cr-L <sub>eq</sub> ) and energies of the complex [Cr <sup>III</sup> (NH <sub>3</sub> ) <sub>4</sub> (X) <sub>2</sub> ] <sup>+</sup> (X= I <sup>-</sup> , Br <sup>-</sup> , Cl <sup>-</sup> , and F <sup>-</sup> , represented by violet, brown, green and light blue colors respectively).	<b>72</b>
<b>Table 5.4.</b>	Calculated hardness values in eV for the studied complex (ground state quartet).	<b>73</b>
<b>Table 5.5.</b>	Comparison of absorption and emission wavelengths in nm (energies in cm <sup>-1</sup> ) in [Cr <sup>III</sup> (NH <sub>3</sub> ) <sub>4</sub> (X) <sub>2</sub> ] <sup>+</sup> (X= I <sup>-</sup> , Br <sup>-</sup> , Cl <sup>-</sup> , and F <sup>-</sup> ).	<b>74</b>
<b>Table 6.1.</b>	Bonding energy decomposition of ground and excited states of the dimer.	<b>79</b>
<b>Table 6.2.</b>	Comparison of the calculated value $\lambda_{max}$ of absorption and fluorescence with experimentally reported values.	<b>81</b>
<b>Table 6.3.</b>	HOMO-LUMO gap of monomer unit and hydrogen bonded dimer.	<b>82</b>

---

## LIST OF FIGURES AND SCHEMES

Figure	Caption	Page
<b>Figure 1.2.1.</b>	Linear (left) and nonlinear (right) interactions of waves and the media.	<b>3</b>
<b>Figure 1.2.2.</b>	Energy band diagram of linear (left) and nonlinear optics (right).	<b>4</b>
<b>Figure 1.2.3.</b>	(a) Polarization response ( $P$ ) plot to an incident electromagnetic wave of field strength $E(\omega)$ in a noncentrosymmetric medium at frequency $\omega$ . (b) to (d) Fourier components of $P$ at frequencies $2\omega$ , $\omega$ , and $\theta$ .	<b>5</b>
<b>Figure 1.2.4.</b>	Nonlinear polarization response ( $P$ ) plot to an incident electromagnetic field in a centrosymmetric medium.	<b>6</b>
<b>Figure 1.2.5.</b>	Model system with electron donor and acceptor substituents which results the asymmetric charge distribution along with large $\beta$ . Considering the reference coordinate system as $z$ - axis which is parallel to the dipolar axis of the molecule, the molecule is most easily polarized along $z$ direction. Hence $\beta_{zzz}$ is the largest component of the $\beta_{ijk}$ tensor.	<b>7</b>
<b>Figure 1.2.6.</b>	Second harmonic generation (SHG)	<b>8</b>
<b>Figure 1.2.7.</b>	Paramagnetic generation.	<b>8</b>
<b>Figure 1.3.1.</b>	Classification of luminescence based on duration of emission.	<b>13</b>
<b>Figure 1.3.2.</b>	Jablonski diagram representing the absorption, fluorescence and phosphorescence. Thick arrow represents absorption of light; dashed ones indicate vibrational relaxation and non-radiative decay.	<b>15</b>
<b>Figure 1.3.3.</b>	Basic set up of a layered OLED structure. Triplet emitters are represented by asterisks.	<b>16</b>
<b>Figure 1.3.4.</b>	Dynamics of exciton formation.	<b>17</b>
<b>Figure 1.3.5.</b>	Electro-luminescence excitation processes for (a) organic and (b) organo-transition metal emitters. (c) and (d) representing triplet and singlet harvesting effect respectively.	<b>18</b>
<b>Figure 2.1.</b>	Two-photon absorption.	<b>30</b>
<b>Figure 2.2.</b>	The excitation channels: $S_0 \rightarrow S_2 \rightarrow S_1$ and $S_0 \rightarrow S_1 \rightarrow S_1$ , the numbers beside the lines are transition moments.	<b>33</b>

<b>Figure 3.1.</b>	Schematic presentation of different oxidation state of NiDT complex.	<b>43</b>
<b>Figure 3.2.</b>	Redox activity of Ni dithiolene complex.	<b>44</b>
<b>Figure 3.3.</b>	The dominant natural transition orbital (NTO) pairs for the systems under study. The “hole” (highest occupied transition orbital; HOTO) is on the left, the “particle” (lowest unoccupied transition orbital; LUTO) on the right. The associate eigenvalues, $\lambda_{max}$ is given over the arrow.	<b>47</b>
<b>Figure 3.4.</b>	The transition dipole moment density of the electronic state transition from ground state for the studied complexes. The purple color implies charge increase upon excitation and the turquoise color implies charge depletion. The isovalue is $4 \times 10^{-4}$ in a.u.	<b>50</b>
<b>Figure 3.5.</b>	Isosurfaces of the static $\beta$ density of all the studied complexes calculated at UB3LYP/6-311++g(d,p) level.	<b>51</b>
<b>Figure 4.1.</b>	Optimized molecular geometry of the diradicals obtained through unrestricted B3LYP exchange correlation functional using the 6-311g(d,p) basis set.	<b>60</b>
<b>Figure 4.2.</b>	Spin density plots of ferromagnetic azulene diradicals. Green and blue surfaces indicate up and down spin density. Same color code is used for schematic representation of spin alternation, <i>i.e.</i> , blue and green arrow for up and down spin respectively.	<b>61</b>
<b>Figure 5.1.</b>	$t_{2g}$ and $e_g$ set of orbitals in $[\text{Cr}^{\text{III}}(\text{NH}_3)_6]^{3+}$ .	<b>70</b>
<b>Figure 5.2.</b>	Oscillation vectors in the (a) 16 <sup>th</sup> vibrational modes in the $D$ state and (b) the 20 <sup>th</sup> vibrational mode in the $Q'$ state of $[\text{Cr}^{\text{III}}(\text{NH}_3)_6]^{3+}$ .	<b>71</b>
<b>Figure 5.3.</b>	Orbital splitting pattern in the ground state quartet ( $Q$ ), excited state quartet ( $Q'$ ), and the doublet state of $[\text{Cr}^{\text{III}}(\text{NH}_3)_6]^{3+}$ .	<b>72</b>
<b>Figure 6.1.</b>	B3LYP-D/TZ2P optimized geometry of 2-aminopyridine at its ground state.	<b>78</b>
<b>Figure 6.2.</b>	The H-bonded dimer (a) front view and (b) side view.	<b>78</b>
<b>Figure 6.3.</b>	Absorption spectra of (a) monomer unit and (b) hydrogen bonded dimer.	<b>80</b>
<b>Figure 6.4.</b>	Fluorescence spectra of (a) monomer unit and (b) hydrogen bonded dimer.	<b>81</b>
<b>Scheme 1.2.1.</b>	P-nitroaniline molecule, the prototypical dipolar $D$ - $\pi$ - $A$ system.	<b>10</b>
<b>Scheme 1.2.2.</b>	Dipolar <i>vs.</i> octupolar charge distribution in prototypical dipolar and trigonal octupolar systems.	<b>10</b>

<b>Scheme 3.1.</b>	Schematic representation of the studied and designed systems.	<b>40</b>
<b>Scheme 4.1.</b>	Schematic representation of the diradicals under investigation.	<b>55</b>

## **APPENDICES**

### **APPENDIX A: List of publications**

#### **PUBLISHED**

1. Ligand Induced Symmetry Breaking and Concomitant Blue Shift of Emission Wavelength in Octahedral Chromium Complex, **M. Majumder**, S. Paul and A. Misra, *J. Mol. Model.*, 2018, 24:230., <https://doi.org/10.1007/s00894-018-3768-7>.
2. Strategic Design of Thiophene-fused Nickel Dithiolene Derivatives for Efficient NLO Response, **M. Majumder** and A. Misra, *Phys. Chem. Chem. Phys.* 2018, 20, 19007-19016.
3. Multifunctional Magnetic Materials of Organic Origin for Biomedical Applications: A Theoretical Study, **M. Majumder**, T. Goswami and A. Misra, *ChemistrySelect*, 2018, 3, 933-939.
4. Photochemical Study of 2-Aminopyridine: A Density Functional Investigation, **M. Majumder**, T. Goswami, A. Misra, S. Bardhan and S. K. Saha, *Commun. Comput. Chem.*, 2013, 1, 225-234.

## APPENDIX B: Acknowledgement

On the occasion of the completion of the thesis, it is my pleasant duty to convey my appreciation for all those whose support and encouragement made my task much easier.

I have no words to thank, admire and appreciate the person behind this thesis Prof. Anirban Misra, my research supervisor, whose precious suggestions and incessant encouragement helped me to love the subject and realize it better. I am deeply thankful to him for his valuable advice and guidance.

I take immense pleasure to offer my special thanks to Prof. Pranab Ghosh, Head, Department of Chemistry, for his support.

I express my gratitude to Prof. M. N. Roy, Prof. S. K. Saha, Prof. B. Basu, Prof. A. K. Panda, Dr. P. Bandyopadhyaya, Dr. A. K. Nanda, Dr. Biswajit Sinha, Dr. Sajal Das and all the non teaching staff members of this Department.

I wish to express my thanks to my colleagues for their most friendly cooperation and support in the needy hours, among whom Dr. Satadal Paul, Dr. Tamal Goswami, Dr. Suranjan Shil, Dr. Rakesh Kar, Dr. Debojit Bhattacharya, Dr. Banita Sinha, Ms. Prodipta Sarbadhikary, Ms. Manoswita Homray, Ms. Tanushree Sutradhar, Mr. Sudip Sarkar, Mr. Soumik Das, Dr. Soumik Bardhan, deserve a special mention.

I cannot express my gratitude in mere words to my parents for their affectionate encouragement and support throughout. I would also like to acknowledge the moral support and cooperation of my brother, sisters, brother-in-law, sister-in-law and nephews and nieces.

Of course, this work would not have been realizable but for the selfless and untiring support give by my wife Sunu.

Darjeeling

Manoj Majumder

August, 2018

# **CHAPTER 1**

## ***Optical properties of organic and metal based systems***

### **Abstract**

---

The first chapter addresses a concise history and momentous advances in the field of optical characterization of molecules. In this chapter a brief description of the origin and advancement of research in several optical properties like nonlinear optical property, luminescence property and two-photon absorption property are given which associate the sequential development for designing new materials. A basic theoretical approach of these optical properties from the viewpoint of electronic structure theory is described for proper understanding of the structure property relationship. A special attention is also given to the luminescent materials for their applications as phosphorescent emitters for organic light emitting diodes (OLEDs) along with basic setup and working principles of OLED devices.

---

## 1.1. Introduction

Exploring the physical and chemical properties of matter by using light is a natural concept and for a long time we have been doing this with our vision. For example, from the color of emitted light one can predict how hot an incandescent object is, thickness variation of a soap film from the colors of light it transmits, from the amount of absorbed light the concentration of solutions can also be judged. With the advancement of civilization, people are using specialized instrumentation technique to extend the range, perception, sensitivity, and precision of our vision or using photons of light to determine materials properties, what we call optical characterization. Many different characterization techniques have been reported so far that use photons with energies in the range of electromagnetic spectrum. Optical properties of materials are one of the most powerful characterization techniques that have played a significant role in the development of science and our current understanding of the universe. A few notable examples are:

- (i) The study of the blackbody radiation, which lead to the formulation of quantum mechanics by Max Planck.
- (ii) The discovery and study of the photoelectric effect, which provide evidence of the dual nature of light.
- (iii) The study of the optical emission from atoms and molecules, which provided evidence of their quantized electron energy levels. The chemical element helium was discovered from the observation of the emission spectrum of the Sun.

Generally optical properties of materials depend on the structural, morphological, electronic and physical properties. When light enters into a matter, its electromagnetic field interacts with the localized electromagnetic field of atoms. After performing the interactions when it emerges from the matter, its characteristics and properties may not be the same. How the matter can affect the light depends on the strength of the field of the light, its wavelength, and the matter itself. In addition, external influences such as temperature, pressure, and other external fields (electrical, magnetic) can also manipulate the interactions. These interactions are also helpful in constructing optical devices. In this chapter our intension is to give a brief introduction to two specific optical properties, *viz.*, nonlinear optical response and luminescence.

## 1.2. Nonlinear optical property

### 1.2.1. Definition of nonlinear optics

The interactions of applied electromagnetic fields with various materials to produce new field that altered in phase, frequency, amplitude or other propagation characteristics from the incident one are termed as nonlinear optics (NLO).<sup>1</sup> This kind of nonlinear interaction can only be observed with a very high intensity (electric field) of the incoming field. Following scheme (Figure 1.2.1) represents linear and nonlinear interactions of the wave and the media.

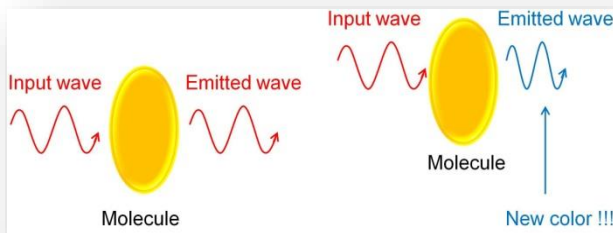


**Figure 1.2.1.** *Linear (left) and nonlinear (right) interactions of waves and the media.*

During the past few decades the field of NLO and photonics has secured a good place as a new frontier science and technology in application areas that has been dominated previously by electronics. In Photonics, in order to acquire, accumulate and transmit information, a photon instead of an electron is used. A photonic circuit is very much similar to that of electronic circuit. The major difference is that in photonic circuit photons are conducted through channels and light can be switched from one channel to another at certain junction points. For optical switching at these junctions, we need to use a material that allows the manipulation of light propagation by application of an electric field or a laser pulse. The materials that can control the light at these junction points are known as NLO materials and these are gaining importance day by day in technologies such as telecommunications, information processing, robotics, optical communication, optical computing, dynamic image processing and so on.<sup>2,3</sup> Photonics has many notable virtues over electronics. The major advantage is that photons are much faster than an electron. Moreover there is no electrical and magnetic interference, thereby making the photonic circuits fully compatible with the existing fiber optics networks.<sup>4</sup>

### 1.2.2. Origin of NLO

In order to explain the physics in Figure 1.2.1; let us consider an energy diagram in Figure 1.2.2. The left part of the diagram represents the weak beam (non-laser light) interaction

with the molecule resulting same energy emission as the input light and hence we achieve same waves for linear optics. On the other part of the diagram, light with high intensity (lasers) interact with the molecule resulting multiple excitation to higher energy level. Hence it results emission of light with higher energy than the input light energy. This is nonlinear optics, in which new waves have been produced.

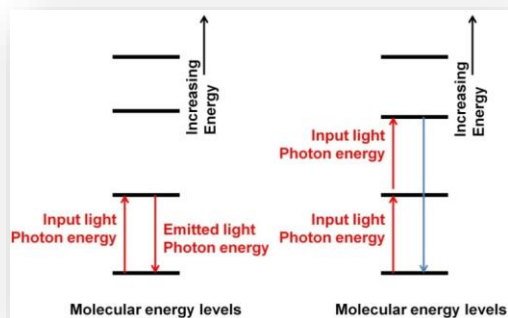


**Figure 1.2.2.** Energy band diagram of linear (left) and nonlinear optics (right).

When electromagnetic radiation interacts with matter, depending on their frequency, various types of polarizations are induced. With low frequency radiation (radiowave and microwave), orientation polarization, vibrational polarization and electronic polarization contributes to the total polarization. The first one implies reorientation of the molecules; the second one is related with the deformation of the nuclear framework of the molecule with the applied field. The electronic polarization can only occur when the radiation has wavelength in the optical range. With small electric field associated with the electromagnetic radiation, the polarization varies linearly with the electric field and the constant of proportionality is the known as polarizability (for molecules) and the linear electric susceptibility  $\chi^{(1)}$  (for bulk solids).<sup>5</sup>

$$Polarization = \mu(\omega) = \alpha(\omega).E(\omega)$$

$$P(\omega) = \chi_{ij}(\omega).E(\omega) \tag{1.2.1}$$

The materials showing this kind of response are termed as linear optical materials. The charge movement may cause reemission of radiation without modifying the frequency of the incident light. Although induced polarization may change in the speed of the light resulting optical phenomena such as refraction or birefringence. The reason for this is that the field strength of conventional light sources is much weaker (below  $10^3$  v/cm) than the atomic and inter-atomic fields ( $10^7$  to  $10^{10}$  v/cm). Therefore the resultant perturbation is too small to cause any change in the optical parameters. But with the advent of lasers the situation has changed drastically. Lasers generate electric field strength varying in the range of  $10^5$  -  $10^9$  v/cm, compatible in resonating with the atomic electric fields of the medium. This resonance affects the optical properties of the medium and thus generates new electromagnetic fields altered in phase, frequency, and amplitude. This is the realm of NLO.<sup>6</sup>

With strong field strength (*e.g.*, lasers) the polarization response of the medium is no longer linear as given in equation (1.2.1) and the higher order terms become more significant. The optical response can be described by expressing the polarization ( $P$ ) as a power series in the field strength ( $E$ ) as<sup>7</sup>

$$P = \chi^{(1)}E + \chi^{(2)}E^2 + \chi^{(3)}E^3 + \dots \quad (1.2.2)$$

$$P = \mu_0 + \alpha E + \beta E^2 + \gamma E^3 + \dots \quad (1.2.3)$$

Equations 1.2.2 and 1.2.3 represent the interaction of radiation with bulk material and a molecule respectively.<sup>8</sup> Where  $\mu_0$  is the permanent dipole moment,  $\chi^{(1)}$  and  $\alpha$  are linear terms responsible for linear optical properties (refractive index, absorption, permittivity *etc.*),  $\chi^{(2)}$  and  $\beta$  are quadratic terms responsible for nonlinear optical properties (second harmonic generation, electro optic effect, *etc.*). The term  $\chi^{(3)}$  and  $\gamma$  are known as cubic nonlinear term responsible for the third harmonic generation, optical phase conjugation and the Kerr effect. Hence, the induced polarization can convert the fundamental frequency to the second, third and higher order frequencies. This is illustrated in Figure 1.2.3 for a medium where the first nonlinear term  $\beta$  makes significant contribution to the induced-frequency components. In this example the medium (a model of non-centrosymmetric molecule) demonstrates an asymmetric polarization response to the applied field  $E(\omega)$ . The polarization occurs from  $D$  (electron rich substituent) to the  $A$  (electron deficient substituent). The nature of polarization can be illustrated as a summation of the Fourier components of frequencies  $\omega$ ,  $2\omega$  and  $3\omega$  *etc.* as shown in the Figure 1.2.3. According to Fourier theorem a non sinusoidal periodic response ( $P$ ) can be represented as a sum of series of sinusoidal functions with harmonics of appropriate coefficients of the elementary frequency  $\omega$ . For asymmetric and symmetric response, an appropriate summation of the even harmonics ( $0, 2\omega, 4\omega, 6\omega$  *etc.*) and the odd terms ( $\omega, 3\omega, 5\omega$  *etc.*) describe the total polarizability function ( $P$ ).

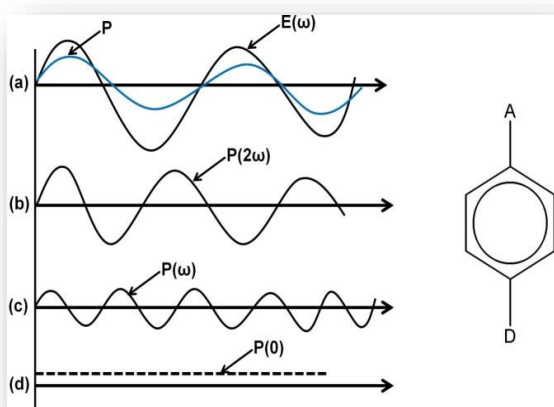


**Figure 1.2.3.** (a) Polarization response ( $P$ ) plot to an incident electromagnetic wave of field strength  $E(\omega)$  in a noncentrosymmetric medium at frequency  $\omega$ . (b) to (d) Fourier components of  $P$  at frequencies  $2\omega$ ,  $\omega$ , and  $0$ .

Similarly Figure 1.2.4 shows an example of a nonlinear response in a centrosymmetric medium like benzene. Here delocalized  $\pi$  electron of system is responsible for the symmetric nonlinear polarization. The Fourier response decomposition occurs at odd harmonics ( $\omega, 3\omega, 5\omega, \text{etc.}$ ) with gradually decreasing amplitudes (coefficients) of the higher order components. In either of these examples, as the incident field  $E(\omega)$  becomes more and more intense, the nonlinear terms contribute more significantly.

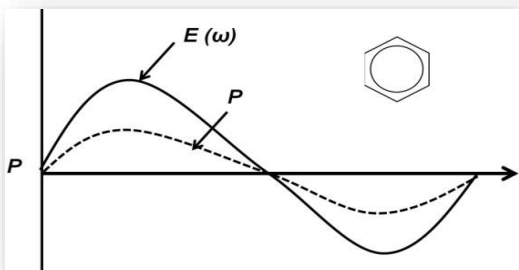


**Figure 1.2.4.** Nonlinear polarization response ( $P$ ) plot of to an incident electromagnetic field in a centrosymmetric medium.

The non-linearity of the optical response is best represented by the second ( $\beta$ ) and third hyperpolarizability ( $\gamma$ ). For a centrosymmetric system, then first order or second hyperpolarizability ( $\beta$ ) is zero, implying the non-responsiveness of centrosymmetric media towards second harmonic generation. This can be explained as follows. If a field  $+E$  is applied to the medium, the first nonlinear term appeared as  $+\beta E^2$  according to equation (1.2.3), with an applied field of  $-E$ , it still appeared as  $+\beta E^2$ . But this is contradictory as the medium is centrosymmetric where polarization should be  $-\beta E^2$ . This contradiction can only be resolved if  $\beta=0$ . Thus we can conclude that the centrosymmetric medium possess zero  $\beta$ -value. In the case of third order NLO susceptibility, if  $+E$  field produces polarization  $+\gamma E^3$  and  $-E$  field produces  $-\gamma E^3$ , so for centrosymmetric media, the second order hyperpolarizability ( $\gamma$ ) is the first non-zero nonlinear term.<sup>1</sup>

### 1.2.3. Microscopic nonlinearities

The description of nonlinear optical processes in the previous section needs more rigorous physical basis. In this section the constitutive relationships will be precisely stated.

The polarization induced in a molecule by an applied electric field is

$$P_i = \alpha_{ij} E_j + \beta_{ijk} E_{jk} + \gamma_{ijkl} E_{jkl} + \dots \quad (1.2.4)$$

Where the subscripts  $i, j, k, l$  refer to the molecular coordinate system and  $E_j, E_{jk}$  etc. denote the components of the applied field. The induced polarization in a molecule is a vector

quantity and is related to the electric field vectors through the components of tensor coefficients, though it has been considered earlier as scalar as expressed in equation (1.2.3). The third-rank tensor ( $\beta_{ijk}$ ) has very similar properties to a vector, but  $\gamma$ , a fourth-rank tensor, has the properties of a scalar. This can be verified from the experimental findings where values of  $\beta$  and  $\gamma$  are related to the components of the tensors according to equations (1.2.5) and (1.2.6).

$$\beta = \beta_{zxx} + \beta_{zyy} + \beta_{zzz} \quad (1.2.5)$$

$$\gamma = \frac{1}{5}(\gamma_{xxxx} + \gamma_{yyyy} + \gamma_{zzzz} + 2\gamma_{xxyy} + 2\gamma_{xxzz} + 2\gamma_{yyzz}) \quad (1.2.6)$$

In order to understand clearly about the vector like nature of  $\beta$  we observed a situation as presented pictorially in Figure 1.2.5 where the z-axis of the molecule is considered passing through two carbon atoms that contains the donor (D) and acceptor (A). It can be noted that the component of any arbitrary chosen field will polarize the molecule mostly in the z direction. If we set up experiments where the applied field is pointed in the direction of the molecular axis, it is clear that  $\beta_{zzz}$  will be the dominant contributor to the nonlinear response.  $\gamma$ , on the other hand, has the characteristics of a scalar with field projections contributing in all molecular directions.

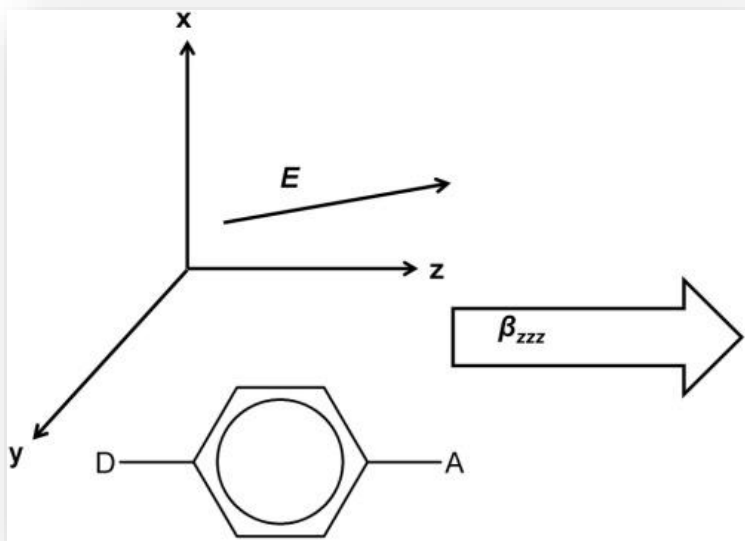


**Figure 1.2.5.** Model system with electron donor and acceptor substituents which results the asymmetric charge distribution along with large  $\beta$ . Considering the reference coordinate system as z- axis which is parallel to the dipolar axis of the molecule, the molecule is most easily polarized along z direction. Hence  $\beta_{zzz}$  is the largest component of the  $\beta_{ijk}$  tensor.

#### 1.2.4. Various types of second-order NLO effects

Various types of second-order NLO effects can be observed experimentally namely,

### 1.2.4.1. Second harmonic generation (SHG)

This has been considered as the most extensively used applications of NLO. SHG is a process where frequency of radiation becomes doubled with respect to the incident light after passing through a certain medium. Suppose two radiations of frequency  $\nu$  are passed through a material having characteristics  $\chi^2$  and  $\beta$ , the emitted radiation will have a frequency of  $2\nu$ . The produced wave will have the same direction as the incident one. Figure 1.2.6 pictorially represents the process of SHG.

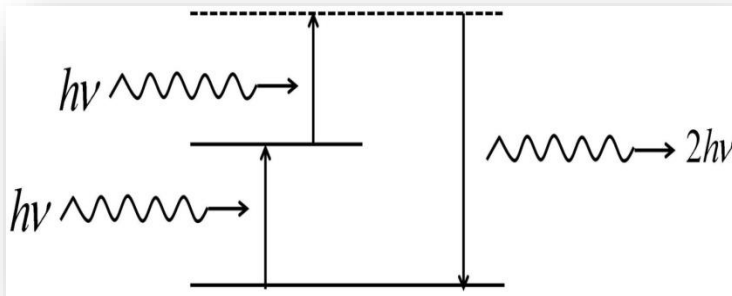


**Figure 1.2.6.** Second harmonic generation (SHG). The dashed (-) line corresponds to the virtual level<sup>9</sup>.

$$h\nu + h\nu = 2h\nu \quad (1.2.7)$$

$$p_1 + p_2 = p \quad (1.2.8)$$

The  $p_1$  and  $p_2$  are the momenta of the absorbed photons, and  $p$  is the momentum of the emitted one.

### 1.2.4.2. Sum frequency generation or parametric generation

Transformation of the light wave with frequency  $\nu$  into two new light waves with frequencies  $\nu_1$  and  $\nu_2$  is termed as parametric generation<sup>9</sup> as shown in Figure 1.2.7.

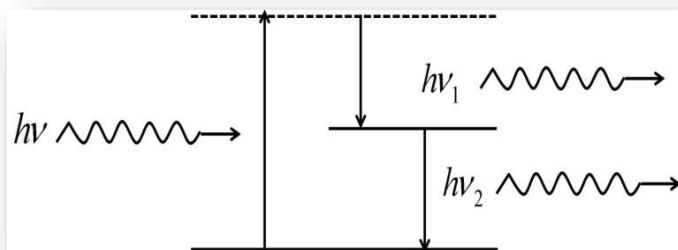


**Figure 1.2.7.** Paramagnetic generation.

$$h\nu = h\nu_1 + h\nu_2 \quad (1.2.9)$$

$$p = p_1 + p_2 \quad (1.2.10)$$

This process is also represented as two-photon process like SHG.

### 1.2.4.3. Linear electrooptic effect or Pockels effect

In presence of an external electric field, a linear change in the refractive index of the medium occurred and is termed as Pockels effect. In this case, a DC field is applied to a medium through which an optical wave propagates. The interacting field component can change the polarization which effectively alters the refractive index of the medium.<sup>1</sup>

### 1.2.4.4. Optical rectification

The optical rectification is defined as the ability to induce a DC voltage between the electrodes placed on the surface of the crystal when an intense laser beam is directed into the crystal.<sup>1</sup>

### 1.2.5. Applications of NLO effects

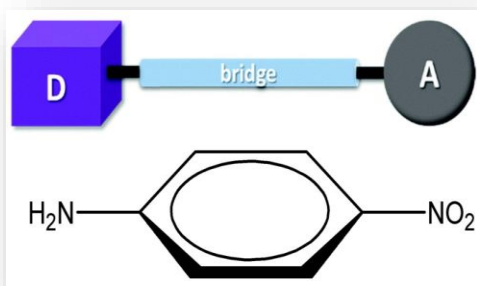
Table 1.2.1 represents various susceptibility and frequency dependent applications in various fields for  $\chi^{(2)}$  and  $\chi^{(3)}$

**Table 1.2.1.** Susceptibility functions ( $\chi^{(2)}$  and  $\chi^{(3)}$ ) for various types for interacting field components, their effects and applications.

Susceptibility	Effect	Applications
$\chi^{(2)}(0; \omega, -\omega)$	Optical rectification	Hybrid bistable device <sup>10</sup>
$\chi^{(2)}(-\omega; \omega, 0)$	Electro-optic (Pockels) effect	Modulators, variable phase retarders <sup>11</sup>
$\chi^{(2)}(-2\omega; -\omega, \omega)$	Frequency doubling	Harmonic generation device <sup>10</sup>
$\chi^{(2)}(-\omega_c; \omega_a, \omega_b)$	Frequency mixing	Parametric amplifiers, IR up converters <sup>11</sup>
$\chi^{(2)}(-\omega; \omega; \omega, -\omega)$	AC electro-optic effect AC Kerr effect	Optical bistability <sup>10</sup> Phase conjugation <sup>12</sup>
$\chi^{(2)}(-3\omega; \omega; \omega, \omega)$	Frequency tripling	Deep UV conversion <sup>12</sup>

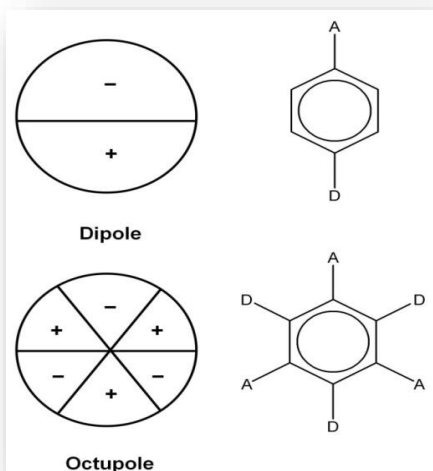
### 1.2.6. Present status of the field

Strong intramolecular charge transfer excitations in a noncentrosymmetric environment have been proved to be the fundamental requirements for second-order NLO materials as prescribed by theoretical model (*vide infra*). Prototypical organic molecules such as *p*-nitroaniline (PNA) (Scheme 1.2.1), dimethylaminonitrisostilbene (DANS) have an asymmetric charge distribution with donor and/ or acceptor group substituents and thus satisfy basic criterion for good NLO response.



**Scheme 1.2.1.** *p*-nitroaniline molecule, the prototypical dipolar  $D-\pi-A$  system.

DANS has long been regarded as typical benchmark compound for evaluating NLO properties.<sup>1</sup> In this respect, scientists have primarily focused on engineering the electronic structure of the donor, acceptor and the bridge structure based on the simple molecular scheme ( $D-\pi-A$  structure) for producing efficient second-order NLO dipolar organic molecules and metal complexes. In addition to dipolar molecules, octupolar molecules have also drawn the attention of scientific community in recent times. These species are multi-polar and their NLO response is due to multidirectional charge transfer excitation. A prototypical example is shown in Scheme 1.2.2.



**Scheme 1.2.2.** Dipolar vs. octupolar charge distribution in prototypical dipolar and trigonal octupolar systems.

### 1.2.6.1. Organic molecules for second-order nonlinear optics

In the early nineties, Marder *et al.* paved the way for developing highly advanced NLO chromophores<sup>13, 14</sup> and found an optimal combination of  $D$  and  $A$  strengths to maximize  $\mu\beta$  for a given conjugation bridge. It was found that the average difference between the single and double bond lengths in the molecule *i.e.*, bond length alteration (BLA) is the key parameter for optimizing the  $\beta$  of molecules.<sup>15</sup> Most of the existing molecules are known to have high BLA to maximize  $\beta$ . For example DANS molecule having aromatic ground state is likely to have more bond length altered than a simple polyene chain of comparable length for a given set of combination of  $D$  and  $A$ . The high degree of BLA in such molecules indicates that insufficient contribution of charge separated resonance takes place in the ground state configuration showing a direct consequence of loss of aromatic stabilization in the charge separated form. Therefore molecules with less aromatic character in the ground state or systems where loss of aromaticity in the ground state is compensated by a gain in aromaticity in the charge separated form have been receiving importance. For example when heterocyclic rings like thiophene, furan replace benzene rings in stilbene derivatives, a decrease in the aromatic character in the ground state leads to enormous high  $\beta$  value.<sup>16, 17</sup> More enhanced nonlinearities can be observed in molecules that can gain aromaticity in their charge separated form.<sup>18</sup>

Molecules with high nonlinearities, designed for electro-optic and SHG applications, should also possess good thermal and chemical stability. Unfortunately, organic molecules discussed so far are thermally unstable in spite of having high degree of nonlinearity. Moylan *et al.*,<sup>19, 20</sup> figured a way out to increase the thermal stability without compromising the nonlinearity of chromophores by replacing aliphatic dialkyl amino donor groups with diaryl amino groups.<sup>21, 22</sup> Lindsay *et al.*,<sup>23</sup> replaced the most reactive cyanide group in the tricyanovinyl group with aryl units in tricyanovinyl thiophenes, which improved the chemical and thermal stability considerably. Another class of extremely thermally stable chromophores with good nonlinearity are symmetrical analogues of the commercially available 4-(dicyanomethylene-2-methyl-6-94-dimethylamino styryl)-4-pyran (DCM) laser dye.<sup>23</sup> This compound with dicyanomethylene pyran acceptor attached to two carbazole donors is found to be thermally stable up to 350°C. Due to their “lambda-shape” structure, these molecules may be less susceptible to loss of nonlinearities in poled polymer films.<sup>24</sup>

### 1.2.6.2. Metal complexes for second-order nonlinear optics

Similar to organic NLO chromophores, most of the second-order NLO metal complexes also possess the structural pattern of  $D-\pi-A$ , where an organometallic bridge can be attached to donor and acceptor moieties. Metal to ligand charge transfer (MLCT), ligand to metal charge transfer (LMCT), or intraligand charge transfer (ILCT) processes make the metal complexes effective for use as donor / acceptor / polarizable bridge. Keep this scheme in mind; several classes of second-order NLO transition metal complexes can be identified.

Metallocene derivatives, one of the most widely investigated classes of NLO metal complexes,<sup>25, 26</sup> generally a ferrocenyl moiety acts as the donor group of the  $D-\pi-A$  structure. The second-order nonlinearity of such complexes is attributed to the CT excitations from low-lying, filled metallocene orbitals to empty  $\pi^*$  orbitals of the conjugated  $\pi-A$  system.<sup>27</sup> Another important classes of NLO metal complexes based on Schiff base ligands have also been introduced.<sup>28</sup> Reports on the NLO properties of these types of compounds based on the tetradentate salen [N,N'-bis(salicyleneamino)ethylene] ligand showed that the role of the metal electronic configuration determines the second-order nonlinearities.<sup>29</sup> It was also confirmed that this family of derivatives shows excellent thermal stability. This discovery indicated the potentiality of metal complexes as building blocks of NLO materials. Another prime important metal based complexes for applications in the areas of conducting, magnetic molecular materials and also relevant optical properties are metal bis-dithiolen complexes.<sup>30</sup> In a works it has been shown that bis-dithiolen complexes of Ni, Pd, Pt can be useful as near-infrared dyes for Q-switching the Nd:YAG lasers.<sup>31</sup> Curreli *et al.*, in one of their works addressed how the different terminal environments ( $\pi$ -conjugated) with the centrosymmetric  $(C_2S_2)Ni(C_2S_2)$  core affects the electronic and NLO properties of the complex.<sup>32</sup> Volger in early 1980s,<sup>33</sup> reported asymmetric bis-dithiolen complexes as potential second-order chromophore.<sup>34</sup>

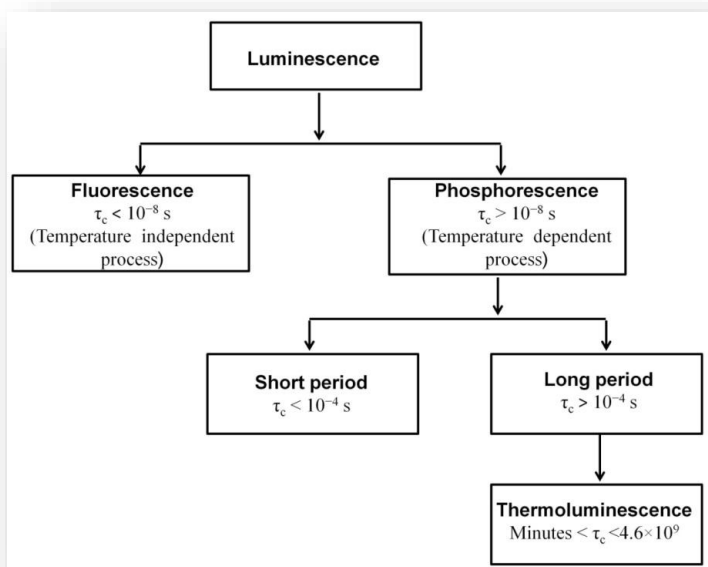
### 1.3. Luminescence

The word luminescence appears from the Latin term 'lumen' signifying light and is presently defined as spontaneous emission of radiation through a process other than incandescence. If we heat something to a high enough temperature, it will begin to glow. When coil of heater or metal in a flame begin to glow 'red hot', this is incandescence. Sun and stars also glow due to this phenomenon. Whereas luminescence is 'cold light' emission phenomenon which takes place at lower or even at normal temperatures. In luminescence some energy source

drags an electron from its ground state (lower energy) into the excited (higher energy) state; then the electron return to its original state with emission of light in the visible region. This is luminescence. We can observe the luminescence phenomena in nature also, like *aurora borealis*, the light of sea, luminous animals (glow-worms, fireflies), phosphorescent woods *etc.* All over the world, scientists are using this phenomena in various fields like geology, physics, chemistry, biomedical engineering, industrial applications for research and development.<sup>35</sup>

### 1.3.1. Luminescence and stokes law

When radiation is incident on a material, some of its energy is absorbed and re-emitted as light of higher wavelength (stocks law). The wavelength of the emitted light is characteristics of the luminescent substance and does not depend on the incident radiation. The emitted light may be in visible, ultra-violet or infrared region. This cold emission (*i.e.*, luminescence) involves two steps: (1) excitation of electronic systems to higher energy level, and (2) subsequent emission of light. After absorption of radiation, emission of light takes place with characteristic time gap ( $\tau_c$ ). This parameter allows us to sub-classify the process of luminescence into fluorescence and phosphorescence. In fluorescence,  $\tau_c < 10^{-8}$ s and is seen to be spontaneous *i.e.*, fluorescence emission occurs instantly with the absorption of radiation and stops immediately as the radiation ceases. Whereas in phosphorescence,  $\tau_c > 10^{-8}$  s and is seen to continue for a long time even after the source of excitation is removed. Phosphorescence can be further divided into two parts: a) short period,  $\tau_c < 10^{-4}$  s, and (b) long period where  $\tau_c > 10^{-4}$  s, also called Thermoluminescence (TL). Fluorescence is essentially independent of temperature, whereas decay of phosphorescence exhibits strong temperature dependence. Each process mentioned above has its own significance



and advantage in the field of science and technology.<sup>35</sup> The family tree of luminescence phenomena is shown in Figure 1.3.1.

**Figure 1.3.1.** Classification of luminescence on based on duration of emission.<sup>35</sup>

### 1.3.2. Types of luminescence

Depending on the source of energy or what trigger luminescence, there are varieties of luminescence namely:

1.3.2.1 Chemiluminescence: Energy source is chemical reactions.

1.3.2.2 Bioluminescence: Living organism produces light due to chemical reactions.

1.3.2.3 Triboluminescence: Light is generated by mechanical energy.

1.3.2.4 Cathodoluminescence: The light emission is a result of electron beam excitation.

1.3.2.5 Electroluminescence: Light is generated in response to an applied electric field on a certain material.

1.3.2.6 Photoluminescence: Emission of the light is the result of the excitation by electromagnetic radiation or photons.

1.3.2.7 Thermoluminescence: It is also known as thermally stimulated luminescence (TSL). It is the luminescence activated thermally after initial irradiation by other means such as  $\alpha$ ,  $\beta$ ,  $\gamma$ , UV or X-rays.

1.3.2.8 Sonoluminescence: It is the phenomenon by which light is produced due to the excitation by ultrasonic waves.

Emphasis in this thesis has been given to electroluminescence and its application for producing organic light emitting diodes (OLEDs).

### 1.3.3. Basic principles of luminescence

The process of luminescence can be illustrated using an energy diagram called Jablonski diagram (Figure 1.3.2). This diagram describes various relaxation mechanisms for the excited state molecules. Every energy level ( $S_0$ ,  $S_1$ ,  $T_1$  etc.) is comprised of several closely spaced vibrational states due to the presence of vibronic motions in a molecule. When larger energy compared to the HOMO–LUMO energy difference is introduced in a molecule, electronic transition may take place either to the lower lying  $S_1$  excited state or even higher singlet excited states  $S_2$ ,  $S_3$  etc. Higher vibronic states within  $S_1$  state relax to the lowest vibronic state of  $S_1$  within a time scale of picoseconds. On the other hand, higher energy singlet state ( $S_2, S_3$ ) relax to  $S_1$  state via nonradiative internal conversion (IC) processes. Triplet states are usually populated

via an intersystem crossing (*ISC*) of  $S_1$  and  $T_1$  states. Radiative transitions take place when electron comes down from the lowest vibronic state of  $S_1$  or  $T_1$  to the ground state  $S_0$ . The radiative transition from  $S_1$  to  $S_0$  is classified as a spin allowed transition with a time scale of the order of a few nanoseconds. On the other hand, the time scale of the  $T_1$  to  $S_0$  transition is much longer, ranging from micro- to milliseconds, because the process is spin-forbidden.<sup>36, 37</sup> Here it is worth mentioning that the population of excited triplet and singlet states depends upon the relative magnitude of rate constant ( $k_r^S$ ) of the process  $S_1 \rightarrow S_0$  and the rate constant ( $k_{ISC}$ ) for a nonradiative intersystem crossing (*ISC*),  $S_1 \rightarrow T_1$ . The rate constant ( $k_r^T$ ) of the  $T_1 \rightarrow S_0$  process is normally low irrespective of the triplet yield because of spin forbidden character. Thus phosphorescence rarely occurs in organic molecules though it is common in metal complexes due to the high degree of spin-orbit coupling, which relaxes the spin selection rule. Radiative emission can then compete with deactivating processes allowing phosphorescence to be observed at room temperature.

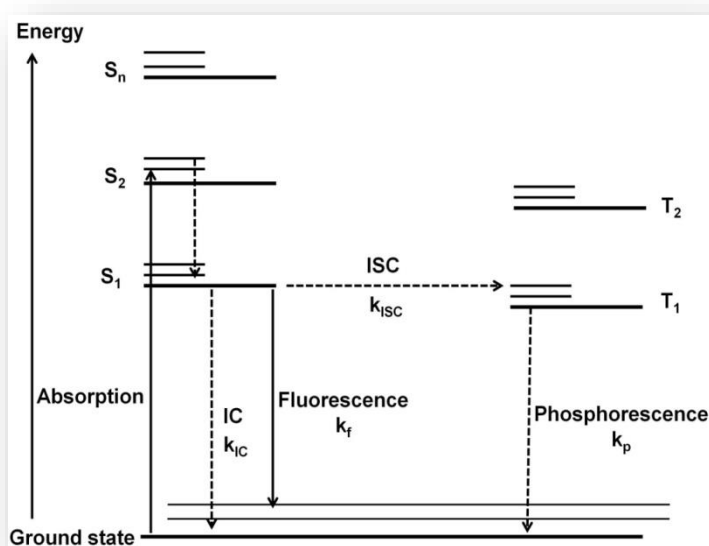


**Figure 1.3.2.** Jablonski diagram representing the absorption, fluorescence and phosphorescence. Thick arrow represents absorption of light; dashed ones indicate vibrational relaxation and non-radiative decay.

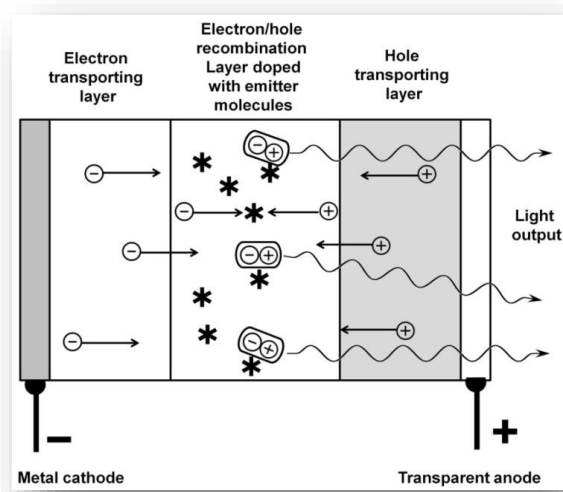
### 1.3.4. Electroluminescence and OLEDs

Luminescent materials fascinated mankind owing to their broad range of applications such as cathode ray tubes (CRTs), projection televisions (PTVs), fluorescent tubes, and X-ray detectors *etc.*<sup>38</sup> Besides traditional areas of application, the demand for new materials for displays and illumination technology has received considerable activity in the last decade. One of the revolutionary technologies for generating light in LEDs is the direct excitation of organic semiconductors by electrical current. Particularly OLEDs has been receiving notable interest

over the world and are already substituting conventional display technologies.<sup>39, 40</sup> In fact, OLEDs offer many appealing advantages such as self emission, easy manufacturing, flexibility *etc.* OLEDs do not require a backlight, polarizers and diffusers which results the formation of much thinner display panels. Moreover in OLEDs, light emission occurs only from the required pixel rather than from the entire panel causing very low power consumption compared to that of LCDs.<sup>41</sup> Finally, OLED displays are aesthetically superior to LCDs providing truer colors, wider viewing angles (up to 170°) and fast switching times (1000 fold faster than traditional displays).

### 1.3.4.1. The OLED structure

The multilayered OLEDs device consists of organic thin layers sandwiched between an anode (generally indium tin oxide) and metallic cathode (Mg–Ag or Li–Al). The organic layers generally compose of three layers namely (a) a hole transport layer, (b) an electron transport layer and the most important one (c) exciton blocking layer such as 2, 9-dimethyl-4, 7-diphenyl-1, 10-phenanthroline (BCP).<sup>42</sup> The organic emitters are generally deposited either between the conducting layers or more commonly doped into the electron transport layer, typically tris(8-



hydroxyquinolate)aluminum ( $\text{Alq}_3$ ). Application of electric voltage causes injection of holes from anode and electrons from cathode. Holes migrate to the hole transport layer and electrons migrate to the electron transport layer where they meet forming exciton. The exciton is then relaxed to the ground state resulting emission of light (Figure 1.3.3).

**Figure 1.3.3.** Basic set up of a layered OLED structure. Triplet emitters are represented by asterisks.

### 1.3.4.2. Mechanism of exciton formation

We have discussed earlier that exciton formation occurs at the emissive layer which are generally consist of organic matrix doped with emitter molecules (dopants). In general the electron hole recombination occurs at the dopants although it may also occur in the organic

matrix. For the latter case relatively high dopant concentration is required for quenching of matrix emission. In early days organic fluorescent molecules had been utilized in OLED devices as dopant molecules.<sup>9</sup> However, in recent times, identification of phosphorescent materials are gaining importance as luminous efficiency of OLEDs can be greatly enhanced with phosphorescent emitters.

According to the mechanism of exciton formation, the first step is characterized by trapping of charge carriers (electron and hole) in emitter molecules. The hole may be trapped first to the emitter molecule *e.g.*, Ir(F-ppy)<sub>3</sub> in PVK<sup>43</sup> and consequently oxidizes it. Simultaneously under applied external potential, electrons from cathode will migrate through the matrix material to the anode. This is known as electron hopping. If the trapped holes are far from the trajectory of electrons, electrons migrate independently to the anode without meeting the holes. In that case, the hole-electron binding energy  $\Delta E(e-h)$  depends on the electron-hole separation,  $R$ . The hole-electron recombination also depends on the spins of both electron and hole. When these spins are coupled, one combination of antiparallel spins gives singlet and three combinations of parallel spins generate a triplet state (Figure 1.3.5b). Thus statistically, 25% of the excitons are singlet and 75% are triplet, which differ from each other with respect to their spin orientations.<sup>44, 45</sup> Thus, excitons produced either directly into the dopants or into the organic matrix will undergo exchange interaction leading to the energy splitting between singlet ( $S$ ) and triplet ( $T$ ) states,  $\Delta E(S-T)$ . Emission between these spin states of exciton, excites the emitter molecules. The process is described to follow singlet or triplet path ( $S$ -path or  $T$ -path) depending on the initial spin orientation of the electron-hole pair (Figure 1.3.4).<sup>46</sup>

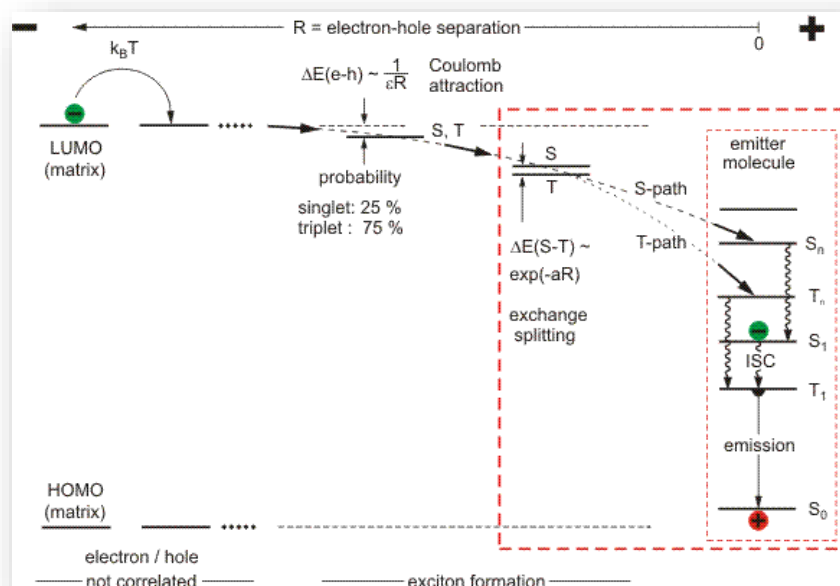


**Figure 1.3.4.**  
*Dynamics of exciton formation.*

### 1.3.4.3. Triplet and singlet harvesting

This section describes the effect of spin-orbit coupling on the efficiency of electroluminescence in an OLED device though the mechanism of exciton formation remains unaltered. In order to illustrate this, we will compare the luminescence efficiency of organic and organometallic complexes, both having equal photoluminescence quantum yields. Relaxation of exciton through singlet or triplet paths populates the lowest excited singlet or triplet state of the emitter. This is true for both organic and organometallic complexes. Figure 1.3.5 schematically represents this phenomenon. In case of organic molecules,  $S_1 \rightarrow S_0$  emission is dominant over  $S_1 \rightarrow T_1$  intersystem crossing. On the other hand  $T_1 \rightarrow S_0$  transition rate is rather small because of spin forbidden nature. The deactivation of  $T_1$  state occurs in non-radiative fashion at ambient temperature. Thus 75% of the triplet excitons do not lead to luminescence and lose their energy as heat (Figure 1.3.6, left hand side). On the contrary, in transition metal complexes, the central metal ion possesses significant spin-orbit coupling (Figure 1.3.6, right hand side) resulting efficient  $S_1 \rightarrow T_1$  ISC and thus singlet  $S_1$  emission is not observed. Rather radiative  $T_1 \rightarrow S_0$  transition occurs significantly allowing phosphorescence even at ambient temperature. Thus all possible spin states of the excitons can be harvested to populate the lowest  $T_1$  state. In conclusion, by this process of triplet harvesting one can in principle obtain a four times larger electro-luminescence efficiency for triplet emitters than for singlet emitters.

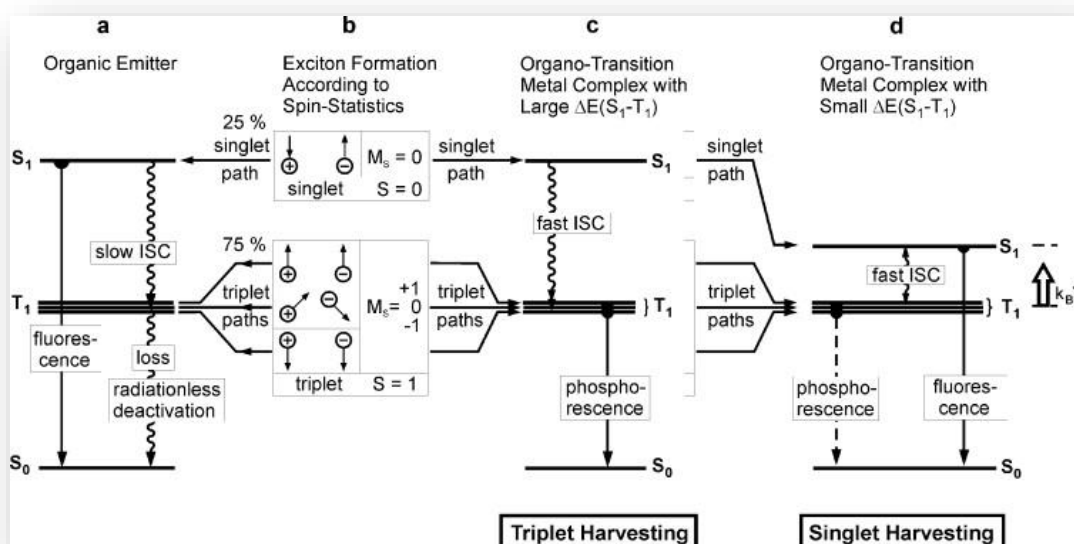


**Figure 1.3.5.** Electro-luminescence excitation processes for (a) organic and (b) organo-transition metal emitters. (c) and (d) representing triplet and singlet harvesting effect respectively.

But the situation is little different for heavier transition metal complexes where average radiative rates for the  $T_1 \rightarrow S_0$  transition is relatively low. In this case if non-radiative processes do not lead to quenching, the emission decay times are relatively very long causing triplet-triplet annihilation and hence make these materials unfit for OLED application. To overcome these problems, Yersin *et al.*<sup>47</sup>, proposed specific emitter molecules with newer electro-luminescence mechanism. This special class of molecules are characterized by small energy gap  $\Delta E(S_1 - T_1)$  between excited singlet ( $S_1$ ) and triplet states ( $T_1$ ).<sup>48, 49</sup> Hence *SOC* induced *ISC* processes are fast as well as upward processes from  $T_1$  to  $S_1$  are effective at ambient temperature, which enables emission from both states ( $S_1$  and  $T_1$ ). In summary, singlet emitters can also take advantage of singlet harvesting effect by gathering both triplet and singlet excitons and might be well suited for OLED applications as already well established for triplet emitter materials.

#### 1.3.4.4. Requirements of triplet emitters for OLEDs

Emission wavelength ( $\lambda_{em}$ ), lifetimes ( $\tau$ ) and quantum yields ( $\Phi_p$ ) of phosphorescent materials are important parameters from the view point of OLED application. Three primary colors, blue (~ 450–470 nm), green (~ 500–550 nm) and red (~ 650–700 nm) are required for full color displays. Although red and green emitters are readily available, blue emitters are hard to find due to the large energy gap between the ground and excited states. On the other hand emitters with long emission lifetimes severely decrease the OLED efficiency. For example, when a molecule remains in the triplet state for an extended period of time, the rapid repopulation of the excited state will be inhibited and this become the limiting factor for the conversion of the electrical energy to photon energy. Ideally a guest phosphor should have phosphorescence lifetimes in the range of 5-50  $\mu$ s at 298 K. In addition, suitable triplet emitters should ideally be stable, exhibit reversible redox behavior and undergo vacuum sublimation for ease of device fabrication.

#### 1.3.5. Structural classes exhibiting room-temperature phosphorescence

Demand of novel luminescent materials exhibiting desired photophysical properties has generated significant activity in the last decades. Concerning OLEDs application, dopant containing organometallic systems offers a series of advantages over conventional organic emitters as pointed out earlier. Thus with judicious ligand selection it is possible to design a series of complexes where the identity of the emitting state is predetermined.<sup>50</sup> This is

particularly important in designing of application-oriented luminescent materials. There are four types of electronic states or transitions expected for transition metal complexes.

- (i)  $d-d$  states (metal-centred (MC) transition): Upon ligand coordination the metal  $d$  orbitals are split. Excited  $d-d$  states arise from promotion of an electron within  $d$  orbitals which are essentially confined to the metal centre.
- (ii)  $d-\pi^*$  states (metal-to-ligand-charge-transfer (MLCT)): These involve excitation of a metal centred electron to a  $\pi^*$  anti-bonding orbital located on the ligand system.
- (iii)  $\pi-\pi^*$  or  $n-\pi^*$  states (intraligand (IL) transition): Promotion of an electron from a  $\pi$ -bonding or non-bonding orbital to a higher energy anti-bonding orbital gives rise to these states.
- (iv)  $\pi-d$  states (ligand-to-metal-charge-transfer (LMCT)): These states arise from the transfer of electronic charge from the ligand  $\pi$  system to a metal centered orbital.

The relative ordering of these four states ( $d$ ,  $n$ ,  $\pi$ ,  $\pi^*$ ) may be altered by changing the metal centre or ligands, or by changing the geometry of the complex.<sup>50</sup> These modification possibilities have led to the design of many new complexes with predetermined luminescent characteristics.<sup>51</sup>

### 1.3.6. Recent status of the field

Numerous research efforts have been put on the photo physical properties of transition metal complexes, some of which are discussed here.

Room temperature phosphorescence is not a common feature for first row transition metal complexes due to weak spin-orbit coupling. However, isolated manganese (I)<sup>52</sup> and manganese (II)<sup>53</sup> have been reported to exhibit low temperature emission in solid glasses and several Ni (0)<sup>54</sup> complexes exhibit weak phosphorescence in solution. Chromium (III) and copper (I) complexes are better examples of room-temperature phosphorescence.

There are several comprehensive reviews regarding the photophysics of chromium (III) complexes.<sup>55, 56</sup> In these complexes  $d \rightarrow d$  excitation populates the  $^4T_2$  state, followed by intersystem crossing to the excited  $^2E$  state. This process is efficient ( $10^{10}$ – $10^{11}$  s<sup>-1</sup>) enough to produce quantum yield close to unity.<sup>57</sup> Although both fluorescence ( $^4T_2 \rightarrow ^4A_2$ ) and phosphorescence ( $^2E \rightarrow ^4A_2$ ) have been reported, phosphorescence occurs quite frequently. Due to the low excited-ground state energy gap in first row transition metal complexes, emission wave lengths are mainly restricted to the red spectral region.<sup>58, 59</sup> Ir(III) complexes with different

combination of ligands *e.g.*, anionic 2-phenyl pyridine (ppy), Acetyl acetonate (acac), 2-carboxy, 4-amino pyridine and neutral bipyridine (bpy) are also reported as effective phosphorescent complexes.<sup>60, 61</sup> Their emission can be tuned from blue to red region by peripheral functionalization of the ligands with different substituents (electron donating and withdrawing).<sup>62, 63</sup> The facial (fac) and meridional (mer) isomers of [Ir (F<sub>n</sub>ppy)<sub>3</sub>] are found crucial for use in OLED devices.<sup>62</sup> A close inspection of their molecular orbitals reveals that introduction of fluorine atom can enlarge the HOMO-LUMO energy gap resulting blue shifted emission. Thus the green emitting fac-[Ir(ppy)<sub>3</sub>] becomes the blue emitting fac-[Ir(F<sub>n</sub>ppy)<sub>3</sub>] complex after fluorination on the ppy ligands. So far it has been found that Ir(ppy)<sub>3</sub> complex is one of the most famous emitters for OLED application and its emission is governed by the nature of cyclo-metallating ligands. However in case of Ir(ppy)<sub>2</sub>LX (LX=ancillary ligand) complexes, their color can be tuned from blue to red by changing the ancillary ligands. For example, complex Ir(ppy)<sub>3</sub> shows deep blue emission at 77K, but its color can be changed from blue (422nm) to orange red (587nm) by using different ancillary ligands like Ir(ppz)<sub>2</sub>(acac) (acac= acetyl acetonate), Ir(ppz)<sub>2</sub>(dbm) (dbm=dibenzoyl methane). It can be noted that the complex Ir(ppy)<sub>2</sub>(pic) (pic=picolinate) shows strong green emission both in the solid state and in solution at room temperature with photoluminescence (PL) efficiency of 19%. Here it is worth mentioning that to tune the emission of Ir (III) complexes, changing the ancillary ligand is more simple and convenient compared to the traditional method of altering the structure of cyclo-metallating ligand. Yersin *et al.* proposed first row transition metal based complexes such as Cu(I)(pop)(Pz<sub>2</sub>BH<sub>2</sub>), (pop = bis(2-diphenyl phosphanyl), pzBH<sub>2</sub> = bis (pyrazol-1-yl)borohydrate) with small energy separation, [ $\Delta E (S_1 - T_1)$ ]. This causes emission from both the singlet and triplet excited state with better efficiency. Therefore efforts have been devoted to the development of materials with smaller  $\Delta E (S_1 - T_1)$  values. Solvent can also control the phosphorescence quantum yield by quenching the emission process of organo-transition metal compound with formation of exciplex between the excited emitter and the solvent molecule.<sup>64, 65</sup> Exciplex quenching occurs more efficiently when emitters are more electrophilic and solvents are more nucleophilic in nature. Recently in an electrophilic Pt(II) compound the emission is found strongly quenched even by poor Lewis bases. On the other hand, in non polar cyclohexane, a high emission quantum yield was obtained.<sup>66</sup>

#### 1.4. Aim of the present work

Computational modeling is an efficient tool for designing potential materials. By modeling it is possible to eliminate the high costs associated with the hit and miss synthetic approach. This also offers the materials scientist the added advantage of quick feedback on a compounds potential usefulness. In many cases it has been found that the optical properties of studied compounds, computed using various methodologies are in good agreement with the experimental values. Thus use of computational methodology before synthesis is now accepted as a state-of-the-art technique in modeling the potential molecules. Keeping in view the success of quantum chemical methods in predicting the quantitative value, the thesis specifically deals with the computational modeling of optical materials as given below:

(1) Ionic donor-acceptor groups can enhance the hyperpolarizability values drastically compared to the neutral substituents, attempts have been put in order to design efficient NLO materials based on organometallic spacer with zwitterionic substituents (donor-acceptor) at the peripheral unit.

(2) Focus of the present research has shifted from heavy to light transition metal complexes for the existence of singlet harvesting effect in the latter. Third row transition metal complexes have also been reported to be quite effective for OLED applications. Therefore our interest centers around designing of luminescent materials especially rare blue emitters based on 3d transition metal complexes.

(3) Magnetic Materials with interesting electrical and optical properties are of enormous importance due to their multifarious applicability in photonic devices. Especially organic magnetic materials with larger nonlinear optical response are of prime importance as they possess biological application as well. A great deal of attention has been paid to the two photon absorption (TPA) property of organic molecules as these systems have potential application in photodynamic therapy (PDT). Hence a single molecule can be used in multidimensional way. Thus by judicious choice of the components that constitute the molecule, it is possible to control the application of designed systems. In nutshell our intention is to design multifunctional molecules.

(4) The effect of weak interaction (intermolecular hydrogen bond formation) on the excited state relaxation process such as luminescence process is one of the fundamental aspects of photochemistry. In some cases it has been found that intermolecular H-bonding interaction

diminishes HOMO-LUMO energy gap resulting red shift in the emission spectra. Here we have studied the effect of hydrogen bond interaction on the luminescence spectra.

## CHAPTER 2

### *Theoretical background of computational methods*

#### **Abstract**

---

The second chapter represents a brief report on the basic theoretical background related to various optical properties along with theoretical techniques to quantify hyperpolarizability ( $\beta$ ) and two-photon absorption cross section ( $\sigma$ ). For theoretical determination of first hyperpolarizability ( $\beta$ ), early models, equivalent field model (EIF), additivity model and two-state model along with quantum chemical approaches *viz.*, sum over states (SOS) methods and coupled perturbed HF (CPHF) methods are also discussed here. A short description of “few-states model” for quantifying two-photon absorption cross section ( $\sigma$ ) is also presented. In case of luminescent materials, principles of computational phosphorescence are clearly stated.

---

## 2.1. Theoretical determination of first hyperpolarizability ( $\beta$ )

### 2.1.1. Early models for the calculation of $\beta$

#### 2.1.1.1. Equivalent field model (EIF)

Equivalent field model was developed by Oduar and Chemla<sup>67, 68</sup> for interpreting the second-order nonlinear optical responses. This method represents  $\beta$  by quantifying the ground state asymmetry of a  $\pi$ -network in a systematic fashion. It is reported that the major portion of the second order response can be predicted by the deformation of the electron distribution due to appended substituents to the chromophore molecules. The perturbation of the  $\pi$ -cloud caused by particular substituents is known as substituent mesomeric moment ( $\mu_R$ ) and is related with  $\beta$  as

$$\beta_{\pi} = \frac{3\gamma\Delta\mu_R}{\alpha} \quad (2.1)$$

Where  $\alpha$  is polarizability,  $\gamma$  is second order hyperpolarizability and  $\beta_{\pi}$  is the static hyperpolarizability at  $h\omega = 0.0$ .

In this model determining the  $\mu_R$  is complicated in predicating the  $\beta_{\pi}$ . For mono substituted benzenes and stilbenes, the  $\pi$ -deformation caused by substituent R is defined as the difference between the ground-state  $\mu$  to the mono substituted aromatic derivative and that for the analogous mono substituted aliphatic molecule. The  $\sigma$ -contributions to the  $\mu$  of the  $\pi$ -chromophores are eliminated. Using the  $\mu_R$ ,<sup>69</sup> the  $\beta_{\pi}$  for a considerable number of mono substituted  $\pi$ -conjugation systems are predicted, which are well correlated with experimental trends in the second order response.<sup>68, 70</sup> This model also accounts for the negative sign in the second order response when the added group is an electron acceptor and a positive  $\beta$  when the attached moiety is an electron donor.

#### 2.1.1.2. Additivity model

This model is an extension of the EIF model and is generally used for predicting the second-order response for disubstituted derivatives *i.e.*, push/pull systems (push/pull substituted benzene). It has been proposed that the total molecular nonlinearity for a complex system should be the sum of the contributions of each important structural component of the system.<sup>71, 72</sup> However this additivity model works well for weakly coupled systems, such as *D* and *A*  $\sigma$ -

networks<sup>73</sup> but fails for strongly coupled disubstituted systems<sup>73, 74</sup> as proposed by Zyss et al. This model also fails predicting high  $\beta$ -values for highly asymmetric systems.

Thus difficulties with both the EIF and additivity model is based on the assumption that  $\beta$  is governed by ground-state electronic distributions and that the substituents act independently of each other.

### 2.1.1.3. Two-state model

In order to explain the high  $\beta$ -value for asymmetric systems, Oudar and Chemla<sup>68, 75</sup> proposed the two-state model. This model proposed that the large NLO response for these type of systems arises due to intramolecular charge transfer (CT) between  $D$  and  $A$ . Hence not only the ground state, the excited state is also responsible for the NLO response. The  $\beta$  can be represented as a sum of two contributions,  $\beta_{add}$  and  $\beta_{CT}$ .

$$\beta = \beta_{CT} + \beta_{add} \quad (2.2)$$

$\beta_{add}$  accounts for the interaction between the individual substituents and spacer (*i.e.*, chromophore) and  $\beta_{CT}$  represents the charge transfer interactions between the  $D$  and  $A$  moieties and is described in terms of a two-level interaction between the ground state ( $g$ ) and the first excited state ( $n$ ) as follows .

$$\beta_{CT} = \frac{3e^2}{2m} \frac{h\omega_{gn} f_{gn} \Delta_{\mu_{gn}}}{[(h\omega_{gn})^2 - (2h\omega)^2][(h\omega_{gn})^2 - (h\omega)^2]} \quad (2.3)$$

Here,

$h\omega$  is the energy of the laser photon,

$h\omega_{gn}$  is the energy difference between ground state ( $g$ ) and the first excited state ( $n$ ),

$f_{gn}$  is the oscillator strength of a  $g$ - $n$  transition,

$\Delta_{gn}$  is the difference in dipole moments between the ground and first excited state.

Thus high  $\beta$ -value for a system is related to the charge transfer excited states and any method that seeks to predict hyperpolarizability must adequately represent the excitation to these states.<sup>76</sup>

## 2.2. Quantum chemical approach for the calculation of $\beta$

Reliable theoretical predictions of nonlinear optical responses are useful for providing guidelines to the synthetic chemists for exploring species of potential interest. Moreover this will

give us a concrete idea about the structure-optical-property relationship which is a key step to search the possible suitable candidate for NLO materials. There are two basic methodologies which can be used with an electronic structure method to compute NLO response *viz.*, Sum over states (SOS) methods and Coupled perturbed HF (CPHF) methods. Both the SOS (field-independent) and CPHF (field-dependent) methods are useful for any model Hamiltonian (*i.e.*, ab initio, semiempirical) for the computation of  $\beta$ .

### 2.2.1. Sum over states (SOS) methods

Sum over states (SOS) approaches constitute one of the most commonly used class of methodologies for theoretical estimation of hyperpolarizabilities. These methods are field independent and calculations are carried out on free molecule where NLO response involves the coupling of the excited state. According to SOS methods, NLO responses calculated by applying perturbation theory to an unperturbed molecule<sup>77, 78</sup> and are suited for studying the interaction between individual orbitals. In the uncoupled formulation, electronic excited states created by the perturbing laser field are treated as an infinite sum over unperturbed particle-hole states. The SOS perturbation equation for calculating  $\beta$  is given here (2.4).

$$\beta_{ijk}^{SHG} = -\frac{e^3}{8h^2} \left[ \begin{aligned} & \sum_{n \neq g} \sum_{\substack{n' \neq g \\ n' \neq n}} \left\{ (r_{gn'}^j r_{n'n}^i r_{gn}^k + r_{gn'}^k r_{n'n}^i r_{gn}^j) \left( \frac{1}{(\omega_{n'g} - \omega)(\omega_{ng} + \omega)} + \frac{1}{(\omega_{n'g} + \omega)(\omega_{ng} - \omega)} \right) + \right. \\ & (r_{gn'}^i r_{n'n}^j r_{gn}^k + r_{gn'}^i r_{n'n}^k r_{gn}^j) \left( \frac{1}{(\omega_{n'g} + 2\omega)(\omega_{ng} + \omega)} \right) \left( \frac{1}{(\omega_{n'g} - 2\omega)(\omega_{ng} - \omega)} \right) + \\ & \left. (r_{gn'}^j r_{n'n}^k r_{gn}^i + r_{gn'}^k r_{n'n}^j r_{gn}^i) \left( \frac{1}{(\omega_{n'g} - \omega)(\omega_{ng} - 2\omega)} + \frac{1}{(\omega_{n'g} + \omega)(\omega_{ng} + 2\omega)} \right) \right\} + \\ & \{ [r_{gn'}^j r_{gn}^k \Delta r_n^i (\omega_{ng}^2 - 4\omega^2) + r_{gn'}^i (r_{gn}^k \Delta r_n^j + r_{gn}^j \Delta r_n^k) (\omega_{ng}^2 + 2\omega^2)] \times \\ & 4 \sum_{n \neq g} \frac{1}{(\omega_{ng}^2 - \omega^2)(\omega_{ng}^2 - 4\omega^2)} \} \end{aligned} \right] \quad (2.4)$$

where,  $\omega$  is the frequency of the applied electric field,  $r_{n,n'}^i$  is the matrix element of displacement operator  $r^i$  along the  $i$ th molecular axis between electronic states  $n$  and  $n'$  and  $h\omega_{ng}$  is the energy separation between the ground state ( $g$ ) and an excited state ( $n$ ). The term  $\Delta r_n^i (= r_{nn}^i - r_{gg}^i)$  is the dipole moment difference between excited and ground state.

From this equation it is clear that in order to compute  $\beta$ , one needs to know the dipole matrix elements between the ground and excited states, excitation energy and excited state dipole moments. Since the ground state is of single determinant type, the polarizability involves only

monoexcited configurations. However, the applied fields mix the molecular ground state with many excited states, the SOS expansion is infinite and generally the sum is truncated after apparent convergence has been reached.

### 2.2.2. Coupled perturbed Hartree Fock (CPHF) methods

These formalism involves molecular Hamiltonian as field term  $(-r.F)$ , which describes the interaction between the external uniform static field and the electronic structure. At a given field strength the molecular wave function is found, from which the appropriated expectation values of the field-dependent molecular energy  $(E(F))$  and the field-dependent dipole moment  $(\mu(F))$  can be evaluated by following equation

$$E(F) = \langle \psi(F) | H(F) | \psi(F) \rangle \quad (2.5)$$

$$\mu(F) = \langle \psi(F) | \sum q_i(F) r_i(F) | \psi(F) \rangle \quad (2.6)$$

The relationship between the  $\mu$  of a molecule interacting with an external electric field and the NLO response can be given as

$$\mu_i(F) = \mu_i^0 + \sum_j \alpha_{ij} F_j + \sum_{j<k} \beta_{ijk} F_j F_k + \sum_{j<k<l} \gamma_{ijkl} F_j F_k F_l + \dots \quad (2.7)$$

where  $\mu_i^0$  is the dipole moment in the absence of the field and  $(\mu_i - \mu_i^0)$  is the polarization in the  $i^{th}$  direction ( $P_i$ ) as defined in equation (1.3). The (hyper) polarizabilities of increased order may be obtained by differentiating  $\mu(F)$  with respect to the field.

The partial derivative of the polarization ( $P_i$ ) with respect to the field can give the polarizability, while the second partial derivative of the polarization gives  $\beta$  and third partial derivative gives  $\gamma$  evaluated at zero field,<sup>79-81</sup>

$$\alpha_{ij} = (\partial \mu_i / \partial F_j)_{F=0} \quad (2.8)$$

$$\beta_{ijk} = (\partial^2 \mu_i / \partial F_j \partial F_k)_{F=0} \quad (2.9)$$

$$\gamma_{ijkl} = (\partial^3 \mu_i / \partial F_j \partial F_k \partial F_l)_{F=0} \quad (2.10)$$

Similarly the  $\alpha$ ,  $\beta$  and  $\gamma$  coefficients can be obtained from the molecular energy expansion<sup>80, 81</sup> as follows. The molecular dipole moment is the negative field derivative of the energy. Thus

$$\mu_i = -(\partial E / \partial F_i) \quad (2.11)$$

$$\alpha_{ij} = -(\partial^2 E / \partial F_i \partial F_j)_{F=0} \quad (2.12)$$

$$\beta_{ijk} = (\partial^3 E / \partial F_i \partial F_j \partial F_k)_{F=0} \quad (2.13)$$

$$\gamma_{ijkl} = (\partial^4 E / \partial F_i \partial F_j \partial F_k \partial F_l)_{F=0} \quad (2.14)$$

The relationships given for  $\alpha$ ,  $\beta$  and  $\gamma$  are valid for the static field limit. Thus, the majority of derivative based NLO response computations have been reported at zero frequency. Numerical differentiation strategies<sup>82, 83</sup> are used to compute the above derivatives. Pulay and others<sup>84, 85</sup> have developed analytic gradient techniques to compute the above derivatives. Generally in CPHF methods analytical gradients techniques are used to compute NLO and other properties. While in FF, numerical methods are used to calculate the derivatives.

### 2.3. One- and two-photon absorptions

The one-photon absorption rate is proportional to the imaginary part of the linear susceptibility that can be derived by time-dependent perturbation theory.<sup>86</sup> It is useful to introduce the oscillator strength to specify the “strength” of the transition. The dimensionless oscillator strength of the  $g \rightarrow e$  transition is defined as<sup>86</sup>

$$f_{eg} = \frac{2m\omega_{eg} \sum_{\alpha}^{x,y,z} \left| \langle e | \mu_{\alpha} | g \rangle \right|^2}{3\hbar e^2} \quad (2.15)$$

where the  $\mu_{\alpha}$  is the dipole moment operator. The name of “oscillator” derives from the classical theory of radiation, imaging the atom as an oscillating electric dipole. The one-photon absorption spectra can be obtained by the calculation of oscillator strength through Lorentzian lineshape broadening

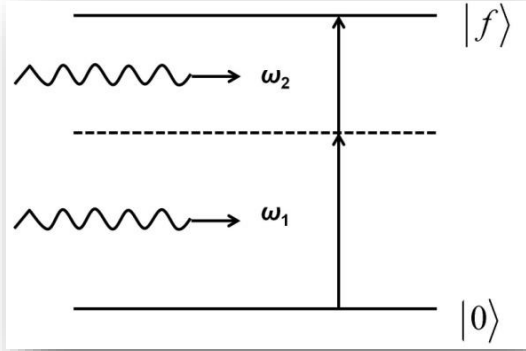
$$g(\omega_f - \omega) = \frac{1}{\pi} \frac{\Gamma_f}{(\omega_f - \omega)^2 + \Gamma_f^2} \quad (2.16)$$

where  $\Gamma_f$  corresponds to level broadening of the final state.

A typical nonlinear absorption process is two-photon absorption which means the molecule can absorb two photons at the same time under the interaction of light field, see Figure 2.1. The probability of a molecule simultaneously absorbing two identical photons is proportional to the square of the light intensity. In comparison with one-photon absorption, TPA has different selection rules and also it is related to the polarization of the light. These properties

make the TPA as a complementary spectroscopic tool for determining the position of energy levels that are not connected to the one photon absorption.

Usually the TPA activity of molecules is described by TPA cross section. The



relationship between molecular structure and two-photon absorption cross section can be also derived from standard time-dependent perturbation theory.<sup>86</sup> The TPA cross sections of random orientated systems are related to imaginary part of the second hyperpolarizability  $Im\gamma(-\omega;\omega,-\omega,\omega)$  by<sup>87</sup>

**Figure 2.1.** Two-photon absorption

$$\sigma = \frac{8\pi^2 \hbar \omega^2}{n^2 c^2} L^4 \text{Im}(\gamma) \quad (2.17)$$

where  $n$  is the refractive index and  $L$  is the local field factor.

Alternatively, the two-photon absorption cross section can be obtained by calculating the two-photon transition matrix elements  $S_{\alpha\beta}$  between the initial state  $I$  and final state  $f$ . Consider  $Im\gamma(-\omega;\omega,-\omega,\omega)$  for frequency  $\omega$  being close to half of the excitation energy of the final state  $f$  and neglect all nonresonant contributions, the expression for  $\gamma$  becomes

$$\gamma_{\alpha\beta\gamma\delta}(-\omega;\omega,-\omega,\omega) = i \frac{2\hbar^{-1}}{\Gamma_f} S_{\alpha\gamma} S_{\beta\delta}^* \quad (2.18)$$

where  $S_{\alpha\beta}$  is the two-photon transition matrix elements defined as<sup>88</sup>

$$S_{\alpha\beta} = \sum_s \left( \frac{\langle i|\mu_\alpha|s\rangle\langle s|\mu_\beta|f\rangle}{\omega_{si} - \omega} + \frac{\langle i|\mu_\beta|s\rangle\langle s|\mu_\alpha|f\rangle}{\omega_{si} - \omega} \right) \quad (2.19)$$

where  $\alpha, \beta (x, y, z)$ ,  $\mu$  is the dipole moment operator,  $\omega_{si}$  represents the excitation energy to each intermediate state  $s$ , and the summation here includes all intermediate, initial and final states.

The TPA transition probability for a molecule is dependent on the polarization of the laser beams. The orientationally averaged two-photon probability is given by<sup>89</sup>

$$\delta_{tp} = \sum_{\alpha\beta} [F \times S_{\alpha\beta} S_{\beta\alpha}^* + G \times S_{\alpha\beta} S_{\alpha\beta}^* + H \times S_{\alpha\beta} S_{\beta\alpha}^*] \quad (2.20)$$

Here  $F$ ,  $G$  and  $H$  are coefficients dependent on the polarization of the light and are defined as

$$F = -|\lambda \cdot \nu^*| + 4|\lambda \cdot \nu|^2 - 1 \quad (2.20a)$$

$$G = -|\lambda \cdot \nu^*|^2 - |\lambda \cdot \nu|^2 + 4 \quad (2.20b)$$

$$H = 4|\lambda \cdot \nu^*| - |\lambda \cdot \nu|^2 - 1 \quad (2.20c)$$

where  $\lambda$  and  $\nu$  are the polarization vectors of the laser beam. The values of  $F$ ,  $G$  and  $H$  are 2, 2 and 2 for linearly polarized light and -2, 3 and 3 for the circular case.

The macroscopic TPA cross section that can be directly compared with the experiment can be obtained by<sup>88, 90</sup>

$$\sigma_{tp} = \frac{4\pi^2 a_0^5 \alpha \omega^2 L^4}{15c \Gamma_f n^2} g(\omega) \delta_{tp} \quad (2.21)$$

where  $a_0$  is the Bohr radius,  $\alpha$  is the fine structure constant,  $L$  is the Lorentz field factor,  $g(\omega)$  provides the spectral line profile,  $n$  is the refractive index and the level broadening  $\Gamma_f$  of final state is assumed to have the commonly used value  $\Gamma = 0.1 f \text{ eV}$ . If the Bohr radius and the speed of light are given in cgs units and the frequency  $\omega$  and the TPA probability  $\delta_{tp}$  are in atomic units, the resulting unit will be  $cm^4s$  which is often expressed as the Göppert-Mayer unit ( $1GM = 10^{50} cm^4s$ ).

### 2.3.1. Few-states model

Equation (2.7), which includes the summation of all the intermediate, initial and final states for computing TP transition matrix elements, represents the so-called sum-over-states (SOS) method. Since it requires the information of all excited states, it means that the *ab initio* calculations could be too expensive to use. In practice, especially for charge-transfer molecules, it is used by truncation of the SOS expression to only include the dominating states and

excitation channels. That is the few-states model.<sup>90, 91</sup> This model not only makes the SOS approach to a manageable extent, but also provides a better understanding for the structure-to-property relations. The validity of the few-states model has been confirmed by comparing its results with those obtained from the analytical response theory.

In the few-states model, for the symmetrically substituted one-dimensional molecules, usually its first excited state is a charge-transfer state, but the two-photon transition is forbidden in this situation. Thus we have to use at least a three-state model for calculation of the TPA cross section, which has a simple form as

$$S_{zz} = \frac{2\mu_z^{01}\mu_z^{1f}}{\omega_1 - \omega} \quad (2.22)$$

As to asymmetrically substituted one-dimensional molecules it is sufficient to include only the ground state and final TPA state because the final TPA state is usually the charge-transfer state

$$S_{zz} = \frac{2\mu_z^{0f}(\mu_z^{ff} - \mu_z^{00})}{\omega_f - \omega} \quad (2.23)$$

For two-dimensional charge-transfer molecules, when the excitation scheme is dominated by two major transitions, from ground state  $0$  to the final excited state  $f$  via the intermediate state  $l$ , the TPA transition matrix for symmetric molecules often can be expressed by a three-state model

$$S_{\alpha\beta} = \frac{\mu_\alpha^{01}\mu_\beta^{1f}}{\Delta E} + \frac{\mu_\beta^{01}\mu_\alpha^{1f}}{\Delta E} \quad (2.24)$$

Where  $\Delta E = \omega_1 - \omega = \omega_1 - \omega_f / 2$ ,  $\mu_\alpha^{ij}$  is the dipole moment between the state  $|i\rangle$  and  $|j\rangle$  and  $\alpha, \beta \in \{x, y\}$ . In asymmetric planer molecules, when the excitation is dominated by the transition from ground state  $|0\rangle$  to the final excited state  $|f\rangle$ , the two-state model can be used.

$$S_{\alpha\beta} = \frac{\mu_\alpha^{0f}\Delta\mu_\beta}{\Delta E} + \frac{\mu_\beta^{0f}\Delta\mu_\alpha}{\Delta E} \quad (2.25)$$

Where  $\Delta E = \omega_f - \omega = \omega_f / 2$ ,  $\Delta\mu$  denotes the dipole moments between the ground state and the final state. More general, if an asymmetric molecule has more than one charge transfer state, there will be several dominant excitation channels (see Figure 2.2). For instance, an

asymmetric molecule has two charge transfer states  $S_1$  and  $S_2$ . If the TPA state is the  $S_1$ , there are two dominant scattering processes involved, *i.e.*,  $S_0 \rightarrow S_2 \rightarrow S_1$  and  $S_0 \rightarrow S_1 \rightarrow S_1$ . Therefore, three-state model should be employed, which can be written as

$$S_{\alpha\beta} = \frac{\mu_{\alpha}^{01}\Delta\mu_{\beta} + \mu_{\beta}^{01}\Delta\mu_{\alpha}}{\Delta E_1} + \frac{\mu_{\alpha}^{02}\mu_{\beta}^{21} + \mu_{\beta}^{02}\mu_{\alpha}^{21}}{\Delta E_2} \quad (2.26)$$

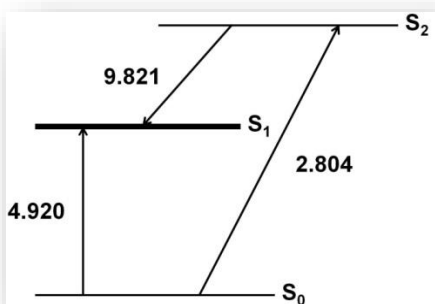


**Figure 2.2.** The excitation channels:  $S_0 \rightarrow S_2 \rightarrow S_1$  and  $S_0 \rightarrow S_1 \rightarrow S_1$ , the numbers beside the lines are transition moments.

Using the few-states model, the transition energy, transition dipole moments and the difference of the permanent dipole moment between the ground and excited states are specified. Then the dependence of the TPA properties on the molecular electronic structure is clearly illustrated. In this thesis, the few-states model is employed to explain the TPA properties of several interacting polar chromophores.

## 2.4. Principles of computational phosphorescence

According to the molecular analogue of Hund's rule in atomic physics, the triplet excited states are always placed lower in energy than the corresponding singlet excited states, which are formulated by this equation,

$$E(S_1) - E(T_1) = 2 \iint \psi_i^*(1)\psi_u^*(2) \left( \frac{e^2}{r_{1,2}} \right) \psi_i(2)\psi_u(1) dv_1 dv_2 \quad (2.27)$$

In the framework of the electric-dipole approximation, the electronic transitions between the ground singlet ( $S_0$ ) and excited singlet ( $S_n$ ) states are spin allowed and are also usually allowed by the orbital symmetry selection rules. In contrast, the absorption and emission involving singlet and triplet states ( $T_n$ ) are strongly spin-forbidden since they proceed as second-order, or nonlinear processes involving both spin-orbit and dipole couplings.

### 2.4.1. Spin-orbit coupling and S-T mixing

Neglecting spin-orbit coupling and other relativistic effects, any singlet state ( $^1\psi$ ) can be represented as a product of a symmetrical spatial wave function ( $\Phi_+$ ) and an unsymmetrical spin wave function ( $\Omega_-$ ):

$$^1\psi = \Phi_+ \Omega_- \quad (2.28)$$

For two electrons, the spatial and spin parts for the singlet state can be written as follows:

$$\Phi_+ = \frac{1}{\sqrt{2}} [\varphi_a(1)\varphi_b(2) + \varphi_a(2)\varphi_b(1)] \quad (2.29)$$

$$\Omega_- = \frac{1}{\sqrt{2}} (\alpha\beta - \beta\alpha) \quad (2.30)$$

where  $\varphi_a(1)$  and  $\varphi_b(2)$  are the molecular orbitals which depend on the spatial coordinates  $x_1, y_1$  and  $z_1$  and  $x_2, y_2$  and  $z_2$  for the first and second electrons, respectively;  $\alpha$  and  $\beta$  are the eigenfunctions of the one-electron  $S_z$  operator, with quantum numbers  $M_s = \pm 1/2$ .

The triplet state wave function ( $^3\psi$ ) is also asymmetrical and can be represented as a product between an asymmetrical spatial wave function ( $\Phi_-$ ) and three different symmetrical spin wave functions ( $\Omega_+^1, \Omega_+^{-1}$  and  $\Omega_+^0$ ):

$$^3\psi = \Phi_- \Omega_+ \quad (2.31)$$

$$\Phi_- = \frac{1}{\sqrt{2}} [\varphi_a(1)\varphi_b(2) - \varphi_a(2)\varphi_b(1)] \quad (2.32)$$

$$\Omega_+^1 = \alpha\alpha, \Omega_+^{-1} = \beta\beta, \Omega_+^0 = \frac{1}{\sqrt{2}} (\alpha\beta + \beta\alpha) \quad (2.33)$$

If ( $^1\psi$ ) and ( $^3\psi$ ) corresponds to the same electronic configuration, the “-” sign in the spatial part of  $^3\psi$  (equation 2.32) leads to the fact that the T state energy is lower than the S state energy (the first Hund’s rule) since the exchange integral between the orthogonal MOs  $\varphi_a$  and  $\varphi_b$  is always positive.

Actually, the  $^1\psi$  and  $^3\psi$  functions are never “pure” singlets or triplets (even for helium and noble gases) because the spin-orbit coupling always mixes the  $^1\psi$  and  $^3\psi$  eigenfunctions.<sup>92, 93</sup> The S-T mixing is responsible for phosphorescence intensity, lifetime and quantum yield.

### 2.4.2. Perturbation theory for S-T transitions

Due to the SOC effect, the singlet states of polyatomic molecules contain some admixture of triplet character. At the same time, the  $T_1$  state is contaminated by singlet state wave functions that can be described by first-order perturbation theory.<sup>92, 94</sup>

$$\tilde{T}_1 = T_1 + \sum_n \delta_n S_n \quad (2.34)$$

where  $\delta_n$  is an admixture coefficient:

$$\delta_n = \frac{\langle S_n | H_{SO} | T_1 \rangle}{E(T_1) - E(S_n)} \quad (2.35)$$

Typically the admixture coefficient values vary in the range of 0.001-0.1 depending on the system. As follows from equation (2.35), larger the value of  $\delta_n$ , the larger the  $\langle S_n | H_{SO} | T_1 \rangle$  integral in the numerator and the smaller the  $\Delta E_{ST}$  gap in the denominator. For radiative  $T_1$  decay (phosphorescence), the intensity of the  $S_0$ - $T_1$  interaction is proportional to the square of the  $\langle S_0 | M | T_1 \rangle$  transition moment ( $M$  is the electric dipole moment operator). Accounting for equations (2.34) and (2.35) and a similar mixing of the  $T_n$  and  $S_0$  states one can get:

$$\begin{aligned} \langle \tilde{S}_0 | M | \tilde{T}_1 \rangle = & \left[ \langle T_1 | M | T_1 \rangle - \langle S_0 | M | S_0 \rangle \right] \frac{\langle T_1 | H_{SO} | S_0 \rangle}{E(T_1) - E(S_0)} \\ & + \sum_n \langle S_n | M | S_0 \rangle \frac{\langle S_n | H_{SO} | T_1 \rangle}{E(T_1) - E(S_n)} \\ & + \sum_n \langle T_1 | M | T_n \rangle \frac{\langle T_n | H_{SO} | S_0 \rangle}{E(S_0) - E(T_n)} \end{aligned} \quad (2.36)$$

In general, the multipole expansion for the interaction between a molecular electronic shell and a light electromagnetic wave can be truncated with account of the electric dipole, magnetic dipole, and electric quadrupole terms. Thus, the transition moment for the  $S$ - $T$  radiation process has the following general definition:

$$\begin{aligned} |M_{S-T}|^2 = & \left\langle S_0 \left| \sum_i e r_i \right| T_1 \right\rangle^2 + \left\langle S_0 \left| \left( \frac{1}{2mc} \sum_i e r_i \right) \times \left( \frac{\hbar}{i} \sum_i \frac{\partial}{\partial r_i} \right) \right| T_1 \right\rangle \\ & + \frac{3\pi^3 (\Delta E_{S-T})^3}{10c^2 h^3} \left\langle S_0 \left| \left( m \sum_i e r_i \right) \times \left( \sum_i r_i \right) \right| T_1 \right\rangle^2 \end{aligned} \quad (2.37)$$

The first component in equation (2.37) is the electric dipole moment contribution, while the second and third terms corresponds to the magnetic dipole moment and electric quadrupole moment contributions respectively. Both magnetic dipole and quadrupole terms are negligibly small compared with the first component, but in the case when the electronic transition is forbidden in the electric dipole approximation due to some selection rules, these small magnetic dipole and quadrupole contributions become very important for molecular phosphorescence.

### 2.4.3. Phosphorescence intensity and lifetime

The oscillator strength of the  $S_0 \rightarrow T_1$  absorption is proportional to the square of the transition moment value  $M_{S-T}$ :

$$M_{S-T}^2 = \sum_{\gamma} \left| \langle \tilde{S}_0 | M_{\gamma} | \tilde{T}_1 \rangle \right|^2 \quad (2.38)$$

and is equal to

$$f_{S-T} = \frac{2}{3} \Delta E_{S-T} M_{S-T}^2 \quad (2.39)$$

where  $M$  and  $\Delta E_{S-T}$  values are in atomic units (a.u.),  $\gamma$  sets the polarization of the transition momentum  $M$  along x, y, or z axes.

The radiative lifetime ( $\tau_{\alpha}$ ) and corresponding rate constant ( $k_{\alpha}$ ) for the selected spin sublevel  $T_1^{\alpha}$  can be estimated as<sup>94</sup>

$$k_{\alpha} = \frac{1}{\tau_{\alpha}} = \frac{64\pi^4 (\Delta E_{TS})^3}{3h^4 c^3} \sum_{\gamma} |M_{\gamma}(T_1^{\alpha})|^2 \quad (2.40)$$

### 2.4.4. Quadratic response theory and phosphorescence

Response theory<sup>95, 96</sup> can be considered as a special representation of time-dependant (TD) perturbation theory<sup>97</sup> where the selected molecular property (at an external perturbation) is characterized by response functions. In the presence of a TD-perturbing field  $V^t$ , a molecular property “A” can be Fourier-transformed yielding coefficient that define the response functions of different orders (indices 1, 2, 3,.....):

$$\begin{aligned} \langle \tilde{O}(t) | A | \tilde{O}(t) \rangle &= \langle 0 | A | 0 \rangle + \int_{-\infty}^{\infty} \langle \langle A; V^{\omega_1} \rangle \rangle e^{-i\omega_1 t} d\omega_1 \\ &+ \frac{1}{2} \int_{-\infty}^{\infty} \int_{-\infty}^{\infty} \langle \langle A; V^{\omega_1}, V^{\omega_2} \rangle \rangle e^{-i(\omega_1 + \omega_2)t} d\omega_1 d\omega_2 \\ &+ \frac{1}{6} \int_{-\infty}^{\infty} \int_{-\infty}^{\infty} \int_{-\infty}^{\infty} \langle \langle A; V^{\omega_1}, V^{\omega_2}, V^{\omega_3} \rangle \rangle e^{-i(\omega_1 + \omega_2 + \omega_3)t} d\omega_1 d\omega_2 d\omega_3 \dots \end{aligned} \quad (2.41)$$

A main feature of the response theory is that the usual algorithms for the excited state summation is replaced by the solving of linear equation sets that can be accomplished without prior calculations of the excited states.<sup>96</sup>

## **CHAPTER 3**

### ***Strategic design of thiophene-fused nickel dithiolenes for efficient NLO response***

#### **Abstract**

---

In the third chapter the NLO property of two synthesized aryl extended thiophene fused Nickel dithiolenes are studied theoretically. Based on these two systems, a systematic modification is done by substituting neutral and zwitterionic donor acceptor group at the aryl (phenyl and thenyl) ring to enlarge their NLO responses. Among the four designed systems, zwitterionic donor-acceptor group significantly reduces the HOMO-LUMO energy gap resulting an enormous hike in the first hyperpolarizability ( $\beta$ ) values. To judge their high NLO response, transition dipole moment (TDM) density is also plotted and it is found that electron dissipation occurs from one donor part to the acceptor part with a large  $\Delta r$  index value. High  $\Delta r$  index values are quantitative measurement to understand the type of transitions, and observed a charge transfer transition in case of zwitterionic systems. Hence a relationship between first hyperpolarizability and TDM is established. In order to highlight the NLO active segment in a molecule, a density analysis is also presented.

---

### 3.1. Introduction

Molecular Materials with high second order ( $\beta$ ) nonlinear optical (NLO) properties have received enormous interest of the scientific community because of their multifarious applicability in optoelectronic and photonic devices<sup>98, 99</sup> as optical switching, optical communications, data storage, signal processing and optical limiting etc. One of the specific requirements related to the above applications, is to develop molecules with high NLO response. Metal dithiolene complexes are often ideal for the above-cited applications because of their unique optical and electrochemical properties.<sup>100, 101</sup> It has been found in the literature that Ni based dithiolene complexes can be potentially used as near infrared dyes for Q-switching Nd:YAG lasers<sup>102</sup> due to their high thermal as well as photochemical stability.<sup>103</sup> Dithiolenes can also be used for energy conversion<sup>104</sup> and the development of photodetectors.<sup>105</sup> Moreover they possess very long excited-state lifetimes and tunable absorption properties which make them useful for applications in photovoltaic devices.<sup>106</sup> Another important aspect about their structures is that they possess multiple stable redox states and planar geometry, an essential criteria for developing semiconductors, superconductors and molecular metals.<sup>105</sup>

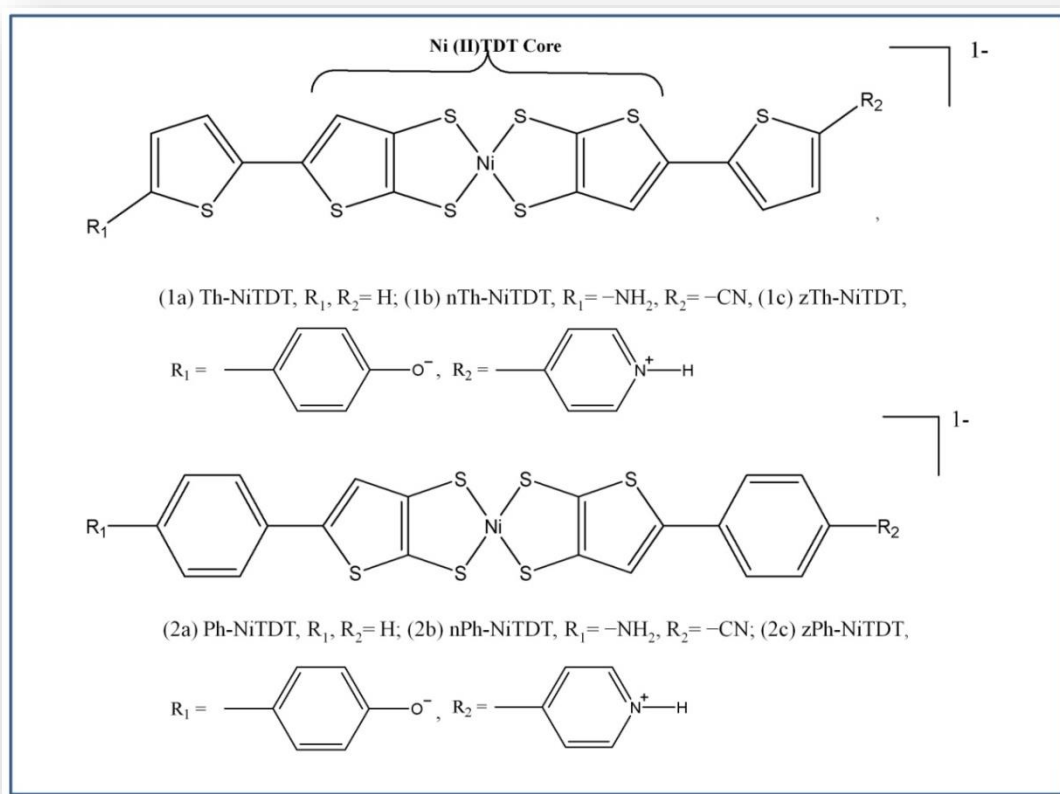
Nickel dithiolenes were first synthesized in 1960.<sup>107</sup> Since then a number of theoretical studies have been performed to understand the electronic structures and bonding schemes of these compounds. A series of interesting studies<sup>108, 109</sup> have revealed that these covalent complexes have high degree of electron delocalization. In a recent work, Herman et al.<sup>109</sup> performed INDO (intermediate neglect of differential overlap) computations for Ni(C<sub>2</sub>S<sub>2</sub>H<sub>2</sub>)<sub>2</sub> and showed that the oxidation state of the nickel atom is +2 with a d<sup>8</sup> configuration which is very common for these type of compounds.<sup>32, 110, 111</sup> Recent theoretical and experimental studies<sup>112, 113</sup> have also confirmed the previous observation in a series of Ni complexes. A more detailed presentation of properties and applications of dithiolene complexes can be found in several articles as well.<sup>103-105, 114</sup> A common tactic is to fuse aromatic rings to the dithiolene core, in order to enhance molecularity and electron delocalization.<sup>115</sup> Many fused-ring dithiolene systems have been studied so far, including fusion of benzene,<sup>116, 117</sup> functionalized benzene,<sup>118, 119</sup> thiophene,<sup>120, 121</sup> pyridine,<sup>122</sup> quinoxaline<sup>123, 124</sup> and other heterocyclic systems.<sup>125, 126</sup> Among various fused-ring dithiolene systems, thiophene-fused metal dithiolenes are of particular interest owing to their stable crystal packing arrangement. Actually, their packing arrangement is determined by the total balance of many weak intermolecular forces (hydrogen bonding, van der Waals forces,  $\pi$ - $\pi$  interactions, and S---S/M---S interactions).<sup>127, 128</sup> Additional thiophene content

would be expected to increase such intermolecular interactions and provide more significant overlap of frontier orbitals, which could result in enhanced electrical conductivity and higher magnetic transition temperatures.

In a recent report, a new family of aryl-extended nickel thiophenedithiolene complexes have been synthesized and their optical, electronic, magnetic and solid-state properties are studied as well.<sup>115</sup> It has been found that aryl-extended metal 2, 3-thiophenedithiolene can retain their planar structure even after the fusion of rings. As a consequence, the conjugation length is maximized along the molecular backbone.<sup>115</sup> These kind of Ni(II) complexes are reported to have high degree of second-order NLO response, which further increases in asymmetric compounds through push-pull mechanism.<sup>129</sup> All these facts motivate us to design nickel dithiolene based complexes for high NLO response. A well known mechanism to enhance hyperpolarizability value is to add organic donor acceptor groups to the core system.<sup>130</sup> As an example, stilbene derivatives have  $\beta$ -values of very large magnitude which is further enhanced by including the ionic donor-acceptor functional groups.<sup>131, 132</sup> Most of the studies on hyperpolarizabilities reported in the literature are on  $\pi$ -electron conjugated organic systems and there are very few reports on inorganic spacer based push-pull systems.<sup>32, 110, 111</sup> In a work by Miller et al. one zwitterionic compound in which donor (D) and acceptor (A) are linked by a sigma bond has been reported for NLO applications.<sup>133</sup> There are a number of reports in the literature<sup>134, 135</sup> in favor of the presence of crystal zwitterions structures of imidazole-1-ylacetic acid, 3-ethoxycarbonyl-2-imidazole-1-ylpropionic acid, 3-pyridinesulphonic acid which emphasizes us to choose zwitterions based substituent.

In this work, we calculate the NLO properties of Thiophene expanded Nickel thiophenedithiolene, Th-NiTDT (1a) and Phenyl expanded Nickel thiophenedithiolene, Ph-NiTDT (2a) synthesized by Amb et al.<sup>115</sup> and based on the structures (1a and 2a) a strategic design has been made (two sets) by replacing neutral and ionic donor-acceptor group as represented in Scheme 1. From the calculations it has been found that the synthesized systems (1a and 2a) possess very low values of  $\beta$  as the molecules are centrosymmetric. Keeping in mind their multifarious applicability and exceptional stability, our strategy is to modify the structure in such a manner so as to have high NLO response. We showed that by replacing the ionic donor-acceptor group at the two end of the inorganic moiety, the  $\beta$ -values enhanced by at least 10-15 times than that of the molecule without the ionic substituent. In our study, the core parts of the

synthesized systems are kept intact, rather the structures are systematically modified by annexing different functional groups to peripheral rings (Scheme 3.1).



**Scheme 3.1.** Schematic representation of the studied and designed systems.

### 3.2. Theoretical Background

The NLO properties may be defined in terms of a power of series of the molecular dipole moment in presence of an oscillating electric field according to eq 1.<sup>136</sup>

$$E = E^0 - \sum_i \mu_i F_i - \frac{1}{2} \sum_{ij} \alpha_{ij} F_i F_j - \frac{1}{3} \sum_{ijk} \beta_{ijk} F_i F_j F_k - \frac{1}{4} \sum_{ijkl} \gamma_{ijkl} F_i F_j F_k F_l - \dots \quad (3.1)$$

Here  $E$  and  $E^0$  are referred to as the energies of the perturbed and zero-field unperturbed states, the  $F_x$ 's are the field strength along a particular direction, the tensors  $\mu_i$ ,  $\alpha_{ij}$ ,  $\beta_{ijk}$  and  $\gamma_{ijkl}$  stands for the dipole moment, linear polarizability, first or static hyperpolarizability and second or cubic hyperpolarizability terms, respectively.<sup>136</sup> In general, the field as well as polarizability and hyperpolarizability terms of the above equation are frequency dependent. The first static hyperpolarizability ( $\beta_{TOTAL}$ ) may be expressed by using x, y, z components as follows,

$$\beta_{tot} = (\beta_x^2 + \beta_y^2 + \beta_z^2)^{1/2} \quad (3.2)$$

and

$$\beta_x = \beta_{xxx} + \beta_{xyy} + \beta_{xzz}$$

$$\beta_y = \beta_{yyy} + \beta_{xxy} + \beta_{yyz}$$

$$\beta_z = \beta_{zzz} + \beta_{xxz} + \beta_{yyz}$$

The charge density function  $\rho(r,F)$  can be explained in the powers of the field  $F$  in the same way as the expansions of energy and dipole moment.<sup>137</sup> The charge density function  $\rho(r,F)$  are expressed as

$$\rho(r, F) = \rho^{(0)}(r) + \sum_j \rho^{(1)}(r) F^j + \frac{1}{2!} \sum_{jk} \rho^{(2)}(r) F^j F^k + \frac{1}{3!} \sum_{jkl} \rho^{(3)}(r) F^j F^k F^l + \dots \quad (3.3)$$

The dipole moment expansion can be represented as follows:

$$\begin{aligned} \mu^i(F) &= -\int r^i \rho(r, F) dr^3 \\ &= \mu_0^i + \sum_j \alpha_{ij} F^j + \sum_{jk} \beta_{ijk} F^j F^k + \sum_{jkl} \gamma_{ijkl} F^j F^k F^l + \dots \\ &= -\int r^i \rho^{(0)}(r) dr^3 - \sum_j \int r^i \rho^{(1)}(r) dr^3 F^j \\ &\quad - \frac{1}{2!} \sum_{jk} \int r^i \rho^{(2)}(r) dr^3 F^j F^k - \frac{1}{3!} \sum_{jkl} \int r^i \rho^{(3)}(r) dr^3 F^j F^k F^l - \dots \end{aligned} \quad (3.4)$$

Here, the  $r^i$  is the  $i$  component of the electron coordinate. From equations (3.3) and (3.4), the first-hyperpolarizabilities can be expressed by

$$\beta_{ijk} = -\frac{1}{2!} \int r^i \rho^{(2)}(r) dr^3$$

Here,

$$\rho^{(2)}(r) = \frac{\partial^2 \rho}{\partial F^j \partial F^k} \quad (3.5)$$

This derivatives of electron densities with respect to external electric fields are referred to as  $\beta$  densities.<sup>137</sup> In this study, we confine our attention to the  $\beta$ -densities which are calculated by using the following 2<sup>nd</sup> order numerical differentiation formula.

$$\rho_{zz}^{(2)}(r) = \frac{\rho(r, F_z) + \rho(r, -F_z) - 2\rho(r, 0)}{F^2} \quad (3.6)$$

where  $\rho(r, F_z)$  represents the charge density at a special point in presence of the field  $F$ . The charge densities over a three-dimensional grid of points are evaluated by the density matrix obtained by the Gaussian 09 program package. The study of  $\beta$  densities is important as it straightforwardly highlight the NLO-active segments in a molecule.

### 3.3. Computational Details

The structures of Thiophene expanded Nickel dithiophenedithiolene, Th-NiTDT (1a) and Phenyl expanded, Ph-NiTDT (2a) complexes are taken from the crystallographic file format (CIF),<sup>115</sup> and the positions of the hydrogen atoms in the synthesized systems were partially optimized using density functional theory (DFT) based methodology with the B3LYP functional<sup>138-140</sup> in conjugation with the 6-311++g(d,p) basis set. It has been reported<sup>115</sup> that the two synthesized systems possess one unpaired electron; all the calculations have been done with unrestricted DFT formalism along with the geometry optimization for the designed systems (1b, 1c, 2b & 2c) at B3LYP functional and 6-311++g(d,p) basis set.

For calculating the  $\lambda_{\max}$  (nm) values of the synthesized systems, we have employed CAM-B3LYP/6-311g(d,p) methodology in the solution phase using the dielectric constant of the experimental solvent (acetonitrile) within polarizable continuum model (PCM) and compared our computed data with the experimentally reported excitation energies values.<sup>115</sup> Thus we have optimized the computational methodology with the help of experimental data provided for two synthesized systems (1a, 2a) and have used the same methodology for calculating excitation energies for our designed systems (1b, 1c, 2b, 2c).

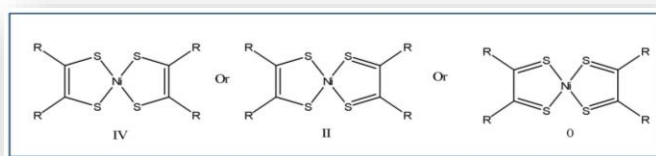
In order to highlight the NLO-active segments in a molecule, a contribution analysis<sup>137, 141</sup> has been carried out to analyze the results of the TD-DFT calculations. The NLO behavior and the first hyperpolarizability ( $\beta$ ), have been quantitatively evaluated for all the studied species by using UB3LYP/6-311++g(d,p) methodology in Gaussian 09 software.<sup>142</sup> Benchmarking of the computational model has been done with a very common push-pull system, 4-amino 4-nitro

stilbene<sup>74</sup> whose experimental first hyperpolarizability ( $\beta$ ) has been measured to be  $(260 \pm 35) \times 10^{-30}$  esu. We could, to a reasonable extent reproduce the  $\beta$  value of this system ( $184 \times 10^{-30}$  esu in gas phase) with same functional and with 6-311++g(d,p) basis set in Gaussian 09 suit of program. The correlation of our computed results with the experimentally reported data provoked us to choose this basis set and functional combination for the estimation of  $\beta$  values of our designed systems. The transition dipole moment (TDM) has been calculated based on dipole moment integral between occupied and virtual MOs. The contribution from each MO pair to the transition dipole moment can be straightforwardly evaluated and visualized with the help of Multiwfn wave function analyzer.<sup>143</sup>  $\Delta r$  index which proposed to measure the charge transfer length during electron excitation has also been calculated in Multiwfn.

### 3.4. Results and Discussions

#### 3.4.1. The electronic structure of Nickel dithiolene (NiDT)

Bisdithioglyoxalnickel,  $\text{Ni}(\text{S}_2\text{C}_2\text{H}_2)_2$ , or simply Nickel dithiolene (NiDT) is a characteristic example of square planar derivatives involving “non-innocent” conjugated sulfur-based ligands. Several bonding structures describing 8, 10 or  $12\pi$ -electron systems have been proposed for NiDT,<sup>144, 145</sup> where the formal oxidation states of Ni is 0, +2 and +4 respectively. For Ni(0) systems, the ligands are expected to retain their diketonic structure, though we hardly found any concrete evidence for such complex.<sup>146</sup> The ligands are assumed to be dithiolatodianions,  $^-\text{S}-\text{CH}=\text{CH}-\text{S}^-$  in Ni (IV) which usually occurs in  $d^8$  neutral NiDT.<sup>146</sup> NiDT is one of the first examples of complex of this family for which an assignment of the nickel



oxidation state proved to be problematic as summarized in Figure 3.1.

**Figure 3.1.** Schematic presentation of different oxidation state of NiDT complex.

A series of interesting studies regarding the electronic structure of such complex have revealed that these complexes are in fact Ni(II) complexes with each ligand bearing a radical.<sup>147, 148</sup> Calculations also showed that the frontier orbitals of such complexes are ligand-based rather than metal-based.<sup>149</sup> Because of this peculiarity, change in oxidation state in such complexes occurs at the ligand center rather than at the metal centre. This property is illustrated by the fact

that nickel dithiolene complexes undergo facile single-electron reductions leading to the formation of paramagnetic radical anion when singly reduced and a diamagnetic nickelate (II) when doubly reduced (Figure 3.2).

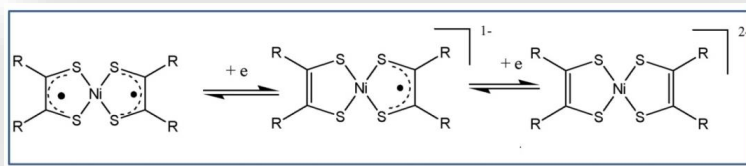


**Figure 3.2.** Redox activity of Ni dithiolene complex.

Two different situations may occur upon addition of an electron to NiTDT species (i.e. formation of  $[\text{NiTDT}]^-$ ). In the first case, electron occupies a metal d-orbital of the  $\text{M}^{\text{II}}$  ion, which is therefore reduced to  $\text{M}^{\text{I}}$  (case of an “innocent” ligand). The Multiplicity of  $[\text{NiTDT}]^{-1}$  anion containing  $\text{Ni}^{\text{I}}$  is 2. In the 2<sup>nd</sup> case, the electron fully or partially occupies an antibonding orbital of  $\text{L}^{-1}$  ligand (in case of non-innocent ligand). In this case two values of different spin states can exist: quartet and open-shell doublet. In a recent report, the magnetic susceptibilities of some synthesized systems based on NiTDT core *i.e.*, Tetrabutylammonium Bis(5-(2-thienyl)-2,3-thiophenedithiolato)-nickelate(II),  $[\text{Bu}_4\text{N}]\text{NiTDT}$  and various salts of NiTDT were measured by NMR in solution using the Evans method<sup>150, 151</sup> and also in the solid state using vibrating-sample magnetometry and the obtained susceptibility values are found to be greater than  $1.73 \mu_B$ , indicating  $S=1/2$ . Hence, all the subsequent computations on the studied complexes are performed assuming the doublet state as the ground state.

### 3.4.2. HOMO-LUMO Gap, Excitation Energies and NTOs analysis

The set of compounds we have studied can be categorized into two subsets: (a) Thiophene expanded NiTDT and its derivatives (1a, 1b, 1c; Scheme 3.1) and (b) Phenyl expanded NiTDT and its derivatives (2a, 2b, 2c; Scheme 3.1). In order to have a clear idea which orbitals are responsible for transitions, we have analyzed natural transition orbitals (NTOs). As can be seen in Figure 3.3, the HOTO (highest occupied transition orbital) of the entire studied complex (1a, 1b, 1c & 2a, 2b, 2c) are found to have comparable contribution from metal and ligand. On the contrary, the LUTO (lowest unoccupied transition orbital) is primarily composed of ligand-based orbitals. For complexes 1a, 1b and 2a, 2b, HOTO is more or less localized at the central metal dithiolene core, with some electron density dissipation onto the

pendent thiophene; whereas for complexes 1c and 2c, the HOTO is mainly constituted from the ionic donor part and the LUTO is from ionic acceptor part clearly indicating electron delocalization at ionic terminals. Hence from the transition orbital analysis it can be noticed that charge transfer takes place from one terminal to the other for zwitterionic complexes (1c, 2c).

From the comparison of HOMO and LUMO energies in these systems (Table 3.1), it can be concluded that attachment of electron donor-acceptor group ( $-\text{NH}_2$  and  $-\text{CN}$ ) in compounds 1b, 2b marginally affect the HOMO energy level, though LUMO is stabilized to some extent. However, the LUMO energies are found to be significantly reduced in zwitterionic complexes 1c and 2c, resulting decrease in HOMO–LUMO energy gap (HLG) (Table 3.1). Hence compared to the two synthesized systems (1a & 2a), all our designed systems possess lower value of HLG. Another important point to note is that both the HOMO and LUMO are oriented in mutually perpendicular fashion in 1b, whereas both the orbital lie in the plane of ring in 2b (Figure S7 in ESI).<sup>152</sup> This difference in the orientation of MOs can be correlated with their first hyperpolarizability value (Table 3.1), which is higher in 2b than 1b.

**Table 3.1.** HOMO/LUMO energies and  $\beta_{\text{tot}}$  values of NiTDT and its derivative computed in gas-phase at UB3LYP/6-311++g(d,p) level of theory.

Molecule	Energies in gas-phase (eV)			$\beta \times 10^{-30}$ esu
	HOMO <sup>a</sup>	LUMO <sup>b</sup>	$\Delta E_{\text{H-L}}$ <sup>c</sup>	
Th-NiTDT	-1.838	0.724	2.562	4.02
nTh-NiTDT	-2.002	0.056	2.058	455.92
zTh-NiTDT	-2.1284	-1.7566	0.3714	5890.9
Ph-NiTDT	-1.805	0.830	2.635	22.67
nPh-NiTDT	-1.962	0.155	2.117	643.08
zPh-NiTDT	-2.34	-1.6587	0.6813	18553.6

<sup>a</sup>HOMO stands for highest occupied molecular orbital.

<sup>b</sup>LUMO stands for lowest unoccupied molecular orbital.

<sup>c</sup> $\Delta E_{\text{H-L}}$  represents HOMO-LUMO energy gap.

**Table 3.2.** TDDFT calculated transitions for Thienyl (1a) and Phenyl (2a) expanded analogues of NiTDT core and its derivative (1b, 1c & 2b, 2c) at CAM-B3LYP/6-311g(d,p) level of theory.

Compound	$\lambda_{\max}^{\text{cal}}$ (nm)	$f$	Primary description
1a	1173	0.2274	130B to 131B
1b	1229	0.1749	140B to 141B
1c	1371	0.6975	175A to 176A
2a	1103	0.2589	128B to 129B
2b	1057	0.2089	138B to 139B
2c	1414	0.3635	172B to 173B

In order to explain the variation of optical properties in NiTDT series, the electronic excitation energies of the monoanions (1a and 2a) are calculated using TDDFT approach and compared with the experimental data. The  $\lambda_{\max}$  values for 1a and 2a have been calculated as 1438 nm and 1281 nm, which are in reasonable range to the experimentally measured values (1108 and 1076 nm).<sup>115</sup> However, the absorption wavelengths (1173 and 1103 nm) when calculated in the gas phase, much closer result compared to the solution phase has been obtained. Thus for the designed systems gas phase only calculations are performed to get the absorption wavelength. For subset 1a, 1b, 1c and 2a, 2b, 2c, excitation energy and HLG follow the same trend (Table 3.2) as explained earlier that the donor-acceptor group decrease the HLG consequently increases the absorption wavelength. There is only one exception, the excitation energy of 2b which is more than 2a. The excitation of the Ni derivatives is an intramolecular charge transfer ( $\pi$ - $\pi^*$ ) over the  $\pi$ -type orbitals of the ligand.

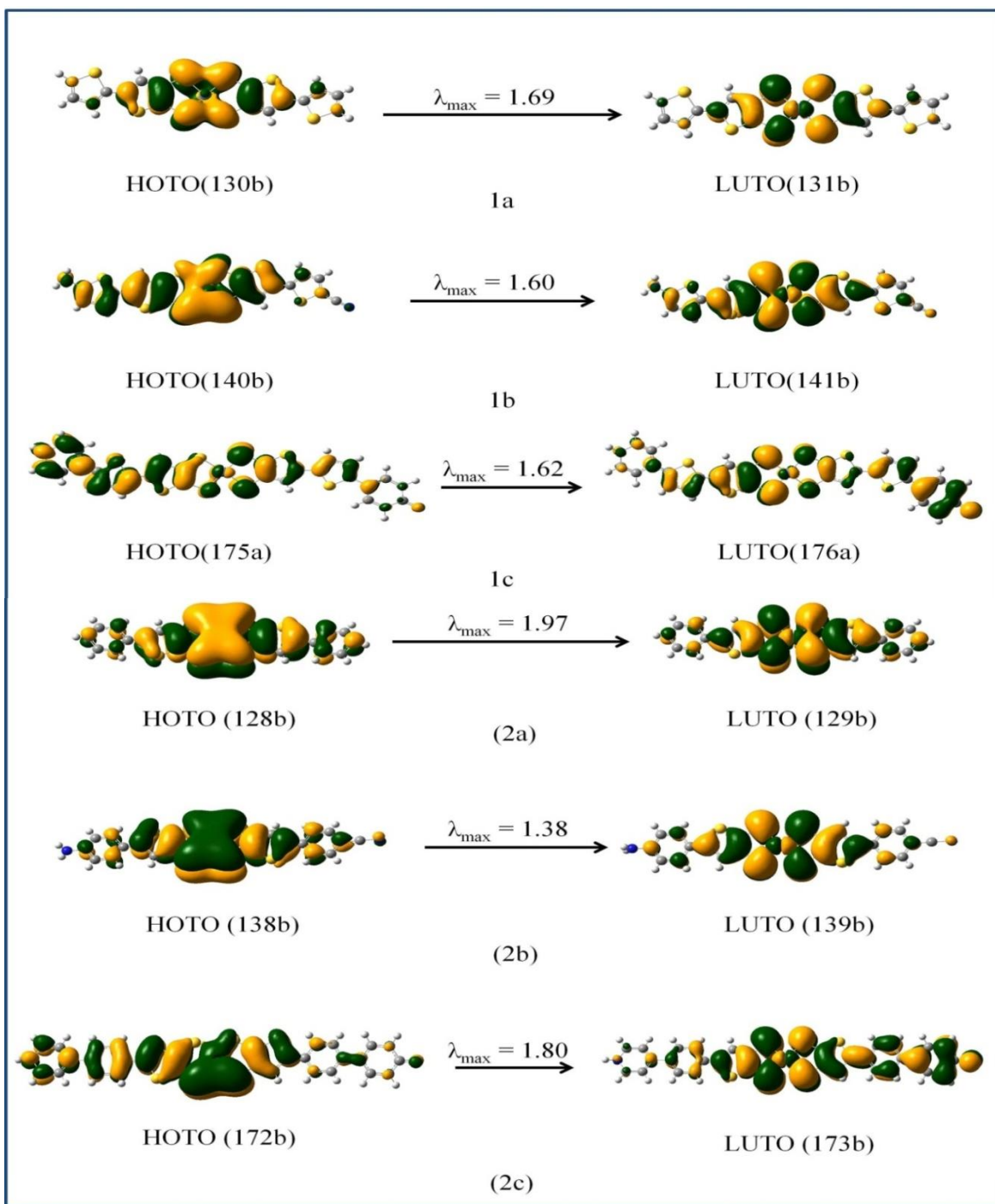


**Figure 3.3.** The dominant natural transition orbital (NTO) pairs for the systems under study. The "hole" (highest occupied transition orbital; HOTO) is on the left, the "particle" (lowest unoccupied transition orbital; LUTO) on the right. The associate eigenvalues,  $\lambda_{\max}$  is given over the arrow.

### 3.4.3. NLO Properties

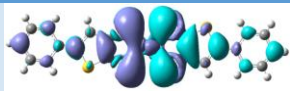
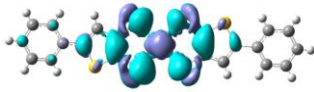
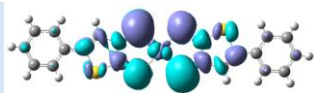
From the reported values in Table 3.1, complexes 1c and 2c with lowest HLG are found to have the highest values of  $\beta_{TOTAL}$  among the members of NiTDT series, which delineate an inversely proportional relation between the HLG and intrinsic first hyperpolarizability.<sup>153, 154</sup> To explain the origin and variation of NLO responses in NiTDT series, the  $\beta$  densities and transition dipole moments (TDM) are also calculated for these systems under investigations. Table 3.3 shows three strong absorption peaks with their oscillator strength ( $f$ ) and pictorial presentation of transition dipole moments (TDM) for the corresponding transition for system 2a. These data are also in agreement with the fact that the oscillator strength ( $f$ ) is directly related to the square of the TDM (in atomic unit),  $f = \frac{2}{3} \Delta E \times (D_x^2 + D_y^2 + D_z^2)$ , where  $\Delta E$  denotes the transition energy between the two states. From the reported TDM plot in Table 3.3, we can also observe that for energy state ( $S_4$ ) with highest oscillator strength, the electrons from one terminal is transferred to the other terminal. For the same system (2a), when we consider the energy states with lower oscillator strength ( $f$ ) values (*e.g.* states  $S_7$  and  $S_9$  in Table 3.3), the transitions are referred to as local excitations indicating electron oscillation of the state  $S_4$  is the strongest. Keeping the previous observations in mind, the transitions with highest oscillator strength for each of the remaining systems have been considered. The results are reported in Table 3.4 along with a pictorial presentation of the transition dipole moment in Figure 3.4. For subset 1a, 1b, 1c, highest value of TDM has been found for 1c which can be evident from their highest  $\Delta r$  index value.<sup>155</sup> This index is introduced with the aim of exploring the metric of excited electronic states in the framework of the time-dependent density functional theory. It is based on the charge centroids of the orbitals involved in the excitations and can be interpreted in term of the hole-electron distance. It has been reported in the literature that the type of excitation can be judged with the help of this index.  $\Delta r \leq 1.5 \text{ \AA}$  indicates local excitations, whereas  $\Delta r \geq 2.0 \text{ \AA}$  indicates long-range excitations.<sup>155</sup> Theoretical predictions can also be outlined here. The hole-particle pair interactions could be related to the distance covered during the excitations, so one possible descriptor could be their average distance, weighted in function of the excitation coefficients. The following definition will be then introduced:

$$\Delta r = \frac{\sum_{i,l} (K_i^l)^2 \left| \langle \varphi_i | r | \varphi_l \rangle - \langle \varphi_i | r | \varphi_i \rangle \right|}{\sum_{i,l} (K_i^l)^2} \quad (3.7)$$

where index  $i$  and  $l$  run over all occupied and virtual MOs, respectively.  $\varphi$  is orbital wave function.

For 1c, the electrons from donor part are transferred to the acceptor part with strongest electron oscillation amongst this set. We found similar observation for the next subset. Hence a nice correlation between  $\Delta r$  index, TDM and first hyperpolarizability has been found. In a nutshell ionic donor-acceptor group can increase the TDM as well as first hyperpolarizability values to a large extent.

**Table 3.3.** Transition energies (eV, nm), their oscillator strengths ( $f$ ) and transition dipole moment densities for three strong transitions for Ph-NiTDT. The purple color implies charge increase upon excitation and the turquoise color implies charge depletion. The isovalue is  $4 \times 10^{-4}$  in a.u.

Energy State	eV	nm	$f$	Transition dipole moment density
S <sub>4</sub>	1.1238	1103.25	0.2589	
S <sub>7</sub>	1.6836	736.44	0.0138	
S <sub>9</sub>	1.9185	646.25	0.02	

**Table 3.4.** Major transition energies (eV, nm), their oscillator strengths ( $f$ ),  $\Delta r$  index and eigenvalues for three strong transitions for two sets of complexes (1a, 1b, 1c & 2a, 2b, 2c) calculated at CAM-B3LYP/6-311g(d,p).

Complex	State	nm	$f$	$\Delta r$ (Å)	Primary description, Eigenvalues ( $\lambda_{\max}$ )
1a	S <sub>4</sub>	1103	0.2589	0.36	128b-129b, 1.97
1b	S <sub>5</sub>	1057	0.2089	1.40	138b-139b, 1.38
1c	S <sub>1</sub>	1414	0.3635	8.60	172b-173b, 1.80
2a	S <sub>5</sub>	1173	0.2274	0.33	130b-131b, 1.69
2b	S <sub>4</sub>	1229	0.1749	0.87	140b-141b, 1.60
2c	S <sub>5</sub>	1371	0.6975	6.51	175a-176a, 1.62

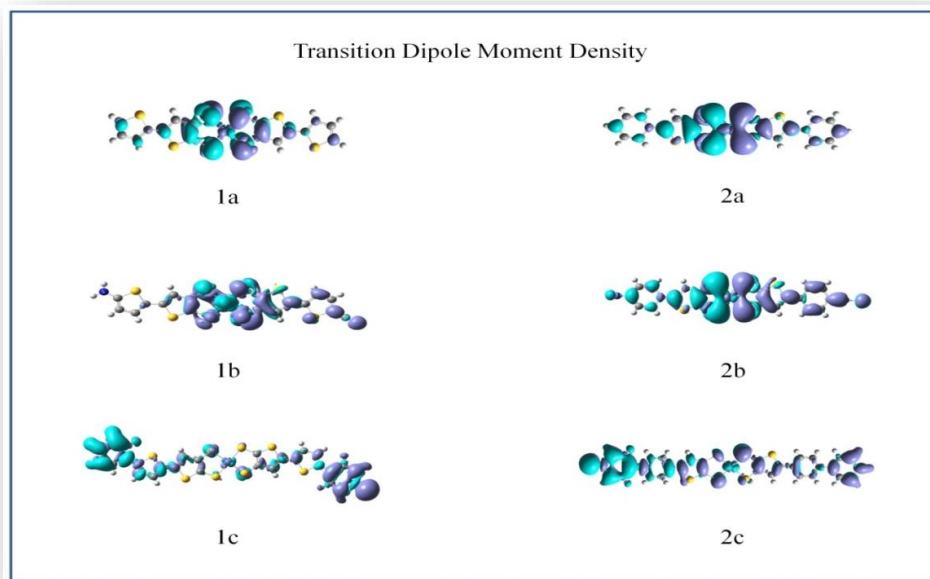


**Figure 3.4.** The transition dipole moment density of the electronic state transition from ground state for the studied complexes. The purple color implies charge increase upon excitation and the turquoise color implies charge depletion. The isovalue is  $4 \times 10^{-4}$  in a.u.

In this part we investigate second harmonic generation of the studied systems from local contribution analysis. The isosurfaces of the dynamic  $\beta$ -density are shown in Figure 3.5. From the isosurfaces, it is clear that the electrons on all the sulfur atoms in the systems are responsible for  $\beta$  density. A little contribution from the  $\pi$ -electron cloud of the extended thiophene has also been observed for complex 1a. When donor-acceptor groups substitute the hydrogens of the thiophene ring (for complexes 1b and 1c),  $\beta$  density shift to the donor acceptor part which highlights the importance of the push-pull mechanism directly. We found similar observation in case of the second set of complexes 2a, 2b. For complex 2c, electron densities are distributed to the whole molecule through the  $\pi$ -electron conjugation of phenyl ring. Electron delocalization is more in case of 2c compared to 1c due to the fact that phenyl expanded systems are more planar compared to thiophene expanded systems. Another important observation is that, in complex 2a compared with complex 1a, a five membered ring has been replaced by a six membered ring which increases push-pull character and electron delocalization resulting in enhancement of  $\beta$  value.

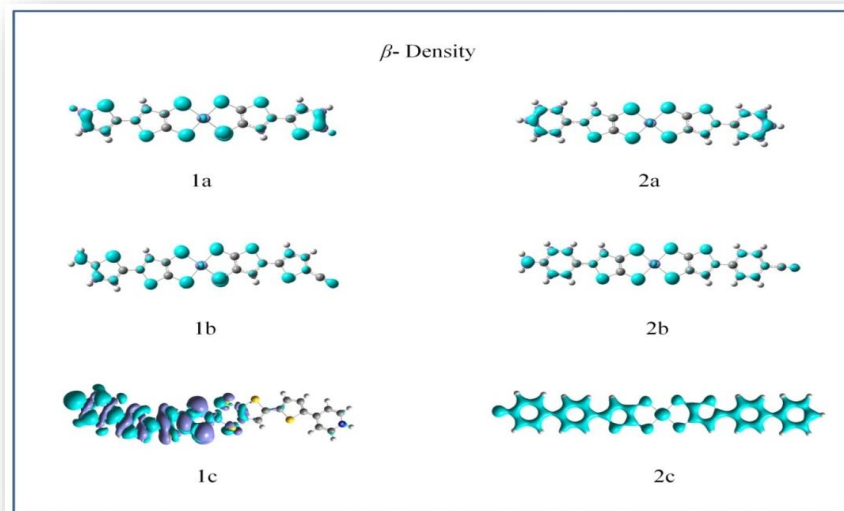


**Figure 3.5.** *Isosurfaces of the static  $\beta$  density of all the studied complexes calculated at UB3LYP/6-311++g(d,p) level.*

### 3.5. Conclusions

In the present computational study, the nonlinear optical properties of two synthesized systems, phenyl expanded and thienyl expanded thiophene fused nickel dithiolenes have been studied. Both the systems possess very low value of first hyperpolarizability. We systematically modify their structures by substituting neutral and zwitterionic donor-acceptor group at the aryl (phenyl and thienyl) ring to have high NLO response. After careful inspection of the HOMO-LUMO energies of all the six systems, we noticed that neutral donor-acceptor group marginally affects the HOMO energy level, whereas the LUMO is stabilized to some extent. Hence HOMO-LUMO energy gap (HLG) decrease. However LUMO energies are found to be significantly reduced for the zwitterionic complexes resulting large decrease in the HOMO-LUMO energy gap. Hence, HLG gradually decreases from neutral to ionic substituents for both sets of the designed systems. This observation has also been supported by the excitation energy calculations with TDDFT approach. From the calculated first hyperpolarizability values, it has been noted that the zwitterionic compounds possess very large values of  $\beta$  with low HLG. We find that by substituting ionic groups at the two ends of the Ni complex, the  $\beta$  values enhanced by at least 10-15 times than that of the molecules without any such substituent. By systematic analysis, a nice correlation between  $\Delta r$  index, TDM and  $\beta$  value have been observed. We anticipated that if synthesized, these molecules may prove to be useful in optical uses.

## **CHAPTER 4**

### ***Multifunctional magnetic materials of organic origin for biomedical applications: A theoretical study***

#### **Abstract**

---

In fourth chapter six different diradical systems based on azulene coupler and nitronyl nitroxide radical moieties are studied theoretically. Among them, three ferromagnetic diradicals are chosen for further calculation to assess their usability in different biological applications such as two-photon absorption photodynamic therapy (TPA-PDT) and magnetic resonance imaging contrast agents (MRICA). The TPA cross-section values are calculated to judge their efficiency as TPA-PDT photosensitizing agents. Calculated values of TPA cross-section lie in the range of commonly used photosensitizers for PDT. It is seen that the ferromagnetic diradicals can act as very good MRI contrast agents due to their high magnetic anisotropy characteristics. In connection to the magnetic anisotropy, the zero-field splitting (ZFS) parameters are also computed using density functional theory (DFT) based methods. It is found that the proposed diradicals can show good relaxation behaviour and consequently act as efficient MRI contrast agents. Thus, one can anticipate the multifunctional biological activity of these diradicals.

---

## 4.1. Introduction

In the past few years, organic magnetic materials have attracted the attention of the materials science community due to its interesting electrical, magnetic and nonlinear optical (NLO) properties. Appealing magnetic behaviour in reduced dimensions, diverse functional characteristics such as photosensitivity, fluorescence activity, highly efficient NLO property etc. promote their potential applications in photonic devices *viz.*, optical switching, three dimensional memory storage and photodynamic therapy (PDT).<sup>156, 157</sup> PDT is recognized as a highly effective treatment to fight oncological diseases in recent times.<sup>158, 159</sup> PDT requires a photosensitizer, which transfers its triplet state energy to molecular oxygen when activated by light. This leads to the genesis of reactive singlet oxygen species ( $^1\text{O}_2$ ) capable of causing oxidative damage to biological substrates and ultimately lead to selective and irreversible apoptosis of malignant tissues, without causing damage to the adjacent healthy ones.<sup>160, 161</sup> The excitation of photosensitizers, induced by two-photon absorption (TPA), is considered as a promising strategy in PDT and this is popularly known as two-photon photodynamic therapy (TP-PDT).<sup>157, 162</sup> Two-photon absorption is a third-order nonlinear optical process in which excitation occurs by the simultaneous absorption of two photons at longer wavelengths instead of a single-photon excitation at a shorter wavelength.<sup>163</sup> A great deal of attention is paid to TPA property of organic  $\pi$ -conjugated systems because of their large nonlinear optical response.<sup>164, 165</sup> In particular the design, preparation and application of efficient multifunctional organic diradicals are of enormous importance in the field of biomedical research.<sup>166, 167</sup> The existence of both magnetic and optical properties in the same molecule will certainly make them appropriate candidates in the field of biophotonics.<sup>168, 169</sup>

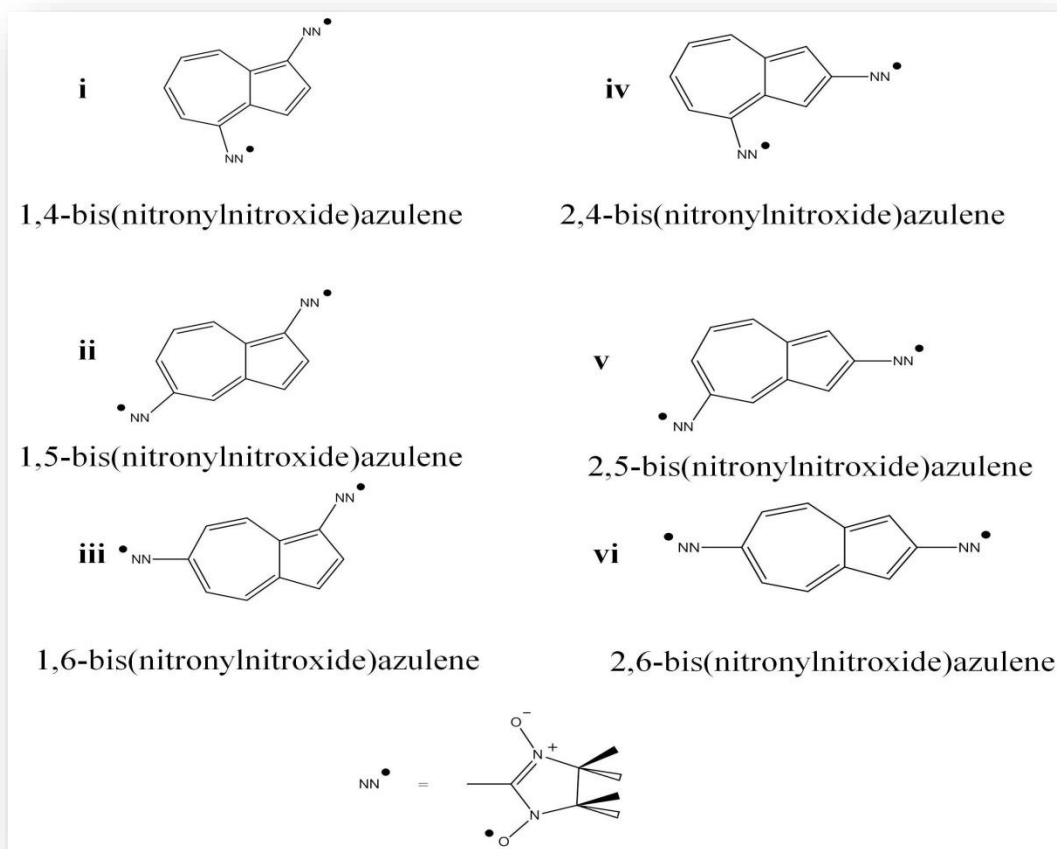
The increase in interest towards nitronyl nitroxide (NN)<sup>170, 171</sup> stems not only from their use as building blocks in the design of molecular magnetic materials,<sup>172</sup> such as purely organic ferromagnetic ordered solids,<sup>173, 174</sup> metal organic exchange coupled complexes<sup>175-177</sup> but also as new agents in bio imaging.<sup>178-180</sup> NN radical is known to be exceptionally stable, easy to prepare and able to generate co-operative magnetic properties.<sup>181</sup> Moreover it has been established that the nitronyl nitroxide radical shows cell permeability, biocompatibility and *in vivo* stability of the nitroxide-drug bonds.<sup>182, 183</sup> Although a number of NN based diradicals have been synthesized and experimentally investigated,<sup>184</sup> combined electro-optic and magnetic materials based on NN diradicals have not received adequate attention. A number of previous reports reveal that the couplers between two radical centers play a decisive role for the magnetic characterization of the

systems.<sup>185, 186</sup> Generally, magnetic coupling arises from spin polarization and spin delocalization.<sup>187</sup> Nevertheless, the magnetic interaction between two radical centers normally depends upon the nature and the spatial linkage to the coupler. Thus by a judicious choice of the coupler and by modifying the spatial orientation of the coupler, the magnetic interaction may change in a useful manner so that the magnetic molecule have some multifunctional features.<sup>187-189</sup> In a nutshell, choice of coupler will be the key factor for designing efficient multifunctional materials.

Highly aromatic couplers are known to induce strong magnetic interaction in organic diradicals.<sup>190</sup> The high aromaticity of azulenes and their strong tendency to retain aromaticity upon exposure to magnetic interaction<sup>191</sup> make them suitable as coupler between radical centers. Though aromaticity of azulene compared to one of its isomer naphthalene is less, it has long been considered to be an interesting candidate for the application in optoelectronic materials due to its unique electronic and optical properties such as large permanent dipole moment, intense blue colour and the domination of fluorescence from  $S_2 - S_0$  with low emission intensity.<sup>192, 193</sup> Stimuli responsive behavior and high luminescence intensity of azulene derivatives also became recognized in recent research.<sup>194, 195</sup> Despite quite a large number of theoretical calculations on the influence of the functional bis-substitution pattern of azulenes on their electronic properties, the theoretical investigation of magnetic and nonlinear optical properties of various diradical substituted azulene derivatives is lacking. Thus there is certainly a possibility of developing multifunctional ferromagnetic molecules with azulene as a coupler and nitronyl nitroxide as radical centers.

In this work six diradicals based on suitable substitution of NN radical in different positions of azulene coupler (Scheme 4.1) are considered as the reference systems of the present theoretical study. The estimation of magnetic exchange coupling constant values ( $J$ ) for all of these diradicals has been performed in the gas phase. The process of calculation is straightforward and well-established in the case of gas phase. However, for calculation in water and in *blood plasma* medium, the polarized continuum model (PCM) has been adopted. TPA cross section ( $\sigma$ ) has been calculated to assess the efficiency of the proposed radicals for multifunctional uses. In the literature it has been shown that diradicals of organic origin can be effective and less hazardous for use in magnetic resonance imaging (MRI) as contrast agents.<sup>196, 197</sup> In order to achieve a good MRI contrast activity, large longitudinal relaxation rate of the contrast agents is highly desired. Zero-field splitting (ZFS) magnitude is the key parameter to ascertain the longitudinal relaxation rate (*vide infra*) and the suitability of a diradical as MRI

contrast agents (MRICAs).<sup>198</sup> Hence, we have evaluated the axial and rhombic ZFS parameters ( $D$  and  $E$ ) of the diradicals so to assess their aptness as MRICAs.



**Scheme 4.1.** Schematic representation of the diradicals under investigation.

## 4.2. Theoretical Background

The magnetic exchange interaction between two magnetic sites 1 and 2, is in general expressed by the Heisenberg spin Hamiltonian,

$$\hat{H} = -2J\hat{S}_1\hat{S}_2 \quad (4.1)$$

where  $S_1$  and  $S_2$  are the spin angular momentum operators of spin-sites 1 and 2 respectively, and  $J$  is the exchange coupling constant. A positive  $J$ -value indicates a ferromagnetic interaction, whereas a negative value of  $J$  signifies an antiferromagnetic interaction. To evaluate the exchange coupling constant with reasonably less computational effort, Noodleman<sup>199, 200</sup> has proposed an unrestricted spin polarized broken symmetry (BS) formalism in the DFT framework. The BS state is not a pure spin state, but a state of mixed spin

symmetry with lower spatial symmetry. Depending on the extent of the magnetic interaction between two magnetic sites, many scientists have developed different formulae to estimate  $J$  using the BS approach.<sup>201-204</sup> Ideally, for diradicals the computed average  $\langle S^2 \rangle$  values for triplet and BS states should be exactly 2.00 or 1.00 respectively. However in reality, their difference is not exactly unity, showing a clear indication of the spin contamination problem. In order to neutralize the spin contamination error associated with the BS state, one can use a spin projection technique. For estimating the  $J$ -values of diradicals of organic origin, the following expression by Yamaguchi et al.<sup>201, 205, 206</sup> is the most widely applied<sup>186, 207, 208</sup> and has been used by us in this work

$$J_Y^{DFT} = \frac{(E_{BS}^{DFT} - E_{HS}^{DFT})}{\langle S^2 \rangle_{HS} - \langle S^2 \rangle_{BS}} \quad (4.2)$$

where  $E_{BS}$ ,  $\langle S^2 \rangle_{BS}$ , and  $E_{HS}$ ,  $\langle S^2 \rangle_{HS}$  are the energy and average spin square values for the corresponding BS and high spin (HS) states, respectively. All the above mentioned calculations are implemented through the Gaussian 09W quantum chemical package.<sup>142</sup>

The electron spin correlation time is important for clear MRI scans with enhanced contrast. The ZFS helps to get an estimation of the electron spin correlation time,<sup>209</sup> and is also one of the important parameters to characterize the geometric and electronic properties of a radical with  $S > 1/2$ .<sup>210</sup> The zero field splitting is treated in the second order of the perturbation theory where two interactions are taken into account, namely the direct spin–spin (SS) interaction and (second-order) spin-orbit coupling (SOC),<sup>210</sup> however, the SS coupling contribution is the main source of ZFS in the case of organic radicals which are formed with light elements.<sup>211</sup> The ZFS value arising from the SS interactions can be estimated through an effective spin Hamiltonian

$$\hat{H}_{ZFS} = \sum_{\mu, \nu} D_{\mu\nu} \hat{S}_\mu \hat{S}_\nu \quad (4.3)$$

where  $D_{\mu\nu}$  are the components of the ZFS tensor,  $\hat{S}_\mu$  is the  $\mu^{th}$  Cartesian component of the total electron–spin operator. After diagonalization and subsequent reframing of the molecular coordinate, Equation (4.3) optimizes to

$$\hat{H}_{ZFS} = D \left( \hat{S}_z^2 - \frac{1}{3} \hat{S}^2 \right) + E (\hat{S}_x^2 - \hat{S}_y^2) \quad (4.4)$$

where  $D$  and  $E$  are axial and rhombic ZFS parameters respectively.<sup>212</sup> The spin–spin coupling interaction appears as a dipole-dipole interaction,<sup>213</sup>

$$\hat{H}_{SS} = \frac{\alpha^2}{2} \sum_{ij} \left[ \frac{\vec{s}_i \cdot \vec{s}_j}{r_{ij}^3} - \frac{3(\vec{s}_i \cdot \vec{r}_{ij})(\vec{s}_j \cdot \vec{r}_{ij})}{r_{ij}^5} \right] \quad (4.5)$$

The ground state Kohn-Sham determinant approximates the ZFS tensor components as expectations over the single determinant,<sup>214</sup>

$$D_{\mu\nu}^{(SS)} = \frac{g_e}{4} \frac{\alpha^2}{S(2S-1)} \langle OSM_S \left| \sum_I \sum_{J \neq I} \frac{r_{ij}^2 \delta_{\mu\nu} - 3(r_{ij})_\mu (r_{ij})_\nu}{r_{ij}^5} \times \left\{ 2\hat{S}_{iz}\hat{S}_{jz} - \hat{S}_{ix}\hat{S}_{jx} - \hat{S}_{iy}\hat{S}_{jy} \right\} OSM_S \right\rangle. \quad (4.6)$$

In the above,  $\alpha$  is the fine structure constant,  $g_e$  is the gyromagnetic ratio. The operators  $\hat{S}_{i\mu}$  signify the  $\mu$ 'th components of  $i$ 'th spin vector, and  $r_{ij}$  is the distance between spin sites  $i$  and  $j$ , while  $\mu$  and  $\nu$  run over  $x, y, z$  coordinates. McWeeny and Mizuno expressed the above equation using the spin density matrix as<sup>215</sup>

$$D_{kl}^{(SS)} = \frac{g_e}{4} \frac{\alpha^2}{S(2S-1)} \sum_{\mu\nu} \sum_{\kappa\lambda} \left\{ P_{\mu\nu}^{\alpha-\beta} P_{\kappa\lambda}^{\alpha-\beta} - P_{\mu\kappa}^{\alpha-\beta} P_{\nu\lambda}^{\alpha-\beta} \right\} \times \langle \mu\nu | r_{12}^{-5} \left\{ 3r_{12,k} r_{12,l} \right\} \left( -\delta_{kl} r_{12}^2 \right) | \kappa\lambda \rangle \quad (4.7)$$

Here,  $P^{\alpha-\beta} = P^\alpha - P^\beta$  is the spin density matrix in the atomic orbital basis, and now  $\mu, \nu, \kappa, \lambda$  label the basis orbitals.<sup>211</sup> The ZFS parameters  $D$  and  $E$  are determined from the tensor components  $D_{kl}^{(SS)}$ , as<sup>216</sup>

$$D = D_{ZZ} - \frac{1}{2}(D_{XX} + D_{YY}) \quad (4.8)$$

$$E = \frac{1}{2}(D_{XX} - D_{YY}) \quad (4.9)$$

and in turn determine the static ZFS magnitude ( $a_2$ ) through

$$a_2 = \sqrt{\left( \frac{2}{3} D^2 + 2E^2 \right)} \quad (4.10)$$

From this  $a_2$ , the longitudinal electron–spin relaxation rate  $1/T_{1e}$  can be estimated by,<sup>217</sup>

$$\frac{1}{T_{1e}(B_0)} = \frac{2}{5} a_2^2 \tau_R \left[ \frac{1}{1 + \omega_0^2 \tau_2^2} + \frac{4}{1 + 4\omega_0^2 \tau_2^2} \right] + \frac{12}{5} a_{2r}^2 \tau' \left[ \frac{1}{1 + \omega_0^2 \tau'^2} + \frac{4}{1 + 4\omega_0^2 \tau'^2} \right] \quad (4.11)$$

Where  $B_0$  is the external magnetic field,  $\omega_0$  is the Larmor frequency,  $\tau_2$  and  $\tau'$  are the reduced spectral densities and  $a_{2T}$  is the transient ZFS magnitude. Larger  $a_2$  values correspond to a faster relaxation rate  $1/T_1$ .<sup>217</sup>

Despite the well established formal theoretical description of TPA,<sup>218</sup> the theory has only been applied in the context of physics of atoms and small molecules. The two-photon-absorption cross section is related to the imaginary part of the third-order polarizability as<sup>87, 219, 220</sup>

$$\sigma_{TPA}(\omega) = \frac{4\pi^2 \hbar \omega^2}{n^2 c^2} L^4 \text{Im} \langle \gamma(\omega, \omega, -\omega) \rangle \quad (4.12)$$

where  $\hbar$  is Plank's constant,  $c$  is the speed of light,  $n$  is the refractive index of the media,  $L$  is the local field factor.  $\langle \gamma \rangle$  is the second hyperpolarizability, average over all orientations, which is represented as

$$\langle \gamma \rangle = \frac{1}{15} \left[ 3 \sum_i \gamma_{iii} + \sum_{i \neq j} (\gamma_{ijj} + \gamma_{iji} + \gamma_{ijj}) \right] \quad (4.13)$$

where indices  $i$  and  $j$  refer to spatial directions  $x$ ,  $y$ , and  $z$ .<sup>221</sup> The evaluation of the third-order polarizability is done by the perturbative sum-over-state (SOS) method utilizing the ground- and excited-state energies, state dipoles, and transition dipole values.<sup>222, 223</sup>

### 4.3. Computational Details

The gas phase molecular geometry of all the azulene diradicals have been fully optimized with the unrestricted B3LYP functional using the 6-311g(d,p) basis set in Gaussian 09W suite of program.<sup>142</sup> The magnetic exchange coupling constant ( $J$ ) is estimated from the single point energies of the triplet and BS state at the UB3LYP/6-311++g (2df, 2p) level utilizing Equation (2). The ZFS parameters ( $D$  and  $E$ ) have been calculated using BPW91 functional, EPR-II basis set in ORCA suit of software.<sup>224</sup> EPR-II basis set has long been considered to be useful for calculating the  $D$  values in case of organic diradicals.<sup>225</sup> The validity of this methodology for computing  $D$  and  $E$  is tested by comparing the computed value of  $D$  and  $E$  against the experimental value available for a diradical synthesized by Rajca. The experimental ZFS parameter has been reported as  $-1.22 \times 10^{-2} \text{ cm}^{-1}$ , which is in close agreement with the computed  $D$  value ( $-1.60 \times 10^{-2} \text{ cm}^{-1}$ ). For this correlation of our computed results with the experimentally reported data by Rajca *et al.*, the same combination of basis set and functional is used for the

estimation of the  $D$  parameters for the systems under investigation. In order to check the effect of solvent on calculated properties, the  $J$  and  $D$  values are also calculated within polarizable continuum model (PCM) using the dielectric constants of water and *blood plasma* (80 and 58 respectively), which are the most common solvents in human body.

The computation of TPA cross section values have been carried out at UB3LYP/6-311++g (2df, 2p) level of theory in DALTON software.<sup>226</sup>

### 4.3. Results and discussions

The optimized geometries of the designed diradicals are shown in Figure 4.1. Frequency calculation on the optimized geometries showed no imaginary frequency for any of the molecules, which indicate intrinsic stability of the optimized structures (zero point energy corrected values are also given in the supporting information in Table S2). The gas phase magnetic exchange coupling constant ( $J$ ) values are presented in Table 4.1. Systems **i**, **iii** and **v** are found to be ferromagnetic and the systems **ii**, **iv** and **vi** are antiferromagnetically coupled. The ferro- and antiferro-magnetic behaviour of the azulene coupled diradical systems can be justified through the popular spin density alternation rules.<sup>227, 228</sup> The spin-density alternation can also be visualized through the spin density plots presented in Figure 4.2., where one can clearly see that the radicals coupled through an odd and even number of conjugated atomic centers always lead to ferro- and antiferromagnetic interactions respectively. A close inspection of Figure 2 further reveals an interesting feature of the spin density alternation. The carbon atoms situated at the junction of two fused five and seven membered rings in azulene always carry similar spins despite being neighbours. It appears that the two junction-carbon atoms in **i**, **iii** and **v** behave as single units in spin density alternation protocol. Owing to their biomedical relevance we consider only the ferromagnetic systems, *i.e.*, **i**, **iii** and **v** for further calculations

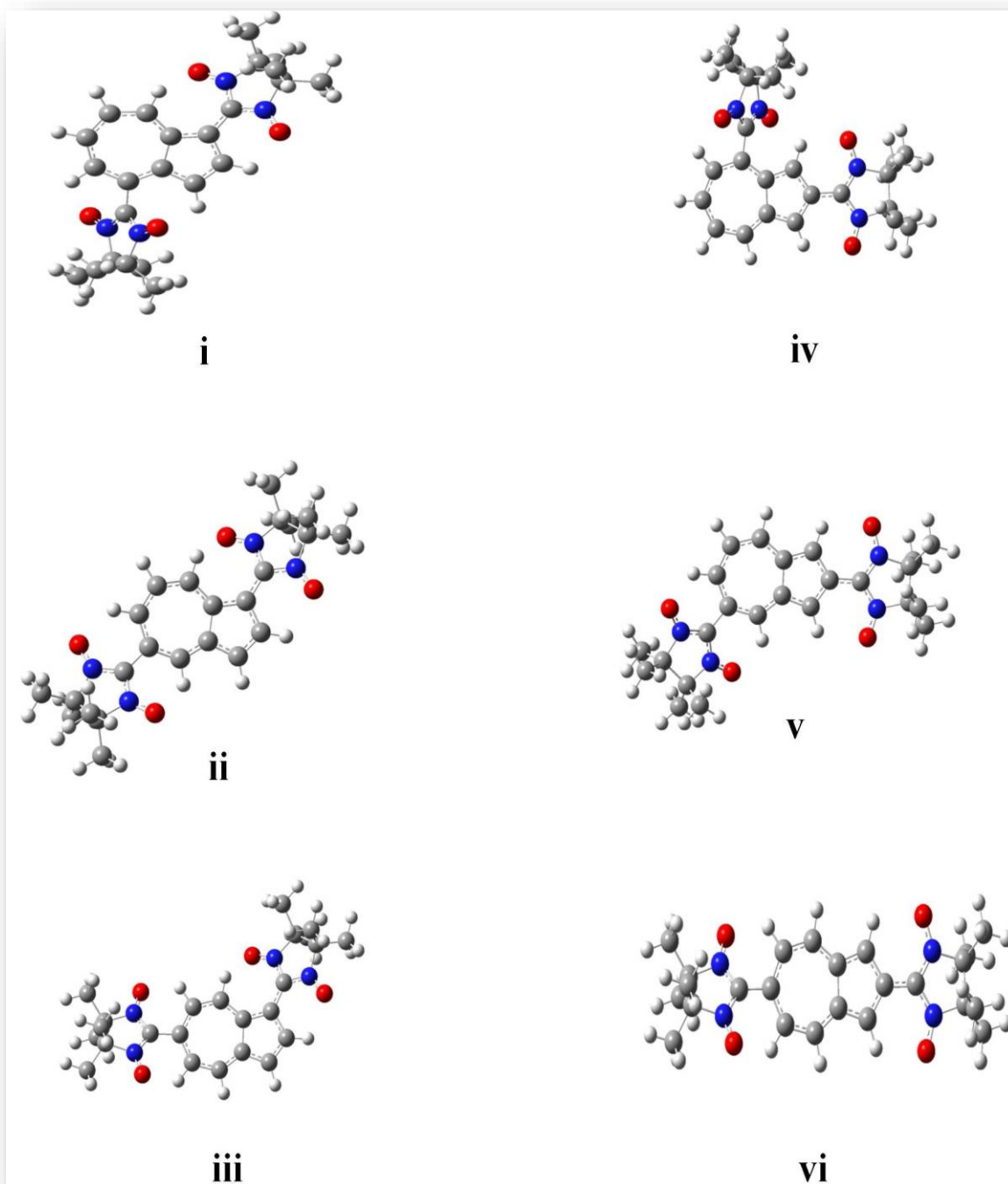


**Figure 4.1.** Optimized molecular geometry of the diradicals obtained through unrestricted B3LYP exchange correlation functional using the 6-311g (d,p) basis set.

**Table 4.1.** Calculated absolute energies in atomic units (au),  $\langle S^2 \rangle$  values, intramolecular magnetic exchange coupling constants ( $J$  in  $\text{cm}^{-1}$ ) between two radical centers for the designed diradicals at UB3LYP/6-311++g (2df, 2p) level.

Diradicals		Energy (au)	$\langle S^2 \rangle$	$J$ in $\text{cm}^{-1}$
i	Triplet	-1452.7267132	2.115519	12.75
	BS	-1452.726656	1.130897	
ii	Triplet	-1452.7346583	2.096137	-193.22
	BS	-1452.7355085	1.130392	
iii	Triplet	-1452.7330113	2.131788	47.70
	BS	-1452.7327901	1.114097	
iv	Triplet	-1452.7333679	2.106828	-81.77
	BS	-1452.7337341	1.123951	
v	Triplet	-1452.7411477	2.149931	90.37
	BS	-1452.7407227	1.117795	
vi	Triplet	-1452.7381936	2.108376	-228.89
	BS	-1452.7391866	1.156251	

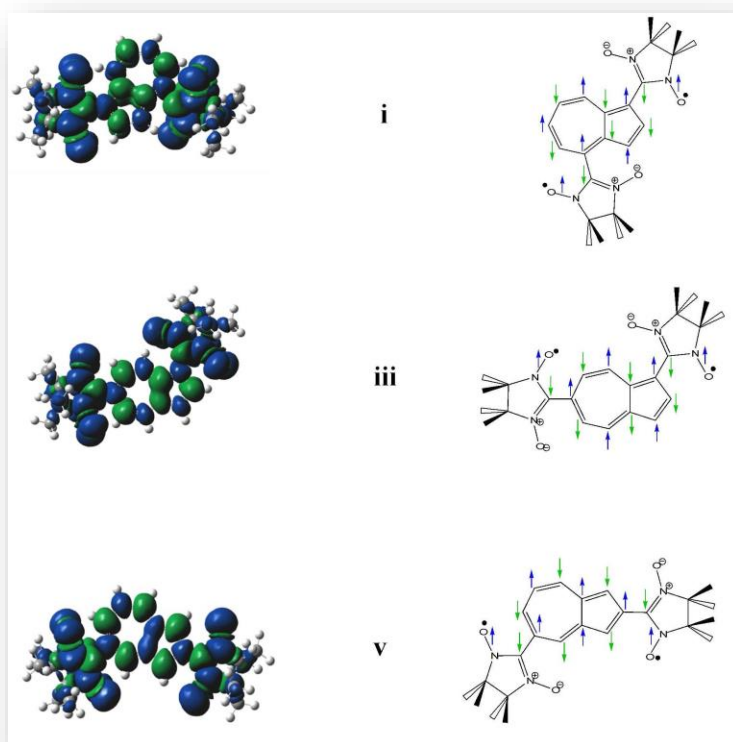


**Figure 4.2.** Spin density plots of ferromagnetic azulene diradicals. Green and blue surfaces indicate up and down spin density. Same color code is used for schematic representation of spin alternation, i.e., blue and green arrow for up and down spin respectively.

Extensive study of two-photon photodynamic therapy revealed that the treatment is relatively benign and gives finer cosmetic outcomes compared to other PDT techniques. In those methods excitation of the drugs are performed through visible light which has very low penetrability into human tissues.<sup>229, 230</sup> Simultaneous absorption of two near-IR photons is much more penetrating through tissues compared to visible light photons. Hence, excitation of the photosensitizer through near-IR photons is more desirable to destroy cancer cells present in deeper tissues.<sup>231, 232</sup> Two-photon PDT also ensures greater penetration depths and highly-selective targeting through intense laser pulse processes. TPA cross-section ( $\sigma_{\text{TPA}}$ ) estimates the efficacy of a photosensitizer that undergoes two-photon absorption. It is measured in Göppert-Mayer units ( $1 \text{ GM} = 10^{-50} \text{ cm}^4 \text{ s photon}^{-1} \text{ molecule}^{-1}$ ). The TPA cross-sections of existing photosensitizers are in the order of 1–100 GM.<sup>233</sup> In a recent report Zhao *et al.*<sup>234</sup> studied the spectroscopic properties of Chlorophyll derivative photosensitizer (CDP) and their TPA cross section is measured as 31.5 GM. The results of the two photon photodynamic therapy (TPPDT) test showed that CDP can kill all of the tested cancer cells. Hence, suitable design of compounds with higher TPA cross-sections is always desirable to ensure efficient phototherapeutic applications. Generation of singlet oxygen ( $^1\Delta_g$ ) is the key to phototherapeutic activity of the photosensitizers in PDT. A good singlet oxygen yield ( $\Phi_\Delta$ ) is desired for photo-biological cell damage or apoptosis. It has been seen that the insertion of radical moieties in a photosensitizer greatly enhances  $\Phi_\Delta$ .<sup>235</sup> Thus a diradical system will be the best candidate for use as photosensitizer in photodynamic therapy. In the present study we have calculated  $\sigma_{\text{TPA}}$  of the designed diradicals which are reported in Table 4.2. It is found that the TPA cross-section values lie in the reported range of the presently used photosensitizers. Among the three designed ferromagnetic diradicals, **v** shows the highest  $\sigma_{\text{TPA}}$  value of 21.1 GM.

Although very promising as noninvasive and safe protocols of cancer treatment, PDT is challenging in connection with the delivery of the photosensitizer to the infected tissue.<sup>[51]</sup> To ensure the monomeric distribution of the photosensitizing agent, diagnostic imaging techniques are preferred compared to regular drug delivery methods.<sup>236</sup> Magnetic resonance imaging has emerged as a powerful imaging technique in recent years. MRI, with the use of contrast agents can provide highly sensitive imaging with minute three dimensional topographical details *in vivo*. Hence, if one can integrate contrast-enhanced MRI imaging capability with PDT, the resulting imaging guided PDT can prove to be the most appreciable strategy for cancer treatment. The design of materials with good imaging and photosensitizing capability is therefore the requirement for developing improved multifunctional agents.

**Table 4.2.** The spin-spin ZFS parameter  $D_{Total}$  ( $cm^{-1}$ ), static ZFS magnitude  $a_2$  ( $cm^{-1}$ ), rhombic ZFS parameter ( $E$ ) for each ferromagnetic diradical at BPW91/EPR-II and two photon absorption cross section ( $\sigma_{TPA}$  in GM), for the same diradicals at UB3LYP/6-311++g(d,p) level.

Diradicals	$\sigma_{TPA}$ (GM)	$D_{Total}$ ( $cm^{-1}$ )	$E$ ( $cm^{-1}$ )	$a_2$ ( $cm^{-1}$ )
<b>i</b>	<b>3.8</b>	$-10.03 \times 10^{-2}$	$-1.7 \times 10^{-2}$	$8.5 \times 10^{-2}$
<b>iii</b>	<b>5.0</b>	$-11.6 \times 10^{-2}$	$-1.51 \times 10^{-2}$	$9.7 \times 10^{-2}$
<b>v</b>	<b>21.1</b>	$-10.6 \times 10^{-2}$	$-0.74 \times 10^{-2}$	$8.7 \times 10^{-2}$

A site-specific MRI contrast agent with a high rate of relaxation of water protons in the target cell is central to efficient magnetic resonance imaging. It is quite evident from the discussion in the previous section and Equation (11) that the ZFS magnitude ( $a_2$ ) is directly proportional to the longitudinal relaxation rate ( $1/T_{1e}$ ). With the increase in the value of  $1/T_{1e}$ , the observed MRI signal is enhanced. In the present work, the ZFS parameter  $D$  and static ZFS magnitude ( $a_2$ ) of the three ferromagnetic systems, namely, **i**, **iii** and **v**, have been estimated and is reported in Table 2. It is notable from Table 2 that all the ferromagnetic diradicals possess high value of  $D$  in the range of  $-8.5 \times 10^{-2} cm^{-1}$  to  $-9.7 \times 10^{-2} cm^{-1}$ . Rajca et al. in one of their pioneering works reported nitroxide based diradicals, synthesized and already been established as a MRICA of organic origin, to have  $D$  values in the range of  $-1.2 \times 10^{-2}$  to  $-1.7 \times 10^{-2} cm^{-1}$ .<sup>196, 197</sup> A diarylnitroxide triplet diradical with  $D$  and  $a_2$  values of  $-1.223 \times 10^{-2}$  and  $1.02 \times 10^{-2} cm^{-1}$  respectively is also found to be usable as MRICA.<sup>198</sup>

In order to gain an assurance of the *in vivo* functionality of the designed systems, we have calculated the magnetic exchange coupling constant ( $J$ ) and the zero field splitting parameters ( $D$ ) in water and as well as in blood plasma medium and the results are reported in Table 4.3. It is clear that the variations in  $J$  and  $D$  values of all the designed systems in different media are negligible.

**Table 4.3.** The magnetic exchange coupling constants ( $J$ ) and ZFS parameter ( $D$ ) values for the proposed ferromagnetic diradical systems in gas phase, water and blood plasma media, computed using PCM model using UB3LYP/6-311++g(2df,2p) and BPW91/EPR-II method.

Diradicals	$J$ (cm <sup>-1</sup> )			$D$ (cm <sup>-1</sup> )		
	Gas Medium	Water Medium	Blood Plasma	Gas Medium	Water Medium	Blood Plasma
i	12.75	12.40	12.42	-10.03×10 <sup>-2</sup>	-10.3×10 <sup>-2</sup>	-10.6×10 <sup>-2</sup>
iii	47.70	41.68	43.03	-11.6×10 <sup>-2</sup>	-10.6×10 <sup>-2</sup>	-10.6×10 <sup>-2</sup>
V	90.37	81.59	81.64	-10.6×10 <sup>-2</sup>	-10.9×10 <sup>-2</sup>	-10.9×10 <sup>-2</sup>

#### 4.4. Conclusion

In the present computational study we have considered the magnetic and optical properties of a few azulene based diradical systems. We have studied six diradical systems based on nitronyl nitroxide radical moiety and azulene as coupler. The magnetic property has been assessed through the magnetic exchange coupling and magnetic anisotropy. The calculated magnetic exchange coupling parameters  $J$  depict that among the six diradicals three are ferromagnetic, and three are antiferromagnetic. The magnetic exchange coupling constants have been corroborated through spin density alternation protocol. The spin density analyses of the three ferromagnetic diradicals depict an interesting alternation behavior in the azulene coupler. The junction carbon atoms of the two rings in azulene coupler always show similar spin density despite being neighbors. This behavior is a fascinating variation of the spin density alternation rule. The ability of the ferromagnetic diradicals as photosensitizer in photodynamic therapy is evaluated through the computation of the two-photon absorption cross-section. The integrative photodynamic therapy (IPDT) of tumors relies on the combined use of different factors that enhance the usefulness of IPDT.<sup>237</sup> The observed TPA cross-section values range in the reported limit of commonly used photosensitizing agents. Another dimension of the multi-property diradical system has also been explored in this work. The magnetic anisotropy of the ferromagnetic diradicals has been estimated through the zero-field splitting parameter  $D$ . A negative ZFS parameter suggests the tendency of the spin vector to orient along a specific Cartesian direction. All the three ferromagnetic diradicals show negative  $D$  values. Radical systems with negative ZFS parameters have been proved to be usable as MRI contrast agents.<sup>188</sup> It has long been shown that the larger the ZFS magnitude  $a_2$ , larger is the spin relaxation time

and the better an MRICA is.<sup>198</sup> The ZFS magnitude  $a_2$  is directly proportional to the ZFS parameter  $D$ . In the designed ferromagnetic diradicals, the ZFS parameters are found to be significantly high as for organic radical systems. The values are at least one order of magnitude higher compared to reported diradical systems usable as MRICA. Ferromagnetic systems are used as efficient probe in the magnetic hyperthermia, a popular treatment in oncology. These diradicals can also be sought for a lateral use as MRICA in magnetic resonance imaging, which is very often utilized for the detection of cancer. Treatment of interstitial tumors with PDT demands the delivery of photosensitizers to the precise location of tumor tissues for effective light irradiations. Thus a single agent that can be injected to the infected body to image tumors through MRI and simultaneously treat them by exposing to light through PDT is greatly welcomed as a proficient cancer treatment protocol. In summary we propose that if synthesized these diradical systems can promote the “see and treat” method<sup>238</sup> by proving themselves efficient in multifarious therapeutic function such as magnetic hyperthermia, MRI contrast agents and photodynamic therapy applications.

## CHAPTER 5

### *Ligand induced symmetry breaking and concomitant blue shift of emission wavelength in octahedral chromium complex*

#### **Abstract**

---

The fifth chapter deals with designing of efficient luminescent materials based on octahedral hexaminechromium(III) complex. It is found that distortion of the octahedral symmetry of  $[\text{Cr}^{\text{III}} (\text{NH}_3)_6]^{3+}$  by replacing the axial ligands with weaker halides influences the stability of the doublet state with respect to the quartet ground state. This replacement affects the doublet to quartet transition responsible for phosphorescence. The relative positions of the halides and ammonia in the spectrochemical series play an important role in the tuning of emission wave length. The proximity of fluorine and ammonia in the spectrochemical series causes blue-shift in the emission wavelength and thus provides a rational way for designing blue emitting phosphorescent materials, essential in OLED application for full color display.

---

## 5.1. Introduction

Luminescent materials have attracted considerable interest<sup>239-241</sup> due to their multifarious applications in organic light emitting diodes (OLEDs),<sup>47, 242, 243</sup> light emitting electrochemical cells (LEECs),<sup>[244]</sup> light absorbers in dye-sensitized solar cells,<sup>245, 246</sup> chemosensors, biosensors,<sup>247, 248</sup> lumophores for cell imaging,<sup>249, 250</sup> chemical photo catalysts,<sup>251, 252</sup> and so on. The suitability of luminescent materials for a specific application depends upon the stability of the system, color purity of the emitted light, high emission quantum yield, specific emission decay time and several other factors. In last decades, considerable efforts have been put in the quest of highly efficient emitters with three primary colors (red, green and blue), which are essential for full-color display. Although, red and green light emitting transition metal complexes are abundant due to triplet harvesting,<sup>253, 254</sup> blue light emitting phosphorescent materials are not easily available for the requirement of wide energy gap between the excited and the ground state.<sup>255</sup> The strong spin-orbit coupling (SOC) in the organometallic complexes containing heavy transition metals weakens the spin forbiddenness of transitions between the ground and the excited states and thus these systems partially fulfill the criteria of an ideal luminescent material.<sup>256</sup> However, the  $dd^*$  transitions in heavy metals largely quench the luminescence of blue phosphorescent materials.<sup>257, 258</sup> Another difficulty with heavy metals is the triplet-triplet annihilation which hinders the process of phosphorescence and in turn makes the materials unfit for OLED application.<sup>254, 259</sup> To surmount these difficulties with heavy metals, the  $3d$  transition metal complexes are the best alternative. For example, recently a Cu (I) complex have been found to be a blue emitter ( $\lambda_{\max}= 436\text{nm}$ ) by Yersin et al.,<sup>260</sup> though it's emission decay time is still too long for high brightness OLED application. Hamada et al. reported some Zn (II) complexes as greenish white emitter as well.<sup>261</sup> However, among the  $3d$  transition metal complexes, the Cr (III) systems have emerged as efficient luminescent materials for their substantial quantum yield and possibility of both the emission processes (fluorescence and phosphorescence) in liquid media at room temperature.<sup>59, 262</sup> Though, there exists sufficient number of experimental reports on the photoresponsive behavior of Cr (III) complexes, a comprehensive theoretical account of the phosphorescence in octahedral ( $O_h$ ) Cr (III) complex is still awaited. All these facts inspire the selection of octahedral Cr (III) complex for the theoretical investigation of its luminescent property.

The present work is divided into two parts. In the first part, a hexa-amine Cr (III) system is opted for the theoretical investigation of its luminescent property. Subsequently, the absorption

and emission wavelengths of the chosen system are computed and the values are compared with the experimental data to standardize the computational methodology. The octahedral Cr (III) complexes are found to exhibit fluorescence with weak ligands like  $F^-$ ,  $Cl^-$ ,  $Br^-$  and phosphorescence with strong ligands such as carbonyl, ammonia, cyano etc.<sup>[262]</sup> However, literature survey reveals the dearth of blue-emitting Cr (III) complexes compared to the red- or green-emitters. These facts form the basis of the second part of the work where we put our effort to find out the appropriate set of ligands which can induce the blue-shift in the emission wavelength. The phosphorescence in  $O_h$  Cr (III) complex involves excitation from ground state quartet ( $Q$ ) to excited state quartet ( $Q'$ ) followed by intersystem crossing (ISC) to the doublet state ( $D$ ). The phosphorescence energy thus depends on the separation between the lowest doublet ( $D$ ) and the quartet ground state ( $Q$ ) which is nearly equal to the absorption energy due to  $Q \rightarrow D$  transition.<sup>262</sup> Hence, in principle, the excitation of the doublet state compared to the quartet ground state can lead to the blue shift in the emission wavelength. The doublet state in the  $O_h$  Cr (III) complex can be realized by lifting the degeneracy of the  $t_{2g}$  states. In order to do so, the symmetry of the  $O_h [Cr^{III} (NH_3)_6]^{3+}$  complex is disturbed by replacing the axial ammonia with the weak halides ( $I^-$ ,  $Br^-$ ,  $Cl^-$  and  $F^-$ ). Thus, imposing the asymmetry to the complex through axial ligand substitution in  $[Cr^{III} (NH_3)_6]^{3+}$ , the doublet state can be induced. Putting different halogens in the axial position, a trend in the change of emission wavelength is observed in order to achieve the blue-shift. This study may provide a useful guideline in rational design of metal complexes with desired degree of luminescence behavior and more specifically blue-emitting phosphorescence.

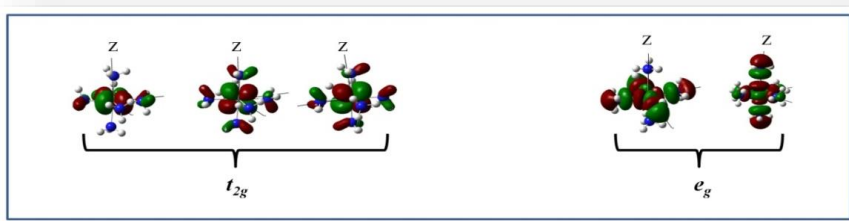
## 5.2. Computational Methods

For the geometry optimization of the studied complexes at their ground state, the B3PW91 functional is employed. This functional works well for the transition metals and has been successfully employed for studying the photo-physical properties.<sup>263, 264</sup> However, to check the performance of other functional, we had also done the same set of calculations with the most popular GGA functional PBE and meta-GGA functional TPSS. However, since the hybrid-GGA functional is placed higher than pure GGA functional in the Jacob's ladder of Perdew because of its ability to partially minimize the self-interaction energy, we present the B3PW91 result in the main text and for comparison PBE and TPSS results are provided in the supplementary. Hay and Wadt's double-zeta effective core potential (LANL2DZ) is chosen as the basis set for all the computations.<sup>265, 266</sup> Since the phosphorescence of the systems under investigation involves the

quartet and doublet spin states, unrestricted formalism is adopted in the density functional theory (DFT) calculations. The absorption and emission energies of the reference systems are obtained through the time dependent DFT (TDDFT) method coupled with same exchange-correlation functional and basis set as applied for geometry optimization of the ground quartet ( $Q$ ) and doublet ( $D$ ) states. The TDDFT approach offers a reliable route for the calculation of vertical electronic excitation spectra.<sup>267, 268</sup> This fact is supported by the good agreement of experimental spectral property with TDDFT results obtained for transition-metal complexes.<sup>269, 270</sup> Although solvent plays important role in determining excitation values. We have calculated the energy values for different energy states (quartet, doublet, excited quartet) of  $[\text{Cr}^{\text{III}}(\text{NH}_3)_6]^{3+}$  complex and found these states are minutely stabilized compared to the gas phase calculation. Hence in order to reduce the computational rigors we rely on the gas phase calculations. However, to get the accurate description of the excited quartet state ( $Q'$ ) of all the reference systems, we resort to more sophisticated complete active space self consistent field (CASSCF) method with an active space of (3, 5) and LANL2DZ basis set. With the initial guess from the state average calculation, the final geometry of the excited quartet state is obtained. Next, a single point calculation at the same DFT level is performed on this optimized geometry of the excited state molecules for comparison with the ground state condition obtained in the level of DFT. In every case, vibrational analysis is performed at the same DFT level to assure the structural stability of the systems. All the computations were done with the GAUSSIAN09W suit of quantum chemical package.<sup>142</sup>

### 5.3. Results and discussions

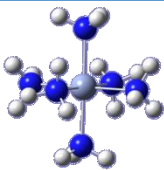
The structural parameters and energies of the optimized geometries of  $[\text{Cr}^{\text{III}}(\text{NH}_3)_6]^{3+}$  in its quartet ground state ( $Q$ ), quartet excited state ( $Q'$ ) and the lowest energy doublet state ( $D$ ) are given in the Table 1. In the quartet ground state, all the Cr-(NH<sub>3</sub>)<sub>6</sub> bond lengths are found to be equal, which ascertains the  $O_h$  symmetry of the system. The molecular orbital (MO) analysis in the quartet ground state reveals that the highest occupied molecular orbital (HOMO) and next two orbitals (HOMO – 1 and HOMO – 2) are composed with maximum contribution from Cr  $d$ -orbitals *viz.*,  $d_{xz}$ ,  $d_{yz}$  and  $d_{xy}$ . On the other hand, the lowest unoccupied molecular orbital (LUMO) and the LUMO + 1 orbitals are mainly constituted by the Cr  $d_{z^2}$  and  $d_{x^2-y^2}$  orbitals (Figure 5.1). Thus, in the octahedral field the splitting of the Cr MOs into  $t_{2g}$  and  $e_g$  set of orbitals can be confirmed in this  $[\text{Cr}^{\text{III}}(\text{NH}_3)_6]^{3+}$  complex (Figure 5.1).



**Figure 5.1.**  $t_{2g}$  and  $e_g$  set of orbitals in  $[\text{Cr}^{\text{III}}(\text{NH}_3)_6]^{3+}$ .

From the analysis of the TDDFT computation, carried out on the ground quartet state of  $[\text{Cr}^{\text{III}}(\text{NH}_3)_6]^{3+}$ , the leading excitations occurs at 420 nm (Table 5.2), which is quite close to the experimental value of absorption wavelength (Table 5.2).<sup>262</sup> The major contribution to this absorption energy comes from the electronic excitation from the 37<sup>th</sup> up-spin occupied orbital ( $\alpha$ -HOMO) to the initially unoccupied 38<sup>th</sup>  $\alpha$ -LUMO [Table S1(a) in Supporting Information]. Thus, the excited quartet state ( $Q'$ ) acquires the electronic configuration  $t_{2g}^2 e_g^1$  due to spin reserved electron excitation from  $t_{2g}$  to  $e_g$  level. The electronic configuration  $t_{2g}^2 e_g^1$  in the excited quartet state is supported from the elongation in the distance between Cr and equatorial ligands compared to the quartet ground state ( $Q$ ) (Table 5.1). In the excited quartet state, the 38<sup>th</sup>  $\alpha$ -MO which is primarily composed of the Cr  $d_{x^2-y^2}$  orbital, gets populated due to electronic excitation and the presence of electron in Cr  $d_{x^2-y^2}$  orbital causes the elongation in the equatorial ( $xy$ ) plane. On the contrary, the axial Cr-(NH<sub>3</sub>) distance remains almost unaltered in the ground and excited quartet states of the molecule (Table 5.1). Unlike the excited quartet state, the geometry in the doublet state is not much distorted compared to the ground state quartet (Table 5.1). In the doublet state the electronic distribution alters within the  $d_{xy}$ ,  $d_{yz}$  and  $d_{zx}$  set of orbitals which are not directly oriented towards the ligands and thus the structural change in the doublet state is nominal with respect to the ground state quartet (Table 5.1).

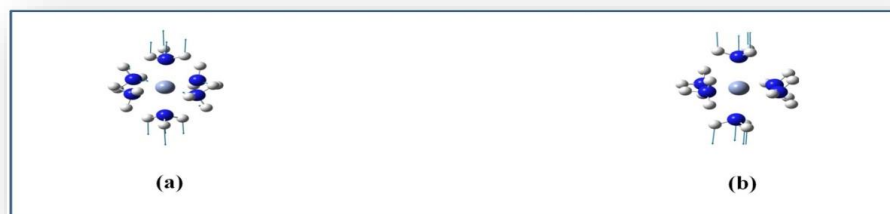
**Table 5.1.** Bond distance between Cr and axial ligand (Cr- $L_{ax}$ ), Cr and equatorial ligand (Cr- $L_{eq}$ ) and energies of the  $[\text{Cr}^{\text{III}}(\text{NH}_3)_6]^{3+}$  at quartet ground state ( $Q$ ), quartet excited state ( $Q'$ ), and doublet ground state ( $D$ ).

	States	Cr- $L_{ax}$ (Å)	Cr- $L_{eq}$ (Å)	Relative energy (Kcal/mol)
	$Q$	2.16	2.16	0
$Q'$	2.11	2.29	9.41	
$D$	2.13	2.13	28.2	

Next, to understand the mechanism of the intersystem crossing between the excited quartet ( $Q'$ ) and doublet state ( $D$ ), the vibrational modes in both the states are closely observed. After a thorough analysis of the vibrational modes, the 20<sup>th</sup> mode of  $Q'$  (vibrational energy = 379  $\text{cm}^{-1}$ ) and 16<sup>th</sup> mode of the  $D$  state (vibrational energy = 318  $\text{cm}^{-1}$ ), are found to have oscillation vectors in the same direction (Figure 5.2). The proximity in the energy and the oscillation pattern in these two vibrational modes suggest that the doublet and the excited quartet states may switch into one another through the vibration as shown in Figure 5.2. From the TDDFT computation on the lowest energy doublet state, the emission wavelength for the  $D \rightarrow Q$  transition is obtained as 877 nm, comparable to the experimental value of phosphorescence (Table 5.2).<sup>262</sup> After standardizing the computational framework for the estimation of absorption and emission wavelength, we move to the next part of this work which is carried out in the same computational methodology.

**Table 5.2.** Comparison of absorption and emission wavelengths in nm (energies in  $\text{cm}^{-1}$ ) with experimental value in  $[\text{Cr}^{\text{III}}(\text{NH}_3)_6]^{3+}$ .

	Computational value	Experimental Value <sup>262</sup>
Absorption( $Q \rightarrow Q'$ )	420 nm (23804 $\text{cm}^{-1}$ )	21550 $\text{cm}^{-1}$
Emission ( $D \rightarrow Q$ )	877 nm (11403 $\text{cm}^{-1}$ )	15120 $\text{cm}^{-1}$

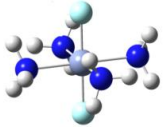


**Figure 5.2.** Oscillation vectors in the (a) 16<sup>th</sup> vibrational modes in the  $D$  state and (b) the 20<sup>th</sup> vibrational mode in the  $Q'$  state of  $[\text{Cr}^{\text{III}}(\text{NH}_3)_6]^{3+}$ .

According to the plan discussed in the introduction, the axial ligands in the  $[\text{Cr}^{\text{III}}(\text{NH}_3)_6]^{3+}$  are substituted by the weaker halogens to destroy the  $O_h$  symmetry of the complex. This is expected to lift the degeneracy of singly occupied  $t_{2g}$  orbitals as shown in Figure 5.3 and induce the doublet state in case the axial and equatorial ligands differ sufficiently in strength according to their position in the spectrochemical series. Table 5.3 displays the structural

parameters of the optimized geometry, and energies of all the halogen substituted octahedral Cr (III) complexes.

**Table 5.3.** Bond distance between Cr and axial ligand (Cr-L<sub>ax</sub>), Cr and equatorial ligand (Cr-L<sub>eq</sub>) and energies of the complex [Cr<sup>III</sup>(NH<sub>3</sub>)<sub>4</sub>(X)<sub>2</sub>]<sup>+</sup> (X= I<sup>-</sup>, Br<sup>-</sup>, Cl<sup>-</sup>, and F<sup>-</sup>, represented by violet, brown, green and light blue colors respectively).

Systems	Electronic States	Cr-L <sub>ax</sub> (Å)	Cr-L <sub>eq</sub> (Å)	Relative energy (Kcal/mol)
 [Cr <sup>III</sup> (NH <sub>3</sub> ) <sub>4</sub> (I) <sub>2</sub> ] <sup>+</sup>	<i>Q</i>	2.71	2.12	0
	<i>Q'</i>	2.76	2.28	18.2
	<i>D</i>	2.69	2.11	27.6
 [Cr <sup>III</sup> (NH <sub>3</sub> ) <sub>4</sub> (Br) <sub>2</sub> ] <sup>+</sup>	<i>Q</i>	2.51	2.11	0
	<i>Q'</i>	2.56	2.32	10.04
	<i>D</i>	2.46	2.13	11.3
 [Cr <sup>III</sup> (NH <sub>3</sub> ) <sub>4</sub> (Cl) <sub>2</sub> ] <sup>+</sup>	<i>Q</i>	2.32	2.10	0
	<i>Q'</i>	2.37	2.34	11.4
	<i>D</i>	2.28	2.12	26.35
 [Cr <sup>III</sup> (NH <sub>3</sub> ) <sub>4</sub> (F) <sub>2</sub> ] <sup>+</sup>	<i>Q</i>	1.85	2.11	0
	<i>Q'</i>	1.83	2.27	10.7
	<i>D</i>	1.80	2.12	38.9

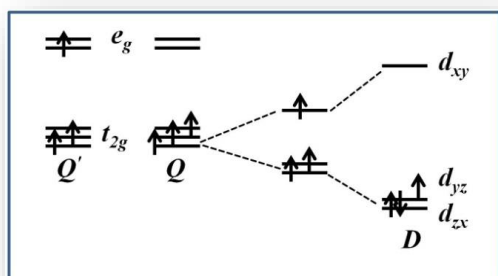


**Figure 5.3.** Orbital splitting pattern in the ground state quartet (*Q*), excited state quartet (*Q'*), and the doublet state of [Cr<sup>III</sup>(NH<sub>3</sub>)<sub>6</sub>]<sup>3+</sup>.

In the quartet ground state (*Q*), the diiodo, dibromo and dichloro substituted complexes are found to be destabilized compared to the [Cr<sup>III</sup>(NH<sub>3</sub>)<sub>6</sub>]<sup>3+</sup>, whereas the difluoro complex is relatively stabilized (Table 5.1 and Table 5. 3). The bond distance between the metal and the apical ligand (Cr-L<sub>ax</sub>) provides the explanation for such an observation. For the first three

substituted complexes, the Cr-L<sub>ax</sub> distance is larger than that in the [Cr<sup>III</sup> (NH<sub>3</sub>)<sub>6</sub>]<sup>3+</sup> whereas for the [Cr<sup>III</sup> (NH<sub>3</sub>)<sub>4</sub>F<sub>2</sub>]<sup>+</sup>, the Cr-L<sub>ax</sub> distance is much shorter than that in the [Cr<sup>III</sup> (NH<sub>3</sub>)<sub>6</sub>]<sup>3+</sup> (Table 5.1 and Table 5.3). Hence, in the present case the bonding between the Cr and axial ligands contributes significantly towards the stability of the halogen substituted complexes. In the excited quartet state (*Q'*) of all the halogen substituted complexes, the bond distances in the equatorial (*xy*) plane are found to be stretched compared to the quartet ground (*Q*) state with little variation in the Cr-L<sub>a</sub> bond distance. The bond stretching in the *xy* plane of the *Q'* state compared to the *Q* state of these new complexes is attributed to the electronic excitation in the *d*<sub>*x*<sup>2</sup>-*y*<sup>2</sup></sub> orbital similar to the case of [Cr<sup>III</sup> (NH<sub>3</sub>)<sub>6</sub>]<sup>3+</sup>. Moreover for stability issue, we calculated hardness of the ground state for all the studied complexes and results are given in tabular form.

**Table 5.4.** Calculated hardness values in eV for the studied complex (ground state quartet).

Systems	Hardness (eV)
[Cr <sup>III</sup> (NH <sub>3</sub> ) <sub>6</sub> ] <sup>3+</sup>	3.34
[Cr <sup>III</sup> (NH <sub>3</sub> ) <sub>4</sub> (F) <sub>2</sub> ] <sup>+</sup>	2.37
[Cr <sup>III</sup> (NH <sub>3</sub> ) <sub>4</sub> (Cl) <sub>2</sub> ] <sup>+</sup>	2.2
[Cr <sup>III</sup> (NH <sub>3</sub> ) <sub>4</sub> (Br) <sub>2</sub> ] <sup>+</sup>	2.18
[Cr <sup>III</sup> (NH <sub>3</sub> ) <sub>4</sub> (I) <sub>2</sub> ] <sup>+</sup>	1.15

From the Table 5.4 it can be concluded that among the halide substituted systems, [Cr<sup>III</sup> (NH<sub>3</sub>)<sub>4</sub>(F)<sub>2</sub>]<sup>+</sup> is found to be the most stable as maximum hardness means maximum stability.<sup>271</sup> From the TDDFT computation on the quartet ground states of the halogen substituted complexes, the lowest transition is found to take place from  $\alpha$ -occupied HOMO (35<sup>th</sup>  $\alpha$ -MO for diiodo, dibromo and dichloro substituted complexes and 37<sup>th</sup>  $\alpha$ -MO for the difluoro substituted complex) to the initially unoccupied LUMO (36<sup>th</sup>  $\alpha$ -MO for diiodo, dibromo and dichloro substituted complexes and 38<sup>th</sup>  $\alpha$ -MO for the difluoro substituted complex) as can be found from Table S1 and Figure S1 in supplementary data. The absorption wavelengths of all the halogen substituted complexes are given in Table 5.5. For these complexes also, the HOMO to HOMO – 2 and LUMO to LUMO + 1 belong to the *t*<sub>2g</sub> and *e*<sub>g</sub> set of orbitals as in case for [Cr<sup>III</sup> (NH<sub>3</sub>)<sub>6</sub>]<sup>3+</sup> [Figure S1 (a) – S1 (h) in the Supporting Information]. In all the halogen-substituted complexes the possibility of intersystem crossing between the excited quartet state and doublet state is verified

by the common mode of vibrations of compatible energies in both the spin states [Table S2 in the Supporting Information].

**Table 5.5.** Comparison of absorption and emission wavelengths in nm (energies in  $\text{cm}^{-1}$ ) in  $[\text{Cr}^{\text{III}}(\text{NH}_3)_4(\text{X})_2]^+$  ( $\text{X} = \text{I}^-, \text{Br}^-, \text{Cl}^-, \text{and F}^-$ ).

Complex	Absorption( $Q \rightarrow Q'$ )	Emission( $D \rightarrow Q$ )
$[\text{Cr}^{\text{III}}(\text{NH}_3)_4\text{I}_2]^+$	618.4(16171)	1280.7 (7808)
$[\text{Cr}^{\text{III}}(\text{NH}_3)_4\text{Br}_2]^+$	554.9(18021)	1416.4 (7060)
$[\text{Cr}^{\text{III}}(\text{NH}_3)_4\text{Cl}_2]^+$	502.2(19912)	968 (10331)
$[\text{Cr}^{\text{III}}(\text{NH}_3)_4\text{F}_2]^+$	555.4(18004)	453.8 (22036)

From the TDDFT computation on the doublet state, the ligands are found to regulate the emission frequency in the halogen substituted complexes. In the viewpoint of application, the most appealing fact has been the trend in the variation of emission wave length, which can be explained by the relative positions of the halogens in the spectrochemical series. The  $\text{I}^-$  and  $\text{Br}^-$  are the weak ligands and hence in stark contrast with the strong ammonia ligand. Thus placing the weak ligand along the  $z$ -axis, the  $d_{xz}$  and  $d_{yz}$  orbitals can be stabilized compared to the  $d_{xy}$  orbital and hence the threefold degeneracy of the  $t_{2g}$  level is lifted (Figure 5.3). This further splitting of the  $t_{2g}$  level stabilizes the doublet state compared to the quartet ground state resulting low energy emission as can be confirmed from Table 5.5. Hence, replacement of the axial ligands in  $[\text{Cr}^{\text{III}}(\text{NH}_3)_6]^{3+}$  with weak  $\text{I}^-$  and  $\text{Br}^-$  causes red shift in the emission wave length. This is further interesting to note that the nearly equal emission wave lengths in the diiodo and dibromo complexes correspond well with their proximate position in the spectrochemical series. Compared to these two complexes, in the difluoro compound the blue shift in the emission wave length is observed with respect to the  $O_h$   $[\text{Cr}^{\text{III}}(\text{NH}_3)_6]^{3+}$  complex. This fact can again be explained on the basis of relative strength of axial and equatorial ligands. Among the halogens, the  $\text{F}^-$  is closest to the ammonia in the spectrochemical series, for which the asymmetry in the  $t_{2g}$  is least imposed and the doublet state becomes less favored. This fact increases the energy gap between the doublet and quartet ground state and is reflected in the maximum value of the emission frequency. In alignment with this explanation, in the chloro-substituted complex, the emission wave length is in between that shown by the  $[\text{Cr}^{\text{III}}(\text{NH}_3)_4\text{F}_2]^+$  and  $[\text{Cr}^{\text{III}}(\text{NH}_3)_4\text{I}_2]^+$  or  $[\text{Cr}^{\text{III}}(\text{NH}_3)_4\text{Br}_2]^+$ . This trend again matches well with the position of chloride lying between the

$\Gamma^-$ ,  $\text{Br}^-$  and  $\text{F}^-$  in the spectrochemical series. In order to see the variation of emission wavelength by replacing ligand other than halide, we include two other ligands,  $\text{OH}^-$  and  $\text{CN}^-$ . The former is close to  $\text{F}^-$  and the later is more separated from  $\text{F}^-$  in the spectrochemical series. The complex containing stronger ligands,  $\text{CN}^-$  exhibit emission almost in the same region (676 nm) as  $[\text{Cr}^{\text{III}}(\text{NH}_3)_6]^{3+}$ , whereas the complex containing  $\text{OH}^-$  giving red shifted emission (1823 nm).

#### 5.4. Conclusion

In the present work, the photophysical property of an  $O_h$  Cr (III) complex is studied in the framework of density functional theory. Primary computational results of the absorption and emission wavelength obtained through TDDFT correspond well with the known phosphorescent behavior of the complex. In the later part, the axial ligands in the  $O_h$   $[\text{Cr}^{\text{III}}(\text{NH}_3)_6]^{3+}$  complex is replaced with comparatively weaker ligand so as to disrupt the  $O_h$  symmetry of the complex. The weaker ligand along the  $z$ -axis is expected to stabilize the  $d_{xz}$  and  $d_{yz}$  orbitals compared to the  $d_{xy}$  orbital and thus lifts the degeneracy of the erstwhile  $t_{2g}$  set of orbitals. This tetragonal distorted structure brings about electronic redistribution leading to the doublet state as illustrated in the Figure 3. Since, the difference in the strength of the axial and equatorial ligands is the key to further split the degenerate  $t_{2g}$  level, we logically replace the axial ligands of  $O_h$   $[\text{Cr}^{\text{III}}(\text{NH}_3)_6]^{3+}$  by  $\Gamma^-$ ,  $\text{Br}^-$ ,  $\text{Cl}^-$ , and  $\text{F}^-$  which are placed at different positions in the spectrochemical series with respect to  $\text{NH}_3$ . The propensity of the doublet state is high in the diiodo and dibromo complexes due to large difference in the strength of the  $\Gamma^-$  and  $\text{Br}^-$  ligands compared to  $\text{NH}_3$ . On the contrary,  $\text{F}^-$  and  $\text{NH}_3$  are close in the spectrochemical series. Hence, the doublet state cannot easily be achieved due to equivalent strength of the axial and equatorial ligands. This fact of differing tendency for doublet state due to the variant strength of axial and equatorial ligands is supported by the low energy emission in the diiodo, dibromo complexes and high energy phosphorescence in the fluoro-substituted complex. The position of  $\text{Cl}^-$  lying between  $\Gamma^-$ ,  $\text{Br}^-$  and  $\text{F}^-$  in the spectrochemical series matches well with the emission frequency of the chloro-substituted complex which is also in between the emission frequencies of iodo-, bromo-substituted complexes and fluoro-substituted complex. Thus, here we can see the relative position of the ligands in the spectrochemical series turns effective in tuning the emission frequency of phosphorescence. The most important finding of the present work is the blue-shift in the emission wave-length of  $[\text{Cr}^{\text{III}}(\text{NH}_3)_4\text{F}_2]^+$ . An emission wave length of 454 nm of this complex may offer significant insight for the rational designing of hitherto rare blue-emitting first row transition metal complexes, important for OLED applications.

## **CHAPTER 6**

### ***Photochemical study of 2-aminopyridine: A density functional investigation***

#### **Abstract**

---

The sixth chapter provides a comprehensive study of molecular mechanism of excited state relaxation induced by intermolecular hydrogen-bond formation. The absorption and fluorescence property of 2-amino pyridine (2-AP) and its dimer (2AP)<sub>2</sub> are analyzed theoretically in order to unveil the effect of intermolecular H-bonding interaction in the photochemical behavior of 2-AP. All the calculations (DFT and TDDFT) are performed using ADF suit of program with dispersion corrected methods (DFT-D). To reveal the cooperativity due to H-bonding, a decomposition analysis (EDA) in the framework of the Kohn-Sham molecular orbital (MO) model is performed. The ETS-NOCV calculations are performed for the equilibrium geometries of the ground and excited states of the dimer. The formation of H-bond has been confirmed by the calculation of synergy ( $\Delta E_{syn}$ ) from the difference of interaction energy ( $\Delta E_{int}$ ) with and without H-bond interactions. H-bond interaction stabilizes the electronic excited state of the dimer resulting red-shift in the emission spectrum.

---

The molecular mechanism of the excited state relaxation induced by intermolecular hydrogen-bond formation is of great interest because it belongs to the most fundamental processes of photochemistry. The process of fluorescence quenching, occurring as a result of intermolecular hydrogen bonding, is a well-known phenomenon.<sup>272-275</sup> Photo induced proton-coupled electron transfers, wherein the proton donor and acceptor are assembled by hydrogen bond interaction, have attracted considerable interest in recent years.<sup>276</sup> Numerous studies by Mataga and co-workers<sup>277, 278</sup> have been devoted to the case when both the proton donor and acceptor atoms belong to  $\pi$ -electronic systems. Moreover, excited state hydrogen bond interactions have also earned potential interest due to its connection with reversible or irreversible proton displacements or H-atom transfer reactions.<sup>278, 279</sup> These reactions play a vital role in a wide range of chemical and biological processes.

Pyridine and its derivatives are currently finding immense interest in the scientific community due to their wide variety of application in various fields. They find use in the chemical industry as reagent and also play a central role in the structure and properties of nucleic acid.<sup>280</sup> Some of amino pyridine derivatives show anaesthetic properties and are used as drugs for certain brain disease. 2-amino pyridine (2-AP) is used in the preparation of cytidine which is used as drug. In spite of this biomedical application, the photochemistry of this molecule has not been thoroughly investigated. In recent years *ab initio* and density functional theory (DFT) based methods have become a popular tool in the investigations of molecular structure and electronic properties. DFT offers a cost effective way for the quantum chemical investigation of the molecular properties and has been proved to be efficient in producing accurate results.<sup>281</sup>

In this study we report a systematic density functional investigation of the absorption and fluorescence property of 2-amino pyridine (2-AP) and its dimer (2-AP)<sub>2</sub>. As the dimerization of 2-AP occurs through hydrogen-bonding (H-bonding), it becomes essential to unveil the effect of intermolecular H-bonding interactions in the photochemical behaviour of 2-AP. It has been reported earlier that H-bonding plays a pivotal role in the photochemical description of a molecule. Moreover, the simple electronic structure of this compound offers simplicity and encourages studying the effect of H-bonding interaction in the photochemistry of this compound as a benchmark.

For the computation of weak interactions like H-bond, the correlated *ab initio* techniques such as second-order Møller-Plesset perturbation theory (MP2) are in wide use.<sup>282, 283</sup> Although the density functional methods, like the popular B3LYP functional, are reported to be

incompetent for the accurate description of H-bonding,<sup>283</sup> the inclusion of correction due to dispersion interactions in the scenario has been proved to be effective. In the present work, we opted for the dispersion corrected DFT (DFT-D) method for the computation of absorption and fluorescence. All the DFT and time dependent DFT (TDDFT) calculations are performed using ADF suit of program. The B3LYP functional has been used, augmented with dispersion correction developed by Grimme (B3LYP-D), along with triple- $\zeta$  TZ2P basis. The solvent effects have been estimated using the conductor-like screening model (COSMO) implemented in ADF.

Structures of the monomer and the dimer are fully optimized at the B3LYP-D/TZ2P level. The optimized ground state structures of the monomer and the dimer are represented in Figures 1 and 2. The dimer is found to prefer a non-planar geometry at ground and excited states (Figure 2).

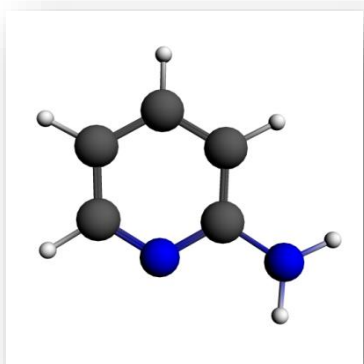


**Figure 6.1.** B3LYP-D/TZ2P optimized geometry of 2-aminopyridine at its ground state.

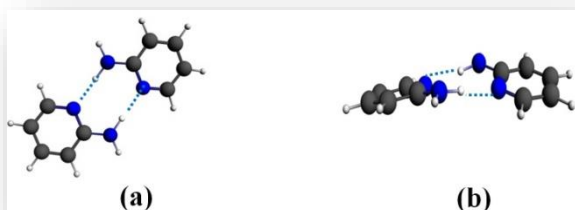


**Figure 6.2.** The H-bonded dimer (a) front view and (b) side view.

To reveal the cooperativity due to H-bonding, an energy decomposition analysis (EDA) in the framework of the Kohn-Sham molecular orbital (MO) model is performed. In this approach, the interaction energy ( $\Delta E_{int}$ ) is partitioned into electrostatic interaction ( $\Delta V_{elstat}$ ), Pauli repulsive orbital interaction ( $\Delta E_{pauli}$ ), attractive orbital interaction ( $\Delta E_{oi}$ ) and dispersion interactions ( $\Delta E_{disp}$ ) as shown in the following,

$$\Delta E_{\text{int}} = \Delta V_{\text{elstat}} + \Delta E_{\text{pauli}} + \Delta E_{\text{oi}} + \Delta E_{\text{disp}} \quad (6.1)$$

This method combines the extended transition state (ETS) energy decomposition approach<sup>284</sup> with the natural orbitals for chemical valence (NOCV) density analysis method.<sup>285</sup> The ETS-NOCV calculations are performed for the equilibrium geometries of the ground and excited states of the dimer. The formation of H-bond has been confirmed by the calculation of synergy ( $\Delta E_{\text{syn}}$ ) from the difference of interaction energy ( $\Delta E_{\text{int}}$ ) with and without H-bond interactions.

$$\Delta E_{\text{syn}} = \Delta E_{\text{int-}eq} - \Delta E_{\text{int-}noneq} \quad (6.2)$$

Here,  $\Delta E_{\text{int-}eq}$  corresponds to the interaction energy of the dimer in its equilibrium geometry. Next, the equilibrium geometry is distorted by moving the monomer units far from each other, so that no H-bond formation is possible, and the interaction energy ( $\Delta E_{\text{int-}noneq}$ ) is estimated. A negative value of synergy indicates stabilization through the formation of H-bonding.  $\Delta E_{\text{int}}$  is the energy change in systems due to formation of the association from individual units. This is interpreted as the amount of energy required to promote the separated fragments to form the dimeric structure. The synergy due to H-bonding is estimated through Equation 2 and the results are given in Table 6.1.

**Table 6.1.** Bonding energy decomposition of ground and excited states of the dimer.

Dimer	$\Delta V_{\text{elstat}}$ (kcal/mol)	$\Delta E_{\text{pauli}}$ (kcal/mol)	$\Delta E_{\text{oi}}$ (kcal/mol)	$\Delta E_{\text{disp}}$ (kcal/mol)	$\Delta E_{\text{int}}$ (kcal/mol)	$\Delta E_{\text{syn}}$ (kcal/mol)
Distorted Geometry	-0.30	-0.12	-0.03	-0.07	-0.52	--
Excited State	-25.93	29.92	-14.64	-4.30	-14.94	-14.42
Ground State	-26.24	30.31	-14.85	-4.26	-15.05	-14.53

From Table 6.1, it is clear that the hydrogen-bond formation is possible at both the ground and excited states. From the comparison of  $\Delta E_{\text{syn}}$  values in Table 6.1, one can infer a greater stabilization of the H-bonded dimer at its ground state than the corresponding excited

state. However, from the components of  $\Delta E_{int}$  it is observed that the dispersion energy change, which corresponds to the H-bonding interaction, is greater in the excited state than the ground state. Hence, it can be concluded that the H-bonding interaction is more pronounced at the excited state.

The absorption and fluorescence spectra are shown in Figures 6.3 and 6.4. It becomes prominent from the figures that there occurs a red-shift of the absorption and fluorescence peaks in the dimeric state compared to the monomer (Table 6.2). This red-shift can be attributed to the lowering in the HOMO-LUMO gap ( $\Delta E_{HL}$ ) due to H-bond formation. Table 6.3 accumulates the HOMOs and the LUMOs of the species in its different states and a lowering of the  $\Delta E_{HL}$  is clearly visible. From the previous studies on H-bonded systems it becomes evident that polarization effects promote H-bonding interaction. It has also been seen that there occurs a mixing of the empty/occupied orbital on one fragment in the presence of another fragment due to polarization effect. From the nature of the HOMO and LUMO orbitals in Table 6.3, the mixing of two fragments is critically exposed. Hence, the diminished HOMO-LUMO gap can be explained as an outcome of the H-bonding interaction.

The red-shift in the fluorescence spectra can be explained from the stabilization of the  $S_1$  electronic state of the dimer due to the formation of the H-bonding. The quenching of the energy gap for the  $S_0 \leftarrow S_1$  leads to a red shift of the fluorescence  $\lambda_{max}$  value.

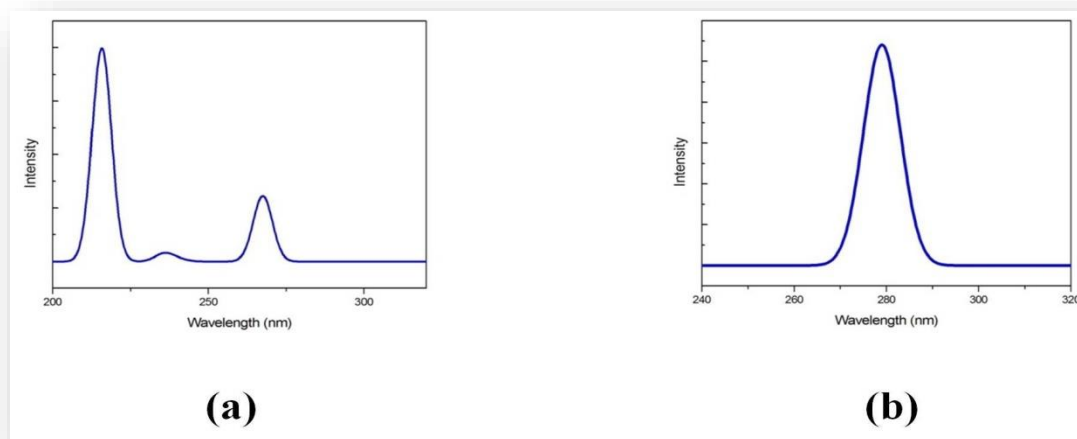


**Figure 6.3.** Absorption Spectra of (a) monomer unit and (b) hydrogen bonded dimer.

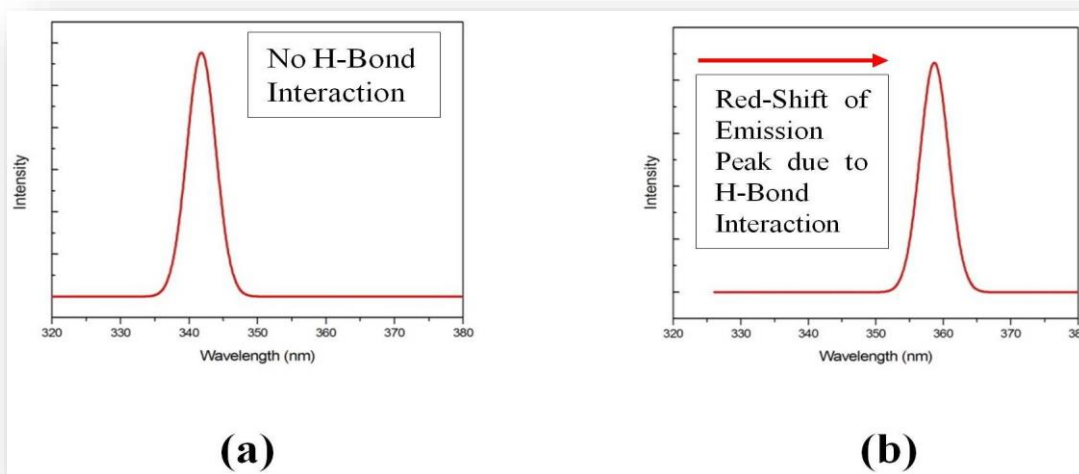


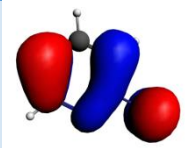
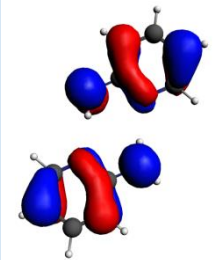
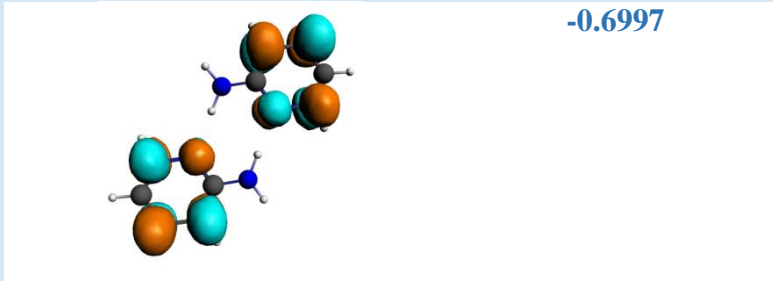
**Figure 6.4.** Fluorescence Spectra of (a) monomer unit and (b) hydrogen bonded dimer.

**Table 6.2.** Comparison of the calculated value  $\lambda_{max}$  of absorption and fluorescence with experimentally reported values.

System	$\lambda_{max}$ of absorption in nm		$\lambda_{max}$ of fluorescence in nm	
	Calculated	Experimental	Calculated	Experimental
2-AMP monomer	216	292 <sup>(a)</sup>	342	363 <sup>(a)</sup>
2-AMP Dimer	279		359	

<sup>(a)</sup> Experimentally reported  $\lambda_{max}$  of absorption and fluorescence in water medium.<sup>286</sup>

**Table 6.3.** HOMO-LUMO gap of monomer unit and hydrogen bonded dimer.

System	Orbitals	Energy in eV	$\Delta E_{HL}$ in eV
2-AMP monomer		-5.8743	6.0044
		0.1257	
2-AMP dimer		-5.6443	4.9446
		-0.6997	

The calculated values of  $\lambda_{max}$  of both the absorption and fluorescence spectra of the 2-AP monomer and dimer are given in Table 6.2. The close agreement of the calculated values with the experimental results suggests that dimers are the most preferable states of 2-AP in water solution. This can also be inferred from the Table 6.1 as the high negative synergy of the dimer in both the ground and excited states indicates the formation of H-bonding. The formation or the change in the strength, of the intermolecular hydrogen bonds following excitation may simply lead to new vibronic dissipative modes that couple excited and ground states.<sup>274, 287, 288</sup>

## **CHAPTER 7**

### ***Conclusion***

#### **Abstract**

---

This chapter presents general and comprehensive conclusions of all the chapters.

---

This chapter deals with the general concluding remarks drawn from the previous chapters. The first chapter provides a brief introduction to the origin and advancement of research in the field of nonlinear optical property, two-photon absorption property and luminescent property. Theoretical formulations have also been outlined here to understand the structure property relationship for designing efficient materials in optical uses. It can be concluded that both organic and metal based systems possessing push-pull character are of enormous importance for use in optical devices due to their large first hyperpolarizability values. From the general discussion of the characterization of the luminescent materials, one can argue that singlet emitters can also take the advantage of singlet harvesting effect by gathering both triplet and singlet excitons and might be well suited for OLED applications as already established for triplet emitter materials.

The second chapter presents a brief theoretical framework of the measurements of hyperpolarizability ( $\beta$ ) and two-photon absorption cross section ( $\sigma$ ). Some of the methods *viz.*, Sum over states (SOS), Few-states model that are utilized in this thesis to quantify optical properties are explained in details.

Chapter three presents computational study of nonlinear optical properties of two synthesized systems, phenyl expanded and thienyl expanded thiophene fused nickel dithiolenes. Both the systems possess very low value of first hyperpolarizability. We systematically modify their structures by substituting neutral and zwitterionic donor-acceptor group at the aryl (phenyl and thienyl) ring to have high NLO response. After careful inspection of the HOMO-LUMO energies of all the six systems, we noticed that neutral donor-acceptor group marginally affects the HOMO energy level, whereas the LUMO is stabilized to some extent. Hence HOMO-LUMO energy gap (HLG) decrease. However LUMO energies are found to be significantly reduced for the zwitterionic complexes resulting large decrease in the HOMO-LUMO energy gap. Hence, HLG gradually decreases from neutral to ionic substituents for both sets of the designed systems. This observation has also been supported by the excitation energy calculations with TDDFT approach. From the calculated first hyperpolarizability values, it has been noted that the zwitterionic compounds possess very large values of  $\beta$  with low HLG. We find that by substituting ionic groups at the two ends of the Ni complex, the  $\beta$  values enhanced by at least 10-15 times than that of the molecules without any such substituent. By systematic analysis, a nice correlation between  $\Delta r$  index, TDM and  $\beta$  value have been observed. We anticipated that if synthesized, these molecules may prove to be useful in optical uses.

Chapter four provides computational study where we have considered the magnetic and optical properties of a few azulene based diradical systems. We have studied six diradical systems based on nitronyl nitroxide radical moiety and azulene as coupler. The magnetic property has been assessed through the magnetic exchange coupling and magnetic anisotropy. The calculated magnetic exchange coupling parameters  $J$  depict that among the six diradicals three are ferromagnetic, and three are antiferromagnetic. The magnetic exchange coupling constants have been corroborated through spin density alternation protocol. The spin density analyses of the three ferromagnetic diradicals depict an interesting alternation behavior in the azulene coupler. The junction carbon atoms of the two rings in azulene coupler always show similar spin density despite being neighbors. This behavior is a fascinating variation of the spin density alternation rule. The ability of the ferromagnetic diradicals as photosensitizer in photodynamic therapy is evaluated through the computation of the two-photon absorption cross-section. The integrative photodynamic therapy (IPDT) of tumors relies on the combined use of different factors that enhance the usefulness of IPDT.<sup>237</sup> The observed TPA cross-section values range in the reported limit of commonly used photosensitizing agents. Another dimension of the multi-property diradical system has also been explored in this work. The magnetic anisotropy of the ferromagnetic diradicals has been estimated through the zero-field splitting parameter  $D$ . A negative ZFS parameter suggests the tendency of the spin vector to orient along a specific Cartesian direction. All the three ferromagnetic diradicals show negative  $D$  values. Radical systems with negative ZFS parameters have been proved to be usable as MRI contrast agents.<sup>188</sup> It has long been shown that the larger the ZFS magnitude  $a_2$ , larger is the spin relaxation time and the better an MRICA is.<sup>198</sup> The ZFS magnitude  $a_2$  is directly proportional to the ZFS parameter  $D$ . In the designed ferromagnetic diradicals, the ZFS parameters are found to be significantly high as for organic radical systems. The values are at least one order of magnitude higher compared to reported diradical systems usable as MRICA. Ferromagnetic systems are used as efficient probe in the magnetic hyperthermia, a popular treatment in oncology. These diradicals can also be sought for a lateral use as MRICA in magnetic resonance imaging, which is very often utilized for the detection of cancer. Treatment of interstitial tumors with PDT demands the delivery of photosensitizers to the precise location of tumor tissues for effective light irradiations. Thus a single agent that can be injected to the infected body to image tumors through MRI and simultaneously treat them by exposing to light through PDT is greatly welcomed as a proficient cancer treatment protocol. In summary we propose that if synthesized these diradical systems can promote the “see and treat” method<sup>238</sup> by proving themselves

efficient in multifarious therapeutic function such as magnetic hyperthermia, MRI contrast agents and photodynamic therapy applications.

In chapter five the photophysical property of an  $O_h$  Cr (III) complex is studied in the framework of density functional theory. Primary computational results of the absorption and emission wavelength obtained through TDDFT correspond well with the known phosphorescent behavior of the complex. In the later part, the axial ligands in the  $O_h$   $[\text{Cr}^{\text{III}}(\text{NH}_3)_6]^{3+}$  complex is replaced with comparatively weaker ligand so as to disrupt the  $O_h$  symmetry of the complex. The weaker ligand along the  $z$ -axis is expected to stabilize the  $d_{xz}$  and  $d_{yz}$  orbitals compared to the  $d_{xy}$  orbital and thus lifts the degeneracy of the erstwhile  $t_{2g}$  set of orbitals. This tetragonal distorted structure brings about electronic redistribution leading to the doublet state as illustrated in the Figure 3. Since, the difference in the strength of the axial and equatorial ligands is the key to further split the degenerate  $t_{2g}$  level, we logically replace the axial ligands of  $O_h$   $[\text{Cr}^{\text{III}}(\text{NH}_3)_6]^{3+}$  by  $\text{I}^-$ ,  $\text{Br}^-$ ,  $\text{Cl}^-$ , and  $\text{F}^-$  which are placed at different positions in the spectrochemical series with respect to  $\text{NH}_3$ . The propensity of the doublet state is high in the diiodo and dibromo complexes due to large difference in the strength of the  $\text{I}^-$  and  $\text{Br}^-$  ligands compared to  $\text{NH}_3$ . On the contrary,  $\text{F}^-$  and  $\text{NH}_3$  are close in the spectrochemical series. Hence, the doublet state cannot easily be achieved due to equivalent strength of the axial and equatorial ligands. This fact of differing tendency for doublet state due to the variant strength of axial and equatorial ligands is supported by the low energy emission in the diiodo, dibromo complexes and high energy phosphorescence in the fluoro-substituted complex. The position of  $\text{Cl}^-$  lying between  $\text{I}^-$ ,  $\text{Br}^-$  and  $\text{F}^-$  in the spectrochemical series matches well with the emission frequency of the chloro-substituted complex which is also in between the emission frequencies of iodo-, bromo-substituted complexes and fluoro-substituted complex. Thus, here we can see the relative position of the ligands in the spectrochemical series turns effective in tuning the emission frequency of phosphorescence. The most important finding of the present work is the blue-shift in the emission wave-length of  $[\text{Cr}^{\text{III}}(\text{NH}_3)_4\text{F}_2]^+$ . An emission wave length of 454 nm of this complex may offer significant insight for the rational designing of hitherto rare blue-emitting first row transition metal complexes, important for OLED applications.

Chapter six concludes with the observation that H-bond interaction stabilizes the electronic excited state in case of 2-amino pyridine resulting red-shift in the emission spectrum.

## **BIBLIOGRAPHY**

1. D. J. Williams, *Angew. Chem. Int. Ed.*, 1984, 23, 690-703.
2. D. R. Ulrich, *Mol. Cryst. Liq. Cryst.*, 1988, 160, 1-31.
3. G. R. Meredith, *J. Mater. Educ.*, 1987, 9, 719.
4. P. N. Prasad and B. A. Reinhardt, *Chem. Mater.*, 1990, 2, 660-669.
5. P. N. Butcher and D. Cotter, *The elements of nonlinear optics*, Cambridge university press, 1991.
6. P. N. Prasad and D. J. Williams, *Introduction to nonlinear optical effects in molecules and polymers*, Wiley, 1991.
7. Y.-R. Shen, *New York, Wiley-Interscience, 1984, 575 p.*, 1984.
8. E. Cariati, M. Pizzotti, D. Roberto, F. Tessore and R. Ugo, *Coord. Chem. Rev.*, 2006, 250, 1210-1233.
9. L. V. e. Tarasov, *Laser age in optics*, Mir Publishers, 1981.
10. P. Smith, *Bell. Labs. Tech. J.*, 1982, 61, 1975-1993.
11. A. Yariv, Wiley and Sons, New York, 1975.
12. D. M. Pepper, in *Laser handbook*, Elsevier, 1985, pp. 333-485.
13. S. Marder, D. Beratan and L.-T. Cheng, *Science*, 1991, 252, 103-106.
14. S. R. Marder, C. B. Gorman, B. G. Tiemann and L. T. Cheng, *J. Am. Chem. Soc.*, 1993, 115, 3006-3007.
15. C. B. Gorman and S. R. Marder, *Proceedings of the National Academy of Sciences*, 1993, 90, 11297-11301.
16. V. Rao and A. KY, *Tetrahedron Lett.*, 1993, 34, 1747.
17. A. KY, *Chem. Soc, Chem. Commun*, 1993, 90.
18. S. R. Marder, L.-T. Cheng, B. G. Tiemann, A. C. Friedli, M. Blanchard-Desce, J. W. Perry and J. Skindhøj, *Science*, 1994, 263, 511-514.
19. C. R. Moylan, R. D. Miller, R. J. Twieg, V. Y. Lee, I. H. McComb, S. P. Ermer, S. M. Lovejoy and D. S. Leung, 1995.
20. C. R. Moylan, R. J. Twieg, V. Y. Lee, S. A. Swanson, K. M. Betterton and R. D. Miller, *J. Am. Chem. Soc.*, 1993, 115, 12599-12600.
21. C. R. Moylan, R. D. Miller, R. J. Twieg, K. M. Betterton, V. Y. Lee, T. J. Matray and C. Nguyen, *Chem. Mater.*, 1993, 5, 1499-1508.

22. Y. Shi, P. M. Ranon, W. H. Steier, C. Xu, B. Wu and L. R. Dalton, *Appl. Phys. Lett.*, 1993, 63, 2168-2170.
23. G. A. Lindsay and K. D. Singer, *Polymers for second-order nonlinear optics*, ACS Publications, 1995.
24. H. S. Nalwa, T. Watanabe and S. Miyata, *Adv. Mater.*, 1995, 7, 754-758.
25. H. S. Nalwa, *Appl. Organomet. Chem.*, 1991, 5, 349-377.
26. S. Barlow and S. R. Marder, *Chem. Commun.*, 2000, 1555-1562.
27. D. R. Kanis, M. A. Ratner and T. J. Marks, *Chem. Rev.*, 1994, 94, 195-242.
28. P. G. Lacroix, *Eur. J. Inorg. Chem.*, 2001, 2001, 339-348.
29. S. Di Bella, G. Consiglio, N. Leonardi, S. Failla, P. Finocchiaro and I. Fragalà, *Eur. J. Inorg. Chem.*, 2004, 2004, 2701-2705.
30. W. Tan, W. Ji, J. Zuo, J. Bai, X. You, J. Lim, S. Yang, D. Hagan and E. Van Stryland, *Appl. Phys. B*, 2000, 70, 809-812.
31. G. Wilkinson and R. D. Gillard, *Comprehensive coordination chemistry: the synthesis, reactions, properties & applications of coordination compounds. Middle transition elements*, Pergamon, 1987.
32. S. Curreli, P. Deplano, C. Faulmann, A. Ienco, C. Mealli, M. L. Mercuri, L. Pilia, G. Pintus, A. Serpe and E. F. Trogu, *Inorg. Chem.*, 2004, 43, 5069-5079.
33. A. Vogler and H. Kunkely, *Angew. Chem. Int. Ed.*, 1982, 21, 77-77.
34. R. Kato, Y. Kashimura, H. Sawa and Y. Okano, *Chem. Lett.*, 1997, 26, 921-922.
35. S. W. McKeever, *Thermoluminescence of solids*, Cambridge University Press, 1988.
36. S. Shionoya and W. Yen, *Boca raton. pp*, 1999, 190.
37. A. H. Kitai, *Solid state luminescence: Theory, materials and devices*, Springer Science & Business Media, 2012.
38. T. Jüstel, H. Nikol and C. Ronda, *Angew. Chem. Int. Ed.*, 1998, 37, 3084-3103.
39. R. C. Evans, P. Douglas and C. J. Winscom, *Coord. Chem. Rev.*, 2006, 250, 2093-2126.
40. E. Holder, B. M. Langeveld and U. S. Schubert, *Adv. Mater.*, 2005, 17, 1109-1121.
41. J. K. Borchardt, *Materials Today*, 2004, 7, 42-46.
42. F. Li, M. Zhang, G. Cheng, J. Feng, Y. Zhao, Y. Ma, S. Liu and J. Shen, *Appl. Phys. Lett.*, 2004, 84, 148-150.
43. S. Lamansky, R. C. Kwong, M. Nugent, P. I. Djurovich and M. E. Thompson, *Organic Electronics*, 2001, 2, 53-62.

44. M. Baldo, M. Thompson and S. Forrest, *Pure Appl. Chem.*, 1999, 71, 2095-2106.
45. A. Burshtein, A. Neufeld and K. Ivanov, *J. Chem. Phys.*, 2001, 115, 10464-10471.
46. H. Yersin, in *Transition Metal and Rare Earth Compounds*, Springer, 2004, pp. 1-26.
47. H. Yersin, *Highly efficient OLEDs with phosphorescent materials*, John Wiley & Sons, 2008.
48. R. Brown, L. Singer and J. Parks, *Chem. Phys. Lett.*, 1972, 14, 193-195.
49. H. Yersin, H. Otto and G. Gliemann, *Theoretica Chimica Acta*, 1974, 33, 63-78.
50. G. A. Crosby, *Acc. Chem. Res.*, 1975, 8, 231-238.
51. X.-y. Wang, A. Del Guerso and R. H. Schmehl, *J. Photochem. Photobiol.C: Photochem. Rev.*, 2004, 5, 55-77.
52. R. M. Carlos and M. G. Neumann, *J. Photochem. Photobiol.A: Chem.*, 2000, 131, 67-73.
53. B. D. Rossenaar, E. Lindsay, D. J. Stufkens and A. Vlček Jr, *Inorg. Chem. Acta.*, 1996, 250, 5-14.
54. H. Kunkely and A. Vogler, *J. Organomet. Chem.*, 2003, 684, 113-116.
55. A. D. Kirk, *Coord. Chem. Rev.*, 1981, 39, 225-263.
56. L. S. Forster, *Chem. Rev.*, 1990, 90, 331-353.
57. A. D. Kirk, P. E. Hoggard, G. B. Porter, M. G. Rockley and M. W. Windsor, *Chem. Phys. Lett.*, 1976, 37, 199-203.
58. M. A. Jamieson, N. Serpone and M. Z. Hoffman, *Coord. Chem. Rev.*, 1981, 39, 121-179.
59. A. Kirk and G. B. Porter, *J. Phys. Chem.*, 1980, 84, 887-891.
60. G. J. Hedley, A. Ruseckas and I. D. Samuel, *J. Phys. Chem. A*, 2010, 114, 8961-8968.
61. F. De Angelis, S. Fantacci, N. Evans, C. Klein, S. M. Zakeeruddin, J.-E. Moser, K. Kalyanasundaram, H. J. Bolink, M. Grätzel and M. K. Nazeeruddin, *Inorg. Chem.*, 2007, 46, 5989-6001.
62. R. Ragni, E. A. Plummer, K. Brunner, J. W. Hofstraat, F. Babudri, G. M. Farinola, F. Naso and L. De Cola, *J. Mater. Chem.*, 2006, 16, 1161-1170.
63. Y. You and S. Y. Park, *J. Am. Chem. Soc.*, 2005, 127, 12438-12439.
64. D. K. C. Tears and D. R. McMillin, *Coord. Chem. Rev.*, 2001, 211, 195-205.
65. C.-W. Chan, L.-K. Cheng and C.-M. Che, *Coord. Chem. Rev.*, 1994, 132, 87-97.
66. M. D. Perez, P. I. Djurovich, A. Hassan, G. Y. Cheng, T. J. Stewart, K. Aznavour, R. Bau and M. E. Thompson, *Chem. Commun.*, 2009, 4215-4217.
67. J. Oudar and D. Chemla, *Opt. Commun.*, 1975, 13, 164-168.

68. D. Chemla, J. Oudar and J. Jerphagnon, *Phys. Rev. B*, 1975, 12, 4534.
69. J. Zyss, *J. Chem. Phys.*, 1979, 70, 3341-3349.
70. J. t. Oudar and H. Le Person, *Opt. Commun.*, 1975, 15, 258-262.
71. C. Miller and J. Ward, *Phys. Rev. A*, 1977, 16, 1179.
72. A. Buckingham and B. Orr, *Quarterly Reviews, Chemical Society*, 1967, 21, 195-212.
73. J. Zyss, *J. Chem. Phys.*, 1979, 71, 909-916.
74. J. d. Oudar, *J. Chem. Phys.*, 1977, 67, 446-457.
75. J.-L. Oudar and D. Chemla, *J. Chem. Phys.*, 1977, 66, 2664-2668.
76. L. T. Cheng, W. Tam, S. H. Stevenson, G. R. Meredith, G. Rikken and S. R. Marder, *J. Phys. Chem.*, 1991, 95, 10631-10643.
77. J. Armstrong, N. Bloembergen, J. Ducuing and P. Pershan, *Phys. Rev.*, 1962, 127, 1918.
78. S. Allen and J. Morely, 1987.
79. R. Feynman, *Phys. Rev.*, 1939, 56, 340.
80. R. Stanton, *J. Chem. Phys.*, 1962, 36, 1298-1300.
81. J. Pople, J. McIver Jr and N. Ostlund, *J. Chem. Phys.*, 1968, 49, 2960-2964.
82. N. Hush and M. Williams, *Chem. Phys. Lett.*, 1970, 5, 507-510.
83. J. E. Gready, G. Bacskay and N. Hush, *Chem. Phys.*, 1977, 22, 141-150.
84. P. Pulay, *Mol. Phys.*, 1969, 17, 197-204.
85. G. J. Hurst, M. Dupuis and E. Clementi, *J. Chem. Phys.*, 1988, 89, 385-395.
86. R. W. Boyd, *Nonlinear optics*, Academic press, 2003.
87. M. Albota, D. Beljonne, J.-L. Brédas, J. E. Ehrlich, J.-Y. Fu, A. A. Heikal, S. E. Hess, T. Kogej, M. D. Levin and S. R. Marder, *Science*, 1998, 281, 1653-1656.
88. Y. Luo, P. Norman, P. Macak and H. Ågren, *J. Phys. Chem. A*, 2000, 104, 4718-4722.
89. P. Monson and W. McClain, *J. Chem. Phys.*, 1970, 53, 29-37.
90. C.-K. Wang, K. Zhao, Y. Su, Y. Ren, X. Zhao and Y. Luo, *J. Chem. Phys.*, 2003, 119, 1208-1213.
91. J.-D. Guo, C.-K. Wang, Y. Luo and H. Ågren, *Phys. Chem. Chem. Phys.*, 2003, 5, 3869-3873.
92. S. Lower and M. El-Sayed, *Chem. Rev.*, 1966, 66, 199-241.
93. D. G. Fedorov, S. Koseki, M. W. Schmidt and M. S. Gordon, *Int. Rev. Phys. Chem.*, 2003, 22, 551-592.

94. B. Minaev, G. Baryshnikov and H. Ågren, *Phys. Chem. Chem. Phys.*, 2014, 16, 1719-1758.
95. B. Minaev, P. Norman, D. Jonsson and H. Ågren, *Chem. Phys.*, 1995, 190, 11-29.
96. Y. Luo, D. Jonsson, P. Norman, K. Ruud, O. Vahtras, B. Minaev, H. Ågren, A. Rizzo and K. Mikkelsen, *Int. J. Quantum Chem.*, 1998, 70, 219-239.
97. A. Messiah, (Amsterdam: North-Holland) p, 1958.
98. B. J. Coe, *Coord. Chem. Rev.*, 2013, 257, 1438-1458.
99. S. Di Bella, *Chem. Soc. Rev.*, 2001, 30, 355-366.
100. A. Coomber, D. Beljonne, R. Friend, J. Brédas, A. Charlton, N. Robertson, A. Underbill, M. Kurmoo and P. Day, *Nature*, 1996, 380, 144-146.
101. T. D. Anthopoulos, S. Setayesh, E. Smits, M. Cölle, E. Cantatore, B. de Boer, P. W. Blom and D. M. de Leeuw, *Adv. Mater.*, 2006, 18, 1900-1904.
102. B. V. U. T. Mueller-Westerhofs, in *In Comprehensive Coord. Chem.*, ed. J. A. M. R. D. Gillard, G. Wilkinson, Oxford, Pergamon, 1987, vol. 2, ch. 16.5, pp. 595-631.
103. S. Dalglish and N. Robertson, *Coord. Chem. Rev.*, 2010, 254, 1549-1558.
104. A. Zarkadoulas, E. Koutsouri and C. A. Mitsopoulou, *Coord. Chem. Rev.*, 2012, 256, 2424-2434.
105. B. Garreau-de Bonneval, K. I. M.-C. Ching, F. Alary, T.-T. Bui and L. Valade, *Coord. Chem. Rev.*, 2010, 254, 1457-1467.
106. C. L. Linfoot, P. Richardson, K. L. McCall, J. R. Durrant, A. Morandeira and N. Robertson, *Solar Energy*, 2011, 85, 1195-1203.
107. M. D. Ward and J. A. McCleverty, *J. Chem. Soc., Dalton Trans.*, 2002, 275-288.
108. G. Schrauzer and V. Mayweg, *J. Am. Chem. Soc.*, 1965, 87, 3585-3592.
109. Z. S. Herman, R. F. Kirchner, G. H. Loew, U. T. Mueller-Westerhoff, A. Nazzari and M. C. Zerner, *Inorg. Chem.*, 1982, 21, 46-56.
110. F. Bigoli, P. Cassoux, P. Deplano, M. L. Mercuri, M. A. Pellinghelli, G. Pintus, A. Serpe and E. F. Trogu, *J. Chem. Soc., Dalton Trans.*, 2000, 4639-4644.
111. F. Bigoli, C.-T. Chen, W.-C. Wu, P. Deplano, M. L. Mercuri, M. A. Pellinghelli, L. Pilia, G. Pintus, A. Serpe and E. F. Trogu, *Chem. Commun.*, 2001, 2246-2247.
112. C. Lauterbach and J. Fabian, *Eur. J. Inorg. Chem.*, 1999, 1999, 1995-2004.
113. J. E. Huyett, S. B. Choudhury, D. M. Eichhorn, P. A. Bryngelson, M. J. Maroney and B. M. Hoffman, *Inorg. Chem.*, 1998, 37, 1361-1367.

114. G. C. Papavassiliou, G. C. Anyfantis and G. A. Mousdis, *Crystals*, 2012, 2, 762-811.
115. C. M. Amb, C. L. Heth, S. J. Evenson, K. I. Pokhodnya and S. C. Rasmussen, *Inorg. Chem.*, 2016, 55, 10978-10989.
116. G.-X. Liu, Y. Liu, S. Nishihara and X.-M. Ren, *Synth. React. Inorg. M.*, 2010, 40, 416-420.
117. K. Ray, S. DeBeer George, E. I. Solomon, K. Wieghardt and F. Neese, *Chem. Eur. J.*, 2007, 13, 2783-2797.
118. F. E. Hahn, T. Eiting, W. W. Seidel and T. Pape, *Eur. J. Inorg. Chem.*, 2010, 2010, 2393-2399.
119. H. Liu, X. Li, L. Chen, X. Wang, H. Pan, X. Zhang and M. Zhao, *J. Phys. Chem. C*, 2016, 120, 3846-3852.
120. D. Belo and M. Almeida, *Coord. Chem. Rev.*, 2010, 254, 1479-1492.
121. J. Nagakubo, M. Ashizawa, T. Kawamoto, A. Tanioka and T. Mori, *Phys. Chem. Chem. Phys.*, 2011, 13, 14370-14377.
122. S. Shibahara, H. Kitagawa, Y. Ozawa, K. Toriumi, T. Kubo and K. Nakasuji, *Inorg. Chem.*, 2007, 46, 1162-1170.
123. R. Bolligarla, G. Durgaprasad and S. K. Das, *Inorg. Chem. Commun.*, 2011, 14, 809-813.
124. R. Bolligarla, S. N. Reddy, G. Durgaprasad, V. Sreenivasulu and S. K. Das, *Inorg. Chem.*, 2012, 52, 66-76.
125. M. C. Aragoni, M. Arca, T. Cassano, C. Denotti, F. A. Devillanova, R. Frau, F. Isaia, F. Lelj, V. Lippolis and L. Nitti, *Eur. J. Inorg. Chem.*, 2003, 2003, 1939-1947.
126. F. Vilela, P. J. Skabara, C. R. Mason, T. D. Westgate, A. Luquin, S. J. Coles and M. B. Hursthouse, *Beilstein J. Org. Chem.*, 2010, 6, 1002.
127. N. Robertson and L. Cronin, *Coord. Chem. Rev.*, 2002, 227, 93-127.
128. R. Kato, *Chem. Rev.*, 2004, 104, 5319-5346.
129. P. Deplano, L. Pilia, D. Espa, M. L. Mercuri and A. Serpe, *Coord. Chem. Rev.*, 2010, 254, 1434-1447.
130. J. Z. D. S. Chemla, Academic Press, New York, 1987, vol. Vol 1 and 2.
131. J. Abe and Y. Shirai, *J. Am. Chem. Soc.*, 1996, 118, 4705-4706.
132. J. Abe, Y. Shirai, N. Nemoto and Y. Nagase, *J. Phys. Chem. B*, 1997, 101, 1910-1915.
133. J. S. Miller and J. C. Calabrese, *J. Chem. Soc., Chem. Commun.*, 1988, 63-64.

134. P. López, P. Zaderenko, J. L. Balcazar, I. Fonseca, F. H. Cano and P. Ballesteros, *J. Mol.Struct.*, 1996, 377, 105-112.
135. M. Yamada and I. Honma, *Chem. Phys. Lett.*, 2005, 402, 324-328.
136. S. Yamada, M. Nakano and K. Yamaguchi, *Int. J. Quantum Chem.*, 1999, 71, 329-336.
137. M. Nakano, I. Shigemoto, S. Yamada and K. Yamaguchi, *J. Chem. Phys.*, 1995, 103, 4175-4191.
138. A. Avramopoulos, H. Reis, G. A. Mousdis and M. G. Papadopoulos, *Eur. J. Inorg. Chem.*, 2013, 2013, 4839-4850.
139. L. Pilia, M. Pizzotti, F. Tessore and N. Robertson, *Inorg. Chem.*, 2014, 53, 4517-4526.
140. P. Romaniello and F. Lelj, *J. Mol.Struct.: THEOCHEM*, 2003, 636, 23-37.
141. P. Chopra, L. Carlacci, H. F. King and P. N. Prasad, *J. Phys. Chem.*, 1989, 93, 7120-7130.
142. M. J. Frisch, G. W. Trucks, H. B. Schlegel, G. E. Scuseria, M. A. Robb, J. R. Cheeseman, G. Scalmani, V. Barone, B. Mennucci, G. A. Petersson, H. Nakatsuji, M. Caricato, X. Li, H. P. Hratchian, A. F. Izmaylov, J. Bloino, G. Zheng, J. L. Sonnenberg, M. Hada, M. Ehara, K. Toyota, R. Fukuda, J. Hasegawa, M. Ishida, T. Nakajima, Y. Honda, O. Kitao, H. Nakai, T. Vreven, J. A. Montgomery, Jr., J. E. Peralta, F. Ogliaro, M. Bearpark, J. J. Heyd, E. Brothers, K. N. Kudin, V. N. Staroverov, R. Kobayashi, J. Normand, K. Raghavachari, A. Rendell, J. C. Burant, S. S. Iyengar, J. Tomasi, M. Cossi, N. Rega, J. M. Millam, M. Klene, J. E. Knox, J. B. Cross, V. Bakken, C. Adamo, J. Jaramillo, R. Gomperts, R. E. Stratmann, O. Yazyev, A. J. Austin, R. Cammi, C. Pomelli, J. W. Ochterski, R. L. Martin, K. V. Morokuma, G. Zakrzewski, G. A. Voth, P. Salvador, J. J. Dannenberg, S. Dapprich, A. D. Daniels, O. Farkas, J. B. Foresman, J. V. Ortiz, J. Cioslowski, D. J. Fox, *Gaussian 09, Revision A.1, Gaussian, Inc., Wallingford CT, 2009*.
143. T. Lu and F. Chen, *J. Comput. Chem.*, 2012, 33, 580-592.
144. Z. S. Herman, R. F. Kirchner, G. H. Loew, U. T. Mueller-Westerhoff, A. Nazzal and M. C. Zerner, *Inorg. Chem.*, 1982, 21, 46-56.
145. M. G. Papadopoulos, J. Waite, C. S. Winter and S. N. Oliver, *Inorg. Chem.*, 1993, 32, 277-280.
146. G. N. Schrauzer and V. P. Mayweg, *J. Am. Chem. Soc.*, 1965, 87, 1483-1489.
147. D. Herebian, K. E. Wieghardt and F. Neese, *J. Am. Chem. Soc.*, 2003, 125, 10997-11005.

148. E. I. Stiefel, J. H. Waters, E. Billig and H. B. Gray, *J. Am. Chem. Soc.*, 1965, 87, 3016-3017.
149. K. Ray, T. Petrenko, K. Wiegardt and F. Neese, *Dalton Trans.*, 2007, 1552-1566.
150. D. Evans, *J. Chem. Soc. (Resumed)*, 1959, 2003-2005.
151. G. S. Girolami, T. B. Rauchfuss and R. J. Angelici, *Synthesis and technique in Inorganic Chemistry: a laboratory manual*, University Science Books, 1999.
152. M. Majumder and A. Misra, *Phys. Chem. Chem. Phys.*, 2018, 20, 19007-19016.
153. D. Avci, H. Cömert and Y. Atalay, *J. Mol. Model.*, 2008, 14, 161-169.
154. S. Paul and A. Misra, *Inorg. Chem.*, 2011, 50, 3234-3246.
155. C. A. Guido, P. Cortona, B. Mennucci and C. Adamo, *J. Chem. Theory Comput.*, 2013, 9, 3118-3126.
156. D. A. Parthenopoulos and P. M. Rentzepis, *Science*, 1989, 245, 843-845.
157. T. Zhao, X. Shen, L. Li, Z. Guan, N. Gao, P. Yuan, S. Q. Yao, Q.-H. Xu and G. Q. Xu, *Nanoscale*, 2012, 4, 7712-7719.
158. R. W. Boyle and D. Dolphin, *Photochem. photobiol.*, 1996, 64, 469-485.
159. W. M. Sharman, C. M. Allen and J. E. Van Lier, *Drug discovery today*, 1999, 4, 507-517.
160. K. Lang, J. Mosinger and D. Wagnerová, *Coord. Chem. Rev.*, 2004, 248, 321-350.
161. S. Kim, T. Y. Ohulchanskyy, H. E. Pudavar, R. K. Pandey and P. N. Prasad, *J. Am. Chem. Soc.*, 2007, 129, 2669-2675.
162. Z.-D. Qi, D.-W. Li, P. Jiang, F.-L. Jiang, Y.-S. Li, Y. Liu, W.-K. Wong and K.-W. Cheah, *J. Mater. Chem.*, 2011, 21, 2455-2458.
163. V. Goppert-Mayer, *Ann. Phys.*, 1931, 9, 273-294.
164. R. Weissleder, *Nature Biotechnol.*, 2001, 19, 316-316.
165. A. Baev, P. N. Prasad and M. Samoc, *J. Chem. Phys.*, 2005, 122, 224309.
166. A. Rajca, K. Lu, S. Rajca and C. R. Ross II, *Chem. Commun.*, 1999, 1249-1250.
167. C. Avendaño and J. Menéndez, Elsevier, Amsterdam, 2008.
168. P. Verwilt, S. Park, B. Yoon and J. S. Kim, *Chem. Soc. Rev.*, 2015, 44, 1791-1806.
169. M. Abe, *Chem. Rev.*, 2013, 113, 7011-7088.
170. J. H. Osiecki and E. F. Ullman, *J. Am. Chem. Soc.*, 1968, 90, 1078-1079.
171. E. F. Ullman, J. H. Osiecki, D. Boocock and R. Darcy, *J. Am. Chem. Soc.*, 1972, 94, 7049-7059.

172. O. Kahn, *Magnetism: a supramolecular function*, Springer Science & Business Media, 2013.
173. M. Tamura, Y. Nakazawa, D. Shiomi, K. Nozawa, Y. Hosokoshi, M. Ishikawa, M. Takahashi and M. Kinoshita, *Chem. Phys. Lett.*, 1991, 186, 401-404.
174. J. Cirujeda, E. Hernández-Gasió, C. Rovira, J.-L. Stanger, P. Turek and J. Veciana, *J. Mater. Chem.*, 1995, 5, 243-252.
175. D. A. Shultz, S. H. Bodnar, K. E. Vostrikova and J. W. Kampf, *Inorg. Chem.*, 2000, 39, 6091-6093.
176. K. Inoue and H. Iwamura, *J. Am. Chem. Soc.*, 1994, 116, 3173-3174.
177. K. Bernot, L. Bogani, A. Caneschi, D. Gatteschi and R. Sessoli, *J. Am. Chem. Soc.*, 2006, 128, 7947-7956.
178. J. Joseph, B. Kalyanaraman and J. S. Hyde, *Biochem. Biophys. Res. Commun.*, 1993, 192, 926-934.
179. T. Nagano and T. Yoshimura, *Chem. Rev.*, 2002, 102, 1235-1270.
180. P. Cabrales, A. G. Tsai and M. Intaglietta, *J Appl Physio.*, 2006, 100, 1181-1187.
181. J. Miller and M. Drillon, Wiley-VCH, Weinheim, 2003.
182. Z. Zhelev, R. Bakalova, I. Aoki, K.-i. Matsumoto, V. Gadjeva, K. Anzai and I. Kanno, *Mol. Pharm.*, 2009, 6, 504-512.
183. L. J. Berliner, H. Fujii, X. Wan and S. Lukiewicz, *Magn. Reson. Med.*, 1987, 4, 380-384.
184. C. Rajadurai, A. Ivanova, V. Enkelmann and M. Baumgarten, *J. Org. Chem.*, 2003, 68, 9907-9915.
185. C. Ling, M. Minato, P. M. Lahti and H. Van Willigen, *J. Am. Chem. Soc.*, 1992, 114, 9959-9969.
186. D. Bhattacharya, A. Panda, S. Shil, T. Goswami and A. Misra, *Phys. Chem. Chem. Phys.*, 2012, 14, 6905-6913.
187. F. Dietz and N. Tyutyulkov, *Chem. Phys.*, 2001, 264, 37-51.
188. D. Bhattacharya, S. Shil and A. Misra, *J. Photochem. Photobiol.A: Chem.*, 2011, 217, 402-410.
189. N. Tanifuji, M. Irie and K. Matsuda, *J. Am. Chem. Soc.*, 2005, 127, 13344-13353.
190. D. Bhattacharya and A. Misra, *J. Phys. Chem. A*, 2009, 113, 5470-5475.
191. D. Cho, K. C. Ko and J. Y. Lee, *J. Phys. Chem. A*, 2014, 118, 5112-5121.
192. N. J. Turro, *Modern molecular photochemistry*, University science books, 1991.

193. Y. Yamaguchi, Y. Maruya, H. Katagiri, K.-i. Nakayama and Y. Ohba, *Org. Lett.*, 2012, 14, 2316-2319.
194. E. Amir, R. J. Amir, L. M. Campos and C. J. Hawker, *J. Am. Chem. Soc.*, 2011, 133, 10046-10049.
195. M. Koch, O. Blacque and K. Venkatesan, *Org. Lett.*, 2012, 14, 1580-1583.
196. G. Spagnol, K. Shiraishi, S. Rajca and A. Rajca, *Chem. Commun.*, 2005, 5047-5049.
197. A. Olankitwanit, V. Kathirvelu, S. Rajca, G. R. Eaton, S. S. Eaton and A. Rajca, *Chem. Commun.*, 2011, 47, 6443-6445.
198. A. Rajca, K. Shiraishi and S. Rajca, *Chem. Commun.*, 2009, 4372-4374.
199. L. Noodleman, *J. Chem. Phys.*, 1981, 74, 5737-5743.
200. L. Noodleman, C. Peng, D. Case and J.-M. Mouesca, *Coord. Chem. Rev.*, 1995, 144, 199-244.
201. K. Yamaguchi, Y. Takahara, T. Fueno and K. Nasu, *Jpn. J. Appl. Phys.*, 1987, 26, L1362.
202. S. Paul and A. Misra, *J. Chem. Theory Comput.*, 2012, 8, 843-853.
203. V. Barone, A. di Matteo, F. Mele, I. de PR Moreira and F. Illas, *Chem. Phys. Lett.*, 1999, 302, 240-248.
204. F. Illas, I. de PR Moreira, J. Bofill and M. Filatov, *Phys. Rev. B*, 2004, 70, 132414.
205. K. Yamaguchi, F. Jensen, A. Dorigo and K. Houk, *Chem. Phys. Lett.*, 1988, 149, 537-542.
206. K. Yamaguchi, Y. Takahara, T. Fueno and K. Houk, *Theo. Chem. Acc.*, 1988, 73, 337-364.
207. S. Shil and A. Misra, *J. Phys. Chem. A*, 2009, 114, 2022-2027.
208. M. E. Ali and S. N. Datta, *J. Phys. Chem. A*, 2006, 110, 10525-10527.
209. B. J. Tucker, *EPR of powders, crystals, and clays of MRI contrast agents: zero field splitting and proton relaxation*, University of Illinois at Urbana-Champaign, 2010.
210. C. Duboc, D. Ganyushin, K. Sivalingam, M.-N. Collomb and F. Neese, *J. Phys. Chem. A*, 2010, 114, 10750-10758.
211. S. Zein, C. Duboc, W. Lubitz and F. Neese, *Inorg. Chem.*, 2008, 47, 134-142.
212. O. Loboda, B. Minaev, O. Vahtras, B. Schimmelpfennig, H. Ågren, K. Ruud and D. Jonsson, *Chem. Phys.*, 2003, 286, 127-137.
213. S. P. McGlynn, T. Azumi and M. Kinoshita, 1969.

214. J. E. Harriman, *Theoretical Foundations of Electron Spin Resonance: Physical Chemistry: A Series of Monographs*, Academic press, 2013.
215. R. McWeeny and Y. Mizuno, 1961.
216. R. Boča, *Theoretical foundations of molecular magnetism*, Elsevier, 1999.
217. M. Benmelouka, A. Borel, L. Moriggi, L. Helm and A. E. Merbach, *J. Phys. Chem. B*, 2007, 111, 832-840.
218. H. Mahr, H. Rabin and C. Tang, *Quantum electronics: A treatise.*, 1975, 1, 285-361.
219. M. Rumi, J. E. Ehrlich, A. A. Heikal, J. W. Perry, S. Barlow, Z. Hu, D. McCord-Maughon, T. C. Parker, H. Röckel and S. Thayumanavan, *J. Am. Chem. Soc.*, 2000, 122, 9500-9510.
220. S. J. Pond, M. Rumi, M. D. Levin, T. C. Parker, D. Beljonne, M. W. Day, J.-L. Brédas, S. R. Marder and J. W. Perry, *J. Phys. Chem. A*, 2002, 106, 11470-11480.
221. A. Garito, J. Heflin, K. Yong and O. Zamani-Khamiri, *Nonlinear Optical Properties of Organic Materials*, 1988, 971, 2-10.
222. B. Orr and J. Ward, *Mol. Phys.*, 1971, 20, 513-526.
223. T. Kogej, D. Beljonne, F. Meyers, J. Perry, S. Marder and J. Brédas, *Chem. Phys. Lett.*, 1998, 298, 1-6.
224. F. Neese, *Density Functional and Semiempirical Program Package, Version*, 2008, 2.
225. E. Y. Misochko, D. V. Korchagin, K. V. Bozhenko, S. V. Chapyshev and S. M. Aldoshin, *J. Chem. Phys.*, 2010, 133, 064101.
226. C. Angeli, K. Bak, V. Bakken, O. Christiansen, R. Cimraglia, S. Coriani, P. Dahle, E. Dalskov, T. Enevoldsen and B. Fernandez, See < <http://www.kjemi.uio.no/software/dalton/dalton.html>, 2005.
227. D. Klein, C. Nelin, S. Alexander and F. Matsen, *J. Chem. Phys.*, 1982, 77, 3101-3108.
228. C. Trindle, S. N. Datta and B. Mallik, *J. Am. Chem. Soc.*, 1997, 119, 12947-12951.
229. M. Ochsner, *J. Photochem. Photobiol.B: Biology*, 1996, 32, 3-9.
230. S. Stolik, J. Delgado, A. Perez and L. Anasagasti, *J. Photochem. Photobiol.B: Biology*, 2000, 57, 90-93.
231. J. D. Bhawalkar, G. S. He and P. N. Prasad, *Rep. Prog. Phys.*, 1996, 59, 1041.
232. W. R. Zipfel, R. M. Williams and W. W. Webb, *Nat. Biotech.*, 2003, 21, 1369-1377.
233. J. R. Starkey, A. K. Rebane, M. A. Drobizhev, F. Meng, A. Gong, A. Elliott, K. McInnerney and C. W. Spangler, *Clinic. Cancer Res.*, 2008, 14, 6564-6573.

234. P. Zhao, P. Chen, G. Tang, J. Liu, L. Lin, P. Guo, Q. Yu, J. Yao, D. Ma, G. Zhang and W. Chen, *Science in China Series B: Chemistry*, 2008, 51, 529.
235. K. Ishii, A. Takayanagi, S. Shimizu, H. Abe, K. Sogawa and N. Kobayashi, *Free Radic. Biol. Med.*, 2005, 38, 920-927.
236. X. Liang, X. Li, L. Jing, X. Yue and Z. Dai, *Biomaterials*, 2014, 35, 6379-6388.
237. H. S. Arakelyan, *OncoRev.*, 2014, 4, A171-A174.
238. G. Li, A. Slansky, M. P. Dobhal, L. N. Goswami, A. Graham, Y. Chen, P. Kanter, R. A. Alberico, J. Sperryak and J. Morgan, *Bioconjugate Chem.*, 2005, 16, 32-42.
239. S. D. Bergman, D. Gut, M. Kol, C. Sabatini, A. Barbieri and F. Barigelletti, *Inorg. Chem.*, 2005, 44, 7943-7950.
240. A. S. Ionkin, W. J. Marshall and Y. Wang, *Organometallics*, 2005, 24, 619-627.
241. M. Baldo, S. Lamansky, P. Burrows, M. Thompson and S. Forrest, *Appl. Phys. Lett.*, 1999, 75, 4-6.
242. R. C. Evans, P. Douglas and C. J. Winscom, *Coord. Chem. Rev.*, 2006, 250, 2093-2126.
243. J. G. Williams, S. Develay, D. L. Rochester and L. Murphy, *Coord. Chem. Rev.*, 2008, 252, 2596-2611.
244. H. C. Su, H. F. Chen, F. C. Fang, C. C. Liu, C. C. Wu, K. T. Wong, Y. H. Liu and S. M. Peng, *J. Am. Chem. Soc.*, 2008, 130, 3413-3419.
245. A. S. Polo, M. K. Itokazu and N. Y. M. Iha, *Coord. Chem. Rev.*, 2004, 248, 1343-1361.
246. M. Gratzel, *Inorg. Chem.*, 2005, 44, 6841-6851.
247. K. K.-W. Lo, M.-W. Louie and K. Y. Zhang, *Coord. Chem. Rev.*, 2010, 254, 2603-2622.
248. Q. Zhao, F. Li and C. Huang, *Chem. Soc. Rev.*, 2010, 39, 3007-3030.
249. S. W. Botchway, M. Charnley, J. W. Haycock, A. W. Parker, D. L. Rochester, J. A. Weinstein and J. G. Williams, *Proceedings of the National Academy of Sciences*, 2008, 105, 16071-16076.
250. M. Yu, Q. Zhao, L. Shi, F. Li, Z. Zhou, H. Yang, T. Yi and C. Huang, *Chem. Commun.*, 2008, 2115-2117.
251. K. Zeitler, *Angew. Chem. Int. Ed.*, 2009, 48, 9785-9789.
252. N. Hoffmann, *Chem. Rev.*, 2008, 108, 1052-1103.
253. T. Hofbeck and H. Yersin, *Inorg. Chem.*, 2010, 49, 9290-9299.
254. M. Baldo and S. Forrest, *Phys. Rev. B*, 2000, 62, 10958.
255. D. J. Stufkens and A. Vlček, *Coord. Chem. Rev.*, 1998, 177, 127-179.

256. T. Hofbeck and H. Yersin, *Inorg. Chem.*, 2010, 49, 9290-9299.
257. T. Sajoto, P. I. Djurovich, A. B. Tamayo, J. Oxgaard, W. A. Goddard III and M. E. Thompson, *J. Am. Chem. Soc.*, 2009, 131, 9813-9822.
258. T. J. Meyer, *Pure Appl. Chem.*, 1986, 58, 1193-1206.
259. S. Reineke, K. Walzer and K. Leo, *Phys. Rev. B*, 2007, 75, 125328.
260. R. Czerwieniec, J. Yu and H. Yersin, *Inorg. Chem.*, 2011, 50, 8293-8301.
261. Y. Hamada, T. Sano, H. Fujii, Y. Nishio, H. Takahashi and K. Shibata, *Jpn. J. Appl. Phys.*, 1996, 35, L1339.
262. H. L. Schläfer, H. Gausmann and H. Witzke, *J. Chem. Phys.*, 1967, 46, 1423-1425.
263. K. A. Barakat, T. R. Cundari and M. A. Omary, *J. Am. Chem. Soc.*, 2003, 125, 14228-14229.
264. K. Nozaki, *J. Chin. Chem. Soc.*, 2006, 53, 101-112.
265. P. J. Hay and W. R. Wadt, *J. Chem. Phys.*, 1985, 82, 270-283.
266. W. R. Wadt and P. J. Hay, *J. Chem. Phys.*, 1985, 82, 284-298.
267. M. E. Casida, C. Jamorski, K. C. Casida and D. R. Salahub, *J. Chem. Phys.*, 1998, 108, 4439-4449.
268. N. N. Matsuzawa, A. Ishitani, D. A. Dixon and T. Uda, *J. Phys. Chem. A*, 2001, 105, 4953-4962.
269. X.-N. Li, Z.-J. Wu, X.-J. Liu and H.-J. Zhang, *Synth. Met.*, 2009, 159, 1090-1098.
270. C. Adamo and V. Barone, *Theor. Chem. Acc.*, 2000, 105, 169-172.
271. D. R. Roy and P. K. Chattaraj, *J. Phys. Chem. A*, 2008, 112, 1612-1621.
272. N. Mataga, Y. Kaibe and M. Koizumi, *Nature*, 1955, 175, 731.
273. D. Rehm and A. Weller, *Isr. J. Chem.*, 1970, 8, 259-271.
274. T. Yatsushashi and H. Inoue, *J. Phys. Chem. A*, 1997, 101, 8166-8173.
275. L. Biczók and P. Valat, *Phys. Chem. Chem. Phys.*, 1999, 1, 4759-4766.
276. N. Mataga and H. Miyasaka, *Prog. React. Kinet. Mech.*, 1994, 19, 317-430.
277. N. Mataga, *Bull. Chem. Soc. Jpn.*, 1958, 31, 481-486.
278. M. M. Martin, N. Ikeda, T. Okada and N. Mataga, *J. Phys. Chem.*, 1982, 86, 4148-4156.
279. H. Miyasaka, A. Tabata, S. Ojima, N. Ikeda and N. Mataga, *J. Phys. Chem.*, 1993, 97, 8222-8228.
280. H. J. Singh and P. Srivastava, 2009.

281. S. Shil, D. Bhattacharya, S. Sarkar and A. Misra, *J. Phys. Chem. A*, 2013, 117, 4945-4955.
282. S. Suzuki, P. G. Green, R. E. Bumgarner, S. Dasgupta, W. A. Goddard and G. A. Blake, *Science*, 1992, 257, 942-945.
283. P. Tarakeshwar, S. J. Lee, J. Y. Lee and K. S. Kim, *J. Chem. Phys.*, 1998, 108, 7217-7223.
284. T. Ziegler and A. Rauk, *Inorg. Chem.*, 1979, 18, 1755-1759.
285. M. Mitoraj and A. Michalak, *J. Mol. Model.*, 2007, 13, 347-355.
286. A. Weisstuch and A. Testa, *J. Phys. Chem.*, 1968, 72, 1982-1987.
287. J. Herbich, J. Waluk, R. P. Thummel and C.-Y. Hung, *J. Photochem. Photobiol.A: Chem.*, 1994, 80, 157-160.
288. L. Biczók, T. Bérces and H. Linschitz, *J. Am. Chem. Soc.*, 1997, 119, 11071-11077.

## INDEX

<u>A</u>		Fluorescence	13
Aditivity model	25	Fourier components	5
Ancillary ligand	21	<u>G</u>	
Antiferromagnetic	55	Göppert-Mayer	31
Axial ZFS parameter	56	Gyromagnetic ratio	57
Azulene	54	<u>H</u>	
<u>B</u>		Heisenberg spin Hamiltonian	55
$\beta$ densities	50	Hyperpolarizability	6
Bioluminescence	14	<u>I</u>	
Biosensor	67	Innocent ligand	43
BLA	11	Intersystem crossing	15
Broken symmetry (BS)	55	Intraligand charge transfer	12
<u>C</u>		Isosurface	50
Cathodoluminescence	14	<u>L</u>	
Centrosymmetric	5	Larmor frequency	58
Chemiluminescence	14	LMCT	12
COSMO	78	Luminescence	12
CPHF	27	<u>M</u>	
<u>D</u>		Magnetic resonance imaging	54
Delta r-index	48	Metal-centered transition	20
Dispersion energy	80	MLCT	20
Dispersion interaction	78	MRICA	63
<u>E</u>		<u>N</u>	
Electroluminescence	14	Natural orbital for chemical valence	79
Electrostatic interaction	79	Natural transition orbitals	44
Electron-hole separation	17	Nickel dithiolenes	38,43
Energy decomposition analysis	79	Nitronyl nitroxide	53
Equivalent field model	25	Non-innocent ligand	43
Exciton	16	Nonlinear optics	3
Extended transition state	79	Nonradiative internal conversion	14
<u>F</u>			
Few-state model	31		
Ferromagnetic	55		

<b><u>Q</u></b>		<b><u>S</u></b>	
Octupolar	10	Second harmonic generation	8
OLEDs	15	Singlet harvesting	18
Optical rectification	9	Singlet oxygen	62
<b><u>P</u></b>		Sonoluminescence	14
Parametric generation	8	Static ZFS magnitude	57
Pauli repulsive orbital interaction	79	Stocks law	13
Photodynamic therapy	62	Sum over states methods	27
Photosensitizer	62	Susceptibility	4
Phosphorescence	13	Synergy	79
Pockels effect	9	<b><u>T</u></b>	
Polarizable continuum model	59	Thermoluminescence	14
Polarization effect	81	TPA cross section	30
Polarizability	4	Transition dipole moment	48
<b><u>R</u></b>		Triboluminescence	14
Radiative transition	15	Triplet harvesting	18
Relaxation rate	54, 57	Triplet-triplet annihilation	19
Rhombic ZFS parameters	56	Two-photon absorption	29
		Two-state model	26
		<b><u>Z</u></b>	
		Zero-field splitting	56
		Zwitterionic compounds	39

## REPRINTS OF PUBLISHED PAPERS IN CONNECTION TO THIS THESIS

1. Strategic Design of Thiophene-fused Nickel Dithiolene Derivatives for Efficient NLO Response, **M. Majumder** and A. Misra, *Phys. Chem. Chem. Phys.* 2018, 20, 19007-19016. (**Chapter 3**).
2. Multifunctional Magnetic Materials of Organic Origin for Biomedical Applications: A Theoretical Study, **M. Majumder**, T. Goswami and A. Misra, *ChemistrySelect*, 2018, 3, 933-939. (**Chapter 4**).
3. Ligand-Induced Symmetry Breaking and Concomitant Blue-shift in the Emission Wavelength of an Octahedral Chromium Complex, **M. Majumder**, S. Paul and A. Misra, *J. Mol. Model* (2018)24:230., <https://doi.org/10.1007/s00894-018-3768-7> (**Chapter 5**).
4. Photochemical Study of 2-Aminopyridine: A Density Functional Investigation, **M. Majumder**, T. Goswami, A. Misra, S. Bardhan and S. K. Saha, *Commun. Comput. Chem.*, 2013, 1, 225-234. (**Chapter 6**).



Cite this: *Phys. Chem. Chem. Phys.*,  
2018, 20, 19007

# Strategic design of thiophene-fused nickel dithiolene derivatives for efficient NLO response†

Manoj Majumder and Anirban Misra \*

The NLO properties of two synthesized aryl extended thiophene fused nickel dithiolenes have been studied theoretically. Based on these two systems, a systematic modification has been made by substituting neutral and zwitterionic donor–acceptor groups at the aryl (phenyl and thenyl) ring to enlarge their NLO responses. Among the four designed systems, the zwitterionic donor–acceptor group significantly reduces the HOMO–LUMO energy gap, resulting in an enormous increase in the first hyperpolarizability ( $\beta$ ) values. To judge their high NLO response, transition dipole moment (TDM) density values have been plotted and it has been found that electron dissipation occurs from one donor part to the acceptor part with a high  $\Delta r$  index value. It should be noted that the high  $\Delta r$  index values are a quantitative measurement to understand the type of transitions, and we noticed that a charge transfer transition occurs in the case of zwitterionic systems. Hence, a relationship between the first hyperpolarizability and TDM has been established. In order to highlight the NLO active segment in a molecule, a density analysis has also been done. We anticipate that as our designed systems possess high  $\beta$  values, they should have significance in optical uses.

Received 12th March 2018,  
Accepted 26th June 2018

DOI: 10.1039/c8cp01592a

rsc.li/pccp

## 1. Introduction

Molecular materials with high second order ( $\beta$ ) nonlinear optical (NLO) properties have received enormous interest from the scientific community because of their multifarious applicability in optoelectronic and photonic devices<sup>1–5</sup> for optical switching, optical communications, data storage, signal processing, optical limiting *etc.* One of the specific requirements related to the above applications is to develop molecules with a high NLO response. Metal dithiolene complexes are often ideal for the above-cited applications because of their unique optical and electrochemical properties.<sup>6,7</sup> It has been found in the literature that Ni based dithiolene complexes can be potentially used as near infrared dyes for Q-switching Nd:YAG lasers<sup>8</sup> due to their high thermal as well as photochemical stability.<sup>9</sup> Dithiolenes can also be used for energy conversion<sup>10</sup> and the development of photodetectors.<sup>11</sup> Moreover, they have very long excited-state lifetimes and tunable absorption properties, which make them useful for applications in photovoltaic devices.<sup>12</sup> Another important aspect about their structures is that they possess multiple stable redox states and a planar geometry, an

essential criterion for developing semiconductors, superconductors and molecular metals.<sup>11</sup>

Nickel dithiolenes were first synthesized in 1960.<sup>13</sup> Since then, a number of theoretical studies have been performed to understand the electronic structures and bonding schemes of these compounds. A series of interesting studies<sup>14–19</sup> revealed that these covalent complexes have a high degree of electron delocalization. In a recent work, Herman *et al.*<sup>18</sup> performed INDO (intermediate neglect of differential overlap) computations for Ni(C<sub>2</sub>S<sub>2</sub>H<sub>2</sub>)<sub>2</sub> and showed that the oxidation state of the nickel atom is +2 with a d<sup>8</sup> configuration, which is very common for this type of compounds.<sup>20–22</sup> Recent theoretical and experimental studies<sup>23–26</sup> have also confirmed the previous observation in a series of Ni complexes. A more detailed presentation of the properties and applications of dithiolene complexes can be found in several articles as well.<sup>9–11,27</sup> A common strategy is to fuse aromatic rings to the dithiolene core, in order to enhance molecular planarity and electron delocalization.<sup>28</sup> Many fused-ring dithiolene systems have been studied so far, including the fusion of benzene,<sup>29–34</sup> functionalized benzene,<sup>35–40</sup> thiophene,<sup>41–46</sup> pyridine,<sup>47</sup> quinoxaline<sup>48,49</sup> and other heterocyclic systems.<sup>50–52</sup> Among various fused-ring dithiolene systems, thiophene-fused metal dithiolenes are of particular interest owing to their stable crystal packing arrangement. Actually, their packing arrangement is determined by the total balance of many weak intermolecular forces (hydrogen bonding, van der Waals forces,  $\pi$ – $\pi$  interactions, and S–S/M–S interactions).<sup>53,54</sup> Additional thiophene content would be expected to

Department of Chemistry, University of North Bengal, Darjeeling, 734013, West Bengal, India. E-mail: anirbanmisra@yahoo.com; Tel: +91-9434228745

† Electronic supplementary information (ESI) available: The optimized coordinates of all the studied systems, the HOMO and LUMO plots and a comparison table of calculated transitions at the TDDFT level of all the systems at the B3LYP and CAM-B3LYP level of theory. See DOI: 10.1039/c8cp01592a

increase such intermolecular interactions and provide a more significant overlap of frontier orbitals, which could result in enhanced electrical conductivity and higher magnetic transition temperatures.

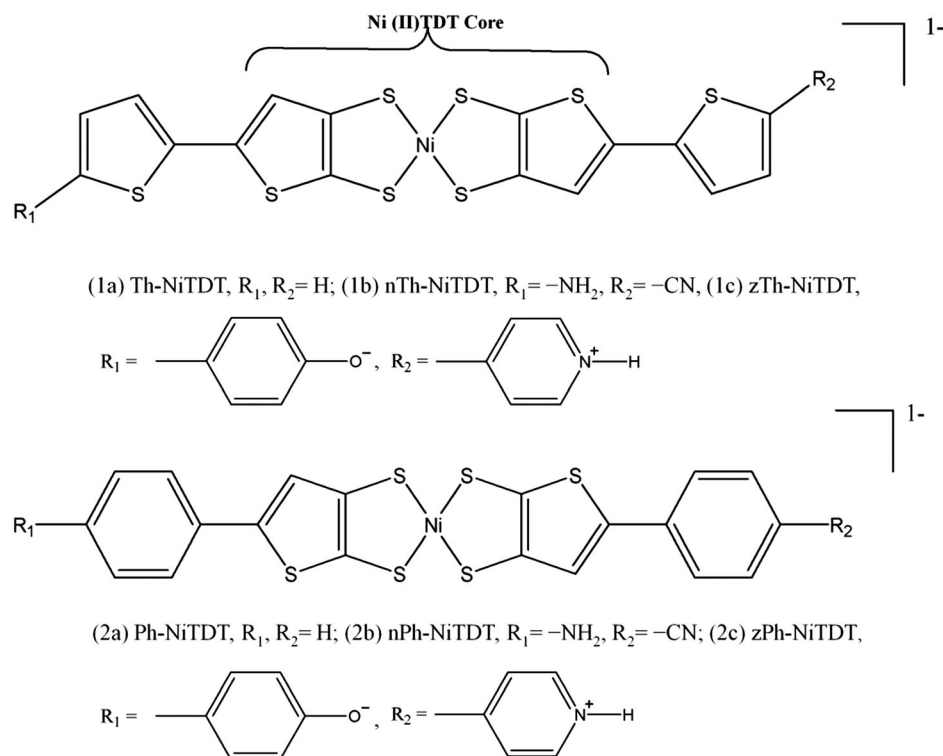
In a recent report, a new family of aryl-extended nickel thiophenedithiolene complexes was synthesized and their optical, electronic, magnetic and solid-state properties were studied as well.<sup>28</sup> It was found that aryl-extended metal 2,3-thiophenedithiolene can retain its planar structure even after the fusion of rings. As a consequence, the conjugation length is maximized along the molecular backbone.<sup>28</sup> These kinds of Ni(II) complexes are reported to have a high degree of second-order NLO response, which further increases in asymmetric compounds through a push-pull mechanism.<sup>55</sup> All these facts motivated us to design nickel dithiolene based complexes with a high NLO response. A well known mechanism to enhance the hyperpolarizability value is to add organic donor-acceptor groups to the core system.<sup>56</sup> As an example, stillbene derivatives have  $\beta$ -values of very large magnitude, which can be further enhanced by including ionic donor-acceptor functional groups.<sup>57–59</sup> Most of the studies on hyperpolarizabilities reported in the literature are on  $\pi$ -electron conjugated organic systems and there are very few reports on inorganic spacer based push-pull systems.<sup>20–22</sup> In a work by Miller *et al.*, one zwitterionic compound in which the donor (D) and acceptor (A) are linked by a sigma bond has been reported for NLO applications.<sup>60</sup> There are a number of reports in the literature<sup>61,62</sup> describing the existence of crystal zwitterion structures of imidazole-1-ylacetic acid, 3-ethoxycarbonyl-2-imidazole-1-ylpropionic acid, and 3-pyridinesulphonic acid that have motivated us to choose zwitterion based substituents.

In this work, we calculate the NLO properties of thiophene expanded nickel thiophenedithiolene, Th-NiTDT (**1a**), and phenyl expanded nickel thiophenedithiolene, Ph-NiTDT (**2a**), synthesized by Amb *et al.*,<sup>28</sup> and based on the structures (**1a** and **2a**), a strategic design has been undertaken (two sets) by replacing the neutral and ionic donor-acceptor groups, as represented in Scheme 1. From the calculations, it has been found that the synthesized systems (**1a** and **2a**) have very low values of  $\beta$  as the molecules are centrosymmetric. Keeping in mind their multifarious applicability and exceptional stability, our strategy is to modify the structure in such a manner so as to gain a high NLO response. We showed that by replacing the ionic donor-acceptor group at the two ends of the inorganic moiety, the  $\beta$ -values were enhanced by at least 10–15 times compared to that of the molecule without the ionic substituent. In our study, the core parts of the synthesized systems are kept intact; rather, the structures are systematically modified by introducing different functional groups to peripheral rings (Scheme 1).

## 2. Theoretical background

The NLO properties may be defined in terms of a power series of the molecular dipole moment in the presence of an oscillating electric field according to eqn (1).<sup>63–65</sup>

$$E = E^0 - \sum_i \mu_i F_i - \frac{1}{2} \sum_{ij} \alpha_{ij} F_i F_j - \frac{1}{3} \sum_{ijk} \beta_{ijk} F_i F_j F_k - \frac{1}{4} \sum_{ijkl} \gamma_{ijkl} F_i F_j F_k F_l - \dots \quad (1)$$



Scheme 1 Schematic representation of the studied and designed systems.

Here,  $E$  and  $E^0$  refer to the energies of the perturbed and zero-field unperturbed states, the  $F_x$  are the field strengths along a particular direction, and the tensors  $\mu_{ij}$ ,  $\alpha_{ij}$ ,  $\beta_{ijk}$  and  $\gamma_{ijkl}$  stand for the dipole moment, linear polarizability, the first or static hyperpolarizability and the second or cubic hyperpolarizability terms, respectively.<sup>63–65</sup> In general, the field as well as polarizability and hyperpolarizability terms of the above equation are frequency dependent. The first static hyperpolarizability ( $\beta_{\text{TOTAL}}$ ) can be expressed by using  $x$ ,  $y$  and  $z$  components as follows,

$$\beta_{\text{tot}} = (\beta_x^2 + \beta_y^2 + \beta_z^2)^{1/2} \quad (2)$$

and

$$\beta_x = \beta_{xxx} + \beta_{xyy} + \beta_{xzz},$$

$$\beta_y = \beta_{yyy} + \beta_{xxy} + \beta_{yzz},$$

$$\beta_z = \beta_{zzz} + \beta_{xxz} + \beta_{yyz}.$$

The charge density function  $\rho(r, F)$  can be explained by the powers of the field  $F$  in the same way as the expansions of the energy and dipole moment.<sup>66</sup> The charge density function  $\rho(r, F)$  can be expressed as

$$\begin{aligned} \rho(r, F) = & \rho^{(0)}(r) + \sum_j \rho^{(1)}(r) F^j + \frac{1}{2!} \sum_{jk} \rho^{(2)}(r) F^j F^k \\ & + \frac{1}{3!} \sum_{jkl} \rho^{(3)}(r) F^j F^k F^l + \dots \end{aligned} \quad (3)$$

The dipole moment expansion can be represented as

$$\begin{aligned} \mu^i(F) = & - \int r^i \rho(r, F) dr^3 \\ = & \mu_0^i + \sum_j \alpha_{ij} F^j + \sum_{jk} \beta_{ijk} F^j F^k + \sum_{jkl} \gamma_{ijkl} F^j F^k F^l + \dots \\ = & - \int r^i \rho^{(0)}(r) dr^3 - \sum_j \int r^i \rho^{(1)}(r) dr^3 F^j \\ & - \frac{1}{2!} \sum_{jk} \int r^i \rho^{(2)}(r) dr^3 F^j F^k - \frac{1}{3!} \sum_{jkl} \int r^i \rho^{(3)}(r) dr^3 F^j F^k F^l - \dots \end{aligned} \quad (4)$$

Here,  $r^i$  is the  $i$  component of the electron coordinate. From eqn (3) and (4), the first-hyperpolarizability can be expressed by

$$\beta_{ijk} = - \frac{1}{2!} \int r^i \rho^{(2)}(r) dr^3.$$

Here,

$$\rho^{(2)}(r) = \frac{\partial^2 \rho}{\partial F^j \partial F^k} \quad (5)$$

And these derivatives of electron densities with respect to external electric fields are referred to as  $\beta$  densities.<sup>66</sup> In this study, we confine our attention to the  $\beta$ -densities, which are

calculated by using the following 2nd order numerical differentiation formula,

$$\rho_{zz}^{(2)}(r) = \frac{\rho(r, F_z) + \rho(r, -F_z) - 2\rho(r, 0)}{F^2} \quad (6)$$

where  $\rho(r, F_z)$  represents the charge density at a special point in the presence of the field  $F$ . The charge densities over a three-dimensional grid of points were evaluated by the density matrix obtained by the Gaussian 09 program package. The study of  $\beta$  densities is important as it straightforwardly highlights the NLO-active segments in a molecule.

### 3. Computational details

The structures of thiophene expanded nickel dithiophene-dithiolene, Th-NiTDT (**1a**), and phenyl expanded nickel thio-phenedithiolene, Ph-NiTDT (**2a**), complexes are taken from the crystallographic file format (CIF),<sup>28</sup> and the positions of the hydrogen atoms in the synthesized systems were partially optimized using a density functional theory (DFT) based methodology with the B3LYP functional<sup>67–69</sup> in conjugation with the 6-311++g(d,p) basis set. It has been reported<sup>28</sup> that the two synthesized systems have one unpaired electron; all the calculations have been done with an unrestricted DFT formalism along with the geometry optimization for the designed systems (**1b**, **1c**, **2b** and **2c**) with the B3LYP functional and the 6-311++g(d,p) basis set.

For calculating the  $\lambda_{\text{max}}$  (nm) values of the synthesized systems, we have employed the CAM-B3LYP/6-311g(d,p) methodology in the solution phase using the dielectric constant of the experimental solvent (acetonitrile) within the polarizable continuum model (PCM) and compared our computed data with the experimentally reported excitation energy values.<sup>28</sup> Thus, we have optimized the computational methodology with the help of experimental data provided for the two synthesized systems (**1a** and **2a**) and we have used the same methodology for calculating excitation energies for our designed systems (**1b**, **1c**, **2b** and **2c**).

In order to highlight the NLO-active segments in a molecule, a contribution analysis<sup>66,70</sup> has been carried out to analyze the results of the TD-DFT calculations. The NLO behavior and the first hyperpolarizability ( $\beta$ ) have been quantitatively evaluated for all the studied species by using the UB3LYP/6-311++g(d,p) methodology in the Gaussian 09 software.<sup>71</sup> Benchmarking of the computational model has been done with a very common push-pull system, 4-amino 4-nitro stilbene,<sup>72</sup> whose experimental first hyperpolarizability ( $\beta$ ) has been measured to be  $(260 \pm 35) \times 10^{-30}$  esu (in methanol). We can reproduce the  $\beta$  value of this system ( $184 \times 10^{-30}$  esu in the gas phase) to a reasonable extent with the same functional and with the 6-311++g(d,p) basis set in the Gaussian 09 suit of program. When we performed the calculation in the solvent phase (methanol), the hyperpolarizability values are found to be high ( $905 \times 10^{-30}$  esu). Actually, polar solvents decrease the HOMO–LUMO gap, thereby increasing the hyperpolarizability values. Here, our intention is to see the effect of the ionic donor–acceptor group on the

hyperpolarizability values, so we keep other tuning parameters constant. Moreover, the error due to not considering the solvent effect is around 45–50%, which is within the range of the experimental margin of error.<sup>73</sup> Hence, we rely on the gas phase values to explain the changes in the NLO response with structural modifications. The correlation of our gas phase computed results with the experimentally reported data provoked us to choose this basis set and functional combination for the estimation of  $\beta$  values of our designed systems. The transition dipole moment (TDM) has been calculated based on the dipole moment integral between the occupied and virtual MOs. The contribution from each MO pair to the transition dipole moment can be straightforwardly evaluated and visualized using a Multiwfn wave function analyzer.<sup>74</sup>  $\Delta r$  index, which is proposed to measure the charge transfer length during electron excitation, has also been calculated in Multiwfn.

## 4. Results and discussion

### 4.1. The electronic structure of nickel dithiolene (NiDT)

Bisdithioglyoxalnickel,  $\text{Ni}(\text{S}_2\text{C}_2\text{H}_2)_2$ , or simply nickel dithiolene (NiDT), is a characteristic example of the square planar derivative involving “non-innocent” conjugated sulfur-based ligands. Several bonding structures describing 8, 10 or 12 $\pi$ -electron systems have been proposed for NiDT,<sup>75,76</sup> where the formal oxidation states of Ni are 0, +2 and +4, respectively. For Ni(0) systems, the dithiolene ligand coordinates to the metal atom as a neutral dithioketone (Fig. 1), though we hardly found any concrete evidence for such a complex.<sup>77</sup> The ligands are assumed to be dithiolatodianions,  $^-\text{S}-\text{CH}=\text{CH}-\text{S}^-$ , in Ni(IV), which usually occurs in d<sup>8</sup> neutral NiDT.<sup>77</sup> NiDT is one of the first examples of a complex of this family for which an assignment of the nickel oxidation state proved to be problematic, as summarized in Fig. 1.

A series of interesting studies regarding the electronic structure of such complexes revealed that these complexes are in fact Ni(II) complexes with each ligand bearing a radical.<sup>78,79</sup> Calculations also showed that the frontier orbitals of such complexes are ligand-based rather than metal-based.<sup>80</sup> Because of this peculiarity, a change in the oxidation state in such complexes occurs at the ligand center rather than at the metal centre. This property is illustrated by the fact that nickel dithiolene complexes undergo facile single-electron reductions, leading to the formation of a paramagnetic radical anion when singly reduced and a diamagnetic nickelate(II) when doubly reduced (Fig. 2).

Two different situations may occur upon the addition of an electron to the NiDT species (*i.e.* formation of  $[\text{NiDT}]^-$ ). In the first case, the electron occupies a metal d-orbital of the  $\text{M}^{\text{II}}$  ion, which is therefore reduced to  $\text{M}^{\text{I}}$  (the case of an “innocent” ligand). The multiplicity of the  $[\text{NiDT}]^{-1}$  anion containing  $\text{Ni}^{\text{I}}$  is 2. In the 2nd case, the electron fully or partially occupies an antibonding orbital of the  $\text{L}^{-1}$  ligand (in the case of a non-innocent ligand). In this case, two values of different spin states can exist: a quartet and an open-shell doublet. In a recent report, the magnetic susceptibilities of some synthesized systems based on the NiDT core, *i.e.*, tetrabutylammonium bis(5-(2-thienyl)-2,3-thiophenedithiolato)-nickelate(II),  $[\text{Bu}_4\text{N}]\text{NiDT}$  and various salts of NiDT, were measured by NMR in solution using the Evans method<sup>81,82</sup> and also in the solid state using vibrating-sample magnetometry, and the obtained susceptibility values were found to be greater than 1.73  $\mu_{\text{B}}$ , indicating  $S = 1/2$ . Hence, all the subsequent computations for the studied complexes were performed assuming the doublet state as the ground state.

### 4.2. HOMO–LUMO gap, excitation energies and NTO analysis

The set of compounds that we have studied can be categorized into two subsets: (a) thiophene expanded NiDT and its derivatives (**1a**, **1b**, **1c**; Scheme 1) and (b) phenyl expanded NiDT and its derivatives (**2a**, **2b** and **2c**; Scheme 1). In order to gain a perceptible idea of which orbitals are responsible for transitions, we have analyzed the natural transition orbitals (NTOs). As can be seen in Fig. 3, the HOTO (highest occupied transition orbital) of the entire studied complex (**1a**, **1b** and **1c** and **2a**, **2b** and **2c**) is found to have a comparable contribution from the metal and the ligand. In contrast, the LUTO (lowest unoccupied transition orbital) is primarily composed of ligand-based orbitals. For complexes **1a** and **1b** and **2a** and **2b**, the HOTO is more or less localized at the central metal dithiolene core, with some electron density dissipation onto the pendent thiophene; whereas for complexes **1c** and **2c**, the HOTOs are mainly constituted from the ionic donor part and the LUTOs arise from the ionic acceptor part, clearly indicating electron delocalization at the ionic terminals. Hence, we find the highest populated origin and the highest populated destination NTOs (Fig. 3), associated with a specific transition (Table 4), and we noticed that the charge transfer takes place from one terminal to the other for the zwitterionic complexes (**1c** and **2c**).

From the comparison of the HOMO and LUMO energies in these systems (Table 1), it can be concluded that attachment of the electron donor–acceptor group ( $-\text{NH}_2$  and  $-\text{CN}$ ) in compounds **1b**

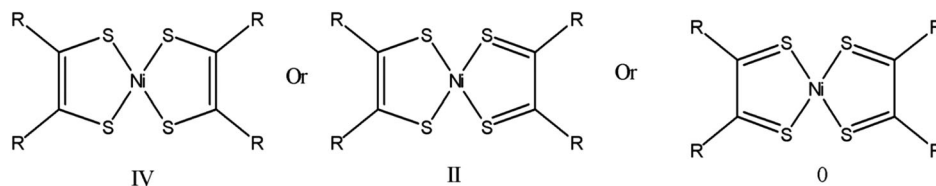


Fig. 1 Schematic representation of different oxidation states of the NiDT complex.

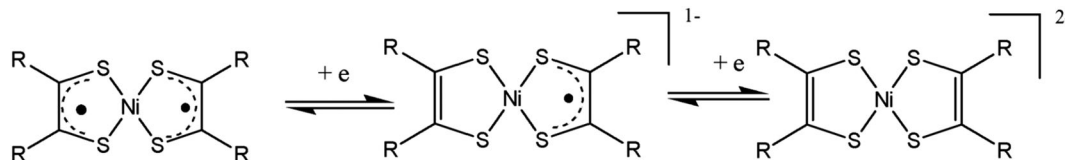


Fig. 2 Redox activity of the Ni dithiolenyl complex.

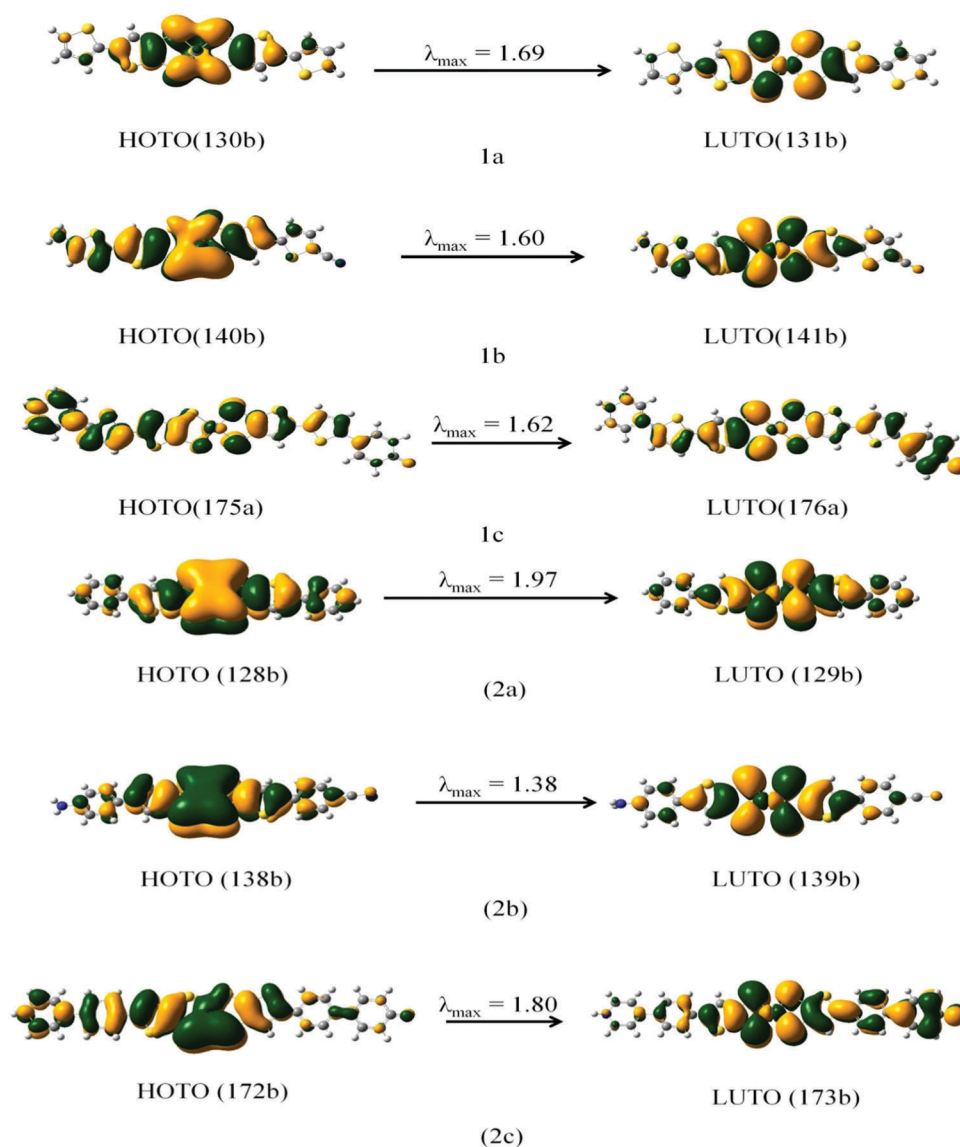


Fig. 3 The dominant natural transition orbital (NTO) pairs for the systems under study. The “hole” (highest occupied transition orbital; HOTO) is on the left, and the “particle” (lowest unoccupied transition orbital; LUTO) is on the right. The associated eigenvalue,  $\lambda_{\max}$ , is given over the arrow.

and **2b** marginally affects the HOMO energy level, though the LUMO is stabilized to some extent. However, the LUMO energies are found to be significantly reduced in zwitterionic complexes **1c** and **2c**, resulting in a decrease in the HOMO–LUMO energy gap (HLG) (Table 1). Hence, compared to the two synthesized systems (**1a** and **2a**), all our designed systems possess a lower value of HLG. Another important point to note is that both the HOMO and LUMO are oriented in a mutually perpendicular fashion in **1b**, whereas

both the orbitals lie in the plane of the ring in **2b** (Fig. S7 in ESI†). This difference in the orientation of MOs can be correlated with their first hyperpolarizability value (Table 1), which is higher in **2b** than in **1b**.

In order to explain the variation of the optical properties in the NiTDT series, the electronic excitation energies of the monoanions (**1a** and **2a**) were calculated using the TDDFT approach and compared with the experimental data. The  $\lambda_{\max}$

**Table 1** HOMO/LUMO energies and  $\beta_{\text{tot}}$  values of NiTDT and its derivatives computed in the gas-phase at the UB3LYP/6-311++g(d,p) level of theory

Molecule	Energies in gas-phase (eV)			$\beta \times 10^{-30}$ esu
	HOMO <sup>a</sup>	LUMO <sup>b</sup>	$\Delta E_{\text{H-L}}$ <sup>c</sup>	
Th-NiTDT	-1.838	0.724	2.562	4.02
nTh-NiTDT	-2.002	0.056	2.058	455.92
zTh-NiTDT	-2.1284	-1.7566	0.3714	5890.9
Ph-NiTDT	-1.805	0.830	2.635	22.67
nPh-NiTDT	-1.962	0.155	2.117	643.08
zPh-NiTDT	-2.34	-1.6587	0.6813	18553.6

<sup>a</sup> HOMO stands for highest occupied molecular orbital. <sup>b</sup> LUMO stands for lowest unoccupied molecular orbital. <sup>c</sup>  $\Delta E_{\text{H-L}}$  represents the HOMO-LUMO energy gap.

values of **1a** and **2a** have been calculated to be 1438 nm and 1281 nm, which are in a similar range to the experimentally measured values (1108 and 1076 nm).<sup>28</sup> However, the absorption wavelengths (1173 and 1103 nm), when calculated in the gas phase, are a much closer result compared to those obtained in the solution phase. Thus, for the designed systems, only gas phase calculations were performed to get the absorption wavelength. For subsets **1a**, **1b** and **1c** and **2a**, **2b** and **2c**, the excitation energy and HLG follow the same trend (Table 2) as explained earlier that the donor-acceptor group decreases the HLG and consequently increases the absorption wavelength. There is only one exception, the excitation energy of **2b**, which is more than that of **2a**. The excitation of the Ni derivatives is an intramolecular charge transfer ( $\pi$ - $\pi^*$ ) over the  $\pi$ -type orbitals of the ligand.

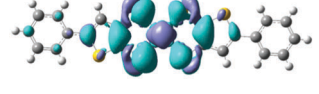
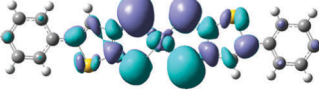
### 4.3. NLO properties

From the reported values in Table 1, complexes **1c** and **2c** with the lowest HLG are found to have the highest values of  $\beta_{\text{TOTAL}}$  among the members of the NiTDT series, which suggests an inversely proportional relation between the HLG and intrinsic first hyperpolarizability.<sup>83,84</sup> To explain the origin and variation of the NLO responses in the NiTDT series, the  $\beta$  densities and transition dipole moments (TDMs) were also calculated for these systems under investigation. Table 3 shows three strong absorption peaks with their oscillator strength ( $f$ ) and the pictorial presentation of the transition dipole moments (TDMs) for the corresponding transition for system **2a**. These data are also in agreement with the fact that the oscillator strength ( $f$ ) is directly related to the square of the TDM (in atomic units),

**Table 2** TDDFT calculated transitions for the thienyl (**1a**) and phenyl (**2a**) expanded analogues of the NiTDT core and its derivatives (**1b** and **1c** and **2b** and **2c**) at the CAM-B3LYP/6-311g(d,p) level of theory

Compound	$\lambda_{\text{max}}^{\text{cal}}$ (nm)	$f$	Primary description
<b>1a</b>	1173	0.2274	130B to 131B
<b>1b</b>	1229	0.1749	140B to 141B
<b>1c</b>	1371	0.6975	175A to 176A
<b>2a</b>	1103	0.2589	128B to 129B
<b>2b</b>	1057	0.2089	138B to 139B
<b>2c</b>	1414	0.3635	172B to 173B

**Table 3** Transition energy (eV, nm), its oscillator strength ( $f$ ) and transition dipole moment density for the three strong transitions of Ph-NiTDT. The purple color implies charge increase upon excitation and the turquoise color implies charge depletion. The isovalue is  $4 \times 10^{-4}$  in a.u.

Energy state	eV	nm	$f$	Transition dipole moment density
S <sub>5</sub>	1.1238	1103.25	0.2589	
S <sub>7</sub>	1.6836	736.44	0.0138	
S <sub>9</sub>	1.9185	646.25	0.02	

$f = \frac{2}{3} \Delta E \times (D_x^2 + D_y^2 + D_z^2)$ , where  $\Delta E$  denotes the transition energy between the two states. From the reported TDM plot in Table 3, we can also observe that for the energy state (S<sub>5</sub>) with the highest oscillator strength, the electron from one terminal is transferred to the other terminal. For the same system (**2a**), when we consider the energy states with lower oscillator strength ( $f$ ) values (e.g. states S<sub>7</sub> and S<sub>9</sub> in Table 3), the transitions are referred to as local excitations, indicating that the electron oscillation of state S<sub>5</sub> is the strongest. Keeping the previous observations in mind, the transitions with the highest oscillator strength for each of the remaining systems have been considered. The results are reported in Table 4 along with a pictorial presentation of the transition dipole moment in Fig. 4. For the subset of **1a**, **1b** and **1c**, the highest value of TDM has been found for **1c**, which is evident from its highest  $\Delta r$  index value.<sup>85</sup> This index was introduced with the aim of exploring the metric of excited electronic states in the framework of the time-dependent density functional theory. It is based on the charge centroids of the orbitals involved in the excitations and can be interpreted in terms of the hole-electron distance. It has been reported in the literature that the type of excitation can be judged with the help of this index.  $\Delta r \leq 1.5$  Å indicates local excitations, whereas  $\Delta r \geq 2.0$  Å indicates long-range excitations.<sup>85</sup>

Theoretical predictions can also be outlined here. The hole-particle pair interactions could be related to the distance

**Table 4** Major transition energy (eV, nm), its oscillator strength ( $f$ ),  $\Delta r$  index and eigenvalues for the three strong transitions for the two sets of complexes (**1a**, **1b** and **1c** and **2a**, **2b** and **2c**) calculated at the CAM-B3LYP/6-311g(d,p) level of theory

Complex	State	nm	$f$	$\Delta r$ (Å)	Primary description, eigenvalues ( $\lambda_{\text{max}}$ )
<b>1a</b>	S <sub>4</sub>	1103	0.2589	0.36	128b-129b, 1.97
<b>1b</b>	S <sub>5</sub>	1057	0.2089	1.40	138b-139b, 1.38
<b>1c</b>	S <sub>1</sub>	<b>1414</b>	<b>0.3635</b>	<b>8.60</b>	<b>172b-173b, 1.80</b>
<b>2a</b>	S <sub>5</sub>	1173	0.2274	0.33	130b-131b, 1.69
<b>2b</b>	S <sub>4</sub>	1229	0.1749	0.87	140b-141b, 1.60
<b>2c</b>	S <sub>5</sub>	1371	<b>0.6975</b>	<b>6.51</b>	<b>175a-176a, 1.62</b>

## Transition Dipole Moment Density

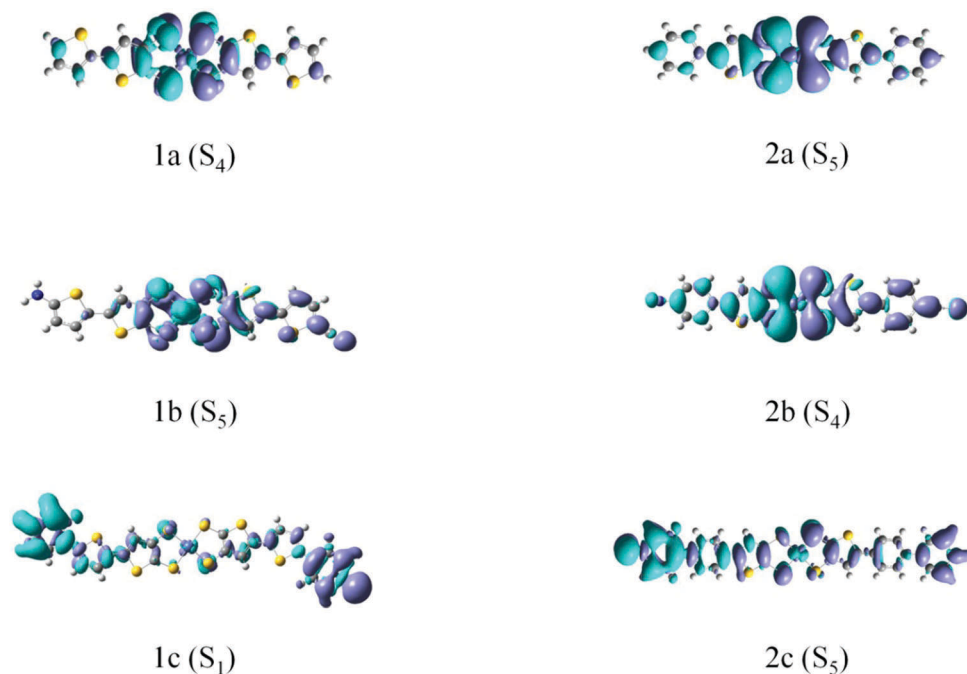


Fig. 4 The transition dipole moment density of the electronic state transition from the ground state for the studied complexes. The purple color implies charge increase upon excitation and the turquoise color implies charge depletion. The isovalue is  $4 \times 10^{-4}$  in a.u.

covered during the excitations, so one possible descriptor could be their average distance, weighted in function of the excitation coefficients. The following definition will be then introduced:

$$\Delta r = \frac{\sum_{i,l} (K_i')^2 |\langle \varphi_l | r | \varphi_i \rangle - \langle \varphi_i | r | \varphi_l \rangle|}{\sum_{i,l} (K_i')^2} \quad (7)$$

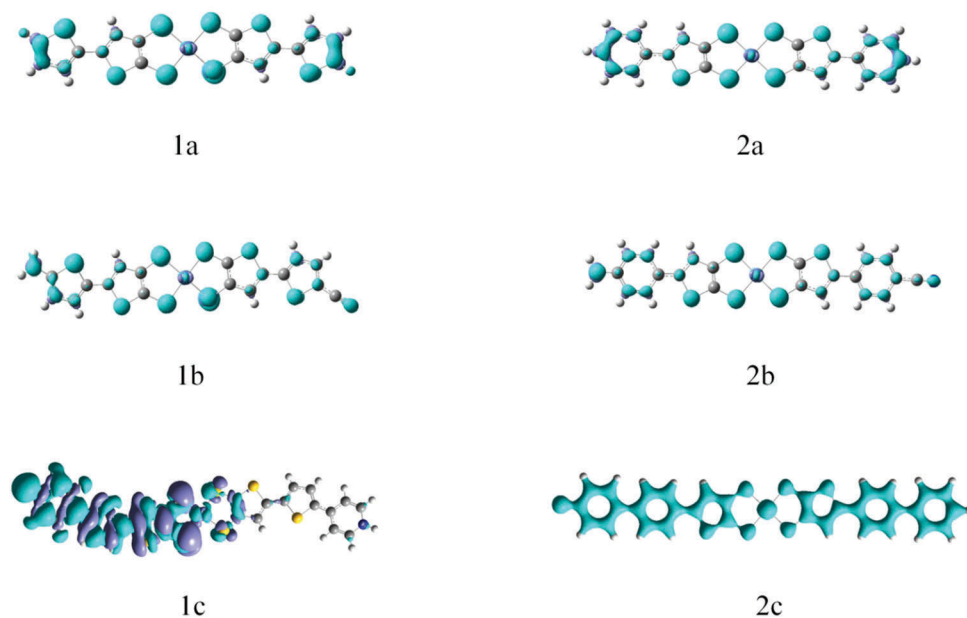
 $\beta$ - Density

Fig. 5 Isosurfaces of the static  $\beta$  density of all the studied complexes calculated at the UB3LYP/6-311++g(d,p) level.

where indices  $i$  and  $l$  run over all the occupied and virtual MOs, respectively.  $\varphi$  is the orbital wave function.

For **1c**, the electrons from the donor part are transferred to the acceptor part with the strongest electron oscillation amongst this set. We found a similar phenomenon for the next subset. Hence, a good correlation between the  $\Delta r$  index, TDM and first hyperpolarizability has been found. In a nutshell, the ionic donor–acceptor group can increase the TDM as well as the first hyperpolarizability values to a large extent.

In this part, we investigate the second harmonic generation of the studied systems from the local contribution analysis. The isosurfaces of the dynamic  $\beta$ -density are shown in Fig. 5. From the isosurfaces, it is clear that the electrons on all the sulfur atoms in the systems are responsible for the  $\beta$  density. A little contribution from the  $\pi$ -electron cloud of the extended thiophene has also been observed for complex **1a**. When donor–acceptor groups substitute the hydrogens of the thiophene ring (for complexes **1b** and **1c**),  $\beta$  density shifts to the donor–acceptor part, which highlights the importance of the push–pull mechanism directly. We found a similar phenomenon in the case of the second set of complexes, **2a** and **2b**. For complex **2c**, electron densities are distributed over the whole molecule through the  $\pi$ -electron conjugation of the phenyl ring. Electron delocalization is higher in the case of **2c** compared to **1c** due to the fact that the phenyl expanded systems are more planar compared to the thiophene expanded systems. Another important observation is that in complex **2a**, compared with complex **1a**, a five membered ring has been replaced by a six membered ring, which increases the push–pull character and electron delocalization, resulting in the enhancement of the  $\beta$  value.

## 5. Conclusions

In the present computational study, the nonlinear optical properties of two synthesized systems, phenyl expanded and thienyl expanded thiophene fused nickel dithiolenes, have been studied. Both the systems have a very low value of the first hyperpolarizability. We systematically modify their structures by substituting neutral and zwitterionic donor–acceptor groups at the aryl (phenyl and thienyl) ring to obtain a high NLO response. After a careful inspection of the HOMO–LUMO energies of all the six systems, we noticed that the neutral donor–acceptor group marginally affects the HOMO energy level, whereas the LUMO is stabilized to some extent. Hence, the HOMO–LUMO energy gap (HLG) decreases. However, the LUMO energies are found to be significantly reduced for the zwitterionic complexes, resulting in a large decrease in the HOMO–LUMO energy gap. Hence, the HLG gradually decreases from the neutral to ionic substituents for both sets of the designed systems. This observation has also been supported by the excitation energy calculations with the TDDFT approach. From the calculated first hyperpolarizability values, it has been noted that the zwitterionic compounds possess very large values of  $\beta$  with low HLG. We find that by substituting ionic groups at the two ends of the Ni complex, the  $\beta$  values were

enhanced by at least 10–15 times compared to that of the molecules without any such substituents. By a systematic analysis, a good correlation between the  $\Delta r$  index, TDM and  $\beta$  value has been observed. We anticipate that if synthesized, these molecules may prove to be useful in optical applications.

## Conflicts of interest

There are no conflicts to declare.

## Acknowledgements

The authors sincerely thank the Department of Science and Technology, India, for financial support.

## References

- 1 B. J. Coe, *Coord. Chem. Rev.*, 2013, **257**, 1438–1458.
- 2 S. Di Bella, *Chem. Soc. Rev.*, 2001, **30**, 355–366.
- 3 Pascal G. Lacroix, *Eur. J. Inorg. Chem.*, 2001, 339–348.
- 4 T. J. Marks and M. A. Ratner, *Angew. Chem., Int. Ed. Engl.*, 1995, **34**, 155–173.
- 5 O. Maury and H. Le Bozec, *Acc. Chem. Res.*, 2005, **38**, 691–704.
- 6 A. Coomber, D. Beljonne, R. Friend, J. Brédas, A. Charlton, N. Robertson, A. Underbill, M. Kurmoo and P. Day, *Nature*, 1996, **380**, 144–146.
- 7 T. D. Anthopoulos, S. Setayesh, E. Smits, M. Cölle, E. Cantatore, B. de Boer, P. W. Blom and D. M. de Leeuw, *Adv. Mater.*, 2006, **18**, 1900–1904.
- 8 B. V. U. T. Mueller-Westerhoff, in *Comprehensive Coordination Chemistry*, ed. J. A. McCleverty, R. D. Gillard and G. Wilkinson, Oxford, Pergamon, 1987, ch. 16.5, vol. 2, pp. 595–631.
- 9 S. Dalglish and N. Robertson, *Coord. Chem. Rev.*, 2010, **254**, 1549–1558.
- 10 A. Zarkadoulas, E. Koutsouri and C. A. Mitsopoulou, *Coord. Chem. Rev.*, 2012, **256**, 2424–2434.
- 11 B. Garreau-deBonneval, K. I. M.-C. Ching, F. Alary, T.-T. Bui and L. Valade, *Coord. Chem. Rev.*, 2010, **254**, 1457–1467.
- 12 C. L. Linfoot, P. Richardson, K. L. McCall, J. R. Durrant, A. Morandeira and N. Robertson, *Sol. Energy*, 2011, **85**, 1195–1203.
- 13 M. D. Ward and J. A. McCleverty, *J. Chem. Soc., Dalton Trans.*, 2002, 275–288.
- 14 G. Schrauzer and V. Mayweg, *J. Am. Chem. Soc.*, 1965, **87**, 3585–3592.
- 15 J. A. McCleverty, *Prog. Inorg. Chem.*, 1968, **10**, 49–221.
- 16 R. Eisenberg, *Prog. Inorg. Chem.*, 1970, **12**, 295–369.
- 17 E. Hoyer, W. Dietzsch and W. Schroth, *Z. Phys. Chem.*, 1971, **11**, 41–53.
- 18 Z. S. Herman, R. F. Kirchner, G. H. Loew, U. T. Mueller-Westerhoff, A. Nazzal and M. C. Zerner, *Inorg. Chem.*, 1982, **21**, 46–56.
- 19 A. Davison, N. Edelstein, R. Holm and A. Maki, *J. Am. Chem. Soc.*, 1963, **85**, 2029–2030.

- 20 S. Curreli, P. Deplano, C. Faulmann, A. Ienco, C. Mealli, M. L. Mercuri, L. Pilia, G. Pintus, A. Serpe and E. F. Trogu, *Inorg. Chem.*, 2004, **43**, 5069–5079.
- 21 F. Bigoli, P. Cassoux, P. Deplano, M. L. Mercuri, M. A. Pellinghelli, G. Pintus, A. Serpe and E. F. Trogu, *J. Chem. Soc., Dalton Trans.*, 2000, 4639–4644.
- 22 F. Bigoli, C.-T. Chen, W.-C. Wu, P. Deplano, M. L. Mercuri, M. A. Pellinghelli, L. Pilia, G. Pintus, A. Serpe and E. F. Trogu, *Chem. Commun.*, 2001, 2246–2247.
- 23 C. Lauterbach and J. Fabian, *Eur. J. Inorg. Chem.*, 1999, 1995–2004.
- 24 C. Rovira, J. J. Novoa, J.-L. Mozos, P. Ordejón and E. Canadell, *Phys. Rev. B: Condens. Matter Mater. Phys.*, 2002, **65**, 081104.
- 25 R. K. Szilagy, B. S. Lim, T. Glaser, R. H. Holm, B. Hedman, K. O. Hodgson and E. I. Solomon, *J. Am. Chem. Soc.*, 2003, **125**, 9158–9169.
- 26 J. E. Huyett, S. B. Choudhury, D. M. Eichhorn, P. A. Bryngelson, M. J. Maroney and B. M. Hoffman, *Inorg. Chem.*, 1998, **37**, 1361–1367.
- 27 G. C. Papavassiliou, G. C. Anyfantis and G. A. Mousdis, *Crystals*, 2012, **2**, 762–811.
- 28 C. M. Amb, C. L. Heth, S. J. Evenson, K. I. Pokhodnya and S. C. Rasmussen, *Inorg. Chem.*, 2016, **55**, 10978–10989.
- 29 G.-X. Liu, Y. Liu, S. Nishihara and X.-M. Ren, *Synth. React. Inorg., Met.-Org., Nano-Met. Chem.*, 2010, **40**, 416–420.
- 30 J. Nishijo, K. Iwama and M. Enomoto, *Eur. J. Inorg. Chem.*, 2015, 348–354.
- 31 K. Ray, T. Weyhermüller, F. Neese and K. Wieghardt, *Inorg. Chem.*, 2005, **44**, 5345–5360.
- 32 T. Petrenko, K. Ray, K. E. Wieghardt and F. Neese, *J. Am. Chem. Soc.*, 2006, **128**, 4422–4436.
- 33 K. Ray, S. DeBeer George, E. I. Solomon, K. Wieghardt and F. Neese, *Chem. – Eur. J.*, 2007, **13**, 2783–2797.
- 34 P. Machata, P. Herich, K. Lušpai, L. Bucinsky, S. Šoralová, M. Breza, J. Kozisek and P. Rapta, *Organometallics*, 2014, **33**, 4846–4859.
- 35 F. E. Hahn, T. Eiting, W. W. Seidel and T. Pape, *Eur. J. Inorg. Chem.*, 2010, 2393–2399.
- 36 T. Kambe, R. Sakamoto, K. Hoshiko, K. Takada, M. Miyachi, J.-H. Ryu, S. Sasaki, J. Kim, K. Nakazato and M. Takata, *J. Am. Chem. Soc.*, 2013, **135**, 2462–2465.
- 37 R. Matsuoka, R. Sakamoto, T. Kambe, K. Takada, T. Kusamoto and H. Nishihara, *Chem. Commun.*, 2014, **50**, 8137–8139.
- 38 E. Delgado, C. J. Gómez-García, D. Hernández, E. Hernández, A. Martín and F. Zamora, *Dalton Trans.*, 2016, **45**, 6696–6701.
- 39 H. Liu, X. Li, L. Chen, X. Wang, H. Pan, X. Zhang and M. Zhao, *J. Phys. Chem. C*, 2016, **120**, 3846–3852.
- 40 S. H. Schlindwein, K. Bader, C. Sibold, W. Frey, P. Neugebauer, M. Orlita, J. v. Slageren and D. Gudat, *Inorg. Chem.*, 2016, **55**, 6186–6194.
- 41 D. Belo and M. Almeida, *Coord. Chem. Rev.*, 2010, **254**, 1479–1492.
- 42 D. Belo, H. Alves, S. Rabaça, L. C. Pereira, M. T. Duarte, V. Gama, R. T. Henriques, M. Almeida, E. Ribera and C. Rovira, *Eur. J. Inorg. Chem.*, 2001, 3127–3133.
- 43 J. Nagakubo, M. Ashizawa, T. Kawamoto, A. Tanioka and T. Mori, *Phys. Chem. Chem. Phys.*, 2011, **13**, 14370–14377.
- 44 T. Higashino, O. Jeannin, T. Kawamoto, D. Lorcy, T. Mori and M. Fourmigue, *Inorg. Chem.*, 2015, **54**, 9908–9913.
- 45 C. Pozo-Gonzalo, R. Berridge, P. J. Skabara, E. Cerrada, M. Laguna, S. J. Coles and M. B. Hursthouse, *Chem. Commun.*, 2002, 2408–2409.
- 46 P. J. Skabara, C. Pozo-Gonzalo, N. L. Miazza, M. Laguna, E. Cerrada, A. Luquin, B. González, S. J. Coles, M. B. Hursthouse and R. W. Harrington, *Dalton Trans.*, 2008, 3070–3079.
- 47 S. Shibahara, H. Kitagawa, Y. Ozawa, K. Toriumi, T. Kubo and K. Nakasuji, *Inorg. Chem.*, 2007, **46**, 1162–1170.
- 48 R. Bolliglarla, G. Durgaprasad and S. K. Das, *Inorg. Chem. Commun.*, 2011, **14**, 809–813.
- 49 R. Bolliglarla, S. N. Reddy, G. Durgaprasad, V. Sreenivasulu and S. K. Das, *Inorg. Chem.*, 2012, **52**, 66–76.
- 50 M. C. Aragoni, M. Arca, T. Cassano, C. Denotti, F. A. Devillanova, R. Frau, F. Isaia, F. Lelj, V. Lippolis and L. Nitti, *Eur. J. Inorg. Chem.*, 2003, 1939–1947.
- 51 J. P. Nunes, M. J. Figueira, D. Belo, I. C. Santos, B. Ribeiro, E. B. Lopes, R. T. Henriques, J. Vidal-Gancedo, J. Veciana and C. Rovira, *Chem. – Eur. J.*, 2007, **13**, 9841–9849.
- 52 F. Vilela, P. J. Skabara, C. R. Mason, T. D. Westgate, A. Luquin, S. J. Coles and M. B. Hursthouse, *Beilstein J. Org. Chem.*, 2010, **6**, 1002.
- 53 N. Robertson and L. Cronin, *Coord. Chem. Rev.*, 2002, **227**, 93–127.
- 54 R. Kato, *Chem. Rev.*, 2004, **104**, 5319–5346.
- 55 P. Deplano, L. Pilia, D. Espa, M. L. Mercuri and A. Serpe, *Coord. Chem. Rev.*, 2010, **254**, 1434–1447.
- 56 D. S. Chemla, *Nonlinear optical properties of organic molecules and crystals*, Elsevier, 2012.
- 57 J. Abe and Y. Shirai, *J. Am. Chem. Soc.*, 1996, **118**, 4705–4706.
- 58 J. Abe, Y. Shirai, N. Nemoto, F. Miyata and Y. Nagase, *J. Phys. Chem. B*, 1997, **101**, 576–582.
- 59 J. Abe, Y. Shirai, N. Nemoto and Y. Nagase, *J. Phys. Chem. B*, 1997, **101**, 1910–1915.
- 60 J. S. Miller and J. C. Calabrese, *J. Chem. Soc., Chem. Commun.*, 1988, 63–64.
- 61 P. López, P. Zaderenko, J. L. Balcazar, I. Fonseca, F. H. Cano and P. Ballesteros, *J. Mol. Struct.*, 1996, **377**, 105–112.
- 62 M. Yamada and I. Honma, *Chem. Phys. Lett.*, 2005, **402**, 324–328.
- 63 S. Yamada, M. Nakano and K. Yamaguchi, *Int. J. Quantum Chem.*, 1999, **71**, 329–336.
- 64 S. Ohta, M. Nakano, T. Kubo, K. Kamada, K. Ohta, R. Kishi, N. Nakagawa, B. Champagne, E. Botek and A. Takebe, *J. Phys. Chem. A*, 2007, **111**, 3633–3641.
- 65 A. Willetts, J. E. Rice, D. M. Burland and D. P. Shelton, *J. Chem. Phys.*, 1992, **97**, 7590–7599.
- 66 M. Nakano, I. Shigemoto, S. Yamada and K. Yamaguchi, *J. Chem. Phys.*, 1995, **103**, 4175–4191.
- 67 A. Avramopoulos, H. Reis, G. A. Mousdis and M. G. Papadopoulos, *Eur. J. Inorg. Chem.*, 2013, 4839–4850.
- 68 L. Pilia, M. Pizzotti, F. Tessore and N. Robertson, *Inorg. Chem.*, 2014, **53**, 4517–4526.
- 69 P. Romaniello and F. Lelj, *THEOCHEM*, 2003, **636**, 23–37.

- 70 P. Chopra, L. Carlucci, H. F. King and P. N. Prasad, *J. Phys. Chem.*, 1989, **93**, 7120–7130.
- 71 M. J. Frisch, G. W. Trucks, H. B. Schlegel, G. E. Scuseria, M. A. Robb, J. R. Cheeseman, G. Scalmani, V. Barone, B. Mennucci, G. A. Petersson, H. Nakatsuji, M. Caricato, X. Li, H. P. Hratchian, A. F. Izmaylov, J. Bloino, G. Zheng, J. L. Sonnenberg, M. Hada, M. Ehara, K. Toyota, R. Fukuda, J. Hasegawa, M. Ishida, T. Nakajima, Y. Honda, O. Kitao, H. Nakai, T. Vreven, J. A. Montgomery, Jr., J. E. Peralta, F. Ogliaro, M. Bearpark, J. J. Heyd, E. Brothers, K. N. Kudin, V. N. Staroverov, R. Kobayashi, J. Normand, K. Raghavachari, A. Rendell, J. C. Burant, S. S. Iyengar, J. Tomasi, M. Cossi, N. Rega, J. M. Millam, M. Klene, J. E. Knox, J. B. Cross, V. Bakken, C. Adamo, J. Jaramillo, R. Gomperts, R. E. Stratmann, O. Yazyev, A. J. Austin, R. Cammi, C. Pomelli, J. W. Ochterski, R. L. Martin, K. V. Morokuma, G. Zakrzewski, G. A. Voth, P. Salvador, J. J. Dannenberg, S. Dapprich, A. D. Daniels, Ö. Farkas, J. B. Foresman, J. V. Ortiz, J. Cioslowski and D. J. Fox, *Gaussian 09, Revision A.1*, Gaussian, Inc., Wallingford CT, 2009.
- 72 J. d. Oudar, *J. Chem. Phys.*, 1977, **67**, 446–457.
- 73 K. Y. Saponitsky, S. Tafur and A. E. Masunov, *J. Chem. Phys.*, 2008, **129**, 044109.
- 74 T. Lu and F. Chen, *J. Comput. Chem.*, 2012, **33**, 580–592.
- 75 Z. S. Herman, R. F. Kirchner, G. H. Loew, U. T. Mueller-Westerhoff, A. Nazzari and M. C. Zerner, *Inorg. Chem.*, 1982, **21**, 46–56.
- 76 M. G. Papadopoulos, J. Waite, C. S. Winter and S. N. Oliver, *Inorg. Chem.*, 1993, **32**, 277–280.
- 77 G. N. Schrauzer and V. P. Mayweg, *J. Am. Chem. Soc.*, 1965, **87**, 1483–1489.
- 78 D. Herebian, K. E. Wieghardt and F. Neese, *J. Am. Chem. Soc.*, 2003, **125**, 10997–11005.
- 79 E. I. Stiefel, J. H. Waters, E. Billig and H. B. Gray, *J. Am. Chem. Soc.*, 1965, **87**, 3016–3017.
- 80 K. Ray, T. Petrenko, K. Wieghardt and F. Neese, *Dalton Trans.*, 2007, 1552–1566.
- 81 D. Evans, *J. Chem. Soc.*, 1959, 2003–2005.
- 82 G. S. Girolami, T. B. Rauchfuss and R. J. Angelici, *Synthesis and technique in inorganic chemistry: a laboratory manual*, University Science Books, 1999.
- 83 D. Avci, H. Cömert and Y. Atalay, *J. Mol. Model.*, 2008, **14**, 161–169.
- 84 S. Paul and A. Misra, *Inorg. Chem.*, 2011, **50**, 3234–3246.
- 85 C. A. Guido, P. Cortona, B. Mennucci and C. Adamo, *J. Chem. Theory Comput.*, 2013, **9**, 3118–3126.

## ■ Electro, Physical &amp; Theoretical Chemistry

# Multifunctional Magnetic Materials of Organic Origin for Biomedical Applications: A Theoretical Study

Manoj Majumder,<sup>[a]</sup> Tamal Goswami,<sup>[b]</sup> and Anirban Misra<sup>\*[c]</sup>

Six different diradical systems based on azulene coupler and nitronyl nitroxide radical moieties have been studied theoretically. Among them, three ferromagnetic diradicals are chosen for further calculation to assess their usability in different biological applications such as two-photon absorption photodynamic therapy (TPA-PDT) and magnetic resonance imaging contrast agents (MRICA). The TPA cross-section values have been calculated to judge their efficiency as TPA-PDT photosensitizing agents. Calculated values of TPA cross-section lie in the range of commonly used photosensitizers for PDT. It is seen

that the ferromagnetic diradicals can act as very good MRI contrast agents due to their high magnetic anisotropy characteristics. In connection to the magnetic anisotropy, the zero-field splitting (ZFS) parameters are also computed using density functional theory (DFT) based methods. It is found that the proposed diradicals can show good relaxation behaviour and consequently act as efficient MRI contrast agents. Thus, one can anticipate the multifunctional biological activity of these diradicals.

## 1 Introduction

In the past few years, organic magnetic materials have attracted the attention of the materials science community due to its interesting electrical, magnetic and nonlinear optical (NLO) properties. Appealing magnetic behaviour in reduced dimensions, diverse functional characteristics such as photosensitivity, fluorescence activity, highly efficient NLO property etc. promote their potential applications in photonic devices viz. optical switching, three dimensional memory storage and photodynamic therapy (PDT).<sup>[1]</sup> PDT is recognized as a highly effective treatment to fight oncological diseases in recent times.<sup>[2]</sup> PDT requires a photosensitizer, which transfers its triplet state energy to molecular oxygen when activated by light. This leads to the genesis of reactive singlet oxygen species ( $^1O_2$ ) capable of causing oxidative damage to biological substrates and ultimately lead to selective and irreversible apoptosis of malignant tissues, without causing damage to the adjacent healthy ones.<sup>[3]</sup> The excitation of photosensitizers, induced by two-photon absorption (TPA), is considered as a promising strategy in PDT and this is popularly known as

two-photon photodynamic therapy (TP-PDT).<sup>[1c,d]</sup> Two-photon absorption is a third-order nonlinear optical process in which excitation occurs by the simultaneous absorption of two photons at longer wavelengths instead of a single-photon excitation at a shorter wavelength.<sup>[4]</sup> A great deal of attention is paid to TPA property of organic  $\pi$ -conjugated systems because of their large nonlinear optical response.<sup>[5]</sup> In particular the design, preparation and application of efficient multifunctional organic diradicals are of enormous importance in the field of biomedical research.<sup>[6]</sup> The existence of both magnetic and optical properties in the same molecule will certainly make them appropriate candidates in the field of biophotonics.<sup>[7]</sup>

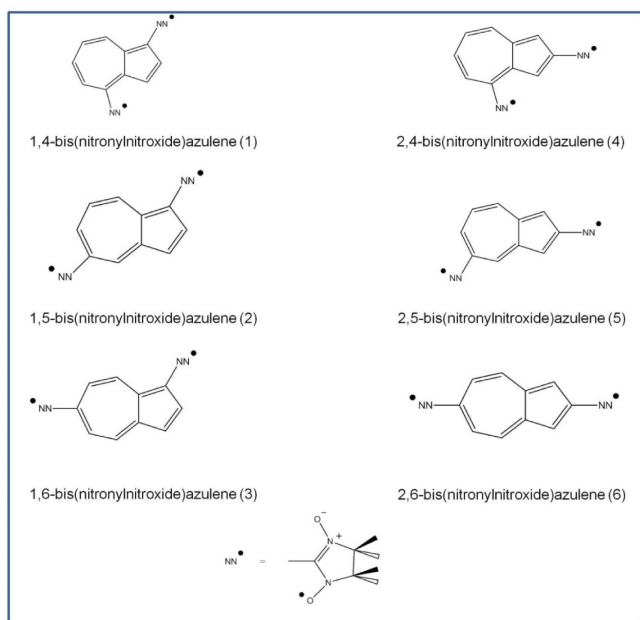
The increase in interest towards nitronyl nitroxide (NN)<sup>[8]</sup> stems not only from their use as building blocks in the design of molecular magnetic materials,<sup>[9]</sup> such as purely organic ferromagnetic ordered solids,<sup>[10]</sup> metal organic exchange coupled complexes<sup>[11]</sup> but also as new agents in bio imaging.<sup>[12]</sup> NN radical is known to be exceptionally stable, easy to prepare and able to generate co-operative magnetic properties.<sup>[13]</sup> Moreover it has been established that the nitronyl nitroxide radical shows cell permeability, biocompatibility and *in vivo* stability of the nitroxide-drug bonds.<sup>[14]</sup> Although a number of NN based diradicals have been synthesized and experimentally investigated,<sup>[15]</sup> combined electro-optic and magnetic materials based on NN diradicals have not received adequate attention. A number of previous reports reveal that the couplers between two radical centers play a decisive role for the magnetic characterization of the systems.<sup>[16]</sup> Generally, magnetic coupling arises from spin polarization and spin delocalization.<sup>[17]</sup> Nevertheless, the magnetic interaction between two radical centers normally depends upon the nature and the spatial linkage to the coupler. Thus by a judicious choice of the coupler and by modifying the spatial orientation of the coupler, the magnetic interaction may change in a useful manner so that the magnetic molecule have some multifunctional features.<sup>[16b,17–18]</sup>

[a] M. Majumder  
Department of Chemistry, University of North Bengal, Darjeeling, 734013,  
West Bengal, India  
E-mail: manojmtbc@gmail.com

[b] Dr. T. Goswami  
Department of Chemistry, University of North Bengal, Darjeeling, 734013,  
West Bengal, India  
E-mail: tamal.nbu@gmail.com

[c] Prof. A. Misra  
Department of Chemistry, University of North Bengal, Darjeeling, 734013,  
West Bengal, India  
Tel.: +919434228745  
E-mail: anirbanmisra@yahoo.com

Supporting information for this article is available on the WWW under  
<https://doi.org/10.1002/slct.201702530>



**Scheme 1.** Schematic representation of the diradicals under investigation.

In a nutshell, choice of coupler will be the key factor for designing efficient multifunctional materials.

Highly aromatic couplers are known to induce strong magnetic interaction in organic diradicals.<sup>[19]</sup> The high aromaticity of azulenes and their strong tendency to retain aromaticity upon exposure to magnetic interaction<sup>[20]</sup> make them suitable as coupler between radical centers. Though aromaticity of azulene compared to one of its isomer naphthalene is less, it has long been considered to be an interesting candidate for the application in optoelectronic materials due to its unique electronic and optical properties such as large permanent dipole moment, intense blue colour and the domination of fluorescence from S<sub>2</sub>–S<sub>0</sub> with low emission intensity.<sup>[21]</sup> Stimuli responsive behavior and high luminescence intensity of azulene derivatives also became recognized in recent research.<sup>[22]</sup> Despite quite a large number of theoretical calculations on the influence of the functional bis-substitution pattern of azulenes on their electronic properties, the theoretical investigation of magnetic and nonlinear optical properties of various diradical substituted azulene derivatives is lacking. Thus there is certainly a possibility of developing multifunctional ferromagnetic molecules with azulene as a coupler and nitronyl nitroxide as radical centers.

In this work six diradicals based on suitable substitution of NN radical in different positions of azulene coupler (Scheme 1) are considered as the reference systems of the present theoretical study. The estimation of magnetic exchange coupling constant values ( $J$ ) for all of these diradicals has been performed in the gas phase. The process of calculation is straightforward and well-established in the case of gas phase. However, for calculation in water and in *blood plasma* medium, the polarized continuum model (PCM) has been adopted. TPA cross section ( $\sigma$ ) has been calculated to assess the efficiency of

the proposed radicals for multifunctional uses. In the literature it has been shown that diradicals of organic origin can be effective and less hazardous for use in magnetic resonance imaging (MRI) as contrast agents.<sup>[23]</sup> In order to achieve a good MRI contrast activity, large longitudinal relaxation rate of the contrast agents is highly desired. Zero-field splitting (ZFS) magnitude is the key parameter to ascertain the longitudinal relaxation rate (*vide infra*) and the suitability of a diradical as MRI contrast agents (MRICAs).<sup>[24]</sup> Hence, we have evaluated the axial and rhombic ZFS parameters ( $D$  and  $E$ ) of the diradicals so to assess their aptness as MRICAs.

## 2 Theoretical Background

The magnetic exchange interaction between two magnetic two magnetic sites 1 and 2, is in general expressed by Heisenberg spin Hamiltonian,

$$\hat{H} = -2J\hat{S}_1\hat{S}_2 \quad (1)$$

where  $\hat{S}_1$  and  $\hat{S}_2$  are the spin angular momentum operators of spin-sites 1 and 2 respectively, and  $J$  is the exchange coupling constant. A positive  $J$ -value indicates a ferromagnetic interaction, whereas a negative value of  $J$  signifies an antiferromagnetic interaction. To evaluate the exchange coupling constant with reasonably less computational effort, Noodleman<sup>[25]</sup> has proposed an unrestricted spin polarized broken symmetry (BS) formalism in the DFT framework. The BS state is not a pure spin state, but a state of mixed spin symmetry with lower spatial symmetry. Depending on the extent of the magnetic interaction between two magnetic sites, many scientists have developed different formulae to estimate  $J$  using the BS approach.<sup>[26]</sup> Ideally, for diradicals the computed average values for triplet and BS states should be exactly 2.00 or 1.00 respectively. However in reality, their difference is not exactly unity, showing a clear indication of the spin contamination problem. In order to neutralize the spin contamination error associated with the BS state, one can use a spin projection technique. For estimating the  $J$ -values of diradicals of organic origin, the following expression by Yamaguchi et al.<sup>[26a-c]</sup> is the most widely applied<sup>[16b-d,27]</sup> and has been used by us in this work

$$J_Y^{DFT} = \frac{(E_{BS}^{DFT} - E_{HS}^{DFT})}{\langle S^2 \rangle_{HS} - \langle S^2 \rangle_{BS}} \quad (2)$$

where  $E_{BS}$ ,  $\langle S^2 \rangle_{BS}$ , and  $E_{HS}$ ,  $\langle S^2 \rangle_{HS}$  are the energy and average spin square values for the corresponding BS and high spin (HS) states, respectively. All the above mentioned calculations are implemented through the Gaussian 09 W quantum chemical package.<sup>[28]</sup>

The electron spin correlation time is important for clear MRI scans with enhanced contrast. The ZFS helps to get an estimation of the electron spin correlation time,<sup>[29]</sup> and is also one of the important parameters to characterize the geometric and electronic properties of a radical with  $S > 1/2$ .<sup>[30]</sup> The zero field splitting is treated in the second order of the perturbation

theory where two interactions are taken into account, namely the direct spin–spin (SS) interaction and (second-order) spin-orbit coupling (SOC),<sup>[30]</sup> however, the SS coupling contribution is the main source of ZFS in the case of organic radicals which are formed with light elements.<sup>[31]</sup> The ZFS value arising from the SS interactions can be estimated through an effective spin Hamiltonian

$$\hat{H}_{ZFS} = \sum_{\mu,\nu} D_{\mu\nu} \hat{S}_\mu \hat{S}_\nu \quad (3)$$

where  $D_{\mu\nu}$  are the components of the ZFS tensor,  $\hat{S}_\mu$  is the  $\mu^{\text{th}}$  Cartesian component of the total electron–spin operator. After diagonalization and subsequent reframing of the molecular coordinate, Equation (3) optimizes to

$$\hat{H}_{ZFS} = D \left( \hat{S}_z^2 - \frac{1}{3} \hat{S}^2 \right) + E (\hat{S}_x^2 - \hat{S}_y^2) \quad (4)$$

where  $D$  and  $E$  are axial and rhombic ZFS parameters respectively.<sup>[32]</sup> The spin–spin coupling interaction appears as a dipole–dipole interaction,<sup>[33]</sup>

$$\hat{H}_{SS} = \frac{\alpha^2}{2} \sum_{ij} \left[ \frac{\vec{S}_i \cdot \vec{S}_j}{r_{ij}^3} - \frac{3(\vec{S}_i \cdot \vec{r}_{ij})(\vec{S}_j \cdot \vec{r}_{ij})}{r_{ij}^5} \right] \quad (5)$$

The ground state Kohn–Sham determinant approximates the ZFS tensor components as expectations over the single determinant,<sup>[34]</sup>

$$D_{\mu\nu}^{(SS)} = \frac{g_e}{4} \frac{\alpha^2}{S(2S-1)} \langle OSM_S | \sum_i \sum_{j \neq i} \frac{r_{ij}^2 \delta_{\mu\nu} - 3(r_{ij})_\mu (r_{ij})_\nu}{r_{ij}^5} \times \{ 2\hat{S}_{iz}\hat{S}_{jz} - \hat{S}_{ix}\hat{S}_{jx} - \hat{S}_{iy}\hat{S}_{jy} \} | OSM_S \rangle. \quad (6)$$

In the above,  $\alpha$  is the fine structure constant,  $g_e$  is the gyromagnetic ratio. The operators  $\hat{S}_{i\mu}$  signify the  $\mu^{\text{th}}$  components of  $i^{\text{th}}$  spin vector, and  $r_{ij}$  is the distance between spin sites  $i$  and  $j$ , while  $\mu$  and  $\nu$  run over  $x, y, z$  coordinates. McWeeny and Mizuno expressed the above equation using the spin density matrix as<sup>[35]</sup>

$$D_{kl}^{(SS)} = \frac{g_e}{4} \frac{\alpha^2}{S(2S-1)} \sum_{\mu\nu} \sum_{\kappa\lambda} \left\{ P_{\mu\nu}^{\alpha-\beta} P_{\kappa\lambda}^{\alpha-\beta} - P_{\mu\kappa}^{\alpha-\beta} P_{\nu\lambda}^{\alpha-\beta} \right\} \times \langle \mu\nu | r_{12}^{-5} \{ \{ 3r_{12,k} r_{12,l} \} (-\delta_{kl} r_{12}^2) \} | \kappa\lambda \rangle \quad (7)$$

Here,  $P^{\alpha-\beta} = P^\alpha - P^\beta$  is the spin density matrix in the atomic orbital basis, and now  $\mu, \nu, \kappa, \lambda$  label the basis orbitals.<sup>[31]</sup> The ZFS parameters  $D$  and  $E$  are determined from the tensor components  $D_{kl}^{(SS)}$ , as<sup>[36]</sup>

$$D = D_{zz} - \frac{1}{2}(D_{xx} + D_{yy}) \quad (8)$$

$$E = \frac{1}{2}(D_{xx} - D_{yy}) \quad (9)$$

and in turn determine the static ZFS magnitude ( $a_2$ ) through

$$a_2 = \sqrt{\left( \frac{2}{3} D^2 + 2E^2 \right)} \quad (10)$$

From this  $a_2$ , the longitudinal electron–spin relaxation rate  $1/T_{1e}$  can be estimated by,<sup>[37]</sup>

$$\frac{1}{T_{1e}(B_0)} = \frac{2}{5} a_2^2 \tau_R \left[ \frac{1}{1 + \omega_0^2 \tau_2^2} + \frac{4}{1 + 4\omega_0^2 \tau_2^2} \right] + \frac{12}{5} a_2^2 \tau' \left[ \frac{1}{1 + \omega_0^2 \tau'^2} + \frac{4}{1 + 4\omega_0^2 \tau'^2} \right] \quad (11)$$

Where  $B_0$  is the external magnetic field,  $\omega_0$  is the Larmor frequency,  $\tau_2$  and  $\tau'$  are the reduced spectral densities and  $a_{2T}$  is the transient ZFS magnitude. Larger  $a_2$  values correspond to a faster relaxation rate  $1/T_{1e}$ .<sup>[37]</sup>

Despite the well established formal theoretical description of TPA,<sup>[38]</sup> the theory has only been applied in the context of physics of atoms and small molecules. The two-photon-absorption cross section is related to the imaginary part of the third-order polarizability as<sup>[39]</sup>

$$\sigma_{TPA}(\omega) = \frac{4\pi^2 \hbar \omega^2}{n^2 c^2} L^4 \text{Im} \langle \gamma(\omega, \omega, -\omega) \rangle \quad (12)$$

where  $\hbar$  is Planck's constant,  $c$  is the speed of light,  $n$  is the refractive index of the media,  $L$  is the local field factor.  $\langle \gamma \rangle$  is the second hyperpolarizability, average over all orientations, which is represented as

$$\langle \gamma \rangle = \frac{1}{15} \left[ 3 \sum_i \gamma_{iii} + \sum_{i \neq j} (\gamma_{ijj} + \gamma_{jji} + \gamma_{ijj}) \right] \quad (13)$$

where indices  $i$  and  $j$  refer to spatial directions  $x, y$ , and  $z$ .<sup>[40]</sup> The evaluation of the third-order polarizability is done by the perturbative sum-over-state (SOS) method utilizing the ground- and excited-state energies, state dipoles, and transition dipole values.<sup>[41]</sup>

### 3 Computational Details

The gas phase molecular geometry of all the azulene diradicals have been fully optimized with the unrestricted B3LYP functional using the 6–311 g(d,p) basis set in Gaussian 09 W suite of program.<sup>[28]</sup> The magnetic exchange coupling constant ( $J$ ) is estimated from the single point energies of the triplet and BS state at the UB3LYP/6-311++g (2df, 2p) level utilizing Equation (2). The ZFS parameters ( $D$  and  $E$ ) have been calculated using BPW91 functional, EPR-II basis set in ORCA suit of software.<sup>[42]</sup> EPR-II basis set has long been considered to be useful for calculating the  $D$  values in case of organic diradicals.<sup>[43]</sup> The validity of this methodology for computing  $D$

and  $E$  is tested by comparing the computed value of  $D$  and  $E$  against the experimental value available for a diradical synthesized by Rajca.<sup>[24]</sup> The experimental ZFS parameter has been reported as  $-1.22 \times 10^{-2} \text{ cm}^{-1}$ , which is in close agreement with the computed  $D$  value ( $-1.60 \times 10^{-2} \text{ cm}^{-1}$ ). For this correlation of our computed results with the experimentally reported data by Rajca *et al.*, the same combination of basis set and functional is used for the estimation of the  $D$  parameters for the systems under investigation. In order to check the effect of solvent on calculated properties, the  $J$  and  $D$  values are also calculated within polarisable continuum model (PCM) using the dielectric constants of water and *blood plasma* (80 and 58 respectively), which are the most common solvents in human body.

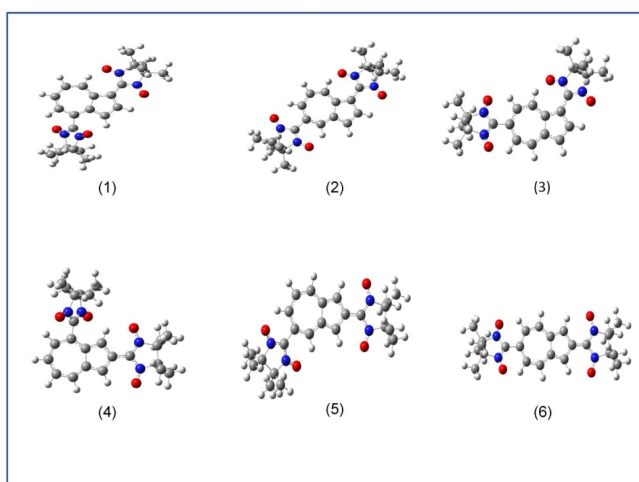


**Figure 1.** Optimized molecular geometry of the diradicals obtained through unrestricted B3LYP exchange correlation functional using the 6-311 g (d,p) basis set.

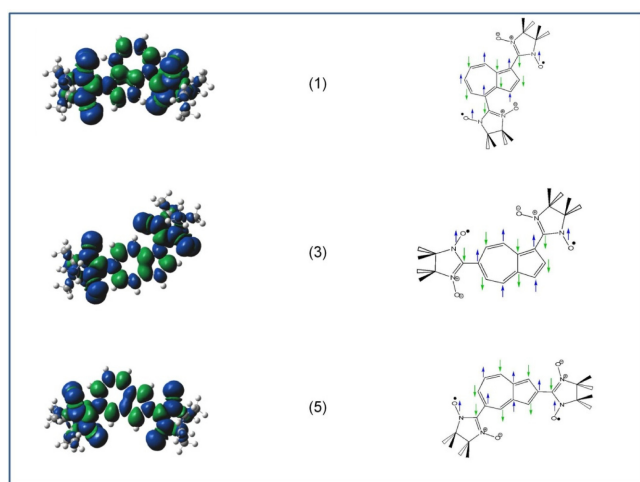


**Figure 2.** Spin density plots of ferromagnetic azulene diradicals. Green and blue surfaces indicate up and down spin density. Same color code is used for schematic representation of spin alternation, i. e., blue and green arrow for up and down spin respectively.

**Table 1.** Calculated absolute energies in atomic units (au),  $\langle S^2 \rangle$  values, intramolecular magnetic exchange coupling constants ( $J$  in  $\text{cm}^{-1}$ ) between two radical centers for the designed diradicals at UB3LYP/6-311 + + g (2df, 2p) level.

Diradicals		Energy (au)	$\langle S^2 \rangle$	$J$ in $\text{cm}^{-1}$
1	Triplet	-1452.7267132	2.115519	12.75
	BS	-1452.726656	1.130897	
2	Triplet	-1452.7346583	2.096137	-193.22
	BS	-1452.7355085	1.130392	
3	Triplet	-1452.7330113	2.131788	47.70
	BS	-1452.7327901	1.114097	
4	Triplet	-1452.7333679	2.106828	-81.77
	BS	-1452.7337341	1.123951	
5	Triplet	-1452.7411477	2.149931	90.37
	BS	-1452.7407227	1.117795	
6	Triplet	-1452.7381936	2.108376	-228.89
	BS	-1452.7391866	1.156251	

The computation of TPA cross section values have been carried out at UB3LYP/6-311 + + g (2df, 2p) level of theory in DALTON software.<sup>[44]</sup>

## 4 Results and discussions

The optimized geometries of the designed diradicals are shown in Figure 1. Frequency calculation on the optimized geometries showed no imaginary frequency for any of the molecules, which indicate intrinsic stability of the optimized structures (zero point energy corrected values are also given in the supporting information in Table S2). The gas phase magnetic exchange coupling constant ( $J$ ) values are presented in Table 1. Systems **1**, **3** and **5** are found to be ferromagnetic and the systems **2**, **4** and **6** are antiferromagnetically coupled. The ferro- and antiferro-magnetic behaviour of the azulene coupled diradical systems can be justified through the popular spin density alternation rules.<sup>[45]</sup> The spin-density alternation can also be visualized through the spin density plots presented in Figure 2., where one can clearly see that the radicals coupled through an odd and even number of conjugated atomic centers always lead to ferro- and antiferromagnetic interactions respectively. A close inspection of Figure 2 further reveals an interesting feature of the spin density alternation. The carbon atoms situated at the junction of two fused five and seven membered rings in azulene always carry similar spins despite being neighbours. It appears that the two junction-carbon atoms in **1**, **3** and **5** behave as single units in spin density alternation protocol. Owing to their biomedical relevance we consider only the ferromagnetic systems, i.e., **1**, **3** and **5** for further calculations.

Extensive study of two-photon photodynamic therapy revealed that the treatment is relatively benign and gives finer cosmetic outcomes compared to other PDT techniques. In those methods excitation of the drugs are performed through visible light which has very low penetrability into human tissues.<sup>[46]</sup> Simultaneous absorption of two near-IR photons is much more penetrating through tissues compared to visible light photons. Hence, excitation of the photosensitizer through

near-IR photons is more desirable to destroy cancer cells present in deeper tissues.<sup>[47]</sup> Two-photon PDT also ensures greater penetration depths and highly-selective targeting through intense laser pulse processes. TPA cross-section ( $\sigma_{\text{TPA}}$ ) estimates the efficacy of a photosensitizer that undergoes two-photon absorption. It is measured in Göppert-Mayer units ( $1 \text{ GM} = 10^{-50} \text{ cm}^4 \text{ s photon}^{-1} \text{ molecule}^{-1}$ ). The TPA cross-sections of existing photosensitizers are in the order of 1–100 GM.<sup>[48]</sup> In a recent report Zhao *et al.*<sup>[49]</sup> studied the spectroscopic properties of Chlorophyll derivative photosensitizer (CDP) and their TPA cross section is measured as 31.5 GM. The results of the two photon photodynamic therapy (TPPDT) test showed that CDP can kill all of the tested cancer cells. Hence, suitable design of compounds with higher TPA cross-sections is always desirable to ensure efficient phototherapeutic applications. Generation of singlet oxygen ( $^1\Delta_g$ ) is the key to phototherapeutic activity of the photosensitizers in PDT. A good singlet oxygen yield ( $\Phi_\Delta$ ) is desired for photo-biological cell damage or apoptosis. It has been seen that the insertion of radical moieties in a photosensitizer greatly enhances  $\Phi_\Delta$ .<sup>[50]</sup> Thus a diradical system will be the best candidate for use as photosensitizer in photodynamic therapy. In the present study we have calculated  $\sigma_{\text{TPA}}$  of the designed diradicals which are reported in Table 2. It is found that the TPA cross-section values

**Table 2.** The spin-spin ZFS parameter  $D_{\text{total}}$  ( $\text{cm}^{-1}$ ), static ZFS magnitude  $a_2$  ( $\text{cm}^{-1}$ ), rhombic ZFS parameter ( $E$ ) for each ferromagnetic diradical at BPW91/EPR-II and two photon absorption cross section ( $\sigma_{\text{TPA}}$  in GM), for the same diradicals at UB3LYP/6-311++g(d,p) level.

Diradicals	$\sigma_{\text{TPA}}$ (GM)	$D_{\text{total}}$ ( $\text{cm}^{-1}$ )	$E$ ( $\text{cm}^{-1}$ )	$a_2$ ( $\text{cm}^{-1}$ )
1	3.8	$-10.03 \times 10^{-2}$	$-1.7 \times 10^{-2}$	$8.5 \times 10^{-2}$
3	5.0	$-11.6 \times 10^{-2}$	$-1.51 \times 10^{-2}$	$9.7 \times 10^{-2}$
5	21.1	$-10.6 \times 10^{-2}$	$-0.74 \times 10^{-2}$	$8.7 \times 10^{-2}$

lie in the reported range of the presently used photosensitizers. Among the three designed ferromagnetic diradicals, **5** shows the highest  $\sigma_{\text{TPA}}$  value of 21.1 GM.

Although very promising as noninvasive and safe protocols of cancer treatment, PDT is challenging in connection with the delivery of the photosensitizer to the infected tissue.<sup>[51]</sup> To ensure the monomeric distribution of the photosensitizing agent, diagnostic imaging techniques are preferred compared to regular drug delivery methods.<sup>[52]</sup> Magnetic resonance imaging has emerged as a powerful imaging technique in recent years. MRI, with the use of contrast agents can provide highly sensitive imaging with minute three dimensional topographical details *in vivo*. Hence, if one can integrate contrast-

enhanced MRI imaging capability with PDT, the resulting imaging guided PDT can prove to be the most appreciable strategy for cancer treatment. The design of materials with good imaging and photosensitizing capability is therefore the requirement for developing improved multifunctional agents.

A site-specific MRI contrast agent with a high rate of relaxation of water protons in the target cell is central to efficient magnetic resonance imaging. It is quite evident from the discussion in the previous section and Equation (11) that the ZFS magnitude ( $a_2$ ) is directly proportional to the longitudinal relaxation rate ( $1/T_{1e}$ ). With the increase in the value of  $1/T_{1e}$ , the observed MRI signal is enhanced. In the present work, the ZFS parameter  $D$  and static ZFS magnitude ( $a_2$ ) of the three ferromagnetic systems, namely, **1**, **3** and **5**, have been estimated and is reported in Table 2. It is notable from Table 2 that all the ferromagnetic diradicals possess high value of  $D$  in the range of  $-8.5 \times 10^{-2} \text{ cm}^{-1}$  to  $-9.7 \times 10^{-2} \text{ cm}^{-1}$ . Rajca *et al.* in one of their pioneering works reported nitroxide based diradicals, synthesized and already been established as a MRICA of organic origin, to have  $D$  values in the range of  $-1.2 \times 10^{-2}$  to  $-1.7 \times 10^{-2} \text{ cm}^{-1}$ .<sup>[23]</sup> A diarylnitroxide triplet diradical with  $D$  and  $a_2$  values of  $-1.223 \times 10^{-2}$  and  $1.02 \times 10^{-2} \text{ cm}^{-1}$  respectively is also found to be usable as MRICA.<sup>[24]</sup>

In order to gain an assurance of the *in vivo* functionality of the systems under investigation, we have calculated the magnetic exchange coupling constant ( $J$ ) and the zero field splitting parameters ( $D$ ) in water and as well as in blood plasma medium and the results are reported in Table 3. It is clear that the variations in  $J$  and  $D$  values of all the designed systems in different media are negligible.

## 5 Conclusion

In the present computational study we have considered the magnetic and optical properties of a few azulene based diradical systems. We have studied six diradical systems based on nitronyl nitroxide radical moiety and azulene as coupler. The magnetic property has been assessed through the magnetic exchange coupling and magnetic anisotropy. The calculated magnetic exchange coupling parameters  $J$  depict that among the six diradicals three are ferromagnetic, and three are antiferromagnetic. The magnetic exchange coupling constants have been corroborated through spin density alternation protocol. The spin density analyses of the three ferromagnetic diradicals depict an interesting alternation behavior in the azulene coupler. The junction carbon atoms of the two rings in azulene coupler always show similar spin density despite being

**Table 3.** The magnetic exchange coupling constants ( $J$ ) and ZFS parameter ( $D$ ) values for the proposed ferromagnetic diradical systems in gas phase, water and blood plasma media, computed using PCM model using UB3LYP/6-311++g(2df,2p) and BPW91/EPR-II method.

Diradicals	$J$ ( $\text{cm}^{-1}$ )			$D$ ( $\text{cm}^{-1}$ )		
	Gas Medium	Water Medium	Blood Plasma	Gas Medium	Water Medium	Blood Plasma
1	12.75	12.40	12.42	$-10.03 \times 10^{-2}$	$-10.3 \times 10^{-2}$	$-10.6 \times 10^{-2}$
3	47.70	41.68	43.03	$-11.6 \times 10^{-2}$	$-10.6 \times 10^{-2}$	$-10.6 \times 10^{-2}$
5	90.37	81.59	81.64	$-10.6 \times 10^{-2}$	$-10.9 \times 10^{-2}$	$-10.9 \times 10^{-2}$

neighbors. This behavior is a fascinating variation of the spin density alternation rule. The ability of the ferromagnetic diradicals as photosensitizer in photodynamic therapy is evaluated through the computation of the two-photon absorption cross-section. The integrative photodynamic therapy (IPDT) of tumors relies on the combined use of different factors that enhance the usefulness of IPDT.<sup>[53]</sup> The observed TPA cross-section values range in the reported limit of commonly used photosensitizing agents. Another dimension of the multi-property diradical system has also been explored in this work. The magnetic anisotropy of the ferromagnetic diradicals has been estimated through the zero-field splitting parameter  $D$ . A negative ZFS parameter suggests the tendency of the spin vector to orient along a specific Cartesian direction. All the three ferromagnetic diradicals show negative  $D$  values. Radical systems with negative ZFS parameters have been proved to be usable as MRI contrast agents.<sup>[16b]</sup> It has long been shown that the larger the ZFS magnitude  $a_2$ , larger is the spin relaxation time and the better an MRICA is.<sup>[24]</sup> The ZFS magnitude  $a_2$  is directly proportional to the ZFS parameter  $D$ . In the designed ferromagnetic diradicals, the ZFS parameters are found to be significantly high as for organic radical systems. The values are at least one order of magnitude higher compared to reported diradical systems usable as MRICA. Ferromagnetic systems are used as efficient probe in the magnetic hyperthermia, a popular treatment in oncology. These diradicals can also be sought for a lateral use as MRICA in magnetic resonance imaging, which is very often utilized for the detection of cancer. Treatment of interstitial tumors with PDT demands the delivery of photosensitizers to the precise location of tumor tissues for effective light irradiations. Thus a single agent that can be injected to the infected body to image tumors through MRI and simultaneously treat them by exposing to light through PDT is greatly welcomed as a proficient cancer treatment protocol. In summary we propose that if synthesized these diradical systems can promote the "see and treat" method<sup>[54]</sup> by proving themselves efficient in multifarious therapeutic function such as magnetic hyperthermia, MRI contrast agents and photodynamic therapy applications.

## Supporting Information

The optimized coordinates of all the diradicals, sample input output section for  $J$ , ZFS parameter and TPA cross section calculations are available in the Supporting Information.

## Acknowledgement

Authors sincerely thank the Department of Science and Technology, India, for financial support.

## Conflict of Interest

The authors declare no conflict of interest.

**Keywords:** Density Functional Theory · Magnetic Properties · Photodynamic Therapy · Two Photon Absorption · Zero-field splitting

- [1] a) D. A. Parthenopoulos, P. M. Rentzepis, *Science* **1989**, *245*, 843–845; b) W. Zhou, S. M. Kuebler, K. L. Braun, T. Yu, J. K. Cammack, C. K. Ober, J. W. Perry, S. R. Marder, *Science* **2002**, *296*, 1106–1109; c) Z. D. Qi, D. W. Li, P. Jiang, F. L. Jiang, Y. S. Li, Y. Liu, W. K. Wong, K. W. Cheah, *J. Mater. Chem.* **2011**, *21*, 2455–2458; d) T. Zhao, X. Shen, L. Li, Z. Guan, N. Gao, P. Yuan, S. Q. Yao, Q. H. Xu, G. Q. Xu, *Nanoscale* **2012**, *4*, 7712–7719.
- [2] a) R. W. Boyle, D. Dolphin, *Photochem. Photobiol.* **1996**, *64*, 469–485; b) W. M. Sharman, C. M. Allen, J. E. Van Lier, *Drug Discovery Today* **1999**, *4*, 507–517.
- [3] a) K. Lang, J. Mosinger, D. Wagnerová, *Coord. Chem. Rev.* **2004**, *248*, 321–350; b) S. Kim, T. Y. Ohulchanskyy, H. E. Pudavar, R. K. Pandey, P. N. Prasad, *J. Am. Chem. Soc.* **2007**, *129*, 2669–2675.
- [4] V. Goppert-Mayer, *Ann. Phys.* **1931**, *9*, 273–294.
- [5] a) R. Weissleder, *Nat. Biotechnol.* **2001**, *19*, 316–316; b) A. Baev, P. N. Prasad, M. Samoc, *J. Chem. Phys.* **2005**, *122*, 224309.
- [6] a) A. Rajca, K. Lu, S. Rajca, C. R. Ross II, *Chem. Commun.* **1999**, 1249–1250; b) C. Avendaño and J. Menéndez in *Medicinal chemistry of anticancer agents*, Vol. Elsevier, Amsterdam, **2008**.
- [7] a) P. Verwilst, S. Park, B. Yoon, J. S. Kim, *Chem. Soc. Rev.* **2015**, *44*, 1791–1806; b) M. Abe, *Chem. Rev.* **2013**, *113*, 7011–7088.
- [8] a) J. H. Osiecki, E. F. Ullman, *J. Am. Chem. Soc.* **1968**, *90*, 1078–1079; b) E. F. Ullman, L. Call, J. H. Osiecki, *J. Org. Chem.* **1970**, *35*, 3623–3631; c) E. F. Ullman, J. H. Osiecki, D. Boocock, R. Darcy, *J. Am. Chem. Soc.* **1972**, *94*, 7049–7059.
- [9] O. Kahn, *Magnetism: a supramolecular function*, Springer Science & Business Media, **2013**, p.
- [10] a) M. Tamura, Y. Nakazawa, D. Shiomi, K. Nozawa, Y. Hosokoshi, M. Ishikawa, M. Takahashi, M. Kinoshita, *Chem. Phys. Lett.* **1991**, *186*, 401–404; b) M. Kinoshita, P. Turek, M. Tamura, K. Nozawa, D. Shiomi, Y. Nakazawa, M. Ishikawa, M. Takahashi, K. Awaga, T. Inabe, *Chem. Lett.* **1991**, *20*, 1225–1228; c) J. Cirujeda, M. Mas, E. Molins, F. Lanfranc de Panthou, J. Laugier, J. G. Park, C. Paulsen, P. Rey, C. Rovira, J. Veciana, *J. Chem. Soc. Chem. Commun.* **1995**, 709–710; d) J. Cirujeda, E. Hernández-Gasió, C. Rovira, J. L. Stanger, P. Turek, J. Veciana, *J. Mater. Chem.* **1995**, *5*, 243–252; e) M. M. Matsushita, A. Izuoka, T. Sugawara, T. Kobayashi, N. Wada, N. Takeda, M. Ishikawa, *J. Am. Chem. Soc.* **1997**, *119*, 4369–4379; f) C. Hirel, D. Luneau, J. Pécaut, L. Öhrström, G. Bussière, C. Reber, *Chem. Eur. J.* **2002**, *8*, 3157–3161.
- [11] a) D. A. Shultz, S. H. Bodnar, K. E. Vostrikova, J. W. Kampf, *Inorg. Chem.* **2000**, *39*, 6091–6093; b) H. O. Stumpf, L. Ouahab, Y. Pei, D. Grandjean, O. Kahn, *Science-New York Then Washington* **1993**, 447–447; c) K. Inoue, T. Hayamizu, H. Iwamura, D. Hashizume, Y. Ohashi, *J. Am. Chem. Soc.* **1996**, *118*, 1803–1804; d) G. Ballester, E. Coronado, C. Giménez-Saiz, F. M. Romero, *Angew. Chem. Int. Ed.* **2001**, *40*, 792–795; e) K. Fegy, D. Luneau, T. Ohm, C. Paulsen, P. Rey, *Angew. Chem. Int. Ed.* **1998**, *37*, 1270–1273; f) C. Benelli, D. Gatteschi, *Chem. Rev.* **2002**, *102*, 2369–2388; g) K. Inoue, H. Iwamura, *J. Am. Chem. Soc.* **1994**, *116*, 3173–3174; h) F. Mathevet, D. Luneau, *J. Am. Chem. Soc.* **2001**, *123*, 7465–7466; i) C. Rajadurai, V. Enkelmann, V. Ilkorski, V. I. Ovcharenko, M. Baumgarten, *Inorg. Chem.* **2006**, *45*, 9664–9669; j) K. Bernot, L. Bogani, A. Caneschi, D. Gatteschi, R. Sessoli, *J. Am. Chem. Soc.* **2006**, *128*, 7947–7956.
- [12] a) J. Joseph, B. Kalyanaraman, J. S. Hyde, *Biochem. Biophys. Res. Commun.* **1993**, *192*, 926–934; b) T. Nagano, T. Yoshimura, *Chem. Rev.* **2002**, *102*, 1235–1270; c) P. Cabrales, A. G. Tsai, M. Intaglietta, *J. Appl. Physiol.* **2006**, *100*, 1181–1187.
- [13] J. Miller, M. Drillon in *From Molecules to Materials IV*, Vol. Wiley-VCH, Weinheim, **2003**.
- [14] a) Z. Zhelev, R. Bakalova, I. Aoki, K.-i. Matsumoto, V. Gadjeva, K. Anzai, I. Kanno, *Mol. Pharmaceut.* **2009**, *6*, 504–512; b) L. J. Berliner, H. Fujii, X. Wan, S. Lukiewicz, *Magn. Reson. Med.* **1987**, *4*, 380–384.
- [15] C. Rajadurai, A. Ivanova, V. Enkelmann, M. Baumgarten, *J. Org. Chem.* **2003**, *68*, 9907–9915.
- [16] a) C. Ling, M. Minato, P. M. Lahti, H. Van Willigen, *J. Am. Chem. Soc.* **1992**, *114*, 9959–9969; b) D. Bhattacharya, S. Shil, A. Misra, *J. Photochem. Photobiol. A: Chem.* **2011**, *217*, 402–410; c) D. Bhattacharya, A. Panda, S.

- Shil, T. Goswami, A. Misra, *Phys. Chem. Chem. Phys.* **2012**, *14*, 6905–6913; d) S. Shil, A. Misra, *J. Phys. Chem. A* **2009**, *114*, 2022–2027.
- [17] F. Dietz, N. Tyutyulkov, *Chem. Phys.* **2001**, *264*, 37–51.
- [18] N. Tanifuji, M. Irie, K. Matsuda, *J. Am. Chem. Soc.* **2005**, *127*, 13344–13353.
- [19] D. Bhattacharya, A. Misra, *J. Phys. Chem. A* **2009**, *113*, 5470–5475.
- [20] D. Cho, K. C. Ko, J. Y. Lee, *J. Phys. Chem. A* **2014**, *118*, 5112–5121.
- [21] a) N. J. Turro, *Modern molecular photochemistry*, University science books, **1991**, p; b) D. R. Mitchell, G. D. Gillispie, *J. Phys. Chem.* **1989**, *93*, 4390–4393; c) Y. Yamaguchi, Y. Maruya, H. Katagiri, K.-i. Nakayama, Y. Ohba, *Org. Lett.* **2012**, *14*, 2316–2319; d) K. Kurotobi, K. S. Kim, S. B. Noh, D. Kim, A. Osuka, *Angew. Chem.* **2006**, *118*, 4048–4051.
- [22] a) E. Amir, R. J. Amir, L. M. Campos, C. J. Hawker, *J. Am. Chem. Soc.* **2011**, *133*, 10046–10049; b) M. Koch, O. Blacque, K. Venkatesan, *Org. Lett.* **2012**, *14*, 1580–1583.
- [23] a) G. Spagnol, K. Shiraishi, S. Rajca, A. Rajca, *Chem. Commun.* **2005**, 5047–5049; b) A. Olankitwanit, V. Kathirvelu, S. Rajca, G. R. Eaton, S. S. Eaton, A. Rajca, *Chem. Commun.* **2011**, *47*, 6443–6445.
- [24] A. Rajca, K. Shiraishi, S. Rajca, *Chem. Commun.* **2009**, 4372–4374.
- [25] a) L. Noodleman, *J. Chem. Phys.* **1981**, *74*, 5737–5743; b) L. Noodleman, E. J. Baerends, *J. Am. Chem. Soc.* **1984**, *106*, 2316–2327; c) L. Noodleman, E. R. Davidson, *Chem. Phys.* **1986**, *109*, 131–143; d) L. Noodleman, C. Peng, D. Case, J. M. Mouesca, *Coord. Chem. Rev.* **1995**, *144*, 199–244.
- [26] a) K. Yamaguchi, Y. Takahara, T. Fueno, K. Nasu, *Jpn. J. Appl. Phys.* **1987**, *26*, L1362; b) K. Yamaguchi, F. Jensen, A. Dorigo, K. Houk, *Chem. Phys. Lett.* **1988**, *149*, 537–542; c) K. Yamaguchi, Y. Takahara, T. Fueno, K. Houk, *Theor. Chem. Acc.* **1988**, *73*, 337–364; d) S. Paul, A. Misra, *J. Chem. Theory Comput.* **2012**, *8*, 843–853; e) R. L. Martin, F. Illas, *Phys. Rev. Lett.* **1997**, *79*, 1539; f) R. Caballo, O. Castell, F. Illas, I. de PR Moreira, J. Malrieu, *J. Phys. Chem. A* **1997**, *101*, 7860–7866; g) V. Barone, A. di Matteo, F. Mele, I. de PR Moreira, F. Illas, *Chem. Phys. Lett.* **1999**, *302*, 240–248; h) F. Illas, I. P. Moreira, C. De Graaf, V. Barone, *Theor. Chem. Acc.* **2000**, *104*, 265–272; i) F. Illas, I. de PR Moreira, J. Bofill, M. Filatov, *Phys. Rev. B* **2004**, *70*, 132414.
- [27] a) M. E. Ali, S. N. Datta, *J. Phys. Chem. A* **2006**, *110*, 10525–10527; b) V. Polo, A. Alberola, J. Andres, J. Anthony, M. Pilkington, *Phys. Chem. Chem. Phys.* **2008**, *10*, 857–864; c) D. Bhattacharya, S. Shil, A. Misra, D. Klein, *Theor. Chem. Acc.* **2010**, *127*, 57–67; d) D. Bhattacharya, S. Shil, A. Panda, A. Misra, *J. Phys. Chem. A* **2010**, *114*, 11833–11841.
- [28] M. J. Frisch, G. W. Trucks, H. B. Schlegel, G. E. Scuseria, M. A. Robb, J. R. Cheeseman, G. Scalmani, V. Barone, B. Mennucci, G. A. Petersson, H. Nakatsuji, M. Caricato, X. Li, H. P. Hratchian, A. F. Izmaylov, J. Bloino, G. Zheng, J. L. Sonnenberg, M. Hada, M. Ehara, K. Toyota, R. Fukuda, J. Hasegawa, M. Ishida, T. Nakajima, Y. Honda, O. Kitao, H. Nakai, T. Vreven, J. A. Montgomery, Jr., J. E. Peralta, F. Ogliaro, M. Bearpark, J. J. Heyd, E. Brothers, K. N. Kudin, V. N. Staroverov, R. Kobayashi, J. Normand, K. Raghavachari, A. Rendell, J. C. Burant, S. S. Iyengar, J. Tomasi, M. Cossi, N. Rega, J. M. Millam, M. Klene, J. E. Knox, J. B. Cross, V. Bakken, C. Adamo, J. Jaramillo, R. Gomperts, R. E. Stratmann, O. Yazyev, A. J. Austin, R. Cammi, C. Pomelli, J. W. Ochterski, R. L. Martin, K. Morokuma, V. G. Zakrzewski, G. A. Voth, P. Salvador, J. J. Dannenberg, S. Dapprich, A. D. Daniels, O. Farkas, J. B. Foresman, J. V. Ortiz, J. Cioslowski and D. J. Fox, *Gaussian 09, Revision A.1, Gaussian, Inc., Wallingford CT*, **2009**.
- [29] B. J. Tucker, EPR of powders, crystals, and clays of MRI contrast agents: zero field splitting and proton relaxation, University of Illinois at Urbana-Champaign, **2010**, p.
- [30] C. Duboc, D. Ganyushin, K. Sivalingam, M. N. Collomb, F. Neese, *J. Phys. Chem. A* **2010**, *114*, 10750–10758.
- [31] S. Zein, C. Duboc, W. Lubitz, F. Neese, *Inorg. Chem.* **2008**, *47*, 134–142.
- [32] O. Loboda, B. Minaev, O. Vahtras, B. Schimmelpfennig, H. Ågren, K. Ruud, D. Jonsson, *Chem. Phys.* **2003**, *286*, 127–137.
- [33] S. P. McGlynn, T. Azumi, M. Kinoshita, **1969**.
- [34] J. E. Harriman, *Theoretical Foundations of Electron Spin Resonance: Physical Chemistry: A Series of Monographs*, Academic press, **2013**, p.
- [35] R. McWeeny and Y. Mizuno, *Proceedings of the Royal Society of London A: Mathematical, Physical and Engineering Sciences* **1961**, pp. 554–577.
- [36] R. Boča, *Theoretical foundations of molecular magnetism*, Elsevier, **1999**, p.
- [37] M. Benmelouka, A. Borel, L. Moriggi, L. Helm, A. E. Merbach, *J. Phys. Chem. B* **2007**, *111*, 832–840.
- [38] H. Mahr, H. Rabin, C. Tang, *Quantum Electronics: A Treatise*, Elsevier, **1975**, *1*, 285–361.
- [39] a) M. Albota, D. Beljonne, J. L. Brédas, J. E. Ehrlich, J. Y. Fu, A. A. Heikal, S. E. Hess, T. Kogej, M. D. Levin, S. R. Marder, *Science* **1998**, *281*, 1653–1656; b) M. Rumi, J. E. Ehrlich, A. A. Heikal, J. W. Perry, S. Barlow, Z. Hu, D. McCord-Maughon, T. C. Parker, H. Röckel, S. Thayumanavan, *J. Am. Chem. Soc.* **2000**, *122*, 9500–9510; c) S. J. Pond, M. Rumi, M. D. Levin, T. C. Parker, D. Beljonne, M. W. Day, J. L. Brédas, S. R. Marder, J. W. Perry, *J. Phys. Chemistry A* **2002**, *106*, 11470–11480.
- [40] A. Garito, J. Hefflin, K. Yong, O. Zamani-Khamiri, *Nonlinear Optical Properties of Organic Materials*, Proc. SPIE, **1988**, *971*, 2–10.
- [41] a) B. Orr, J. Ward, *Mol. Phys.* **1971**, *20*, 513–526; b) T. Kogej, D. Beljonne, F. Meyers, J. Perry, S. Marde, J. Brédas, *Chem. Phys. Lett.* **1998**, *298*, 1–6.
- [42] F. Neese, *Density Functional and Semiempirical Program Package*, Version **2008**, 2.
- [43] E. Y. Misochko, D. V. Korchagin, K. V. Bozhenko, S. V. Chapyshev, S. M. Aldoshin, *J. Chem. Phys.* **2010**, *133*, 064101.
- [44] C. Angeli, K. Bak, V. Bakken, O. Christiansen, R. Cimraglia, S. Coriani, P. Dahle, E. Dalskov, T. Enevoldsen and B. Fernandez, *See http://www.kjemi.uio.no/software/dalton/dalton.html* **2005**.
- [45] a) D. Klein, C. Nelin, S. Alexander, F. Matsen, *J. Chem. Phys.* **1982**, *77*, 3101–3108; b) C. Trindle, S. Nath Datta, *Int. J. Quantum Chem.* **1996**, *57*, 781–799; c) C. Trindle, S. N. Datta, B. Mallik, *J. Am. Chem. Soc.* **1997**, *119*, 12947–12951.
- [46] a) M. Ochsner, *J. Photochem. Photobiol. B: Biology* **1996**, *32*, 3–9; b) J. Eichler, J. Knof, H. Lenz, *Radiat. Environ. Biophys.* **1977**, *14*, 239–242; c) S. Wan, J. A. Parrish, R. Anderson, M. Madden, *Photochem. Photobiol.* **1981**, *34*, 679–681; d) S. Stolik, J. Delgado, A. Perez, L. Anasagasti, *J. Photochem. Photobiol. B: Biology* **2000**, *57*, 90–93.
- [47] a) J. D. Bhawalkar, G. S. He, P. N. Prasad, *Rep. Prog. Phys.* **1996**, *59*, 1041; b) W. R. Zipfel, R. M. Williams, W. W. Webb, *Nat. Biotechnol.* **2003**, *21*, 1369–1377.
- [48] a) J. R. Starkey, A. K. Rebane, M. A. Drobizhev, F. Meng, A. Gong, A. Elliott, K. McInerney, C. W. Spangler, *Clin. Cancer Res.* **2008**, *14*, 6564–6573; b) A. Karotki, M. Khurana, J. R. Lepock, B. C. Wilson, *Photochem. Photobiol.* **2006**, *82*, 443–452; c) C. Xu, R. Williams, W. Zipfel and W. W. Webb, *Bioimaging* **1996**, *4*, 198–207.
- [49] P. Zhao, P. Chen, G. Tang, J. Liu, L. Lin, P. Guo, Q. Yu, J. Yao, D. Ma, G. Zhang, W. Chen, *Sci. China, Ser. B: Chem.* **2008**, *51*, 529.
- [50] K. Ishii, A. Takayanagi, S. Shimizu, H. Abe, K. Sogawa, N. Kobayashi, *Free Radical Biol. Med.* **2005**, *38*, 920–927.
- [51] B. Chen, B. W. Pogue, T. Hasan, *Expert Opin. Drug Delivery* **2005**, *2*, 477–487.
- [52] X. Liang, X. Li, L. Jing, X. Yue, Z. Dai, *Biomaterials* **2014**, *35*, 6379–6388.
- [53] H. S. Arakelyan, *OncoReview* **2014**, *4*, A171–A174.
- [54] G. Li, A. Slansky, M. P. Dobhal, L. N. Goswami, A. Graham, Y. Chen, P. Kanter, R. A. Alberico, J. Sperryak, J. Morgan, *Bioconjugate Chem.* **2005**, *16*, 32–42.

Submitted: October 25, 2017

Revised: January 7, 2018

Accepted: January 8, 2018



# Ligand-induced symmetry breaking and concomitant blueshift in the emission wavelength of an octahedral chromium complex

Manoj Majumder<sup>1</sup> · Satadal Paul<sup>1</sup> · Anirban Misra<sup>1</sup>

Received: 12 March 2018 / Accepted: 27 July 2018  
© Springer-Verlag GmbH Germany, part of Springer Nature 2018

## Abstract

The resulting distortion of the octahedral symmetry of the complex  $[\text{Cr}^{\text{III}}(\text{NH}_3)_6]^{3+}$  upon replacing the axial ligands with halides (i.e., weaker ligands) affects the stability of the doublet state with respect to that of the quartet ground state. This substitution affects the doublet-to-quartet transition responsible for phosphorescence. The position of the halide with respect to ammonia in the spectrochemical series is a major influence on the emission wavelength of the complex. The close proximity of fluorine and ammonia in the spectrochemical series leads to a blueshift in the emission wavelength when fluoride ions are introduced into the complex, thus providing a rational approach to the design of blue-phosphorescent materials, which are desirable for OLEDs used in full-color displays.

**Keywords** Blueshift · Quartet · Luminescence · OLED · TDDFT

## Introduction

Luminescent materials have attracted considerable interest [1–6] due to their multifarious applications in, for example, organic light-emitting diodes (OLEDs) [7–14] and light-emitting electrochemical cells (LEECs) [15–18], as light absorbers in dye-sensitized solar cells [19–22], and in chemosensors, biosensors [23–27], lumophores for cell imaging [27–30], and chemical photocatalysts [31–34]. The suitability of luminescent materials for a specific application depends upon the stability of the system, the color purity of the emitted light, the quantum yield of the emission, the specific emission decay time, and several other factors. In the last few decades, considerable effort has been directed into identifying highly efficient emitters of the three primary colors (red,

green, and blue), which are required in order to develop full-color displays. Although transition metal complexes that emit red and green light are abundant due to triplet harvesting [35–37], phosphorescent materials that emit blue light are relatively rare because a wide energy gap between the excited and the ground states is needed [38]. The strong spin–orbit coupling (SOC) that occurs in organometallic complexes containing heavy transition metals weakens the spin-forbiddenness of transitions between the ground and the excited states, so these systems partially fulfill the criteria of an ideal luminescent material [35, 39, 40]. However, the  $dd^*$  transitions that take place in heavy metals strongly quench the luminescence of blue-phosphorescent materials [39, 41–45]. Another difficulty with heavy metals is triplet–triplet annihilation, which hinders the process of phosphorescence, making the material unfit for OLED applications [46–49]. The best option for circumventing these difficulties with heavy metals is to use  $3d$  transition metal complexes. For example, a Cu(I) complex was recently found by Yersin et al. [50] to be a blue emitter ( $\lambda_{\text{max}} = 436$  nm), although its emission decay time was too long to allow its use in high-brightness OLED applications. Hamada et al. reported that some Zn(II) complexes are greenish-white emitters [51]. However, among  $3d$  transition metal complexes, Cr(III) systems have emerged as the most efficient luminescent materials due to their substantial quantum yields and their ability to both fluoresce and phosphoresce in liquid media at room temperature [52–54].

This paper belongs to Topical Collection International Conference on Systems and Processes in Physics, Chemistry and Biology (ICSPPCB-2018) in honor of Professor Pratim K. Chattaraj on his sixtieth birthday

**Electronic supplementary material** The online version of this article (<https://doi.org/10.1007/s00894-018-3768-7>) contains supplementary material, which is available to authorized users.

✉ Anirban Misra  
anirbanmisra@yahoo.com

<sup>1</sup> Department of Chemistry, University of North Bengal, Darjeeling, West Bengal 734013, India

While there are a reasonable number of experimental reports on the photoresponsive behavior of Cr(III) complexes, a comprehensive theoretical account of the phosphorescence of an octahedral ( $O_h$ ) Cr(III) complex is still awaited. All of these facts inspired us to theoretically investigate the luminescence properties of an octahedral Cr(III) complex.

In the first part of this paper, we introduce the hexa-amine Cr(III) system that we chose for this theoretical investigation. Subsequently, we provide the computational results for the absorption and emission wavelengths of this system, which are compared with corresponding experimental data in order to standardize the computational methodology. Octahedral Cr(III) complexes with weak ligands such as  $F^-$ ,  $Cl^-$ , and  $Br^-$  have been found to exhibit fluorescence, and those with strong ligands such as carbonyl, ammonia, and cyano have been observed to yield phosphorescence [52]. However, a literature survey reveals a dearth of blue-emitting Cr(III) complexes compared to those emitting red or green. The second part of the paper summarizes our attempts to utilize the data obtained in the first part in order to identify an appropriate set of ligands for inducing a blueshift in the emission wavelength. Phosphorescence of a  $O_h$  Cr(III) complex involves excitation from the quartet ground state (Q) to the quartet excited state (Q') followed by intersystem crossing (ISC) to the doublet state (D). The phosphorescence energy thus depends on the separation between the lowest doublet state (D) and the quartet ground state (Q), which is nearly equal to the absorption energy due to the  $Q \rightarrow D$  transition [52]. Hence, in principle, excitation to the doublet state from the quartet ground state can lead to a blueshift in the emission wavelength. The doublet state can be attained for the  $O_h$  Cr(III) complex by lifting the degeneracy of the  $t_{2g}$  orbitals. To do this, the symmetry of the  $O_h$   $[Cr^{III}(NH_3)_6]^{3+}$  complex is disturbed by replacing the axial ammonia ligands with weak halides ( $I^-$ ,  $Br^-$ ,  $Cl^-$ , and  $F^-$ ). Thus, the doublet state can be induced by introducing asymmetry into the complex by substituting the axial ligands of  $[Cr^{III}(NH_3)_6]^{3+}$ . A trend in the change in the emission wavelength depending on the halogens included in the complex was observed. This study may therefore provide a useful guideline for the rational design of metal complexes with tailored luminescence behavior such as blue phosphorescence.

## Computational methods

The B3PW91 functional was employed to optimize the geometries of the studied complexes in their ground states. This functional, based on generalized gradient approximations (GGAs), mixes some exact exchange with the trial DFT exchange–correlation functional, and works well for transition metals [55]. It has been successfully employed to study photophysical properties [56, 57]. However, to check how well other functionals perform, we also carried out the same

set of calculations with the most popular GGA functional PBE and the meta-GGA functional TPSS. Since the hybrid GGA functional is higher than the pure GGA functional on the Jacob's ladder of Perdew due to its ability to partially minimize the self-interaction energy, we present the results obtained using B3PW91 in the main text of this paper, while the PBE and TPSS results are given in the “[Electronic supplementary material](#)” (ESM). Hay and Wadt's double-zeta effective core potential (LANL2DZ) was chosen for use as the basis set in all of the computations [58, 59]. Since the phosphorescence of the systems under investigation involves quartet and doublet spin states, an unrestricted formalism was adopted in the density functional theory (DFT) calculations. The absorption and emission energies of the reference systems were obtained using a time-dependent DFT (TDDFT) method coupled with the same exchange–correlation functional and basis set applied for geometry optimization of the ground quartet (Q) and doublet (D) states. The TDDFT approach offers a reliable route for the calculation of vertical electronic excitation spectra [60, 61], as demonstrated by the good agreement of experimental spectral properties with TDDFT results obtained for transition-metal complexes [62–64]. However, the solvent also plays an important role in determining excitation values. We calculated the energy values for different energy states (quartet, doublet, excited quartet) of the  $[Cr^{III}(NH_3)_6]^{3+}$  complex and found that these states are only slightly more stable than expected from gas-phase calculations. Hence, in order to reduce computational effort, we performed gas-phase calculations in this work. That said, to get an accurate description of the quartet excited state (Q') of each reference system, we resorted to a more sophisticated complete active space self-consistent field (CASSCF) method with an active space of (3, 5) and the LANL2DZ basis set. Using the initial guess obtained from the state-average calculation, the final geometry of the quartet excited state was then determined. Next, a single-point calculation was performed at the same DFT level for this optimized geometry of the excited-state molecule for comparison with the ground-state condition obtained at the DFT level. In each case, vibrational analysis was performed at the same level of DFT to check the structural stability of the system. All computations were done with the Gaussian 09W quantum chemical software package [65].

## Results and discussion

The structural parameters and energies of the optimized geometries of  $[Cr^{III}(NH_3)_6]^{3+}$  in its quartet ground state (Q), quartet excited state (Q'), and lowest-energy doublet state (D) are given in Table 1. In the quartet ground state, all of the Cr–NH<sub>3</sub> bond lengths were found to be equal, indicating that the system has  $O_h$  symmetry. Molecular orbital (MO) analysis in the quartet ground state revealed that the main

**Table 1** Bond distances between Cr and the axial ligands (Cr–L<sub>ax</sub>) and between Cr and the equatorial ligands (Cr–L<sub>eq</sub>), and the energies of the [Cr<sup>III</sup>(NH<sub>3</sub>)<sub>6</sub>]<sup>3+</sup> complex in the quartet ground state (Q), quartet excited state (Q'), and doublet ground state (D)

	States	Cr–L <sub>ax</sub> (Å)	Cr–L <sub>eq</sub> (Å)	Relative energy (kcal/mol)
	Q	2.16	2.16	0
Q'	2.11	2.29	9.41	
D	2.13	2.13	28.2	

contributors to the highest occupied molecular orbital (HOMO) and the next two orbitals (HOMO – 1 and HOMO – 2) are the Cr *d* orbitals (*d*<sub>xz</sub>, *d*<sub>yz</sub>, and *d*<sub>xy</sub>). On the other hand, the main contributors to the lowest unoccupied molecular orbital (LUMO) and the LUMO + 1 orbitals are the Cr *d*<sub>z<sup>2</sup> and *d*<sub>x<sup>2</sup>–y<sup>2</sup> orbitals (Fig. 1). Thus, in the octahedral field, we can confirm that the Cr MOs in this [Cr<sup>III</sup>(NH<sub>3</sub>)<sub>6</sub>]<sup>3+</sup> complex split into *t*<sub>2g</sub> and *e*<sub>g</sub> orbitals (Fig. 1).</sub></sub>

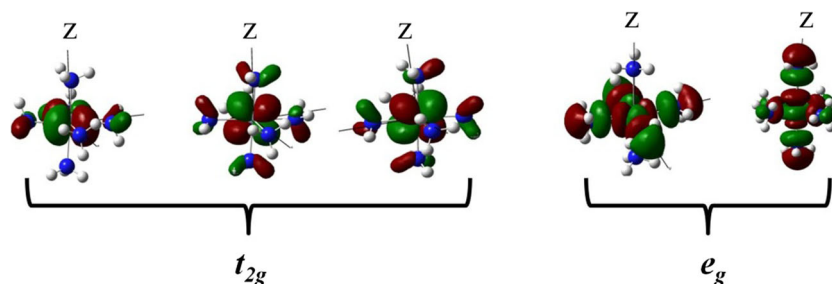
According to an analysis of the TDDFT computations carried out for the quartet ground state of [Cr<sup>III</sup>(NH<sub>3</sub>)<sub>6</sub>]<sup>3+</sup>, the main excitations occur at 420 nm (Table 2), which is quite close to the experimental value of the absorption wavelength for this complex (Table 2) [52]. The main contribution to this absorption energy comes from electronic excitation from the occupied 37th spin-up orbital ( $\alpha$ -HOMO) to the initially unoccupied 38th  $\alpha$ -LUMO (Table S1a in the ESM). Thus, the quartet excited state (Q') acquires the electronic configuration *t*<sub>2g</sub><sup>2</sup> *e*<sub>g</sub><sup>1</sup> due to spin-reserved electron excitation from the *t*<sub>2g</sub> to the *e*<sub>g</sub> level. The electronic configuration *t*<sub>2g</sub><sup>2</sup> *e*<sub>g</sub><sup>1</sup> in the excited quartet state is supported by an elongation in the distance between Cr and each equatorial ligand compared to the corresponding distance in the quartet ground state (Q) (Table 1). In the quartet excited state, the 38th  $\alpha$ -MO, which is primarily composed of the Cr *d*<sub>x<sup>2</sup>–y<sup>2</sup> orbital, becomes populated through electronic excitation, and this occupation of the Cr *d*<sub>x<sup>2</sup>–y<sup>2</sup> orbital leads to elongation in the equatorial (*xy*) plane. On the contrary, the axial Cr–NH<sub>3</sub> distance remains almost unaltered in the quartet ground and excited states of the molecule (Table 1). Unlike the quartet excited state, the geometry in the doublet state is barely distorted compared to the quartet ground state (Table 1). In the doublet state, the electron distribution within the *d*<sub>xy</sub>, *d*<sub>yz</sub>, and *d*<sub>zx</sub> orbitals alters, but these orbitals are not directly oriented towards the ligands, so structural changes</sub></sub>

in the doublet state are nominal with respect to the quartet ground state (Table 1).

Then, to explore the mechanism for the intersystem crossing between the quartet excited state (Q') and the doublet state (D), the vibrational modes of both states were closely examined. After a thorough analysis of the vibrational modes, the 20th mode of Q' (vibrational energy = 379 cm<sup>-1</sup>) and the 16th mode of D (vibrational energy = 318 cm<sup>-1</sup>) were found to have oscillation vectors in the same direction (Fig. 2). The similar energies and oscillation patterns of these two vibrational modes suggest that the doublet and the quartet excited states may interconvert through these vibrations, as shown in Fig. 2. From the TDDFT computations for the lowest-energy doublet state, the emission wavelength for the D → Q transition was obtained as 877 nm, which is comparable to the experimental value for phosphorescence (Table 2) [52]. After standardizing the computational framework for estimating absorption and emission wavelengths, we shifted to the second part of this work, which was carried out using the same computational methodology as employed in the first part.

As outlined in the “Introduction,” the axial ammonia ligands in [Cr<sup>III</sup>(NH<sub>3</sub>)<sub>6</sub>]<sup>3+</sup> were substituted by (weaker) halogen ligands to disrupt the *O<sub>h</sub>* symmetry of the complex. This was expected to lift the degeneracy of the singly occupied *t*<sub>2g</sub> orbitals, as shown in Fig. 3, and to induce the doublet state when the axial and equatorial ligands differed sufficiently in strength based on their positions in the spectrochemical series. Table 3 displays the structural parameters of the optimized geometries and the energies of all the halogen-substituted octahedral Cr(III) complexes.

In the quartet ground state (Q), the diiodo-, dibromo-, and dichloro-substituted complexes were found to be less stable than [Cr<sup>III</sup>(NH<sub>3</sub>)<sub>6</sub>]<sup>3+</sup>, whereas the difluoro complex was more

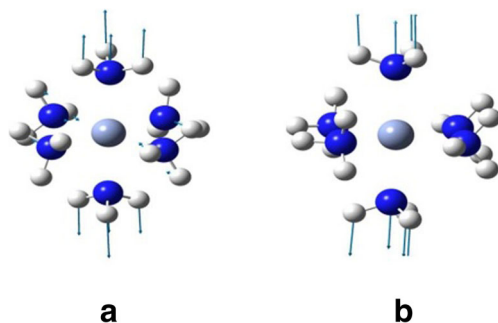
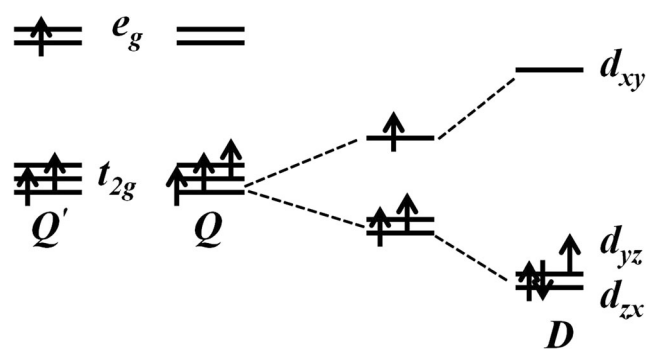
**Fig. 1** *t*<sub>2g</sub> and *e*<sub>g</sub> orbitals in [Cr<sup>III</sup>(NH<sub>3</sub>)<sub>6</sub>]<sup>3+</sup>

**Table 2** Comparison of the computed absorption and emission wavelengths in nm (energies in  $\text{cm}^{-1}$ ) with experimental values for  $[\text{Cr}^{\text{III}}(\text{NH}_3)_6]^{3+}$ 

	Computed value	Experimental value [52]
Absorption ( $Q \rightarrow Q'$ )	420 nm ( $23,804 \text{ cm}^{-1}$ )	$21,550 \text{ cm}^{-1}$
Emission ( $D \rightarrow Q$ )	877 nm ( $11,403 \text{ cm}^{-1}$ )	$15,120 \text{ cm}^{-1}$

stable (Tables 1 and 3). The distance between the metal and each apical ligand ( $\text{Cr-L}_{\text{ax}}$ ) provides the explanation for this observation. For the first three substituted complexes, the  $\text{Cr-L}_{\text{ax}}$  distance was larger than that in  $[\text{Cr}^{\text{III}}(\text{NH}_3)_6]^{3+}$ , whereas for  $[\text{Cr}^{\text{III}}(\text{NH}_3)_4\text{F}_2]^+$ , the  $\text{Cr-L}_{\text{ax}}$  distance was much shorter than that in  $[\text{Cr}^{\text{III}}(\text{NH}_3)_6]^{3+}$  (Tables 1 and 3). Hence, in the present case, the bonding between the Cr and the axial ligands contributes significantly to the stability of the halogen-substituted complexes. In the quartet excited states ( $Q'$ ) of all the halogen-substituted complexes, the bond distances in the equatorial ( $xy$ ) plane were found to be stretched compared to those in the quartet ground state ( $Q$ ), with little variation observed in the  $\text{Cr-L}_{\text{a}}$  distance. The bond stretching that occurs in the  $xy$  plane of the  $Q'$  states compared to the  $Q$  states of these complexes can be attributed to electronic excitation in the  $d_{x^2-y^2}$  orbital, similar to the case for  $[\text{Cr}^{\text{III}}(\text{NH}_3)_6]^{3+}$ . To explore the stabilities of the complexes, we calculated the hardness of the quartet ground state for each complex, and the results are given in Table 4.

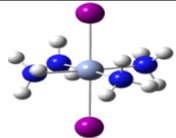
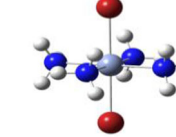
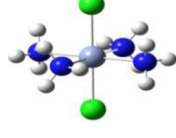
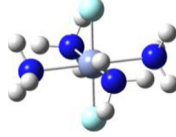
From Table 4, we can conclude that  $[\text{Cr}^{\text{III}}(\text{NH}_3)_4(\text{F})_2]^+$  is the most stable of the halide-substituted systems, as the largest hardness value implies the greatest stability [66]. Based on the TDDFT computations of the quartet ground states of the halogen-substituted complexes, the lowest transition was found to occur from the  $\alpha$ -occupied HOMO (the 35th  $\alpha$ -MO for the diiodo-, dibromo-, and dichloro-substituted complexes and the 37th  $\alpha$ -MO for the difluoro-substituted complex) to the initially unoccupied LUMO (the 36th  $\alpha$ -MO for the diiodo-, dibromo-, and dichloro-substituted complexes and the 38th  $\alpha$ -MO for the difluoro-substituted complex), as

**Fig. 2a–b** Oscillation vectors for **a** the 16th vibrational mode in the D state and **b** the 20th vibrational mode in the  $Q'$  state of  $[\text{Cr}^{\text{III}}(\text{NH}_3)_6]^{3+}$ **Fig. 3** Orbital splitting patterns in the quartet ground state ( $Q$ ), the quartet excited state ( $Q'$ ), and the doublet state ( $D$ ) of  $[\text{Cr}^{\text{III}}(\text{NH}_3)_6]^{3+}$ 

indicated by Table S1 and Fig. S1 of the ESM. The absorption wavelengths of all the halogen-substituted complexes are given in Table 5. Also, for these complexes, HOMO to HOMO – 2 and LUMO to LUMO + 1 belong to the  $t_{2g}$  and  $e_g$  orbitals, as also seen for  $[\text{Cr}^{\text{III}}(\text{NH}_3)_6]^{3+}$  (Fig. S1a–h in the ESM). In all of the halogen-substituted complexes, there is a high possibility of intersystem crossing between the quartet excited state and the doublet state, as verified by the similar vibrational modes and energies of these two spin states (Table S2 in the ESM).

According to TDDFT computations for the doublet state, the ligands control the emission frequency of each halogen-substituted complex. From an application perspective, the most interesting observation is the trend in the variation of the emission wavelength with the halogen ligands included in the complex, which can be explained by the different positions of the different halogens in the spectrochemical series.  $\text{I}^-$  and  $\text{Br}^-$  are weak ligands, in contrast to ammonia, which is a strong ligand. When weak ligands are placed along the  $z$ -axis, the  $d_{xz}$  and  $d_{yz}$  orbitals become more stable than the  $d_{xy}$  orbital, so the threefold degeneracy of the  $t_{2g}$  level is lifted (Fig. 3). This splitting of the  $t_{2g}$  level stabilizes the doublet state compared to the quartet ground state, resulting in a decrease in the emission energy, as confirmed by Table 4. Hence, replacing the axial ligands in  $[\text{Cr}^{\text{III}}(\text{NH}_3)_6]^{3+}$  with weak  $\text{I}^-$  or  $\text{Br}^-$  ligands causes a redshift in the emission wavelength. It is also interesting to note that the almost equal emission wavelengths of the diiodo and dibromo complexes correlate with the similar positions of  $\text{I}^-$  and  $\text{Br}^-$  in the spectrochemical series. On the other hand, a blueshift in the emission wavelength is observed for the difluoro compound with respect to the  $O_h$   $[\text{Cr}^{\text{III}}(\text{NH}_3)_6]^{3+}$  complex. This can again be explained by the relative strengths of the axial and equatorial ligands. Among the halogens,  $\text{F}^-$  is closest to ammonia in the spectrochemical series, meaning that  $\text{F}^-$  substitution of the axial ligands leads to a less asymmetric  $t_{2g}$  than if  $\text{I}^-$  or  $\text{Br}^-$  ligands are inserted into the complex. This in turn implies that the doublet state becomes less favored,

**Table 3** Distances between Cr and each axial ligand (Cr-L<sub>ax</sub>), and between Cr and each equatorial ligand (Cr-L<sub>eq</sub>), and energies of the complexes [Cr<sup>III</sup>(NH<sub>3</sub>)<sub>4</sub>(X)<sub>2</sub>]<sup>+</sup> (X = I<sup>-</sup>, Br<sup>-</sup>, Cl<sup>-</sup>, or F<sup>-</sup>, shown in violet, brown, green, and light blue, respectively)

Systems	Electronic States	Cr-L <sub>ax</sub> (Å)	Cr-L <sub>eq</sub> (Å)	Relative energy (Kcal/mol)
 [Cr <sup>III</sup> (NH <sub>3</sub> ) <sub>4</sub> (I) <sub>2</sub> ] <sup>+</sup>	<i>Q</i>	2.71	2.12	0
	<i>Q'</i>	2.76	2.28	18.2
	<i>D</i>	2.69	2.11	27.6
 [Cr <sup>III</sup> (NH <sub>3</sub> ) <sub>4</sub> (Br) <sub>2</sub> ] <sup>+</sup>	<i>Q</i>	2.51	2.11	0
	<i>Q'</i>	2.56	2.32	10.04
	<i>D</i>	2.46	2.13	11.3
 [Cr <sup>III</sup> (NH <sub>3</sub> ) <sub>4</sub> (Cl) <sub>2</sub> ] <sup>+</sup>	<i>Q</i>	2.32	2.10	0
	<i>Q'</i>	2.37	2.34	11.4
	<i>D</i>	2.28	2.12	26.35
 [Cr <sup>III</sup> (NH <sub>3</sub> ) <sub>4</sub> (F) <sub>2</sub> ] <sup>+</sup>	<i>Q</i>	1.85	2.11	0
	<i>Q'</i>	1.83	2.27	10.7
	<i>D</i>	1.80	2.12	38.9

increasing the energy gap between the doublet state and the quartet ground state, which is reflected in an increased emission frequency. In line with this explanation, in the dichloro-substituted complex, the emission wavelength is between those of [Cr<sup>III</sup>(NH<sub>3</sub>)<sub>4</sub>F<sub>2</sub>]<sup>+</sup> and [Cr<sup>III</sup>(NH<sub>3</sub>)<sub>4</sub>I<sub>2</sub>]<sup>+</sup> or [Cr<sup>III</sup>(NH<sub>3</sub>)<sub>4</sub>Br<sub>2</sub>]<sup>+</sup>. This trend again correlates well with the position of chloride (i.e., between F<sup>-</sup> and I<sup>-</sup>, Br<sup>-</sup>) in the spectrochemical series. In order to explore the variation in the emission wavelength

caused by replacing the axial ligands with ligands other than halides, we also inserted OH<sup>-</sup> and CN<sup>-</sup> ligands. The former ligand is close to F<sup>-</sup> and the latter is quite far from F<sup>-</sup> in the spectrochemical series. The complex containing the stronger ligand, CN<sup>-</sup>, exhibited emission in virtually the same region (676 nm) as [Cr<sup>III</sup>(NH<sub>3</sub>)<sub>6</sub>]<sup>3+</sup>, whereas the complex containing OH<sup>-</sup> showed redshifted emission (1823 nm).

**Table 4** Calculated hardness values (in eV) for the studied complexes (quartet ground state)

System	Hardness (eV)
[Cr <sup>III</sup> (NH <sub>3</sub> ) <sub>6</sub> ] <sup>3+</sup>	3.34
[Cr <sup>III</sup> (NH <sub>3</sub> ) <sub>4</sub> (F) <sub>2</sub> ] <sup>+</sup>	2.37
[Cr <sup>III</sup> (NH <sub>3</sub> ) <sub>4</sub> (Cl) <sub>2</sub> ] <sup>+</sup>	2.2
[Cr <sup>III</sup> (NH <sub>3</sub> ) <sub>4</sub> (Br) <sub>2</sub> ] <sup>+</sup>	2.18
[Cr <sup>III</sup> (NH <sub>3</sub> ) <sub>4</sub> (I) <sub>2</sub> ] <sup>+</sup>	1.15

**Table 5** Comparison of the absorption and emission wavelengths in nm (energies in cm<sup>-1</sup>) of the complexes [Cr<sup>III</sup>(NH<sub>3</sub>)<sub>4</sub>(X)<sub>2</sub>]<sup>+</sup> (X = I<sup>-</sup>, Br<sup>-</sup>, Cl<sup>-</sup>, or F<sup>-</sup>)

Complex	Absorption (Q → Q')	Emission (D → Q)
[Cr <sup>III</sup> (NH <sub>3</sub> ) <sub>4</sub> I <sub>2</sub> ] <sup>+</sup>	618.4 (16171)	1280.7 (7808)
[Cr <sup>III</sup> (NH <sub>3</sub> ) <sub>4</sub> Br <sub>2</sub> ] <sup>+</sup>	554.9 (18021)	1416.4 (7060)
[Cr <sup>III</sup> (NH <sub>3</sub> ) <sub>4</sub> Cl <sub>2</sub> ] <sup>+</sup>	502.2 (19912)	968 (10331)
[Cr <sup>III</sup> (NH <sub>3</sub> ) <sub>4</sub> F <sub>2</sub> ] <sup>+</sup>	555.4 (18004)	453.8 (22036)

## Conclusions

In the present work, the photophysical properties of an  $O_h$  Cr(III) complex was studied in the framework of density functional theory. In the first part of this study, the absorption and emission wavelengths for this complex were obtained using TDDFT, and were found to correspond well with the known phosphorescent behavior of the complex. In the second part of the study, the axial ligands in the  $O_h$   $[\text{Cr}^{\text{III}}(\text{NH}_3)_6]^{3+}$  complex were replaced with weaker ligands in order to disrupt the  $O_h$  symmetry of the complex. The presence of weaker ligands along the  $z$ -axis was expected to stabilize the  $d_{xz}$  and  $d_{yz}$  orbitals compared to the  $d_{xy}$  orbital and thus lift the degeneracy of the  $t_{2g}$  orbitals. The resulting distorted tetragonal structure undergoes electron redistribution, leading to the doublet state, as illustrated in Fig. 3. Since ensuring that the axial and equatorial ligands differ significantly in strength is the key to splitting the degenerate  $t_{2g}$  orbitals, we investigated the effects of replacing the axial ligands of  $O_h$   $[\text{Cr}^{\text{III}}(\text{NH}_3)_6]^{3+}$  with  $\Gamma^-$ ,  $\text{Br}^-$ ,  $\text{Cl}^-$ , or  $\text{F}^-$ , which occur at quite different positions in the spectrochemical series with respect to  $\text{NH}_3$ . The propensity for the doublet state is high for the diiodo and dibromo complexes due to the large difference in strength between the  $\Gamma^-$  or  $\text{Br}^-$  ligand and  $\text{NH}_3$ . On the contrary,  $\text{F}^-$  and  $\text{NH}_3$  are close together in the spectrochemical series, so the doublet state cannot easily be achieved in the difluoro complex due to the almost equivalent strengths of the axial and equatorial ligands. This dependence of the likelihood of the doublet state on the difference in the strengths of the axial and equatorial ligands is supported by the relatively low emission energies of the diiodo and dibromo complexes and the high phosphorescence energy of the difluoro-substituted complex. The position of  $\text{Cl}^-$  (between  $\text{F}^-$  and  $\Gamma^-$ ,  $\text{Br}^-$ ) in the spectrochemical series correlates well with the emission frequency of the dichloro-substituted complex, which is also between the emission frequencies of the difluoro-substituted complex and those of the diiodo- and dibromo-substituted complexes. Thus, we can see that the emission frequency of the phosphorescence of the complex can be tuned by appropriately selecting the axial ligands of the complex, based on the difference in strength between those ligands and the equatorial  $\text{NH}_3$  ligands. The most important finding of the present work is the blueshift in the emission wavelength of  $[\text{Cr}^{\text{III}}(\text{NH}_3)_4\text{F}_2]^+$  as compared to the original  $O_h$   $[\text{Cr}^{\text{III}}(\text{NH}_3)_6]^{3+}$  complex. This blueshift in the emission wavelength to 454 nm may offer useful insights for the rational design of hitherto rare blue-emitting first-row transition metal complexes, which are desirable for OLED applications.

**Acknowledgements** The Department of Science and Technology, India is gratefully acknowledged for its financial assistance. This work is dedicated to Professor P. K. Chattaraj on the occasion of his 60th birthday.

## References

- Bergman SD, Kol M, Gut D, Sabatini C, Barbieri A, Barigelletti F (2005) Eilatin complexes of ruthenium and osmium. Synthesis, electrochemical behavior, and near-IR luminescence. *Inorg Chem* 44:7943–7950
- Draper SM, Gregg DJ, Schofield ER, Browne WR, Duati M, Vos JG, Passaniti P (2004) Complexed nitrogen heterosuperbenzene: the coordinating properties of a remarkable ligand. *J Am Chem Soc* 126:8694–8870
- Wilson MH, Ledwaba PL, Field JS, McMillin DR (2005) Push-pull effects and emission from ternary complexes of platinum(II), substituted terpyridines, and the strong-field cyanide ion. *Dalton Trans* 16:2754–2759
- Siu PKM, Ma DL, Che CM (2005) Luminescent cyclometalated platinum(II) complexes with amino acid ligands for protein binding. *Chem Commun* 8:1025–1027
- Ionkin AS, Marshall WJ, Wang Y (2005) Syntheses, structural characterization, and first electroluminescent properties of monocyclusmetalated platinum(II) complexes with greater than classical  $\pi$ - $\pi$  stacking and Pt–Pt distances. *Organometallics* 24:619–627
- Baldo MA, O'Brien DF, You Y, Shoustikov A, Sibley S (1998) Highly efficient phosphorescent emission from organic electroluminescent devices. *Nature* 395:151–154
- Yersin H (2008) Highly efficient OLEDs with phosphorescent materials. Wiley–VCH, Weinheim
- Kafafi ZH (2005) Organic electroluminescence. CRC, Boca Raton
- Shinar J, Savvateev V (2004) Introduction to organic light-emitting devices. In: Shinar J (ed) Organic light-emitting devices. Springer, Heidelberg, pp 1–4
- Chou PT, Chi Y (2007) Phosphorescent dyes for organic light-emitting diodes. *Chem Eur J* 13:380–395
- Borek C, Hanson K, Djurovich PL, Thompson ME, Aznavour K, Bau R, Sun Y, Forrest SR, Brooks J, Michalski L, Brown J (2007) Highly efficient, near-infrared electrophosphorescence from a Pt–metalloporphyrin complex. *Angew Chem Int Ed* 46:1109–1112
- Evans RC, Douglas PC, Winscom J (2006) Coordination complexes exhibiting room-temperature phosphorescence: evaluation of their suitability as triplet emitters in organic light emitting diodes. *Coord Chem Rev* 250:2093–2126
- Williams JAG, Develay S, Rochester DL, Murphy L (2008) Optimising the luminescence of platinum(II) complexes and their application in organic light emitting devices (OLEDs). *Coord Chem Rev* 252:2596–2611
- Xiao L, Chen Z, Qu B, Luo J, Kong S, Gong Q, Kido J (2011) Recent progresses on materials for electrophosphorescent organic light-emitting devices. *Adv Mater* 23:926–952
- Su HC, Chen HF, Fang FC, Liu CC, Wu CC, Wong KT, Liu YH, Peng SM (2008) Solid-state white light-emitting electrochemical cells using iridium-based cationic transition metal complexes. *J Am Chem Soc* 130:3413–3419
- Bolink HJ, Coronado E, Costa RD, Lardies N, Orti E (2008) Near-quantitative internal quantum efficiency in a light-emitting electrochemical cell. *Inorg Chem* 47:9149–9151
- Slinker J, Bernards D, Houston PL, Abruña HD, Bernhard S, Malliaras GG (2003) Solid-state electroluminescent devices based on transition metal complexes. *Chem Commun* 2392–2399
- Kapturkiewicz A (2010) Electrochemiluminescent systems as devices and sensors. In: Ceroni P, Credi A, Venturi M (eds)

- Electrochemistry of functional supramolecular systems. Wiley, Hoboken, p 477
19. Polo ASP, Itokazu MK, Iha NYM (2004) Metal complex sensitizers in dye-sensitized solar cells. *Coord Chem Rev* 248:1343–1361
  20. Robertson N (2006) Optimizing dyes for dye-sensitized solar cells. *Angew Chem Int Ed* 45:2338–2345
  21. Wong WY, Wang XZ, He Z, Djurišić AB, Yip CT, Cheung KY, Wang H, CSK M, Chan WK (2007) Metallated conjugated polymers as a new avenue towards high-efficiency polymer solar cells. *Nat Mater* 6:521–527
  22. Gratzel M (2005) Solar energy conversion by dye-sensitized photovoltaic cells. *Inorg Chem* 44:6841–6851
  23. Lo KKW, Louie MW, Zhang KY (2010) Design of luminescent iridium(III) and rhenium(I) polypyridine complexes as in vitro and in vivo ion, molecular and biological probes. *Coord Chem Rev* 254:2603–2622
  24. O'Neil EJ, Smith BD (2006) Anion recognition using dimetallic coordination complexes. *Coord Chem Rev* 250:3068–3080
  25. Keefe MH, Benkstein KD, Hupp JT (2000) Luminescent sensor molecules based on coordinated metals: a review of recent developments. *Coord Chem Rev* 205:201–228
  26. Zhao Q, Li F, Huang C (2010) Phosphorescent chemosensors based on heavy-metal complexes. *Chem Soc Rev* 39:3007–3030
  27. Fernandez-Moreira V, Thorp-Greenwood FL, Coogan MP (2010) Application of  $d^6$  transition metal complexes in fluorescence cell imaging. *Chem Commun* 46:186–202
  28. Botchway SW, Charnley M, Haycock JW, Parker AW, Rochester DL, Weinstein JA, Williams JAG (2008) Time-resolved and two-photon emission imaging microscopy of live cells with inert platinum complexes. *Proc Natl Acad Sci USA* 105:16071
  29. Stephenson KA, Banerjee SR, Besanger T, Sogbein OO, Levadala MK, McFarlane N, Lemon JA, Boreham DR, Maresca KP, Brennan JD, Babich JW, Zubieta J, Valliant JF (2004) Bridging the gap between in vitro and in vivo imaging: isostructural Re and  $^{99m}\text{Tc}$  complexes for correlating fluorescence and radioimaging studies. *J Am Chem Soc* 126:8598–8599
  30. Yu M, Zhao Q, Shi L, Li F, Zhou Z, Yang H, Yi T, Huang C (2008) Cationic iridium(III) complexes for phosphorescence staining in the cytoplasm of living cells. *Chem Commun* 2115–2117
  31. Kalyanasundaram K (1982) Photophysics, photochemistry and solar energy conversion with tris(bipyridyl)ruthenium(II) and its analogues. *Coord Chem Rev* 46:159–244
  32. Zeitler K (2009) Photoredox catalysis with visible light. *Angew Chem Int Ed* 48:9785–9789
  33. Hoffmann N (2008) Photochemical reactions as key steps in organic synthesis. *Chem Rev* 108:1052–1103
  34. Losse S, Vos JG, Rau S (2010) Catalytic hydrogen production at cobalt centres. *Coord Chem Rev* 254:2492–2504
  35. Hofbeck T, Yersin H (2010) The triplet state of fac-Ir(ppy)<sub>3</sub>. *Inorg Chem* 49:9290–9299
  36. Baldo MA, Forrest SR (2000) Transient analysis of organic electrophosphorescence: I. Transient analysis of triplet energy transfer. *Phys Rev B* 62:10958
  37. Baldo MA, Lamansky S, Burrows PE, Thompson ME, Forrest SR (1999) Very high-efficiency green organic light-emitting devices based on electrophosphorescence. *Appl Phys Lett* 75:4–6
  38. Stufkens DJ, Vleck A (1998) Ligand-dependent excited state behaviour of Re(I) and Ru(II) carbonyl–diimine complexes. *Coord Chem Rev* 177:127–179
  39. Sajoto T, Djurovich PI, Tamayo AB, Oxgaard J, Goddard III WA, Thompson ME (2009) Temperature dependence of blue phosphorescent cyclometalated Ir(III) complexes. *J Am Chem Soc* 131:9813–9822
  40. Goushi K, Kawamura Y, Sasabe H, Adachi C (2004) Unusual phosphorescence characteristics of Ir(ppy)<sub>3</sub> in a solid matrix at low temperatures. *Jpn J Appl Phys* 43:L937
  41. Islam A, Ikeda N, Nozaki K, Okamoto Y, Gholamkhash B, Yoshimura A, Ohno T (1998) Non-radiative processes of excited CT states of Ru(II) and Pt(II) compounds and excited d-d states of Rh(III) compounds in the solid state and at higher temperatures. *Coord Chem Rev* 171:355–363
  42. Barigelletti F, Sandrini D, Maestri M, Balzani V, von Zelewsky A, Chassot L, Jolliet P, Maeder U (1988) Temperature dependence of the luminescence of cyclometalated palladium(II), rhodium(III), platinum(II), and platinum(IV) complexes. *Inorg Chem* 27:3644–3647
  43. Meyer TJ (1986) Photochemistry of metal coordination complexes: metal to ligand charge transfer excited states. *Pure Appl Chem* 58:1193–1206
  44. van Houten J, Watts RJ (1978) Photochemistry of tris(2,2'-bipyridyl)ruthenium(II) in aqueous solutions. *Inorg Chem* 17:3381–3385
  45. Caspar JV, Meyer TJ (1983) Photochemistry of tris(2,2'-bipyridine)ruthenium(II) ion (Ru(bpy)<sub>3</sub><sup>2+</sup>). Solvent effects. *J Am Chem Soc* 105:5583–5590
  46. Reineke S, Walzer K, Leo K (2007) Triplet-exciton quenching in organic phosphorescent light-emitting diodes with Ir-based emitters. *Phys Rev B* 75:125328
  47. Giebink NC, Forrest SR (2008) Quantum efficiency roll-off at high brightness in fluorescent and phosphorescent organic light emitting diodes. *Phys Rev B* 77:235215
  48. Reineke S, Schwartz G, Walzer K, Leo K (2007) Reduced efficiency roll-off in phosphorescent organic light emitting diodes by suppression of triplet–triplet annihilation. *Appl Phys Lett* 91:123508
  49. Baldo MA, Adachi C, Forrest SR (2000) Transient analysis of organic electrophosphorescence. II. Transient analysis of triplet–triplet annihilation. *Phys Rev B* 62:10967
  50. Czerwieniec R, Yu J, Yersin H (2011) Blue-light emission of Cu(I) complexes and singlet harvesting. *Inorg Chem* 50:8293–8301
  51. Hamada Y, Sano T, Fujii H, Nishio Y, Takahashi H, Shibata K (1996) White-light-emitting material for organic electroluminescent devices. *Jpn J Appl Phys* 35:L1339
  52. Schlafer HL, Gausmann H, Witzke H (1967) Correlation between the luminescence behavior of octahedral chromium(III) complexes and the ligand-field strength. *J Chem Phys* 46:1423
  53. DeRosa F, Bu X, Pohaku K, Ford PC (2005) Synthesis and luminescence properties of Cr(III) complexes with cyclam-type ligands having pendant chromophores, *trans*-[Cr(L)Cl<sub>2</sub>]Cl. *Inorg Chem* 44:4166–4174
  54. Kirk AD, Porter GB (1980) Luminescence of chromium(III) complexes. *J Phys Chem* 84:887–891
  55. Perdew JP, Ziesche P, Eschrig H (1991) Electronic structure of solids. Akademie, Berlin, p 11
  56. Barakat KA, Cundari TR, Omary MA (2003) Jahn–Teller distortion in the phosphorescent excited state of three-coordinate Au(I) phosphine complexes. *J Am Chem Soc* 125:14228–14229
  57. Nozaki K (2006) Theoretical studies on photophysical properties and mechanism of phosphorescence in [fac-Ir(2-phenylpyridine)<sub>3</sub>]. *J Chin Chem Soc* 53:101–112
  58. Hay PJ, Wadt WR (1985) Ab initio effective core potentials for molecular calculations. Potentials for the transition metal atoms Sc to Hg. *J Chem Phys* 82:270
  59. Wadt WR, Hay PJ (1985) Ab initio effective core potentials for molecular calculations. Potentials for main group elements Na to Bi. *J Chem Phys* 82:284
  60. Casida MK, Jamorski C, Casida KC, Salahub DR (1998) Molecular excitation energies to high-lying bound states from time-dependent density-functional response theory: characterization and correction of the time-dependent local density approximation ionization threshold. *J Chem Phys* 108:4439

61. Matsuzawa NN, Ishitani A, Uda T (2001) Time-dependent density functional theory calculations of photoabsorption spectra in the vacuum ultraviolet region. *J Phys Chem A* 105:4953–4962
62. Li XN, Wu ZJ, Liu XJ, Zhang HJ (2009) Theoretical studies on electronic structures, spectra and charge transporting properties of a series of Pt(C<sup>λ</sup>N)<sub>2</sub> complexes. *Synth Met* 159:1090–1098
63. Li XN, Wu ZJ, Liu XJ, Zhang H (2010) Comparative study of electronic structure and optical properties of a series of Pt(II) complexes containing different electron-donating and -withdrawing groups: a DFT study. *J Phys Org Chem* 23:181–189
64. Adamo C, Barone V (2000) Inexpensive and accurate predictions of optical excitations in transition-metal complexes: the TDDFT/PBE0 route. *Theor Chem Acc* 105:169
65. Frisch MJ et al (2009) Gaussian 09, revision B.01, Gaussian Inc., Wallingford
66. Roy DN, Chattaraj PK (2008) Reactivity, selectivity and aromaticity of Be<sub>3</sub><sup>2-</sup> and its complexes. *J Phys Chem A* 112:1612–1621

## COMMUNICATION

# Intermolecular Interaction in 2-Aminopyridine: A Density Functional Study

Manoj Majumder, Tamal Goswami, Anirban Misra<sup>1\*</sup>, Soumik Bardhan, Swapan

K. Saha<sup>2\*</sup>

*Department of Chemistry, University of North Bengal, Siliguri 734013, West Bengal, India*

Received 3 July 2013; Accepted (in revised version) 30 July 2013

---

**Abstract:** The absorption and fluorescence property of 2-amino pyridine (2-AP) and its dimer (2AP)<sub>2</sub> have been investigated using dispersion corrected density functional theory (DFT-D) method using B3LYP-D functional along with triple- $\zeta$  TZ2P basis in ADF suite of program. For the equilibrium geometries of the dimer, the ETS-NOCV calculations are performed. The formation of H-bond has been confirmed by the calculation of synergy ( $\Delta E_{syn}$ ) as well as from the spectral shift. A close agreement of the calculated spectra with that of experimental results has been found suggesting the dimers to be the preferable states of 2-AP in water medium.

**AMS subject classifications:** 74E40, 78M50

**Key words:** Density functional theory, 2-amino pyridine, absorption, fluorescence, H-bond

---

The excited state relaxation is of paramount importance in the photochemical process. Recently it has been noticed that the excited state relaxation can be induced through intermolecular Hydrogen bonding [1-4]. Photo induced proton-coupled electron transfers, where the proton donor and acceptor are held together by hydrogen bond (H-bond), have attracted considerable interest in recent years [5]. A number of studies by Han and co-workers [6-12] have shown that the gradual strengthening of the H-bond brings about the stabilization of the electronically excited state. H-bonded systems are ubiquitous within the

---

<sup>1</sup> Corresponding author. *Email address:* [anirbanmisra@yahoo.com](mailto:anirbanmisra@yahoo.com)

<sup>2</sup> Corresponding author. *Email address:* [ssahanbu@hotmail.com](mailto:ssahanbu@hotmail.com)

<http://www.global-sci.org/cicc>

biological macromolecules and hence the H-bond induced relaxation of excited state is deemed to be important in biological systems as well (13-15, 16). Pyridine and its derivatives are currently finding immense interest in the scientific community due to their luminescence property. Some of amino pyridine derivatives show anaesthetic properties and are used as drugs for certain brain disease [17-19]. 2-amino pyridine (2-AP) is used in the preparation of cytidine which is used as drug [20]. In spite of this biomedical application the photochemistry of this molecule has not been thoroughly investigated.

In this study we report a systematic density functional investigation of the absorption and fluorescence property of 2-amino pyridine (2-AP) and its dimer (2AP)<sub>2</sub>. As the dimerization of 2-AP occurs through hydrogen bonding (H-bonding), it becomes essential to unveil the effect of intermolecular H-bonding interactions in the photochemical behaviour of 2-AP. It has been reported earlier that H-bonding plays a pivotal role in the photochemical description of a molecule. Moreover, the simple electronic structure of this compound offers simplicity and encourages studying the effect of H-bonding interaction in the photochemistry of this compound as a benchmark.

For the computation of weak interactions like H-bond, the correlated *ab initio* techniques such as second-order Møller-Plesset perturbation theory (MP2) are in wide use [21]. In recent years *ab initio* and density functional theory (DFT) based methods have become popular tool in the investigations of structure and electronic properties of molecules. DFT offers a cost effective way for the quantum chemical investigation of the molecular properties and has been proved to be efficient in producing accurate results [22]. Although the density functional methods, like the popular B3LYP functional, are reported to be incompetent for the accurate description of H-bonding [23], the inclusion of correction due to dispersion interactions in the scenario has been proved to be effective. In the present work, we opted for the dispersion corrected DFT (DFT-D) method for the computation of absorption and fluorescence spectra. All the DFT and time dependent DFT (TDDFT) calculations are performed using ADF suit of program [24]. The B3LYP functional has been used, augmented with dispersion correction developed by Grimme (B3LYP-D) [25], along with triple- $\zeta$  TZ2P basis. The solvent effects have been estimated using the conductor-like screening model (COSMO) implemented in ADF [26].

Structures of the monomer and the dimer are optimized at the B3LYP-D/TZ2P level. The optimized ground state structures of the monomer and the dimer are represented in Figures 1 and 2. The dimer is found to prefer a non-planar geometry at ground and excited states (Figure 2).

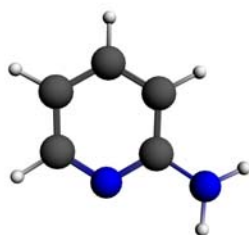


**Figure 1:** B3LYP-D/TZ2P optimized geometry of 2-Aminopyridine at its ground state.

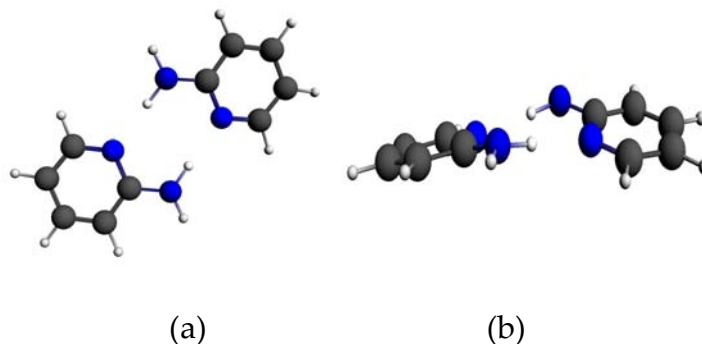


**Figure 2:** The H-bonded dimer (a) front view and (b) side view

To reveal the cooperativity due to H-bonding, an energy decomposition analysis (EDA) in the framework of the Kohn-Sham molecular orbital (MO) model is performed. In this approach, the interaction energy ( $\Delta E_{int}$ ) is partitioned into electrostatic interaction ( $\Delta V_{elstat}$ ), Pauli repulsive orbital interaction ( $\Delta E_{pauli}$ ), attractive orbital interaction ( $\Delta E_{oi}$ ) and dispersion interactions ( $\Delta E_{disp}$ ) as shown in the following,

$$\Delta E_{int} = \Delta V_{elstat} + \Delta E_{pauli} + \Delta E_{oi} + \Delta E_{disp} \quad (1)$$

This method combines the extended transition state (ETS) energy decomposition approach [27] with the natural orbitals for chemical valence (NOCV) density analysis method [28]. The ETS-NOCV calculations are performed for the equilibrium geometries of the ground and excited states of the dimer. The formation of H-bond has been confirmed by the calculation of synergy ( $\Delta E_{syn}$ ) from the difference of interaction energy ( $\Delta E_{int}$ ) with and without H-bond interactions

$$\Delta E_{syn} = \Delta E_{int-eq} - \Delta E_{int-noneq} \quad (2)$$

Here,  $\Delta E_{int-eq}$  corresponds to the interaction energy of the dimer in its equilibrium geometry. Next, the equilibrium geometry is distorted by moving the monomer units far from each other, so that no H-bond formation is possible, and the interaction energy ( $\Delta E_{int-$

*noneq*) is estimated. A negative value of synergy indicates stabilization through the formation of H-bonding.  $\Delta E_{int}$  is the energy change in systems due to formation of the association from individual units [29]. This is interpreted as the amount of energy required to promote the separated fragments to form the dimeric structure [30]. The synergy due to H-bonding is estimated through eq 2 and the results are given in Table 1.

**Table 1:** Bonding energy (kcal/mol) decomposition of ground and excited states of the dimer

Dimer	$\Delta V_{elstat}$	$\Delta E_{pauli}$	$\Delta E_{oi}$	$\Delta E_{disp}$	$\Delta E_{int}$	$\Delta E_{syn}$
Distorted Geometry	-0.30	-0.12	-0.03	-0.07	-0.52	--
Excited State	-25.93	29.92	-14.64	-4.30	-14.94	-14.42
Ground State	-26.24	30.31	-14.85	-4.26	-15.05	-14.53

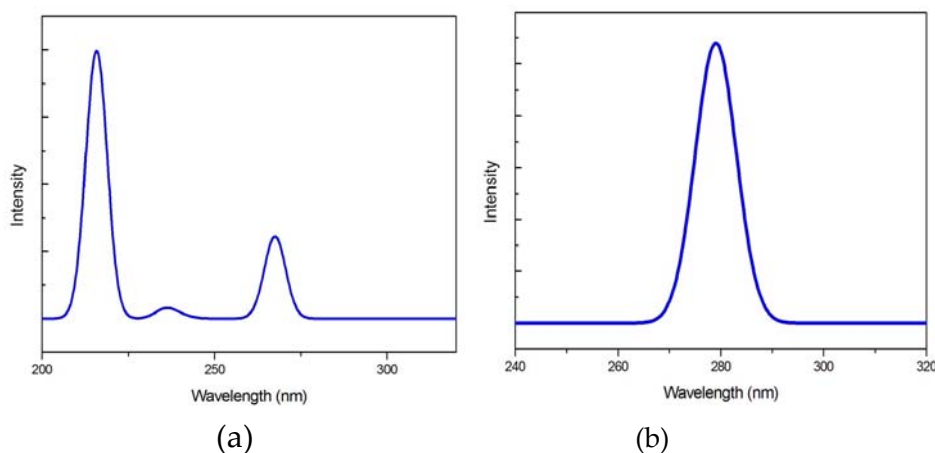


**Figure 3:** Absorption Spectra of (a) monomer unit and (b) hydrogen bonded dimer.

From Table 1, it is clear that the hydrogen-bond formation is possible at both the ground and excited states. From the comparison of  $\Delta E_{syn}$  values in Table 1, one can infer a greater stabilization of the H-bonded dimer at its ground state than the corresponding excited state. However, from the components of  $\Delta E_{int}$  it is observed that the dispersion energy change ( $\Delta E_{disp}$ ), which corresponds to the H-bonding interaction, is greater in the excited state than the ground state. Hence, it can be concluded that the H-bonding interaction is strengthened at the excited state.

The absorption and fluorescence spectra are shown in Figures 3 and 4. It becomes prominent from the figures that there occurs a red-shift of the absorption and fluorescence peaks in the dimeric state compared to the monomer (Table 2). This red-shift can be attributed to the lowering in the HOMO-LUMO gap ( $\Delta E_{HL}$ ) due to H-bond formation. Table

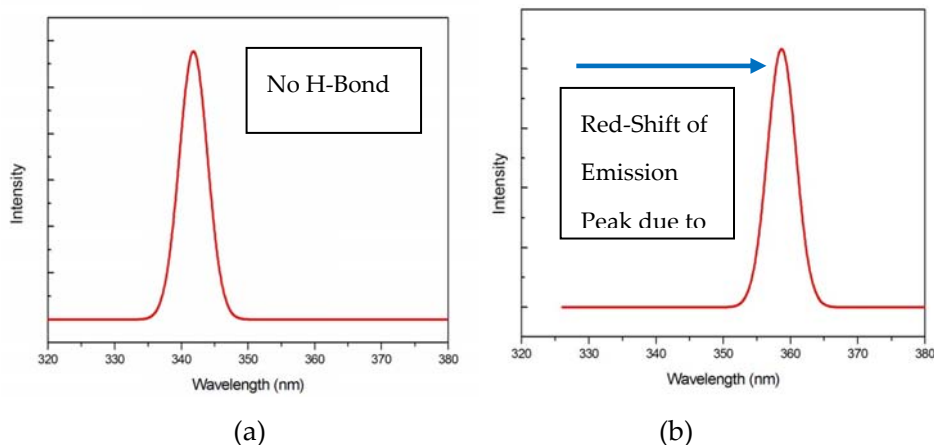
3 accumulates the HOMOs and the LUMOs of the species in its different states and a lowering of the  $\Delta E_{HL}$  is clearly visible. From the previous studies on H-bonded systems it becomes evident that polarization effects promote H-bonding interaction [31]. It has also been seen that there occurs a mixing of the empty/occupied orbital on one fragment in the presence of another fragment due to polarization effect. From the nature of the HOMO and LUMO orbitals in Table 3, the mixing of two fragments is critically exposed. Hence, the diminished HOMO-LUMO gap can be explained as an outcome of the H-bonding interaction [32-33].

**Table 2:** Comparison of the calculated value  $\lambda_{max}$  of absorption and fluorescence with experimentally reported values.

System	$\lambda_{max}$ of absorption in nm		$\lambda_{max}$ of fluorescence in nm	
	Calculated	Experimental	Calculated	Experimental
2-AMP monomer	216	292 <sup>(a)</sup>	342	363 <sup>(a)</sup>
2-AMP dimer	279		359	

<sup>(a)</sup> Experimentally reported (in reference [37])  $\lambda_{max}$  of absorption and fluorescence in water medium

The red-shift in the fluorescence spectra can be explained from the stabilization of the  $S_1$  electronic state of the dimer due to the formation of the H-bonding. The decrease in the energy gap for the  $S_0 \leftarrow S_1$  leads to a red-shift of the fluorescence  $\lambda_{max}$  value.

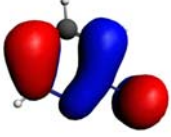
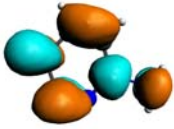
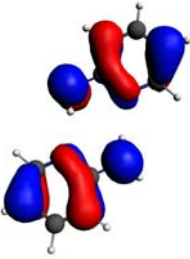
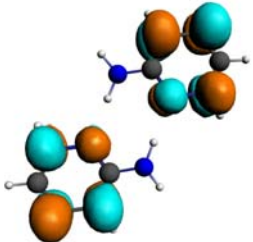


**Figure 4:** Fluorescence Spectra of (a) monomer unit and (b) hydrogen bonded dimer.

The calculated values of  $\lambda_{max}$  of both the absorption and fluorescence spectra of the 2-AP monomer and dimer are given in Table 2. The close agreement of the calculated values with

the experimental results suggests that the dimers are the most preferable states of 2-AP in water solution. This can also be inferred from the Table 1 since the high negative synergy of the dimer in both the ground and excited states indicates the formation of H-bonding. The formation or the change in the strength of the intermolecular hydrogen bonds following the excitation, may simply lead to new vibronic dissipative modes that couple the excited and the ground states [34-36]. Hence, the study of relaxation induced red shift in the emission spectra due to strengthening of H-bond seems to be useful tool to unveil many biological systems [38].

**Table 3:** HOMOs and LUMOs of the monomer and the dimer with corresponding energy values and HOMO-LUMO gap ( $\Delta E_{HL}$ ).

System	Orbitals	Energy in eV	$\Delta E_{HL}$ in eV
2-AP monomer	 HOMO	-5.8743	6.0044
	 LUMO	0.1257	
2-AP dimer	 HOMO	-5.6443	4.9446
	 LUMO	-0.6997	

## Acknowledgement:

Financial assistance from the UGC, New Delhi, India, under Special Assistance Programme is gratefully acknowledged. TG thanks CSIR, New Delhi, India for Senior Research Fellowship. S.B thanks UGC, New Delhi, India for UGC-BSR Research Fellowship.

## References

- [1] N. Mataga, Y. Kaibe, M. Koizumi, Equilibrium of hydrogen-bond formation in the excited state, *Nature*, 175 (1955), 731-732.
- [2] J. Herbich, M. Kijak, A. Zielin'ska, R. P. Thummel, J. Waluk, Fluorescence quenching by pyridine and derivatives induced by intermolecular hydrogen bonding to pyrrole-containing heteroaromatics, *J. Phys. Chem. A*, 106 (2002), 2158-2163.
- [3] T. Yatsunami, H. Inoue, Molecular mechanism of radiationless deactivation of amino anthraquinones through intermolecular hydrogen-bonding interaction with alcohols and hydroperoxides, *J. Phys. Chem. A*, 101 (1997), 8166-8173.
- [4] L. Biczok, P. Valat, V. Wintgens, Effect of molecular structure and hydrogen bonding on the fluorescence of hydroxy-substituted naphthalimides, *Phys. Chem. Chem. Phys.*, 1 (1999), 4759-4766.
- [5] H. Miyasaka, A. Tabata, S. Ojima, N. Ikeda, N. Mataga, Femtosecond-picosecond laser photolysis studies on the mechanisms of fluorescence quenching induced by hydrogen-bonding interactions - 1-pyrenol-pyridine systems, *J. Phys. Chem.*, 97 (1993), 8222-8228.
- [6] G.-J. Zhao, K.-L. Han, Early time hydrogen-bonding dynamics of photoexcited coumarin 102 in hydrogen-donating solvents: Theoretical Study, *J. Phys. Chem. A*, 111 (2007), 2469-2474.
- [7] G.-J. Zhao, K.-L. Han, Ultrafast hydrogen bond strengthening of the photoexcited fluorenone in alcohols for facilitating the fluorescence quenching *J. Phys. Chem. A* 111 (2007), 9218-9223.
- [8] G.-J. Zhao, J.-Y. Liu, L.-C. Zhou, K.-L. Han, Site-selective photo induced electron transfer from alcoholic solvents to the chromophore facilitated by hydrogen bonding: a new fluorescence quenching mechanism, *J. Phys. Chem. B*, 111 (2007), 8940-8945.
- [9] G.-J. Zhao, K.-L. Han, Novel infrared spectra for intermolecular dihydrogen bonding of the phenol-borane-trimethylamine complex in electronically excited state, *J. Chem. Phys.*, 127 (2007), 024306-6.
- [10] G.-J. Zhao, K.-L. Han, Y.-B. Lei, Y.-S. Dou, Ultrafast excited-state dynamics of tetraphenylethylene studied by semiclassical simulation, *J. Chem. Phys.*, 127 (2007), 094307-6.
- [11] G.-J. Zhao, Y.-H. Liu, K.-L. Han, Y. Dou, Dynamic simulation study on ultrafast excited-state torsional dynamics of 9,9'-bianthryl (BA) in gas phase: Real-time observation of novel oscillation behavior with the torsional coordinate, *Chem. Phys. Lett.* 453 (2008), 29-34.

- [12] G.-J. Zhao, K.-L. Han, Time-dependent density functional theory study on hydrogen-bonded intramolecular charge-transfer excited state of 4-dimethylamino-benzonitrile in methanol, *J. Comput. Chem.*, DOI: 10.1002/jcc.20957.
- [13] D. J. Heyes, C. N. Hunter, I. H. M. van Stokkum, R. van Grondelle, Ultrafast enzymatic reaction dynamics in protochlorophyllide oxidoreductase, *Nat. Struct. Biol.*, 10 (2003), 491–492.
- [14] H. Deng, R. Callender, E. Howell, Vibrational structure of dihydrofolate bound to R67 dihydrofolate reductase, *J. Biol. Chem.*, 276 (2001), 48956–48960.
- [15] H. Cheng, I. Nikolic-Hughes, J. H. H. Wang, H. Deng, P. J. O'Brien, L. Wu, Z. Y. Zhang, D. Herschlag, R. Callender, Environmental effects on phosphoryl group bonding probed by vibrational spectroscopy: implications for understanding phosphoryl transfer and enzymatic catalysis, *J. Am. Chem. Soc.*, 124 (2002), 11295–11306.
- [16] G.-J. Zhao, K.-L. Han, Site-specific solvation of the photoexcited protochlorophyllide a in methanol: formation of the hydrogen-bonded intermediate state induced by hydrogen-bond strengthening, *Biophys. J.*, 94 (2008), 38–46.
- [17] K. J. Smith, P. A. Felts, G. R. John, *J. Neurology*, 123 (1999), 171-184.
- [18] S Sedehzadeh, M. Keogh, P. Maddison, The use of aminopyridines in neurological disorders, *Clin. Neuropharmacol.*, 35 (2012) 191-200.
- [19] R. R. Hansebout, A. R. Blight, S. Fawcett, K. Reddy, 4-Aminopyridine in chronic spinal cord injury: a controlled, double-blind, crossover study in eight patients, *J. Neurotrauma.*, 10 (1993), 1-18.
- [20] A. W. Fraley, D. Chen, K. Johnson, L. W. McLaughlin, An HIV reverse transcriptase-selective nucleoside chain terminator, *J. Am. Chem. Soc.*, 125 (2003), 616–617.
- [21] S. Suzuki, P. G. Green, R. E. Bumgarner, S. Dasgupta, W. A. Goddard, G. A. Blake, Benzene forms hydrogen bonds with water, *Science*, 257 (1992), 942-944. P. Tarakeshwar, S. J. Lee, J. Y. Lee, K. S. Kim, Benzene-hydrogen halide interactions: Theoretical studies of binding energies, vibrational frequencies, and equilibrium structures, *J. Chem. Phys.*, 108 (1998), 7217-7223. D. Feller, Strength of the benzene–water hydrogen bond, *J. Phys. Chem. A*, 103 (1999), 7558-7561. P. Tarakeshwar, K. S. Kim, B. Brutschy, Interaction of the water dimer with p-systems: A theoretical investigation of structures, energies, and vibrational frequencies, *J. Chem. Phys.*, 112 (2000), 1769-1781. T. van Mourik, S. L. Price, D. C. Clary, Ab initio calculations on indole–water, 1-methylindole–water and indole–(water)<sub>2</sub>, *Chem. Phys. Lett.*, 331 (2000), 253-261. T. van Mourik, Comment on “Theoretical study of indole: protonation, indolyl radical, tautomers of indole, and its interaction with water”, *Chem. Phys.*, 304 (2004), 317-319. P. Tarakeshwar, H. S. Choi, K. S. Kim, Olefinic vs aromatic  $\pi$ -h interaction: A theoretical investigation of the nature of interaction of first-row hydrides with ethene and benzene, *J. Am. Chem. Soc.*, 123 (2001), 3323-3331.
- [22] S. Shil, D. Bhattacharya, S. Sarkar, A. Misra, Performance of the widely used minnesota density functionals for the prediction of heat of formations, ionization potentials of some benchmarked first row transition metal Complexes, *J. Phys. Chem. A*, 117 (2013), 4945–4955.

- [23] S. Tsuzuki, H. P. Luthi, Interaction energies of van der Waals and hydrogen bonded systems calculated using density functional theory: Assessing the PW91 model, *J. Chem. Phys.* 114 (2001), 3949-3957. Y. Zhao, D. G. Truhlar, Hybrid meta density functional theory methods for thermochemistry, thermochemical kinetics, and noncovalent interactions: The mpw1b95 and mpwb1k models and comparative assessments for hydrogen bonding and van der waals interactions, *J. Phys. Chem. A*, 108 (2004), 6908-6918. Y. Zhao, D. G. Truhlar, Benchmark databases for nonbonded interactions and their use to test density functional theory, *J. Chem. Theory Comput.*, 1 (2005), 415-432.
- [24] Computer code ADF2010.01, SCM, Theoretical Chemistry, Vrije Universiteit, Amsterdam, The Netherlands, <http://www.scm.com>.
- [25] S. Grimme, Accurate description of van der Waals complexes by density functional theory including empirical corrections, *J. Comput. Chem.*, 25 (2004), 1463-1473. S. Grimme, Semiempirical GGA-type density functional constructed with a long-range dispersion correction, *J. Comput. Chem.*, 27 (2006), 1787-1799.
- [26] A. Klamt, G. Schüürmann, COSMO: A new approach to dielectric screening in solvents with explicit expressions for the screening energy and its gradient, *J. Chem. Soc. Perkin Trans. 2* (1993), 799-805. A. Klamt, Conductor-like screening model for real solvents: A new approach to the quantitative calculation of solvation phenomena, *J. Phys. Chem.*, 99 (1995), 2224-2235. C. C. Pye, T. Ziegler, An implementation of the conductor-like screening model of solvation within the Amsterdam density functional package, *Theor. Chem. Acta*, 101 (1999), 396-408.
- [27] T. Ziegler, A. Rauk, Carbon monoxide, carbon monosulfide, molecular nitrogen, phosphorus trifluoride, and methyl isocyanide as  $\sigma$  donors and  $\pi$  acceptors. A theoretical study by the Hartree-Fock-Slater transition-state method, *Inorg. Chem.*, 18 (1979), 1755-1759. T. Ziegler, A. Rauk, On the calculation of bonding energies by the Hartree Fock Slater method, *Theor. Chim. Acta* 46 (1977), 1-10.
- [28] M. Mitoraj, A. Michalak, Natural orbitals for chemical valence as descriptors of chemical bonding in transition metal complexes, *J. Mol. Model*, 13 (2007), 347-355. M. Srebro, A. Michalak, Theoretical analysis of bonding in n-heterocyclic carbene-rhodium complexes, *Inorg. Chem.*, 48 (2009) 5361-5369. A. Michalak, M. Mitoraj, T. Ziegler, Bond orbitals from chemical valence theory, *J. Phys. Chem. A*, 112 (2008) 1933-1939.
- [29] C. F. Guerra, H. Zijlstra, G. Paragi, F. M. Bickelhaupt, Telomere structure and stability: covalency in hydrogen bonds, not resonance assistance, causes cooperativity in guanine quartets, *Chem. Eur. J.*, 17 (2011), 12612 - 12622.
- [30] M. P. Mitoraj, R. Kurczab, M. Boczar, A. Michalak, Theoretical description of hydrogen bonding in oxalic acid dimer and trimer based on the combined extended-transition-state energy decomposition analysis and natural orbitals for chemical valence (ETS-NOCV), *J. Mol. Model*, 16 (2010) 1789-1795.

- [31] L. X. Dang, Importance of polarization effects in modeling the hydrogen bond in water using classical molecular dynamics techniques, *J. Phys. Chem. B*, 102 (1998), 620-624. Y.-F. Chen, J. J. Dannenberg, The effect of polarization on multiple hydrogen-bond formation in models of self-assembling materials, *J. Comput. Chem.*, 32 (2011), 2890–2895.
- [32] G.-J. Zhao, K.-L. Han, Hydrogen bonding in the electronic excited state, *Accounts Chem. Research*, 45 (2012), 404 – 413.
- [33] Y.-H. Liu, M. S. Mehata, J.-Y. Liu, Excited-state proton transfer via hydrogen-bonded acetic acid (acoh) wire for 6-hydroxyquinoline, *J. Phys. Chem. A*, 115 (2011), 19–24.
- [34] J. Herbich, J. Waluk, R. P. Thummel, C.-Y. Hung, Mechanisms of fluorescence quenching by hydrogen bonding in various aza aromatics, *J. Photochem. Photobiol. A: Chem.*, 80 (1994) 157-160.
- [35] L. Biczó'k, T. Berces, H. Linschitz, Quenching processes in hydrogen-bonded pairs: interactions of excited fluorenone with alcohols and phenols, *J. Am. Chem. Soc.*, 119 (1997) 11071-11077.
- [36] T. Yatsunami, H. Inoue, Molecular mechanism of radiationless deactivation of aminoanthraquinones through intermolecular hydrogen-bonding interaction with alcohols and hydroperoxides, *J. Phys. Chem. A*, 101 (1997) 8166-8173.
- [37] A. Weisstuch, A. C. Testa Fluorescence study of aminopyridines, *J. Phys. Chem.*, 72 (1968), 1982–1987.
- [38] M. A. Thompson, M. C. Zerner, On the red shift of the bacteriochlorophyll-b dimer spectra, *J. Am. Chem. Soc.* 110 (1988), 606-607.